ETH Institute for
Particle Physics

Spectroscopy in
ep Scattering at HERA

A dissertation submitted to the

Swiss Federal Institute of Technology Zurich

for the degree of

Doctor of Sciences
(Dr. sc. ETH Zürich)

presented by

Marc A. Del Degan

Dipl. Phys. ETH
born on April 14, 1978
citizen of Buja (Italy)

accepted on the recommendation of
Prof. Dr. Ralph Eichler, examiner and
Prof. Dr. Urs Langenegger, co-examiner

2008

Abstract

The production of neutral strange mesons K_s^0 and strange baryons Λ is studied with the H1 experiment at the electron-proton collider HERA. The measurements are performed using deep-inelastic scattering events in the phase space defined by the negative four-momentum transfer squared of the photon $2 < Q^2 < 100\,\mathrm{GeV}^2$, the inelasticity $0.1 < y < 0.6$, the transverse momentum of the strange hadrons $0.5 < p_T < 3.5\,\mathrm{GeV}$ and the pseudorapidity $-1.3 < \eta < 1.3$. The K_s^0 and Λ production cross-sections are found to be:

$$\sigma_{vis}(ep \to e'K_s^0 X) = 21.18 \pm 0.09(\text{stat.})^{+1.19}_{-1.23}(\text{syst.})\ \text{nb},$$

$$\sigma_{vis}(ep \to e'[\Lambda + \overline{\Lambda}]X) = 7.88 \pm 0.10(\text{stat.})^{+0.45}_{-0.47}(\text{syst.})\ \text{nb}.$$

The $\Lambda - \overline{\Lambda}$ asymmetry is measured and found to be consistent with zero. Predictions by leading order calculations are compared to the data. In general the predictions are able to describe the overall features of the measurements, however they fail in specific details. Constraints on the hadronisation parameters within the Lund model of string fragmentation are derived.

Furthermore, a search for narrow baryonic resonances decaying into $\Xi^-\pi^-$ or $\Xi^-\pi^+$ and their antiparticles is carried out in the deep-inelastic scattering regime at HERA. No signal is observed for a new baryonic state in the mass range $1.6-2.3\,\mathrm{GeV}$ in either the double charged or neutral decay channels. The known baryon $\Xi(1530)^0$ is observed through its decay mode into $\Xi^-\pi^+$. Upper limits are derived on the ratio of the production rates of new baryonic states, such as the hypothetical pentaquark states Ξ_{5q}^{--} or Ξ_{5q}^0, to the $\Xi(1530)^0$ baryon state.

A search for new particles decaying into $K_s^0\Lambda$ is performed. A possible resonant structure of 48 ± 12 events at a mass of $1.71\,\mathrm{GeV}$ is observed. The width of this resonance is found to be compatible with the detector resolution of about $5\,\mathrm{MeV}$. A possible interpretation of the observed structure as the pentaquark state N_s^0 is discussed.

Zusammenfassung

Mit dem H1-Experiment am Elektron-Proton-Beschleuniger HERA wird eine neue Messung der neutralen, seltsamen K_s^0 Mesonen und Λ Baryonen durchgeführt. Für die Messung werden tief-inelastische ep Ereignisse verwendet. Der Phasenraum der Messung ist durch den Betrag des Viererimpulsübertrages, Q^2, die Inelastizität, y, sowie des transversalen Impulses, p_T, der seltsamen Hadronen und deren Pseudorapidität, η, festgelegt: $2 < Q^2 < 100\,\mathrm{GeV}^2$, $0.1 < y < 0.6$, $0.5 < p_T < 3.5\,\mathrm{GeV}$ und $-1.3 < \eta < 1.3$. Die Produktionswirkungsquerschnitte der K_s^0 und Λ Hadronen bestimmen sich zu:

$$\sigma_{vis}(ep \to e'K_s^0 X) = 21.18 \pm 0.09(\text{stat.})^{+1.19}_{-1.23}(\text{syst.})\ \mathrm{nb},$$

$$\sigma_{vis}(ep \to e'[\Lambda + \overline{\Lambda}]X) = 7.88 \pm 0.10(\text{stat.})^{+0.45}_{-0.47}(\text{syst.})\ \mathrm{nb}.$$

Des Weiteren wird die Asymmetrie der Λ Produktion gemessen. Es wurde keine Asymmetrie festgestellt. Die Vorhersagen von Berechnungen in führender Ordnung werden mit den Daten verglichen. Im Allgemeinen beschreiben die Vorhersagen die Daten gut, obwohl die spezifischen Details der Messung nicht immer wiedergegeben werden. Aus den Messungen werden einige der freien Parameter des Lund String-Fragmentationsmodelles bestimmt.

In einer zweiten Analyse wird eine Suche nach neuen baryonischen Resonanzen im Zerfallskanal $\Xi^-\pi^-$ und $\Xi^-\pi^+$ sowie deren Antiteilchen durchgeführt. Dazu werden wiederum Daten der tief-inelastischen ep Streuung verwendet. Im Massenbereich von 1.6 bis 2.3 GeV wurden keine neuen baryonischen Zustände gefunden; weder im geladenen noch im neutralen Zerfallskanal. Das etablierte $\Xi(1530)^0$ Baryon wird im Zerfallskanal $\Xi^-\pi^+$ nachgewiesen. Aus den gemessenen Verteilungen werden obere Grenzen für die Produktionsraten von neuen baryonischen Zuständen, wie zum Beispiel der hypothetischen Pentaquarks Ξ_{5q}^{--} oder Ξ_{5q}^0, relativ zu derjenigen des $\Xi(1530)^0$ Baryons extrahiert.

Ausserdem wird eine Suche nach neuen Teilchen, die in ein K_s^0 Meson und ein Λ Baryon zerfallen, präsentiert. Es wird eine mögliche Resonanz von 48 ± 12 Ereignissen bei einer Masse von 1.71 GeV beobachtet. Die Breite dieser Resonanz ist mit der Detektorauflösung von ungefähr 5 MeV verträglich. Eine Interpretation der Beobachtung als Pentaquark N_s^0 wird diskutiert.

Contents

Dedicated to Jana Alina and Dario Leandro, my children

Chapter 1

Introduction

The standard model of particle physics (SM) is a very successful theory in describing the structure of matter and its interactions. The main building blocks of the SM are elementary fermions, the quarks and the leptons, as well as the interaction between these particles, the electromagnetic, the weak and the strong interaction. The gravitational force is not explored within the SM. The forces are described by quantum field theories where the interaction of particles is explained by the exchange of gauge bosons. In case of the electromagnetic force the exchanged particle is a photon described by quantum electrodynamics (QED), while for the weak interaction the exchanged bosons are the $W^\pm$ and the Z^0. The strong force is mediated by so-called gluons which are described within the quantum chromodynamics (QCD). In the following an overview of the developments leading to the SM is discussed.

The long way to our present understanding of matter and its interactions started as early as 1897 when J. Thomson discovered the electron [1]. A next step forward was achieved by E. Rutherford who has discovered the atomic nucleus in 1911 by his famous experiments with α particles [2] [1]. In the early thirties of the last century three further particles have been observed: The neutron by Chadwick [3], the positron by Anderson [4] and the muon by J. C. Street and E. C. Stevenson [5]. The muon was discovered with a cloud chamber in the cosmic rays in 1937. Following the idea of QED, H. Yukawa had suggested two years earlier that the strong interaction is mediated by a massive particle [6] with a mass around $100\,\mathrm{MeV}$. The newly discovered muon was a hot candidate for this particle because its mass was found to be close to that predicted by Yukawa. However, soon after the observation of muons it was clear that this particle is not participating in the strong interaction at all and the idea came up that the muon is a decay product of the mediating particle. It took another 10 years until a promising candidate was found. The pion was discovered in 1947 by C. Powell, C. Lattes, H. Muirhead and G. Occhialini in cosmic rays [7]. Soon after its discovery Powell's group announced the first observation of pions decaying into muons [8, 9]: The particle picture was beginning to take shape.

In the year 1947 another major discovery was achieved: the first observation of a Kaon decay by G. D. Rochester and C. C. Butler [10]. They have observed two special events in cosmic ray interactions using a cloud chamber. One turned out to be a decay of a neutral

---

[1]Prior to Rutherford's experiments the existence of atomic nuclei has been observed by E. Goldstein, but the experiments were misinterpreted.

particle into two charged ones and one of a charged particle into a charged and a neutral one. The mass of these particles was estimated to be roughly half of the proton mass. Further studies of these new particles have been carried out in the following years at the California Institute of Technology. A surprisingly long lifetime of these particles in the order of 10^{-10} s has been measured. Beside the Kaon another long living particle was discovered, the Lambda baryon. The long lifetime lead to the introduction of a new quantum number, the strangeness, by M. Gell-Mann and A. Pais [11]. The strangeness is found to be conserved in strong interactions but violated in weak interactions.

A huge progress in particle physics was achieved in 1953 with the commissioning of a new cyclotron for particle acceleration at the Brookhaven National Laboratory (BNL). This was the beginning of collider based particle physics experiments that lead to a wide variety of particle discoveries. This "particle zoo" was disentangled by Gell-Mann and Zweig in 1964 by introducing constituents (quarks) that make up the particles [12, 13] (Quark Parton Model, QPM). At that time all observed particles could be interpreted as bound states of an quark and an antiquark, $q\bar{q}$ (mesons), or of three quarks, qqq (baryons). For the quarks three different "types" have been needed, labeled up-, down- and strange quarks. The building blocks of the SM were completed by the discovery of the other three quarks (charm, bottom and top), the tau lepton with its corresponding neutrino and the gauge bosons $W^{\pm}$, Z^0 and the gluon [2].

In parallel to the exploration of the particle zoo, dedicated collider experiments at the Stanford Linear Accelerator Center (SLAC) in the fifties of the last century have started to explore the structure of the proton. In these experiments electrons were scattered elastically from atomic nuclei. The measured cross-section has differed from the expectation for the scattering at a point like target and R. Hofstadter concluded that the proton is not a point-like particle but has a spatial expansion [14]. In the late sixties the first deep-inelastic scattering (DIS) experiments have been performed at SLAC. The electron energies became large enough to resolve the proton. From these experiments it was concluded from J. I. Friedman, H. W. Kendall and R. E. Taylor that the nucleon has a substructure of point-like constituents [15]. This discovery was awarded with the physics Nobel prize of the year 1990. Further experiments have shown that these point-like constituents have spin $\frac{1}{2}$ and correspond to the quarks introduced by Gell-Mann and Zweig.

Beside this nearly complete picture of particles and their interactions provided by the SM, exotic states with other quark configurations as $q\bar{q}$ and qqq have been predicted since the early days of QCD. Such states could be hybrid baryons containing quarks and gluons (G) ($qqqG$) and multi-quark baryons like dibaryons ($qqqqqq$) or pentaquarks ($qqqq\bar{q}$). Dibaryon states have been proposed as early as 1977 [16]. An extensive search for such exotic states has been performed over the last decades. It took more than 30 years until the first promising candidate for such an exotic state had been observed. In 2003 the LEPS Collaboration [17] at SPring-8 announced a $4.6\,\sigma$ discovery of a new resonance, Θ^+, which was predicted by Diakonov *et al.* in 1997 [18] (originally denoted Z^+) in the reaction $\gamma\,^{12}C \rightarrow C'K^-\Theta^+ \rightarrow C'K^-(K^+n)$, with a mass of $1.54 \pm 0.01\,\text{GeV}$ and a width of less than $25\,\text{MeV}$. The Θ^+, having baryon number $+1$ and strangeness $+1$, cannot be a qqq state. Its minimal quark content is $uudd\bar{s}$. The observation of a pentaquark candidate is one of the most exciting events in particle spectroscopy of the past decades. The discovery of a manifestly exotic baryon is providing

---

[2]Actually, one piece is still missing: the higgs boson.

an opportunity to refine the understanding of quark dynamics at low energy where it is not perturbative.

Nowadays, the *ep* collider HERA (**H**adron-**E**lektron-**R**ing-**A**nlage) provides the unique possibility to study the structure of the proton at high energies. From the data collected by the two multi-purpose experiments H1 and ZEUS the structure of the proton is measured in a wide kinematic range. Another major achievement of HERA is the measurement of the running coupling constant of the strong interaction, α_s, at high precision, see figure 1.1. This coupling constant increases for large distances, resulting in a breakdown of the perturbative treatment of QCD at a certain (low) energy scale. The confinement of quarks into hadrons cannot be calculated from first principles and therefore phenomenological models are needed. An important contribution to the understanding of the QCD is provided by comparing the measured hadronic final state particles with the predictions obtained by these models.
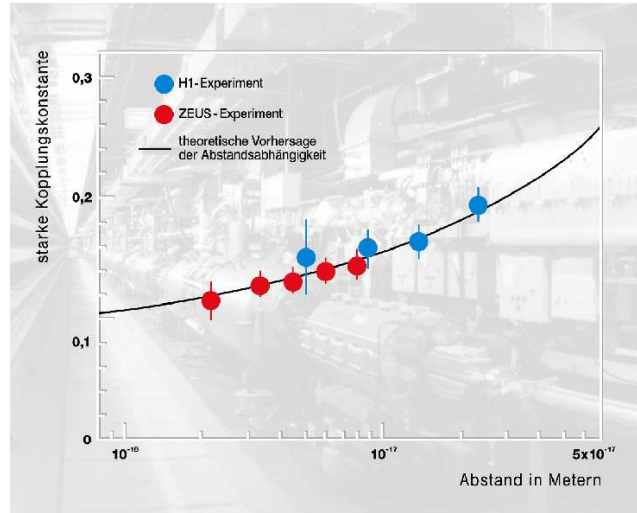
Figure 1.1: The strong coupling constant as measured at HERA.

Within the present work the production of the strange mesons K_s^0 and the strange baryons Λ in DIS events is measured. In contrast to the heavy quarks (charm and bottom) the strange quark production cannot be treated perturbatively due to its relatively light mass. Furthermore, the strange quarks are predominantly produced in the hadronisation process allowing to test the phenomenological models. With this measurement a contribution to the parameterisation of the QCD is provided. Beside this "bread and butter" measurement a search for potential pentaquark states is performed.

The thesis is structured as follows: The theoretical basics which are important for the presented measurements are introduced in chapter 2. This includes a general introduction to *ep* scattering as well as a summary of theoretical and experimental achievements related to strange hadrons and pentaquarks and an overview of the Monte Carlo generators used within this work. The main features of the HERA collider and the H1 experiment are given in chapter 3. After outlining the data selection and introducing some relevant technical issues, the measurement of the strange hadrons K_s^0 and Λ is presented in chapters 5 and 6. A comparison of the data with model predictions obtained from leading order Monte Carlo simulations is also provided in chapter 6. Furthermore, implications of the measured results on some of the model parameters are discussed. The measurement of the strange hadrons is about to be published [19].

The second part is dedicated to the search for narrow baryonic resonances in the $\Xi\pi$ decay channel. This analysis led directly to a publication [20].

In the last part a search for pentaquarks in the $K_s^0\Lambda$ decay channel is performed which was inspired by the results of the STAR Collaboration [21] and already examined within the author's diploma thesis [22].

Chapter 2

Theory

The theoretical basics of relevance to the measurements presented in the following chapters are introduced. In the first part, the scattering of electrons[1] on protons at HERA is described. In the second part, the properties of strange hadrons is recapitulated while in the last part a short introduction to Pentaquarks is presented.

2.1 Deep-Inelastic ep Scattering at HERA

At HERA electrons are brought to collision with protons at a center-of-mass energy of 319 GeV. This process can be described in leading order by the exchange of a virtual gauge boson, as illustrated in figure 2.1. Two basic classes of events are distinguished: The neutral
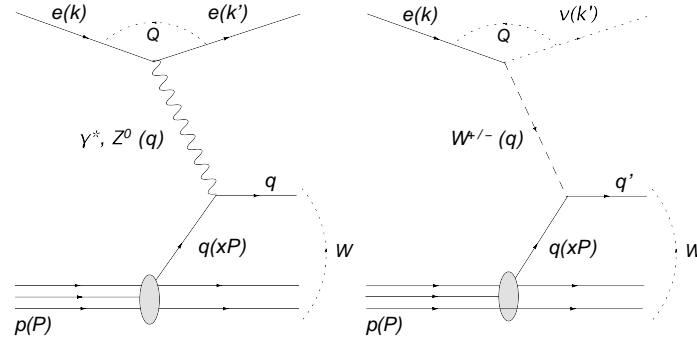
Figure 2.1: The Feynman diagram for leading order ep scattering in the neutral current (left) and in the charged current (right). The variables are described in the text.

current (NC) where the exchanged gauge boson is neutral (γ^* or Z^0) and the charged current (CC) where the boson carries electrical charge ($W^\pm$). In the first case the incoming electron is preserved: $e\,p \to e'\,X$ (X denotes the hadronic final state, including the proton remnant), while in CC events the electron transforms into a neutrino: $e\,p \to \nu_e\,X$. The exchange of the massive gauge bosons (Z^0 and $W^\pm$) is highly suppressed with respect to the virtual photon exchange at the energies relevant to this analysis (see section 2.1.2). Hence, the focus is turned on NC events.

---

[1]If not stated otherwise, the term "electron" is used generically to refer to both electrons and positrons.

2.1.1 Kinematics at HERA

The scattering process at HERA can be described by four Lorentz-invariant quantities which are expressed in terms of the four-vector of the incoming electron $\mathbf{k}$, the outgoing electron $\mathbf{k}'$, the incoming proton $\mathbf{P}$ and the exchanged boson $\mathbf{q}$ [23]:

$$s = (\mathbf{P} + \mathbf{k})^2 \tag{2.1}$$

$$Q^2 = -(\mathbf{k} - \mathbf{k}')^2 = -q^2 \tag{2.2}$$

$$y = \frac{\mathbf{P} \cdot \mathbf{q}}{\mathbf{P} \cdot \mathbf{k}} \tag{2.3}$$

$$x = \frac{Q^2}{2\mathbf{P} \cdot \mathbf{q}}. \tag{2.4}$$

Here $\sqrt{s}$ is the center-of-mass energy of the electron proton system. In the case of negligible particle masses ($m_{e/p} \ll E_{e/p}$), the center-of-mass energy can be written as:

$$\sqrt{s} \approx \sqrt{4E_e E_p}. \tag{2.5}$$

For the HERA beam energies $E_e = 27.6\,\text{GeV}$ and $E_p = 920\,\text{GeV}$ ($820\,\text{GeV}$ before 1999) the center-of-mass energy is $319\,\text{GeV}$ ($301\,\text{GeV}$). The negative photon four-momentum transfer squared, Q^2, is also known as the virtuality of the exchanged photon and is related to the energy E_e' and the polar angle θ_e (see figure 3.3) of the scattered electron by:

$$Q^2 = 4E_e E_e' \cos^2(\frac{\theta_e}{2}). \tag{2.6}$$

The resolution power Δb of the exchanged boson is given by:

$$\Delta b \sim \frac{\hbar c}{\sqrt{Q^2}} = \frac{0.197}{\sqrt{Q^2}}\,\text{GeV fm}. \tag{2.7}$$

At HERA two regimes are distinguished: *Photoproduction* ($Q^2 \approx 0\,\text{GeV}^2$) where a quasi-free photon is exchanged and *Deep-Inelastic Scattering, DIS* ($Q^2 \gtrsim 1\,\text{GeV}^2$) where a virtual photon (or a Z^0, $W^\pm$) is exchanged. For the analysis presented here the focus is turned on DIS events. In the proton rest frame, the inelasticity y gives the relative energy loss of the scattered electron and can be expressed as:

$$y = 1 - \frac{E_e'}{E_e} \sin^2(\frac{\theta_e}{2}). \tag{2.8}$$

The Bjorken scaling variable x corresponds (in the Quark Parton Model) to the energy fraction of the incoming proton that is carried by the struck quark and therefore going into the hard interaction. By neglecting the electron and the proton masses these four quantities are related by:

$$Q^2 = xys. \tag{2.9}$$

Another quantity being used to describe the scattering process is the invariant mass of the hadronic final state, W, given by:

$$W^2 = (q + P)^2 = ys - Q^2 + m_p^2, \tag{2.10}$$

where m_p denotes the proton mass.

2.1.2   Structure Functions and Inclusive *ep* Cross-Section

The differential cross-section for inelastic electron proton scattering as shown in figure 2.1 is given in its most general form by a contraction of the leptonic tensor, $L^e_{\mu\nu}$, and the hadronic tensor, $W^{\mu\nu}$ (see for example [24] or [25]):

$$d\sigma \sim L^e_{\mu\nu} W^{\mu\nu}. \tag{2.11}$$

The leptonic and hadronic tensors describe the current at the corresponding vertices. While the leptonic part is calculable from the electroweak theory, the hadronic tensor is parameterizing the ignorance of the form of the current at the proton vertex. The most general form of the hadronic tensor is given by [24]:

$$\begin{aligned}
W^{\mu\nu} &= -W_1 g^{\mu\nu} + p^\mu p^\nu \frac{W_2}{m^2} - i\epsilon^{\mu\nu\alpha\beta} p_\alpha p_\beta \frac{W_3}{2m^2} \\
&\quad + q^\mu q^\nu \frac{W_4}{m^2} + (p^\mu q^\nu + q^\mu q^\nu) \frac{W_5}{m^2} + i(p^\mu p^\nu - q^\nu q^\mu) \frac{W_6}{2m^2},
\end{aligned} \tag{2.12}$$

where $g^{\mu\nu}$ is the metric, p^μ is the four vector of the incoming proton, m its mass and q^μ that one of the exchanged gauge boson. Equation 2.12 can be simplified since not all terms can contribute to the cross-section. The asymmetric term proportional to W_6 is absent for unpolarised scattering. The term proportional to W_3 is parity violating and can therefore not contribute for the pure electromagnetic γ^* exchange. Furthermore, current conservation yields $q_\mu W^{\mu\nu} = q_\nu W^{\mu\nu} = 0$. The only two remaining independent factors are W_1 and W_2. Conventionally they are substituted by $F_1 = W_1$ and $F_2 = p \cdot q \frac{W_2}{m^2}$, which are commonly called *structure functions*. A physical interpretation of the structure function is given in section 2.1.3. The resulting cross-section in terms of x, y and Q^2 can be written as [24]:

$$\frac{d^2\sigma}{dxdy} = \frac{4\pi\alpha^2 s}{Q^4} \left[xy^2 F_1(x,y) + (1-y) F_2(x,y) \right]. \tag{2.13}$$

Introducing the longitudinal structure function $F_L = F_2 - 2xF_1$ and defining $Y_+ = 1 + (1-y)^2$ equation 2.13 can be rewritten to:

$$\frac{d^2\sigma}{dxdQ^2} = \frac{2\pi\alpha^2}{xQ^4} \left[Y_+ F_2(x,Q^2) - y^2 F_L(x,Q^2) \right]. \tag{2.14}$$

If Q^2 becomes comparable in size with the mass of the Z^0 boson squared [2] ($m_{Z^0} = 91.2\,\text{GeV}$), an additional term proportional to $\left(\frac{Q^2}{Q^2 + m^2_{Z^0}} \right)$ contributes to the cross-section [23]. This additional term is derived from the parity violating term (W_3) in equation 2.12.

For the CC cross-section the propagator $\left(\frac{2\pi\alpha^2}{xQ^4} \right)$ is exchanged by $\frac{G_F^2}{4\pi x} \left[\frac{M_W^2}{M_W^2 + Q^2} \right]^2$, where $G_F = 1.17\,\text{GeV}^{-2}$ [26] denotes the Fermi constant and $M_W = 80.4\,\text{GeV}$ [26] the mass of the exchanged $W^\pm$ bosons (see for example [23]).

---

[2]Throughout this thesis natural units are used, i.e. $c = \hbar = 1$.

2.1.3 Interpretation of the Structure Functions in the Quark-Parton-Model

The most illustrative picture of the interacting proton is given by the so-called Quark-Parton-Model (QPM). This model is based on the assumption that a fast moving hadron consists of point-like constituents (partons, later called quarks and gluons) with negligible transverse momentum (infinitesimal momentum frame). The momentum of the proton (p) is shared by the constituents (q_i), i.e. each parton carries a momentum fraction x_i of the proton's momentum: $q_i = x_i \cdot p$. Another important assumption is that the partons do not interact for the duration of the scattering process. Thus, the cross-section can be calculated as an incoherent sum over the interactions of the photon with the partons:

$$\frac{d^2\sigma^{QPM}}{dxdQ^2} = \sum_i (f_i(x) \cdot \frac{d^2\sigma^{Mott}}{dxdQ^2}) = \frac{2\pi\alpha^2}{Q^4} \cdot [1 + (1-y)^2] \cdot \sum_i (q_i^2 \cdot f_i(x)), \tag{2.15}$$

where $\frac{d^2\sigma^{Mott}}{dxdQ^2}$ is the Mott-cross-section describing the elastic scattering of an electron on a structure-less spin $\frac{1}{2}$ particle [25], q_i denotes the charge of the parton i and $f_i(x)dx$ gives the probability that a parton i with momentum fraction x is found in the proton. The probability density $f_i(x)$ is called *parton density function* (PDF). In the QPM picture the PDF depends only on the momentum fraction x and not on Q^2. This effect was predicted by Bjorken in the late 1960's and is therefore referred to as *Bjorken scaling*[3] [27].

Comparing equations 2.13 and 2.15 the following relations of the PDF to the structure functions are found:

$$F_1(x, Q^2) = F_1(x) = \frac{1}{2} \cdot \sum_i (q_i^2 \cdot f_i) \tag{2.16}$$

$$F_2(x, Q^2) = F_2(x) = x \cdot \sum_i (q_i^2 \cdot f_i) \tag{2.17}$$

Hence, the two structure function are related by:

$$F_2 = 2xF_1. \tag{2.18}$$

This relation is known as the *Callan-Gross relation* [28].

In the first instance the Bjorken scaling and the Callan-Gross relation have been confirmed experimentally by measurements at the SLAC facility for $Q^2 < 7.4\,\mathrm{GeV}^2$ [29, 30]. However, later measurements at higher energies have shown that the Bjorken scaling is not fulfilled exactly [31, 32]. This effect has later been studied in great detail at HERA (see for example [33]). The violation of the Bjorken scaling is not caused by a substructure of the partons (see section 2.1.4). The breakdown of the universal scaling cannot be understood within the QPM but needs a refined theory of the strong interaction, the Quantum ChromoDynamics (QCD). The deficits of the QPM and the main features of QCD are outlined in section 2.1.4.

2.1.4 Quantum Chromodynamics

Within the QPM it is expected that the sum over all partons fulfill:

$$\sum_i \int_0^1 x \cdot f_i(x)dx = 1. \tag{2.19}$$

---

[3]Note that these statements are only valid in the Bjorken limits, $Q^2 \to \infty, p \cdot q \to \infty$ with fixed value of x.

This relation is know as the *momentum sum rule*. The measured value for this quantity was found to be around 0.5. This lead to the suggestion that there must be a kind of a *'glue'* holding the proton together. This glue would carry the missing momentum. Nowadays this glue is identified as the gluons, the carriers of the strong force.

The other major problem with the QPM was the assumption of quasi-free partons in the proton. This is in clear contradiction with the experimental non-observation of free partons in the final state. Hence, it was necessary to assume that the force between the partons is strong enough to keep them in the hadrons.

Both these problems where solved by the development of a non-Abelian gauge theory for the strong interaction, the quantum chromodynamics. Within this theory the strong interaction is mediated by gluons. The quarks as well as the gluons have an additional degree of freedom, the colour charge. There are three colours denoted as red, yellow and blue. The quarks carry one single colour while the gluons are bi-coloured. This is in clear contrast to the quantum electrodynamics (QED), the field theory describing the electromagnetic force, where the mediating boson does not carry electrical charged. The self-interaction of the gluons leads to a increasing coupling of the strong force for decreasing momentum transfer Q^2. After renormalisation using a scale μ_R $(= Q^2)$ the strong coupling constant can be written as [24]:

$$\alpha_s(Q^2) = \frac{1}{b_0 * \ln(\frac{Q^2}{\Lambda^2})} \left[1 - \frac{b_1}{b_0} \frac{\ln[\ln(\frac{Q^2}{\Lambda^2})]}{\ln(\frac{Q^2}{\Lambda^2})} + \cdots \right], \tag{2.20}$$

where $b_0 = (33 - 2n_f)/12\pi$, $b_1 = (153 - 19n_f)/24\pi^2$ and n_f being the number of active quark flavours. The first term corresponds to leading order (LO) calculations while the second one shows the result of a next-to-leading order (NLO) calculation. Λ, sometimes denoted as Λ_{QCD}, is a constant that has to be determined experimentally, $\Lambda \approx 200\,\text{MeV}$ (see for example [34]). According to equation 2.20 the strong coupling decreases towards zero for $Q^2 \to \infty$. This behavior is commonly known as *asymptotic freedom* and was first discovered by Politzer, Gross and Wilczek [35, 36] who were awarded the 2004 Nobel Prize in Physics for this discovery. The asymptotic freedom can be traced back to the fact that the gluons carry a colour charge and explains why the naive QPM model is successful in describing *ep* scattering processes at large Q^2. On the other hand, for $Q^2 \to \Lambda^2$ the strong coupling diverges, indicating the break down of the perturbative approach. The increase of the strong coupling at large scales is called *confinement* and implies that free quarks are not observable.

The scaling violation mentioned in section 2.1.3 can be explained within the QCD: The larger the momentum of the exchanged photon the higher is its resolutions power. Therefore, at high Q^2 the photon resolves more and more constituents with smaller and smaller momentum fraction x, as illustrated in figure 2.2. This leads to an increase of the structure function for small x with increasing Q^2, which is confirmed by the H1 measurements [37] (among others), see figure 2.3.

In contrast to the QPM process shown in figure 2.1, the quark can radiate a gluon before or after the interaction with the photon within the QCD. These processes are referred to as QCD Compton processes. Furthermore a gluon can be emitted by the proton splitting into an quark-antiquark pair. One of these quarks absorbs the photon. Such processes are called boson-gluon fusion. Both processes are illustrated in figure 2.4.
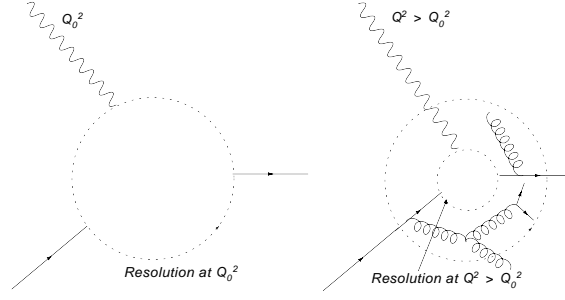
Figure 2.2: The structure of the proton as resolved by the virtual photon at a low scale Q_0^2 and at a larger scale $Q^2 > Q_0^2$.
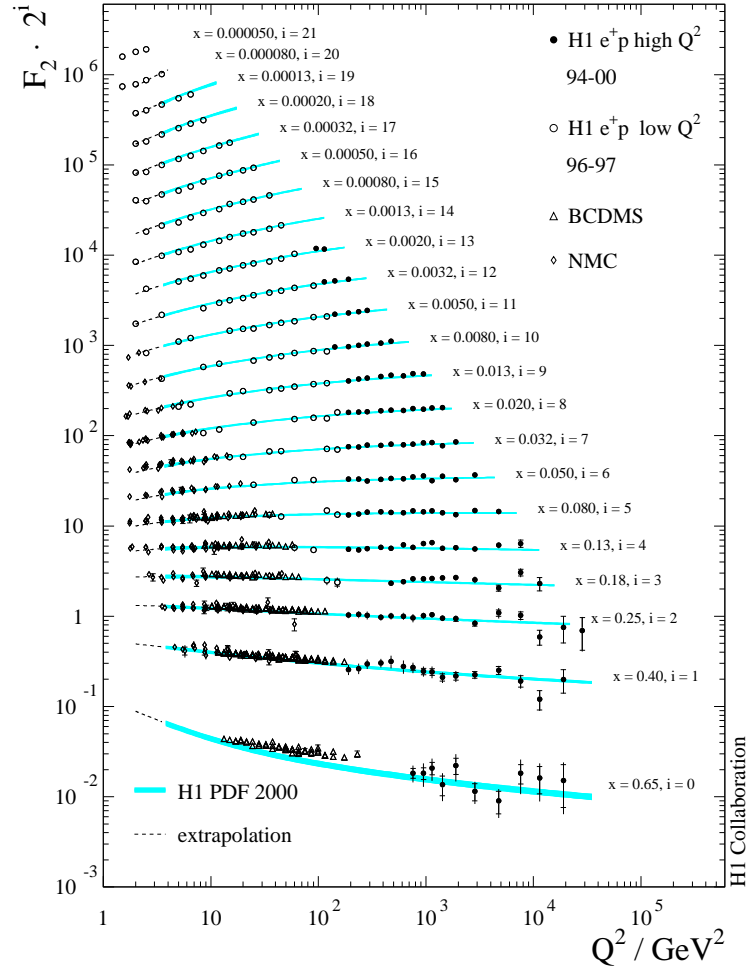

Figure 2.3: The proton structure function F_2 as measured by H1, BCDMS and NMC. The results are compared to the Standard model prediction determined from the H1 PDF 2000 fit. The figure is taken from [37].
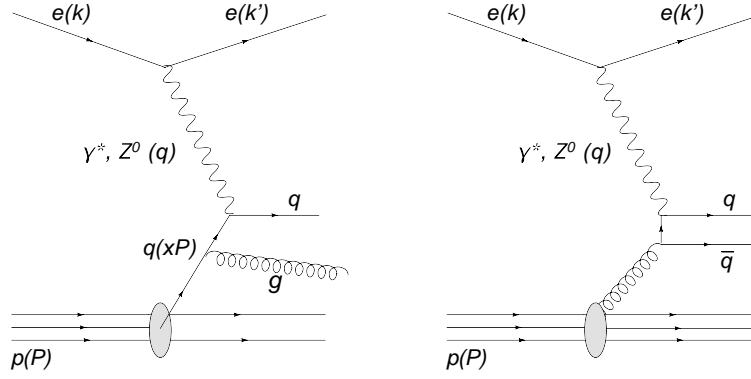
Figure 2.4: The Feynman diagrams for leading order *ep* scattering in neutral current interactions according to QCD. The left graph shows the QCD Compton scattering and the right one the boson-gluon fusion process.

2.1.5 Factorisation and Parton Evolution

Because of the break down of the perturbative approach at large scales the need arises to separate the different processes contributing to the cross-section. The hard interaction in deep-inelastic scattering (corresponding to the γq vertex in figure 2.1) provides a hard scale and can therefore be treated perturbatively. Other contributions to the cross-section, like the parton density functions, cannot be treated perturbatively. The factorisation theorem of the QCD [24] separates these two different contributions:

$$\sigma(e\,p \to e'\,X) = \sum_i \left(\int f_i(x, \mu_F^2) \cdot \hat{\sigma}(\hat{s}, \mu_F, \mu_R)\,dx \right). \qquad (2.21)$$

The cross-section for DIS can be written as the convolution of a calculable hard scattering cross-section $\hat{\sigma}$ depending on the center-of-mass energy of the hard interaction $\hat{s}$ as well as on the factorisation and renormalisation scale μ_F and μ_R and a non-perturbative parton density f_i. A natural choice of the scales is $\mu_F = \mu_R = Q^2$. The factorisation theorem has only been proofed in the so-called "Bjorken limit" by Collins and Soper [38]. The separation of the hard and the non-perturbative part is not unambiguous but depends on the factorisation scheme. The most commonly used schemes are the DIS and the $\overline{MS}$ scheme. The factorisation scale μ_F, being a lower cut off scale, is introduced because perturbative calculations are only reliable if a hard scale is present. The non-perturbative part is absorbed in the PDF's $f_i(x, \mu_F^2)$. The PDF's at the scale μ_F have to be measured experimentally. Two points for a predictive theory are important: firstly, the PDF's are universally valid and do not depend on the process studied and secondly, once measured at the scale μ_F their values at any scale can be calculated. The evolution of the PDF's can be predicted using perturbative QCD. In most cases the evolution is provided by the $DGLAP$ (Dokshitzer, Gribov, Lipatov, Altarelli and Parisi) [39, 40, 41, 42] evolution equation. For certain regions in the phase space this equation is not adequate and other approaches like the $BFKL$ (Balitsky, Fadin, Kuraev, Lipatov) [43, 44, 45] or the $CCFM$ (Catani, Ciafaloni, Fioranu, Marchesini) [46, 47, 48, 49] evolution are used. The evolution of the PDF's take different processes into account like the gluon splitting or the gluon radiation. Such processes can occur several times resulting in a gluon ladder as illustrated in figure 2.5. All parton evolutions mentioned above take the full

gluon ladder into account, but they make different approximations. For a detailed description see for example [24].
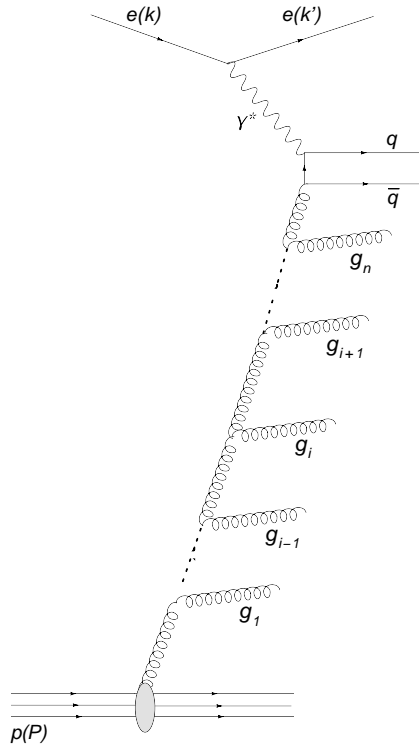
Figure 2.5: The emission of gluons as used in the parton evolution models.

2.1.6 The Hadronisation Process

The cross-section for deep-inelastic ep scattering is so far only calculated for quasi-free quarks and gluons in the final state. As pointed out in section 2.1.4 only hadrons and not free quarks are observed. The transition of the free, coloured quarks into colour-neutral hadrons is called *hadronisation* and is briefly discussed in the following.

The hadronisation process takes place at large distances and can therefore not be predicted using perturbative QCD. Instead, a phenomenological approach is needed. These hadronisation models are expected to be universally valid, i.e. they should not depend on the hard process. Therefore, the hadronisation parameters which have been studied in great detail at $e^+ e^-$ colliders should also be applicable to ep collisions. However, there are differences complicating this comparison. In contrast to $e^+ e^-$ collisions in ep scattering there is always the proton remnant. This proton remnant builds together with the quarks and gluons a colour-charged object entering the hadronisation process. Measuring the production of strange hadrons provides an additional test of the hadronisation model.

The hadronisation model is implemented in the Monte Carlo generator. All generators used within this work (see section 2.5) exploit the so-called Lund string model [50, 51, 52] as implemented for example in JETSET [53, 54] [4]. Within this model the colour field between

---

[4]Various other models exist, like the cluster model implemented in the HERWIG generator but are not

two coloured objects is squeezed into a tube-like region (string) and is described by a potential of the form:

$$V(r) = -\frac{4\alpha_s}{3r} + \kappa \cdot r, \tag{2.22}$$

where r is the distance between the two coloured objects and $\kappa \approx 1\,\mathrm{GeV\,fm^{-1}}$ describes the energy density of the string. The second term rapidly increases for rising separation of the two quarks. The string breaks up as soon as the energy in the colour field is large enough to produce a $q\bar{q}$ pair. This process is repeated until the energy is exhausted and bound states are produced. The subsequent break up of the colour strings is illustrated in figure 2.6.
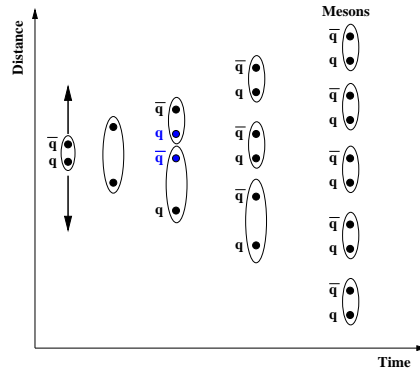
Figure 2.6: Illustration of the Lund string hadronisation model. The string between the initial $q\bar{q}$ pair breaks up as they fly apart and new $q\bar{q}$ pairs are produced from the vacuum.

For the conservation of the quantum numbers like charge or colour the quark and the anti-quark have to be produced at the same point in the four-dimensional phase space. This is (classically) forbidden and can only be achieved by a quantum mechanical tunnel-effect. The tunnel-probability into the forbidden region drops exponentially with the mass of the produced quarks. This leads to a suppression of heavy quarks like charm with respect to the light quarks up and down in the order of 10^{-11}. For the strange quarks which are not much heavier than the up and down quarks this effect is less distinct and is in the order of 0.3. The relative production probability of strange to up quarks in the hadronisation process within the Lund model is called *strangeness suppression factor (λ_s)*:

$$\lambda_s = \frac{P(s)}{P(u)}. \tag{2.23}$$

Because of the not precisely known mass of the up and strange quarks this factor is taken to be a free parameter of the Lund model. The default value used in the events generators, $\lambda_s = 0.3$, is obtained from measurements at the e^+e^- collider LEP (see sections 2.3).

So far only meson production is described. Baryons are obtained in a similar way: Instead of a $q\bar{q}$ a diquark pair can be produced from the vacuum. The production of a diquark pair leads to a break up of the string as sketched in figure 2.7, which shows the production of a $\overline{\Lambda}$ and a Σ baryon together with a π meson. Within the Lund string model, baryons are always produced in pairs and two of the three quarks in each of the two baryons have to have the same flavour. The probability of producing a light diquark pair, $P(qq)$, relative to a light

considered within this work.
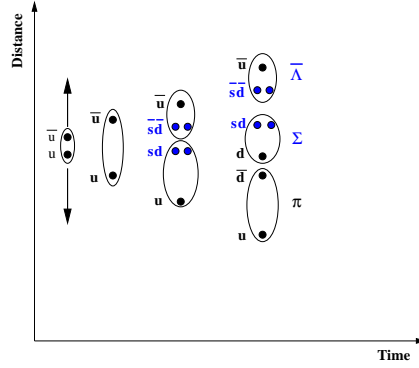
Figure 2.7: Illustration of the baryon production within the Lund string model.

single quark pair, $P(q)$, is a free parameter of the Lund model and is set within JETSET by the parameter λ_{qq}:

$$\lambda_{qq} = \frac{P(qq)}{P(q)}. \tag{2.24}$$

The default value is $\lambda_{qq} = 0.1$. Furthermore, the relative production of diquarks containing a strange quark, $P(qs)$, to those consisting only of light quarks (up and down) is set within JETSET by the parameter λ_{sq}. This parameter is normalised to the strangeness suppression factor and given by:

$$\lambda_{sq} = \frac{P(us)}{P(ud)} / \frac{P(s)}{P(u)} = \frac{P(us)}{P(ud)} / \lambda_s. \tag{2.25}$$

The default value is $\lambda_{sq} = 0.4$. Beside the parameters mentioned here further parameters are needed to control the hadronisation process, see for example [53].

Finally, all processes contributing to the ep cross-section are summarised in figure 2.8.

2.2 Properties and Production Mechanism of Strange Hadrons

The main part of the analysis presented within this thesis is dedicated to the measurement of strange hadrons. The different production mechanisms of such hadrons are briefly summarised in the following and the main properties of the particles relevant for this work are outlined. An overview of existing measurements is presented in the last part.

2.2.1 Production of Strange Hadrons in Deep-Inelastic ep Scattering

Strange particles can be produced in various processes. A sketch of the different processes is provided in figure 2.9 in the form of Feynman graphs.

Direct production Strange quarks can be produced directly in the hard scattering if a strange sea quark from the proton enters the QPM or the QCD Compton process. Due to the relatively small strange quark mass the emittance of a strange sea quark is not much suppressed with respect to light (u and d) sea quark emittance. This is not the case for the heavy quarks (c and b) where the probability that such a quark is emitted from the proton sea is very small. Furthermore, strange quarks can be produced in
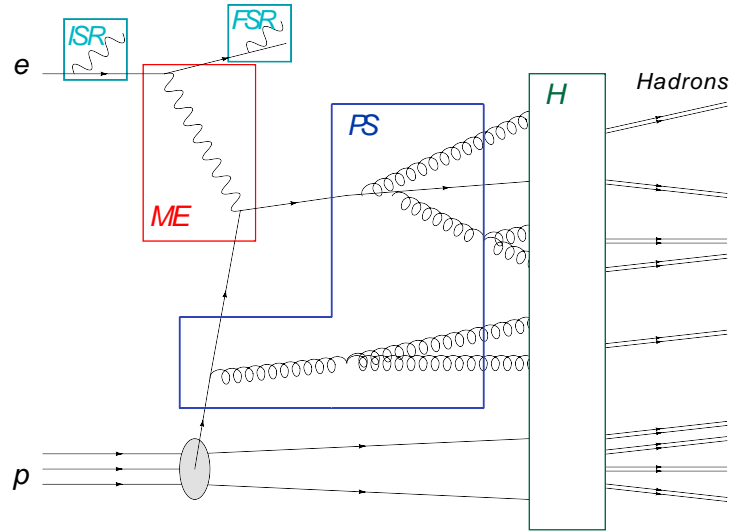
Figure 2.8: Overview of all processes contributing to the *ep* cross-section: The matrix element (ME) describing the hard process, the initial and final state parton shower (PS), the initial (ISR) and final (FSR) state QED radiation and the hadronisation process (H).

BGF processes if the gluon splits into a $s\bar{s}$ quark pair. For the heavy quarks this is the main production mechanism while for the lighter strange quarks the contribution from BGF process to the direct production is small. The rate of the BGF process to the direct production depends strongly on the Bjorken scaling variable x because the gluon density rises strongly (more than the sea quark distribution) towards small values of x. Therefore one may expect that for very small values of x the BGF process becomes dominant also for the strange quark production. The strange quark produced in such ways can then fragment into a strange hadron. According to Monte Carlo predictions, in about $13\,\%$[5] of the cases where a strange hadron is seen in the final state, a strange quark is participating in the hard interaction.

Hadronisation The largest contribution to strange hadron production is provided by the hadronisation process as described in section 2.1.6.

Decays Strange quarks are also produced by decays of the heavy quarks c and b. Another source of strange hadrons are decays of heavy hyperons like $\Sigma's$ and $\Xi's$. Decays of hypothetical states like glueballs (bound state of gluons) [55, 56] or instantons [57] could in principle also contribute to the production of strange hadrons since such states are expected to decay flavour democratically and therefore enhance the relative fraction of strange particles with respect to light ones.

The contributions of the different processes to the production of the strange hadrons K_s^0 and Λ is provided in section 6.8.1 for different regions of the phase space.

---

[5]This number is obtained by the DJANGO generator using the CTEQ6L PDF set.
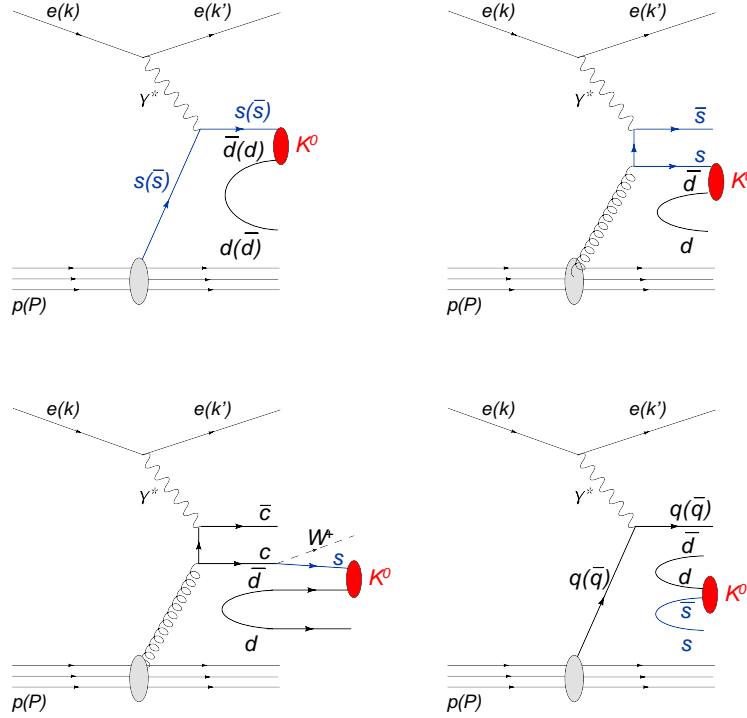
Figure 2.9: Sketch of the different processes contributing to strangeness production. Shown are the direct production in the QPM (top left), in the BGF process (top right) and from the decay of a charm quarks (bottom left), as well as the strangeness production in hadronisation (bottom right).

2.2.2 Properties of Strange Hadrons

Strange hadrons were first observed in 1947 in the cosmic rays. The unexpected long lifetime of these particles was explained by introducing of a new quantum number, the strangeness S, which shall be conserved in the strong interaction. This picture was refined within the quark parton model, where strange hadrons contain at least one strange quark. Each strange quark has $S = -1$ and each anti-strange quark $S = +1$. As the strangeness quantum number is preserved in the strong and electromagnetic interaction, those particles can only be produced in pairs. In the weak interaction the strangeness is not preserved.

2.2.2.1 The K_s^0 Meson

The lightest mesons containing strange quarks are called kaons. Their quark content is:

$$
\begin{aligned}
|K^0\rangle &= d\bar{s} & |\overline{K}^0\rangle &= \bar{d}s \\
|K^+\rangle &= u\bar{s} & |K^-\rangle &= \bar{u}s
\end{aligned} \tag{2.26}
$$

The kaons are members of an isospin doublet as shown in table 2.1 and have played a crucial role in the understanding of the P-Parity (mirror symmetry in space) and C-Parity (particle-antiparticle conjugation) violation. From β-decay studies it was known that the weak interaction violates P- and C-Parity, but respects the combination of these two operations (CP), see [58]. A special property of neutral kaons is that they can both decay weakly

Table 2.1: Isospin doublets of the lightest strange mesons.

	$I_3 = -\frac{1}{2}$	$I_3 = +\frac{1}{2}$
$S = +1$	K^0	K^+
$S = -1$	K^-	$\overline{K}^0$

into two or three pions [11]:

$$K^0 \longleftrightarrow \begin{pmatrix} 2\pi \\ 3\pi \end{pmatrix} \longleftrightarrow \overline{K}^0. \tag{2.27}$$

This leads to a mixing of the neutral kaon states. The short-distance mixing graphs are illustrated as box diagrams in figure 2.10. Assuming that the weak interaction is respecting
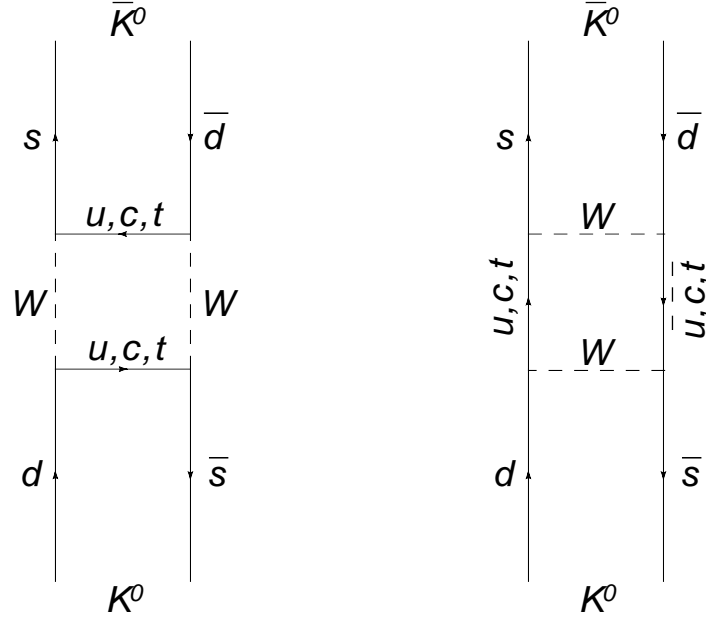
Figure 2.10: The box diagram for $K^0 - \overline{K}^0$ mixing

CP-Parity, the kaons have to be in a CP-eigenstate before they decay (weakly). These states can be obtained by superimposing the K^0 and $\overline{K}^0$ mass-eigenstates:

$$|K_1^0\rangle = \frac{1}{\sqrt{2}}\left(|K^0\rangle - |\overline{K}^0\rangle\right) \qquad CP|K_1^0\rangle = +1|K_1^0\rangle \tag{2.28}$$

$$|K_2^0\rangle = \frac{1}{\sqrt{2}}\left(|K^0\rangle + |\overline{K}^0\rangle\right) \qquad CP|K_2^0\rangle = -1|K_2^0\rangle$$

For a CP respecting theory the decay of the neutral kaon has to be described by the decay of a K_1^0 into two pions ($CP|\pi^+\pi^-\rangle = +1|\pi^-\pi^+\rangle$) and a K_2^0 into three pions ($CP|\pi^+\pi^-\pi^0\rangle = -1|\pi^-\pi^+\pi^0\rangle$). Due to the very small phase space available for the $K_2^0 \to \pi^+\pi^-\pi^0$ decay the lifetime of the K_2^0 should be much larger than that one of the K_1^0. Theses states are denoted as K_s^0 (short) and K_L^0 (long). However, experiments have shown that the K_2^0 decays also into

two pions with a probability of $3 \cdot 10^{-3}$ [59, 60]. Therefore either the mass-eigenstate K_L^0 is not identical with the CP-eigenstate K_2^0 or the matrix element for the decay of the K_2^0 has a part that allows a decay into two pions. However, the experimental behaviour of the K^0 shows clearly that CP-Parity is violated by the weak interaction. The main properties of the neutral kaons are summarised in table 2.2 and the decay into two charged pions is sketched in figure 2.11.

Table 2.2: Main properties of the neutral kaons K_s^0 and K_L^0. The values are taken from [26].

	K_s^0	K_L^0
Mass [MeV]	497.648 ± 0.022	
Lifetime τ [10^{-10}s]	0.8953 ± 0.0005	511.4 ± 2.1
decay length $c\tau$ [cm]	2.6842 ± 0.0015	$1'533 \pm 6.3$
Decay [branching ratio]	$\pi^+\pi^-$ [$(69.20 \pm 0.05)\,\%$]	$\pi^+\pi^-\pi^0$[$(12.56 \pm 0.05)\,\%$]
	$\pi^0\pi^0$ [$(30.69 \pm 0.05)\,\%$]	$\pi^0\pi^0\pi^0$ [$(19.56 \pm 0.14)\,\%$]
	$\pi^+\pi^-\pi^0$ [$(3.5 \pm 1.0)\cdot 10^{-7}$]	$\pi^\pm l^\mp \nu_l$ [$(67.55 \pm 0.22)\,\%$]
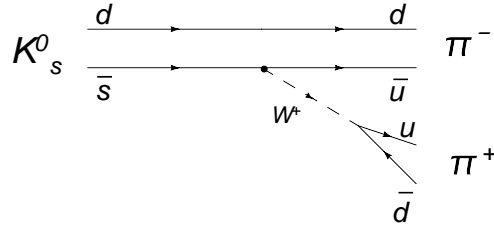
Figure 2.11: The main decay of the neutral kaon into two charged pions.

2.2.2.2 The Strange Baryons

This section focuses on the three baryons with strangeness studied within this work: the Λ, the Ξ^- and the $\Xi(1530)^0$ baryons. The lightest baryon with strangeness is the Λ baryon. The Λ and the Ξ^- baryons are members of the baryon-octet displayed in figure 2.12 with $J^P = \frac{1}{2}^+$, see for example [25]. For the $J^P = \frac{1}{2}^+$ case no baryon with three strange quarks exists because in this case the spins of the quarks have to be in a parallel configuration for symmetry reasons, resulting in $J^P = \frac{3}{2}^+$ state. The $\Xi(1530)^0$ baryon is an orbitally excited state of the ground state baryon Ξ^0 and belongs to the $J^P = \frac{3}{2}^+$ multiplet. The main properties of the baryons of interest are summarised in table 2.3. The Λ as well as the Ξ^- baryon are again long-living due to the weak decays, while the $\Xi(1530)^0$ baryon is decaying strongly into a $\Xi\pi$ state with a branching ratio of nearly $100\,\%$.
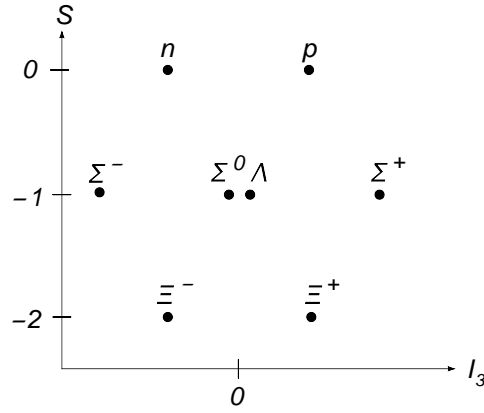
Figure 2.12: The baryon octet with $J^P = \frac{1}{2}^+$.
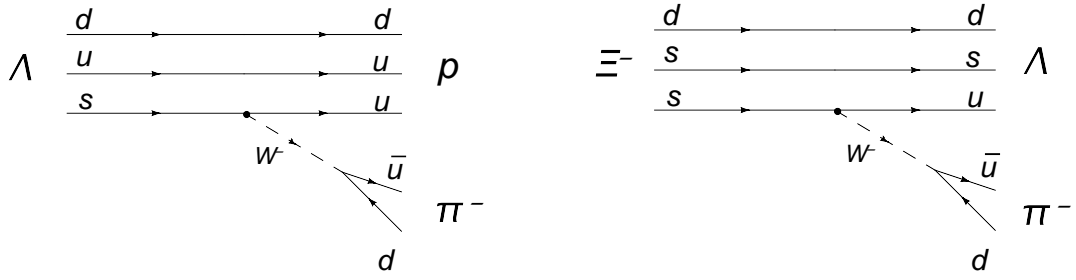
Figure 2.13: The main decays of the strange baryons Λ and Ξ^-.

Table 2.3: Main properties of the strange baryons Λ, Ξ^- and $\Xi(1530)^0$. The values are taken from [26].

	Λ	Ξ^-	$\Xi(1530)^0$
Constituent quarks	uds	dss	uss
J^P	$\frac{1}{2}^+$	$\frac{1}{2}^+$	$\frac{3}{2}^+$
Mass [MeV]	1115.683 ± 0.006	1321.31 ± 0.13	1531.80 ± 0.32
Lifetime τ [10^{-10}s]	2.63 ± 0.02	1.639 ± 0.015	~ 0
Decay length $c\tau$ [cm]	7.89 ± 0.06	4.91 ± 0.04	~ 0
Decay [branching ratio]	$p\,\pi^-$ $[(63.9 \pm 0.5)\,\%]$ $n\,\pi^0$ $[(35.8 \pm 0.5)\,\%]$	$\Lambda\,\pi^-$ $[(99.89 \pm 0.04)\,\%]$	$\Xi\,\pi[\sim 100\,\%]$

2.3 Existing Measurements of Strangeness Production

In this section an overview of existing measurements of strangeness production is given. Emphasis is only given to the measurement relevant to the studies presented within this work. For a detailed review on strangeness suppression see for example [61, 62]. The focus is turned on the previous measurements at HERA and those at $e^+ e^-$ colliders. Latter ones are used to extract the free parameter of the Lund string fragmentation model introduced in section 2.1.6.

2.3.1 Measurements at $e^+ e^-$ Colliders

Strangeness production in $e^+ e^-$ collisions has been studied in great detail. The free parameters of the Lund string model are studied by measuring the production of different strange hadrons like K_s^0, Λ, $K^{*\pm}$, $\Sigma(1385)^{\pm}$, Ξ^- and $\Xi(1530)^0$.

Historically, the first measurement that is discussed was carried out at the **P**ositron **E**lectron **T**andem **R**ing **A**nlage (PETRA) at DESY by the JADE collaboration [63] who studied the charge multiplicity and the K_s^0 production at a center-of-mass energy between 12 GeV and 35 GeV. The average value of the strangeness suppression factor was found to be $\lambda_s = 0.27 \pm 0.03 \pm 0.05$. Within the statistical limitations of the measurement no dependence of λ_s on the center-of-mass energy (12, 14, 22, 30 and 35 GeV) was found.

A following publication by the TASSO collaboration [64] using also the PETRA beams has measured the production of K_s^0 and Λ at center-of-mass energies of 14, 22 and 34 GeV. A strangeness suppression factor of $\lambda_s = 0.35 \pm 0.02 \pm 0.05$ was extracted.

The HRS (**H**igh **R**esolution **S**pectrometer) at the PEP $e^+ e^-$ storage ring at the SLAC facility has investigated the production of charged pions, charged and neutral Kaons as well as Lambda baryons at a center-of-mass energy of 29 GeV [65]. A suppression factor of $\lambda_s = 0.34 \pm 0.03$ was extracted. Furthermore, the relative production of diquarks containing a strange quark to those consisting only of up and down quarks (see equation 2.25) was measured to $\lambda_{sq} = 0.87 \pm 0.06$.

A whole series of measurements dedicated to strangeness production have been performed at the LEP (**L**arge **E**lectron **P**ositron) collider at CERN (**C**onseil **E**uropéenne pour la **R**echerche **N**ucléaire) by its four collaborations ALEPH, OPAL, DELPHI and L3 [66, 67, 68, 69, 70, 71, 72]. These experiments have used hadronic Z^0 decays to study the strangeness production in the hadronisation process and suggest a strangeness suppression factor of $\lambda_s \approx 0.3$. This value is used as the default value within the JETSET program. However, a more recent measurement [73] came up with $\lambda_s = 0.422 \pm 0.049 \pm 0.059$.

All these measurements indicate that the data of different experiments cannot be described by one single parameter-set of the Lund string model.

2.3.2 Measurements at ep Colliders

The next class of experiments that is briefly discussed are some older measurements of the strangeness production at ep colliders.

The H1 collaboration has measured the production of K_s^0 and Λ in DIS ($10 < Q^2 < 70$ GeV^2) [74] as well as in photoproduction ($Q^2 \approx 0$) [75]. Both measurements have analysed the data recorded in the year 1994 corresponding to an integrated luminosity of 1.32 pb^{-1},

almost a factor of 40 less than the available statistics analysed within this work. The DIS analysis did not show an excess of strange particles with respect to the model predictions and an upper limit of 0.9 nb on the cross-section of instanton induced processes has been derived at 95 % confidence level. The data were best described by a strangeness suppression factor of $\lambda_s = 0.2 - 0.23$. The results found in photoproduction are comparable with those from DIS. Only at high p_T a deficit of strange hadron production with respect to DIS events was found. Predictions from Monte Carlo models for photoproduction (PYTHIA and JETSET) as well as QCD calculations provide a reasonable description of the K_s^0 production rates while the Λ production is underestimated in the models. A comparison to $p\bar{p}$ experiments shows a good agreement on the K_s^0 rate while the Λ rate is lower in photoproduction. A more recent (unpublished) analysis of DIS events using $17.8\,\mathrm{pb}^{-1}$ and a wider range in Q^2, $2 < Q^2 < 100\,\mathrm{GeV}^2$, is available [76]. Like the other measurements a lower strangeness suppression factor is favored. Best description of the data is achieved with $\lambda_s = 0.23 - 0.25$.

Strangeness production was also studied in great detail by the ZEUS collaboration. In a first measurement $0.55\,\mathrm{pb}^{-1}$ of DIS data ($10 < Q^2 < 640\,\mathrm{GeV}^2$) was analysed [77]. The data could not be described by the models with the standard suppression factor of 0.3. The best description was achieved with $\lambda_s = 0.2$. But also in this case the K_s^0 production is slightly overestimated while the Λ production is underestimated. This implies the requirement of a further tuning of the Lund parameters, specially the ratio of diquark pair production to $q\bar{q}$ production, which was not done within this publication. In a more recent work $121\,\mathrm{pb}^{-1}$ of ep scattering data was analysed [78]. Within this publication strangeness production in DIS as well as in photoproduction was evaluated. The main conclusions are:

1. The DJANGO model (see section 2.5) described the overall features of the data
2. In the DIS regime $\lambda_s = 0.3$ is preferred to 0.22
3. No hint for a Λ-asymmetry is found
4. The ratio of Λ to K_s^0 production varies from 0.2 to 0.5 and DJANGO follows the shape of the data on selected observables but fails in quantitative description up to 20 %

2.3.3 Other Measurements

Beside the e^+e^- and ep experiments strangeness production has been studied in muon, neutrino and heavy ion collisions [79, 80]. The muon nucleon scattering experiment at CERN, where a 280 GeV muon beam collides with a liquid hydrogen target has investigated the production of strange particles in DIS [81]. The observed rates of K^+, K^- and Λ could be described by Monte Carlo models with a suppression factor of $\lambda_s = 0.3 \pm 0.01 \pm 0.07$.

The measurements of the strangeness suppression factors by the different experiments is summarised in figure 2.14.

2.4 Introduction to Pentaquarks

Exotics with the quark content of the Θ^+ ($udud\bar{s}$) had been proposed since the early days of quantum chromodynamics (QCD) using the MIT bag model [82]. The observation of the Θ^+ [17] has revived theory activity on this topic. More recently the SU(3)-flavour antidecuplet $(\overline{10_f})^6$ representation has emerged as an interesting feature of chiral soliton models of baryons.

---

[6]$\overline{10_f}$ denotes a multiplet of ten states (pentaquarks) in the flavour space represented by a antidecuplet representation of $SU(3)_f$, see figure 2.16.
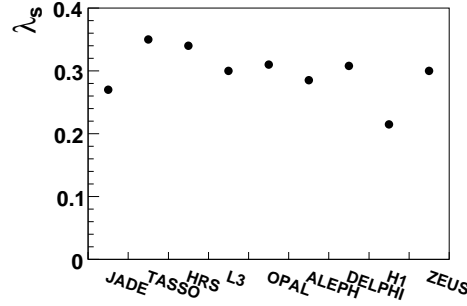
Figure 2.14: The strangeness suppression factor λ_s as extracted by the different experiments.

As early as 1987 Praszalowicz predicted that the Y=2 isospin member of the J=$\frac{1}{2}$ $\overline{10_f}$ would lie near 1540 MeV [83]. In 1997 Diakonov *et al.* not only predicted a Θ^+ at about the same mass but also estimated its width at less than 15 MeV [18], see also [84]. This width estimation was the most important theoretical contribution to the discovery of the Θ^+ pentaquark (see below).

In the last years many theories appeared trying to interpret these exotic states. Among them the Jaffe and Wilczek's (JW) diquark model [85] and the Karliner and Lipkin's (KL) [86] diquark-triquark model are the most promising ones. In the following these models are introduced and their predictions are outlined.

2.4.1 Jaffe Wilczek Diquark Model

Previous attempts have shown that a single cluster description of the ($uudd\bar{s}$) system fails since the colour magnetic repulsion between flavour symmetric states prevents them from binding. Therefore quarks with the same flavour have to be separated within the pentaquark. Jaffe and Wilczek proposed that the PQ's can be considered as a bound state of an antiquark with two highly correlated spin zero diquarks where the quarks within one diquark have different flavours. In figure 2.15 a schematic representation of the Θ^+ pentaquark in the JW model is shown. The four quarks are bound into two spin zero, colour anti-triplet ($\overline{3_c}$) and flavour anti-triplet ($\overline{3_f}$) diquarks, see figure 2.15. The diquarks obey Bose statistics, but may experience a repulsive Pauli blocking interaction at short distances. Since the PQ is in a colour singlet state the two diquarks have to combine to a colour triplet 3_c in order to build a colour singlet together with the antiquark. Because the triplet's wave function is the antisymmetric part of $\overline{3_c} \times \overline{3_c}$, the diquark-diquark wave function must be antisymmetric with respect to its other labels. Considering identical diquarks, like the two [ud] diquarks in the Θ^+, only space labels remain and the diquark-diquark wave function must be antisymmetric in space, i.e. with negative parity. Combined with the antiquark the resulting $q^4\bar{q}$ system has positive parity. For unlike diquark pairs, like the [ud][sd] diquarks in the N_s^0 (see figure 2.16), the wave function can also be symmetrised in flavour and therefore such states can have positive parity too. The diquark pairs with different quark flavours can also be anti-symmetrised in flavour resulting in a negative parity state. The following notation is used:

$$[q_1q_2][q_3q_4]_+ = \sqrt{\frac{1}{2}}([q_1q_2][q_3q_4] + [q_3q_4][q_1q_2]) \tag{2.29}$$

$$[q_1 q_2][q_3 q_4]_- = \sqrt{\frac{1}{2}}([q_1 q_2][q_3 q_4] - [q_3 q_4][q_1 q_2]). \tag{2.30}$$

In contrast, the uncorrelated quark model, in which all quarks are in a ground state, predicts negative parity for the pentaquark.
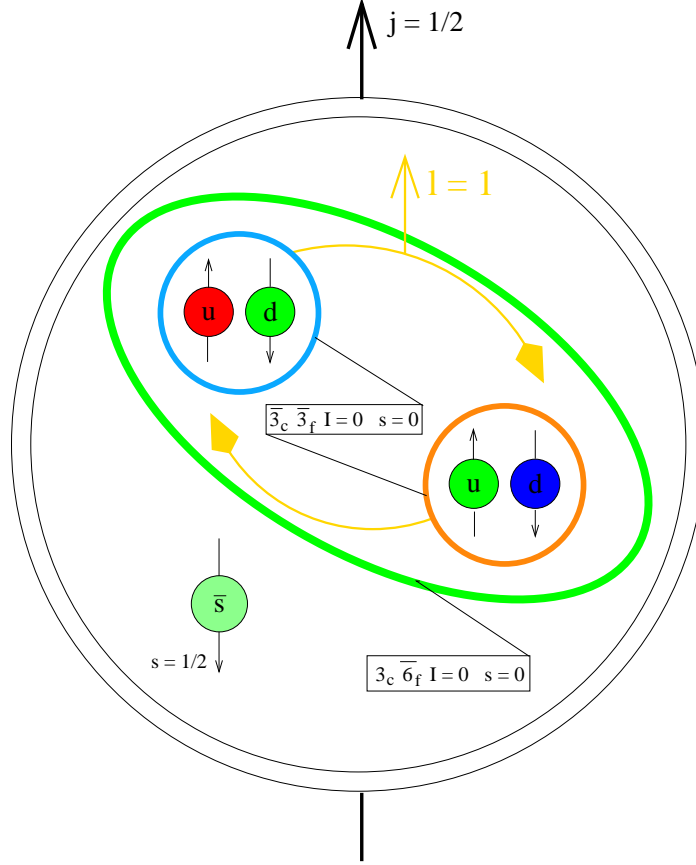
Figure 2.15: Schematic representation of the Θ^+ pentaquark in the Jaffe Wilczek model.

The flavour symmetric and therefore spatially antisymmetric diquark-diquark states form a flavour anti-sextet $\overline{6_f}$. These states are:

$$\overline{6_f}, J^P = 1^- : \qquad [ud][ud], [ud][us]_+, [us][us], [us][ds]_+, [ds][ds], [ds][ud]_+, \tag{2.31}$$

see equation 2.29. The flavour anti-symmetric and therefore spatially symmetric two diquark states from a flavour triplet 3_f. These states are:

$$3_f, J^P = 0^+ : \qquad [ud][us]_-, [us][ds]_-, [ds][ud]_-, \tag{2.32}$$

see equation 2.30. These diquark pairs have positive parity and the resulting pentaquark $(q^4 \bar{q})$ when such a diquark pair is combined with an antiquark has negative parity.

2.4.1.1 Light Pentaquarks in the Jaffe Wilczek Diquark Model

The states mentioned above can be combined with either a $\bar{u}$, $\bar{d}$ or a $\bar{s}$ quark. Using the $\overline{6_f}$ diquark pairs from equation 2.31 the result is a degenerated SU(3) flavour octet and

antidecuplet ($8_f \oplus \overline{10_f}$), as shown in figure 2.16. As pointed out in section 2.4.1, these states have positive parity. The spatially antisymmetric wave function of the diquark pairs would likely correspond to an angular momentum of one. Therefore the angular momentum of the pentaquark in the correlated diquark picture would be either $\frac{1}{2}$ or $\frac{3}{2}$. Jaffe and Wilczek assumed that the pentaquarks with $J^P = \frac{3}{2}^+$ are elevated to higher energies where they fall apart quickly and do not produce prominent resonances. For pentaquarks containing strange quarks the SU(3)-flavour symmetry is broken. It is known from baryon spectroscopy that the [ud] diquark is more tightly bound than the [us] or the [ds] diquark, see [87]. By exchanging a u or d quark by a s quark a contribution α from the binding energy difference rises, additional to the mass difference of the quarks itself. This contribution can be related to the Σ - Λ mass difference by:

$$\alpha \equiv \frac{3}{4}(M_\Lambda - M_\Sigma) \approx 60 \, \text{MeV}. \tag{2.33}$$

Jaffe and Wilczek proposed a Hamiltonian including SU(3) violation given by:

$$H_s = M_0 + (n_s + n_{\overline{s}}) \cdot m_s + n_s \cdot \alpha, \tag{2.34}$$

where n_s and $n_{\overline{s}}$ are the number of strange and antistrange quarks in the pentaquark, respectively and m_s is the contribution from the strange quark mass.

In the following the masses of some $8_f \oplus \overline{10_f}$ members are calculated.

- **Θ^+(udud$\overline{s}$)**: This state fixes $M_0 + m_s \approx 1540 \, \text{MeV}$. The small width of the Θ^+ may be explained by a weak coupling to the $K^+ n$ state from which it differs in colour and spin.

- **N^0(udud$\overline{d}$)**: This is the lightest particle in the $8_f \oplus \overline{10_f}$ representation. According to equation 2.34 the mass of this state is M_0. Jaffe and Wilczek proposed to identify this state with the so called Roper resonance $N(1440)P_{11}$ (see [26]). This fixes $M_0 \approx 1440 \, \text{MeV}$.

- **N_s^0(udsd$\overline{s}$)**: This state has the same quantum numbers like the nucleon but with hidden strangeness and is therefore heavier than the nucleon and should couple strongly to strange particles. According to equation 2.34 the mass of this state is:

$$m(N_s^0) \approx M_0 + 2m_s + \alpha \approx 1700 \, \text{MeV}. \tag{2.35}$$

  There is a known candidate for this state, the $N(1710)P_{11}$. If this assignment proves to be correct, the N(1710) should couple stronger to $N\eta$, $K\Lambda$ and $K\Xi$ than currently expected.

- **Σ_s^+(usus$\overline{s}$)**: In the Jaffe Wilczek picture this is the heaviest member of the $8_f \oplus \overline{10_f}$ representation, $m(\Sigma_s^+) \approx M_0 + 3m_s + 2\alpha \approx 1850 \, \text{MeV}$. This state should couple predominately to $\Sigma\eta$ and $\Xi\overline{K}$.

- **Ξ^{--}(dsds$\overline{u}$)**: The isospin $\frac{3}{2}$ multiplet contains two Ξ's with ordinary charge assignments (0,-) and additionally it includes the two exotic states $\Xi^{+,--}$. The mass is estimated to approximately 1760 MeV which is about 100 MeV below the mass of the resonance observed by the NA49 collaboration in the $\Xi\pi$ mass spectrum [88].
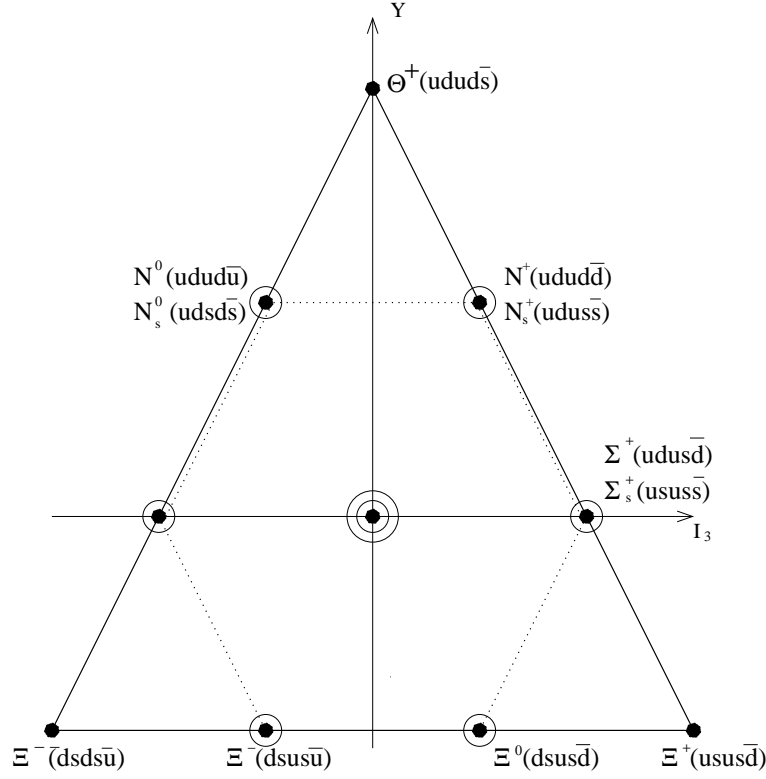
Figure 2.16: Representation of the degenerated flavour octet and antidecuplet $(8_f \oplus \overline{10_f})$. The axis are the hypercharge Y and the third component of the isospin vector I_3. The N_s^0 for example has Y = 1 and $I_3 = -\frac{1}{2}$.

Combining the 3_f diquark pairs from equation 2.32 with either a $\overline{u}$, $\overline{d}$ or a $\overline{s}$ quark, the result is a nonet of pentaquarks with negative parity and flavour content $1_f \oplus 8_f$. But these states have none exotic quantum numbers and are not considered further.

The correlated diquark picture differs in several ways from the prediction of the chiral soliton model. The main differences are:

- In the chiral soliton model the Θ^+ is the lightest pentaquark and therefore there is no candidate for the Roper resonance.

- In the correlated diquark picture the Σ_s is the heaviest member of the $8_f \oplus \overline{10_f}$ representation, whereas the Ξ is the heaviest pentaquark in the chiral soliton model. The mass hierarchy of these two models is shown in figure 2.17.

- The chiral soliton model predicts only a SU(3)-flavour antidecuplet (no octet).

2.4.1.2 Heavy Pentaquarks in the Jaffe Wilczek Diquark Model

The antiquark from a light pentaquark can be substituted by a heavy antiquark ($\overline{c}$ or $\overline{b}$) to form a heavy pentaquark. The heavy quarks are in a SU(3)-flavour singlet. They form a SU(3)-flavour anti-sextet ($\overline{6_f}$) with even parity when combined with the diquark pairs
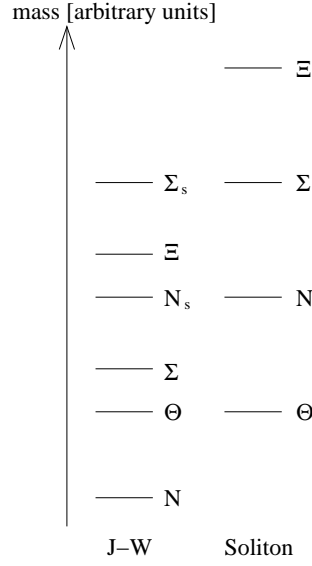
Figure 2.17: The mass hierarchy in the Jaffe Wilczek diquark model and in the chiral soliton model.

(symmetric in flavour, antisymmetric in space) listed in equation 2.31. Combining a heavy antiquark with the diquark pairs from equation 2.32 (antisymmetric in flavour, symmetric in space) they from a SU(3)-flavour triplet (3_f) with odd parity, see [89, 90]. These states are schematically shown in figure 2.18. The flavour wave function of the heavy pentaquarks are
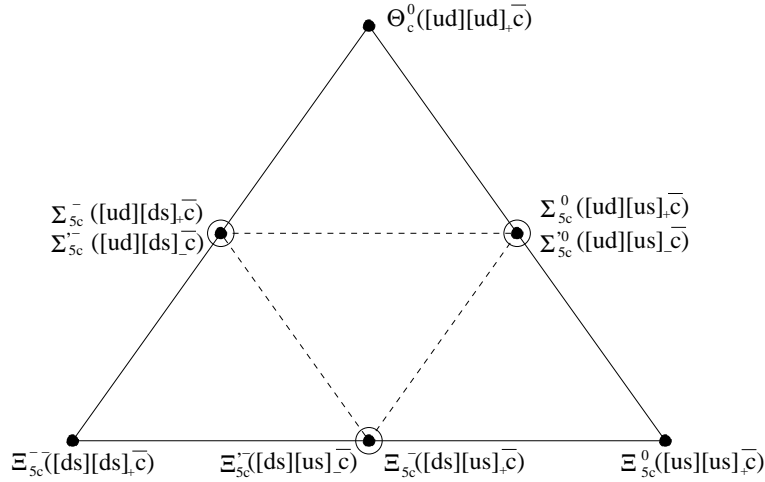
Figure 2.18: The flavour triplet $(3_f : \Sigma'^{0,-}_{5c}$ and Ξ'^{-}_{5c}, open circles) and anti-sextet $(\overline{6_f} : \Theta^0_c, \Sigma^{0,-}_{5c}$ and $\Xi^{0,-,--}_{5c}$, solid circles) of charmed pentaquarks. The triplet consists of three antisymmetric diquark pairs $[q_1q_2][q_3q_4]_-$, while the diquark pairs $[q_1q_2][q_3q_4]_+$ belong to the flavour symmetric anti-sextet, see also [91]

listed in table 2.4 [7].

_____

[7]Stewart [92] uses another notation for the 3_f-states: $\Sigma'^{0,-}_{5c} = T^{0,-}_s$ and $\Xi'^{-}_{5c} = T^{-}_{ss}$ for the charmed PQ and $\Sigma'^{+,0}_{5b} = R^{+,0}_s$ and $\Xi'^{0}_{5b} = R^0_{ss}$ for the beauty PQ.

Table 2.4: The flavour wave functions of the heavy pentaquarks in the Jaffe Wilczek model, where $\bar{q} = \bar{c}$ or $\bar{b}$ and $[q_1 q_2][q_3 q_4]_\pm$ is defined in equation 2.29 and 2.30.

$\overline{6_f}$-states	Flavor wave function	3_f-states	Flavor wave function
Θ_c^0, Θ_b^+	$[ud][ud]\bar{q}$		
$\Sigma_{5c}^0, \Sigma_{5b}^+$	$[ud][us]_+\bar{q}$	$\Sigma_{5c}'^0, \Sigma_{5b}'^+$	$[ud][us]_-\bar{q}$
$\Sigma_{5c}^-, \Sigma_{5b}^0$	$[ud][ds]_+\bar{q}$	$\Sigma_{5c}'^-, \Sigma_{5b}'^0$	$[ud][ds]_-\bar{q}$
Ξ_{5c}^0, Ξ_{5b}^+	$[us][us]\bar{q}$		
Ξ_{5c}^-, Ξ_{5b}^0	$[us][ds]_+\bar{q}$	$\Xi_{5c}'^-, \Xi_{5b}'^0$	$[us][ds]_-\bar{q}$
$\Xi_{5c}^{--}, \Xi_{5b}^-$	$[ds][ds]\bar{q}$		

The Θ_c^0 differs from the Θ^+ by the replacement of the antiquark $\bar{s} \to \bar{c}$. The mass difference arising from this exchange can be related to the $\Lambda(1116)$ and $\Lambda_c(2285)$ masses, because the $[ud]$ diquark in the Λ is coupled to colour $\overline{3_c}$ and spin zero and hence provides an environment for the s quark nearly identical to the environment of the $\bar{s}$ in the Θ^+. Jaffe and Wilczek estimated the mass of the Θ_c^0 by:

$$m(\Theta_c^0) \approx m(\Theta^+) + m(\Lambda_c) - m(\Lambda) \approx 2710 \, \text{MeV}^8, \qquad (2.36)$$

which is about $100 \, \text{MeV}$ below the threshold for the strong decay $\Theta_c^0 \to p \, D^-$. The mass of the Θ_b^+ is estimated likewise:

$$m(\Theta_b^+) \approx m(\Theta^+) + m(\Lambda_b) - m(\Lambda) \approx 6050 \, \text{MeV}, \qquad (2.37)$$

which is about $165 \, \text{MeV}$ below the threshold for the strong decay $\Theta_b^+ \to p \, B^0$. At first sight the controversy about the mass of the Θ_c^0 should be settled down with the recent observation by the H1 collaboration of a narrow resonance in the $D^{*-} p$ and $D^{*+} \bar{p}$ invariant mass spectrum at $3099 \, \text{MeV}$ [94]. But as pointed out in [95] it is possible that the H1 state $\Theta_c^0(3099)$ is an excited state of an yet undiscovered ground state $\Theta_c^0(2700)$ with opposite parity. Therefore it is important to measure the parity of the $\Theta_c^0(3099)$. If this state has negative parity this may imply the existence of a charmed pentaquark with positive parity and a mass below the D meson-nucleon threshold. On the other hand if the H1 state $\Theta_c^0(3099)$ proves to be a truly ground state this would have an important impact on the Jaffe and Wilczek model. In that case the diquarks should not be treated as a point like particle and there are significant attractive hyperfine interactions between the antiquark and the other four quarks of the pentaquark [96]. However, it must be mentioned that the $\Theta_c^0(3099)$ state could not been confirmed by any other collaboration and even at H1 this state is not seen anymore using the high statistic HERA II data, see section 2.4.3.

Assuming that the $\Theta_c^0(3099)$ is not a ground state Cheng *et al.* [89] followed the argumentation of Jaffe and Wilczek to estimate the masses of the other flavour anti-sextet $(\overline{6_f})$ members. Their results are listed in table 2.5.

Stewart *et al.* [92] estimated the masses of the 3_f members within the Jaffe and Wilczek model. As mentioned above it is expected that these states have negative parity and that

---

[8]The chiral soliton model yields a mass of $m(\Theta_c^0) \approx 2704 \, \text{MeV}$ [93] .

Table 2.5: Mass estimation of the $\overline{6_f}$ states in the J-W model.

$\overline{6_f}$-states	Mass in the J-W model
Θ_c^0	2710 MeV
$\Sigma_{5c}^{0,-}$	2860 MeV
$\Xi_{5c}^{0,-,--}$	3014 MeV
Θ_b^+	6050 MeV
$\Sigma_{5b}^{+,0}$	6199 MeV
$\Xi_{5b}^{+,0,-}$	6351 MeV

they are in the 3_f representation of SU(3)-flavour. Therefore there is no P-wave expected between the two diquarks. The masses can be estimated as follows:

$$m(T_s) \approx m(\Theta_c^0) + \Delta_s - U_P, \qquad (2.38)$$

where Δ_s is the mass difference arising when a u or d quark is exchanged by a s quark and U_P is the excitation energy associated with the P-wave. These terms can be estimated by $\Delta_s \approx m(\Xi_c) - m(\Lambda_c) \approx 184$ MeV or $\Delta_s \approx m(\Lambda) - m(p) \approx 177$ MeV and $U_P \approx m(\Lambda_c') - m(\Lambda_c) \approx 310$ MeV, where Λ_c' denotes the excitation of the Λ_c with (ud) in a P-wave relative to c. The mass of the T_{ss} can be estimated by $m(T_{ss}) \approx m(T_s) + \Delta_s$. In a similar way the masses of R_s and R_{ss} have been estimated. The resulting masses are listed in table 2.6. These mass

Table 2.6: Mass estimation of the 3_f states in the J-W model.

3_f-states	Mass in the J-W model
$\Sigma_{5c}^{\prime 0,-} = T_s^{0,-}$	2580 MeV
$\Xi_{5c}^{\prime -} = T_{ss}^-$	2770 MeV
$\Sigma_{5b}^{\prime +,0} = R_s^{+,0}$	5920 MeV
$\Xi_{5b}^{\prime 0} = R_{ss}^0$	6100 MeV

estimations are well below threshold for the strong decays and therefore it is likely that the 3_f states decay weakly. For the T_s pentaquarks that would be $\bar{c} \rightarrow \bar{s}\, d\, \bar{u}$. Possible decay modes are [92]:

$$
\begin{aligned}
\Sigma_{5c}^{\prime 0} = T_s^0 &\rightarrow \Lambda^0 K_s^0, p\,\pi^-, p\,\phi\,\pi^-, \Lambda^0 K^+\pi^-, K_s^0 K^- p, \\
\Sigma_{5c}^{\prime -} = T_s^- &\rightarrow \Lambda^0 K_s^0 \pi^-, p\,\pi^-\pi^-, p\,\phi\,\pi^-\pi^-, \Lambda^0 K^+\pi^-\pi^-, \\
\Xi_{5c}^{\prime -} = T_{ss}^- &\rightarrow \Lambda^0 \pi^-, \Xi^- K_s^0, \Lambda^0 K_s^0 K^-, K^- p\,\pi^-.
\end{aligned}
\qquad (2.39)
$$

In the last part of this thesis the invariant mass spectrum $m_{inv}(K_s^0, \Lambda^0)$ is studied where the decay $T_s^0 \rightarrow \Lambda^0 K_s^0$ could in principal be observed.

2.4.2 Karliner Lipkin Diquark-Triquark Model

As mentioned in section 2.4.1 quarks with the same flavour have to be separated within the PQ. Therefore a single cluster model for the description of the pentaquarks is not adequate

and Karliner and Lipkin (KL) [86] proposed that the system is divided into two colour non singlet clusters which separates the quarks of identical flavour. The two clusters are a diquark (for example a ud for the Θ^+) and a triquark (for example a $ud\bar{s}$ for the Θ^+), see figure 2.19. In the KL model these clusters are separated by a distance larger than the range of the colour magnetic force and are kept together by the colour electric force, so that the colour hyperfine interaction operates only within but not between the clusters. The diquark has the same configuration as in the JW model, namely they are in a colour anti-triplet state $(\overline{3_c})$ and in flavour anti-triplet state $(\overline{3_f})$ and have isospin I = 0 and spin S = 0. The two quarks $q_1 q_2$ in the triquark $(q_1 q_2 \overline{Q})$ are in a colour sextet representation (6_c) of $SU(3)_c$ and in a flavour anti-triplet representation $(\overline{3_f})$ of $SU(3)_f$ and have I = 0 and S = 1. The state of these two quarks is symmetric in spin as well as in colour. The triquark is in a flavour anti-sextet representation of $SU(3)_f$ and in a colour triplet representation of $SU(3)_c$ so that the pentaquark builds a colour singlet state. The triquark has I = 0 and S = $\frac{1}{2}$. The KL model predicts a flavour antidecuplet and a flavour octet, because $\overline{3_f} \otimes \overline{6_f} = 8_f \oplus \overline{10_f}$. This is in agreement with the JW model. However, unlike the JW model Karliner and Lipkin *assume* a P-wave between the diquark and the triquark[9].

Karliner and Lipkin used a SU(6) spin-colour algebra (introduced by Jaffe [98]) for the description of the hyperfine interaction between two quarks i and j:

$$V_{hyp} = -V\,(\vec{\lambda_i} \cdot \vec{\lambda_j})(\vec{\sigma_i} \cdot \vec{\sigma_j}), \tag{2.40}$$

where $\vec{\lambda}$ and $\vec{\sigma}$ denote the generators of $SU(3)_c$ and the spin operators (Pauli matrices), respectively and V is a constant greater than zero. This hyperfine interaction is attractive for states that are symmetric in colour and spin where $\vec{\lambda_i} \cdot \vec{\lambda_j}$ and $\vec{\sigma_i} \cdot \vec{\sigma_j}$ have the same sign and repulsive in antisymmetric states where they have opposite signs. Therefore the quarks within one diquark must have different flavours: Pauli principle forces two identical fermions at short distance to be in a state that is antisymmetric in spin and colour where the interaction from equation 2.40 is repulsive, resulting in a hyperfine interaction that is always repulsive between two quarks of the same flavour.

For the heavy pentaquarks the KL model predicts a flavour triplet and a flavour anti-sextet, like the JW model. Due to the fact that KL assumes a P-wave between the two clusters (diquark-triquark) this model predicts a positive parity (P = +1) for both, the flavour triplet and anti-sextet states. This is in contrast to the JW model where $P(3_f) = -1$. Measuring the parity of the flavour triplet heavy pentaquarks can thus discriminate between the JW model and the KL model. But up to date no pentaquarks from the flavour triplet are observed.

2.4.2.1 Mass Estimation in the Karliner Lipkin Model

Estimating the mass of the Θ^+ KL uses the SU(6) spin-colour algebra. It can be shown that the hyperfine interaction for the diquark-triquark system is stronger by $\frac{1}{6} \cdot (m_\Delta - m_N) \approx 50\,\mathrm{MeV}$ than for the kaon-nucleon system, where $m_\Delta = 1232\,\mathrm{MeV}$ is the mass of the Δ

---

[9]To get a picture of the KL model (for the Θ^+) consider a K^+ and a neutron which are far enough apart so that they don't 'feel' each other. Then move a d quark from the neutron over to the kaon and recouple the colour and spin of the 'K^+' to optimize the hyperfine interaction. Moving a quark from point r_1 to r_2 requires an energy in the potential of the neutron of V(r_2) - V(r_1), where V is the confining potential (for example Coulomb + linear). The energy is in the colour electric field that has been generated between r_1 and r_2. The tradeoff between the hyperfine and the confining interaction reproduces the mass of the pentaquark, see [97].
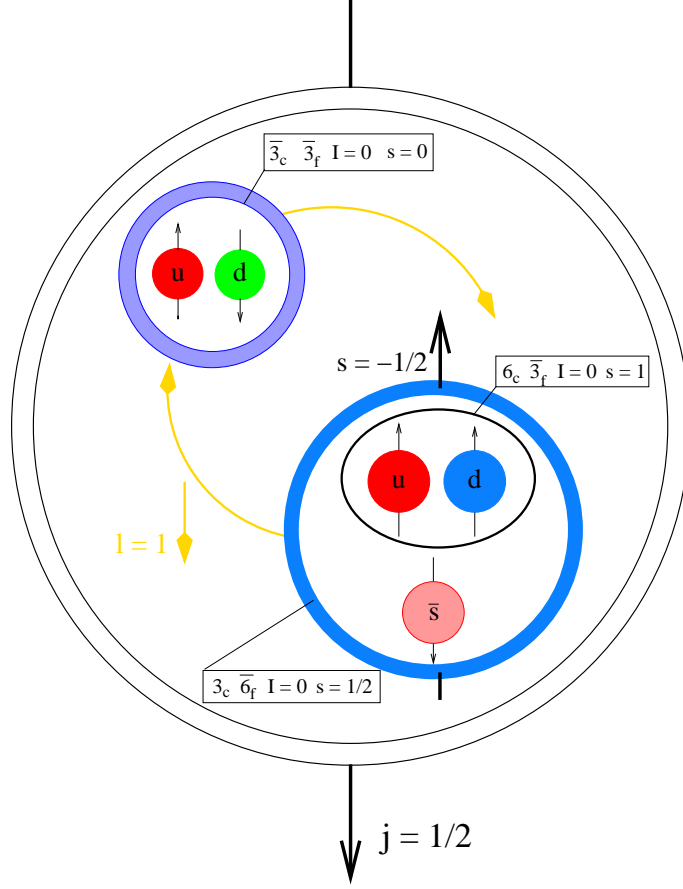
Figure 2.19: Schematic representation of the Θ^+ pentaquark in the Karliner Lipkin model.

resonance and m_N the mass of the nucleon. Therefore the diquark-triquark system is tighter bound than the kaon-nucleon system. The diquark triquark system has a colour electric interaction between the two clusters which is identical to the quark antiquark interaction in mesons. Neglecting the finite size of the diquark and the triquark this system can be compared with analogous mesons. KL considered the D_s meson whose reduced mass m_{red} is similar to that one of the diquark triquark system in the Θ^+:

$$m_{red}(c\bar{s}) = \frac{m_c \cdot m_s}{m_c + m_s} = 410\,\text{MeV} \approx m_{red}(di - tri) = \frac{m_{di} \cdot m_{tri}}{m_{di} + m_{tri}} = 458\,\text{MeV}, \qquad (2.41)$$

where $m_u = 360\,\text{MeV}$, $m_s = 540\,\text{MeV}$, $m_c = 1710\,\text{MeV}$, $m_{di} = 720\,\text{MeV}$ and $m_{tri} = 1260\,\text{MeV}$ are taken. Furthermore it has been proposed that the $D_s(2317)$ meson is a $J^P = 0^+$ excited state of the ground state $D_s(1969)$[99]. This implies an excitation energy of 350 MeV consisting of contributions from a P-wave (δ^{P-wave}) and from colour hyperfine splitting. KL estimated the colour hyperfine splitting based on the mass difference of the D_s^* and D_s mesons. They obtained:

$$\delta^{P-wave} \approx 350\,\text{MeV} - (m_{D_s^*} - m_{D_s}) = 207\,\text{MeV}. \qquad (2.42)$$

This yields a Θ^+ mass of:

$$m(\Theta^+) \approx m(N) + m(K_s^0) - \frac{1}{6} \cdot (m_\Delta - m_N) + \delta^{P-wave} = 1592 \, \text{MeV}, \qquad (2.43)$$

which is about 3% above the observed mass.

The mass of the Θ_c^0 has also been estimated within the KL model. The main difference to the estimation above is the mass of the antiquark $\bar{c}$, which breaks the SU(3) symmetry. KL estimated the mass of the Θ_c^0 without the P-wave excitation ($m^0(\Theta_c^0)$) to [97]:

$$m^0(\Theta_c^0) \approx m(N) + m(D) - \frac{1}{12}(1 + \zeta_c) \cdot (m(\Delta) - m(N)) \approx 2778 \, \text{MeV}, \qquad (2.44)$$

where $\zeta_c = \frac{m_u}{m_c} = 0.21$ describes the symmetry breaking. The mass including the P-wave excitation is therefore:

$$m(\Theta_c^0) \approx 2778 \, \text{MeV} + 207 \, \text{MeV} = 2985 \, \text{MeV}. \qquad (2.45)$$

The uncertainty of this mass is estimated to be approximately $50 \, \text{MeV}$:

$$m(\Theta_c^0) = (2985 \pm 50) \, \text{MeV}. \qquad (2.46)$$

This mass is clearly above the mass predicted by the JW model, but is more or less compatible with the mass measured by the H1 collaboration.

2.4.3 Observations and Non-Observations of Pentaquarks

Soon after the possible discovery of the Θ^+ many experiments have performed a search for this and other pentaquark candidates which have been predicted by various models. In a first instance some of those experiments have reported evidence for pentaquark candidates. However, the following states have only been observed by one single experiment:

- The exotic pentaquark $\Xi^{0,--}$ observed by the NA49 Collaboration [88] in the decay mode $\Xi\pi$ with a mass of $1862 \pm 2 \, \text{MeV}$ and a width of less than $18 \, \text{MeV}$. Its minimal quark content is $dsus\bar{d}$ and $dsds\bar{u}$.

- The heavy pentaquark Θ_c^0 observed by the H1 Collaboration [94] in the decay mode D^*p with a mass of $3099 \pm 8 \, \text{MeV}$ and a width of $12 \pm 3 \, \text{MeV}$. Its minimal quark content is $udud\bar{c}$.

- A candidate for the N_s^0 pentaquark with minimal quark content $duds\bar{s}$ was found in the year 2004 by the STAR Collaboration at RHIC [21] in the decay mode $\Lambda^0 K_s^0$. They observed a narrow peak at $1734 \pm 5 \, \text{MeV}$ with a width consistent with the experimental resolution of about $6 \, \text{MeV}$.

However, in a second round where analyses with improved statistics were available, some claims have been revised. At this point only three representative examples for the (non-) discovery of PQ states are given. For a comprehensive overview see for example [100, 101, 102].

The Θ_c^0 at H1: A candidate state for the Θ_c^0 was claimed in the HERA I data in the decay channel $D^* p$ with a significance of $5.4\,\sigma$. The analysed data comprises a luminosity of $\mathcal{L} = 75\,\mathrm{pb}^{-1}$ and yields 50.6 ± 11.2 reconstructed Θ_c^0 candidates. Soon after this discovery FOCUS has performed a search for this new state in γBeO reactions [103]. Their sample of D^* events is roughly 30 times larger than that used for the H1 analysis and an upper limit of $0.075\,\%$ at $95\,\%$ confidence level (C.L.) on the production cross-section of the Θ_c^0 to D^* mesons has been extracted. This limit is more than 10 times stronger than the Θ_c^0 to D^* ratio found at H1, implying that the state observed by H1 is either a statistical fluctuation or the production mechanism of the Θ_c^0 is suppressing its production in $\gamma p(n)$ reactions. There are two reasons why the later interpretation is disfavouerd. Firstly, the ZEUS collaboration analysing also *ep* data with a luminosity of $\mathcal{L} = 126\,\mathrm{pb}^{-1}$ has not found any evidence for the Θ_c^0 and an upper limit at $95\,\%$ C.L. on the relative production to D^* mesons of $0.32\,\%$ has been extracted [104] and secondly, a preliminary anaysis of HERA II data with an integrated luminosity of $\mathcal{L} = 348\,\mathrm{pb}^{-1}$ by the H1 collaboration has not seen any evidence for the Θ_c^0 anymore, indicating an upper limit at $95\,\%$ C.L. on the relative production to D^* mesons of $0.1\,\%$ [105] which is clearly contradicting the first measurement.

The Θ^+ at CLAS: The CLAS Collaboration at the JLAP has preformed two experiments dedicated to the Θ^+ search. A first experiment has studyied the reaction $\gamma p \rightarrow \pi^+ K^- K^+ n$ using a tagged photon beam with an energy range of 3 to $5.47\,\mathrm{GeV}$. A narrow resonance was found in the invariant mass distribution of the $K^+ n$ spectrum with a width consistent with the detector resolution and a significance of 7.8 ± 0.1 [106]. This is the highest significance ever reported for pentaquark findings. Another experiment was analysing the reaction $\gamma d \rightarrow p K^- K^+ n$ with photon energies up to $3.8\,\mathrm{GeV}$ [107]. Again a resonant structure in the $K^+ n$ spectrum was observed with a width consistent with the detector resolution and a statistical significance of 5.3 ± 0.3. In a second round these results have been revised by two high statistics experiments. One of those has examined the reaction $\gamma p \rightarrow K_s^0 K^+ n$ [108]. No structure was found in the $K^+ n$ mass spectrum and an upper limit at $95\,\%$ C.L. of $0.8\,\mathrm{nb}$ was put on the total production cross-section of a Θ^+ which is in clear contradiction to other experiments, see for example [101]. The second high statistic experiment was again analysing the reaction $\gamma d \rightarrow p K^- K^+ n$ [109] and is therefore directly comparable with the first experiment mentioned above. No resonant structure was observed in this analysis, clearly contradicting the first observation in the same channel. It turned out that the first experiment has understimated the background and that the significance was rather $3\,\sigma$ and not $5.3\,\sigma$. Further explanations trying to justify the decrepancy of the different CLAS experiments and outlining tests for future disoveries can be found in [110].

The Ξ^{--} and Ξ^0 at NA49: The observation of candidates for the Ξ^{--} and the Ξ^0 PQ states by the NA49 collaboration has lead to an examination of the $\Xi \pi$ spectra by various experiments. Although some of these experiments are close to the NA49 kinematics and have a similar sensitivity to the examined decay channel, none of them could confirm the results of the NA49 Collaboration [20, 111, 112, 113, 114, 115, 116, 117, 118], including the H1 search discussed in part II of this work.

These examples show the controversal situation about PQ discoveries. Beside these 'negative' examples there are also experiments that could confirm their initial findings, like the DIANA collaboration [119].

In conclusion it must be said that the initial evidence for PQ states has cleary lost much of its original significance over the past years. Nevertheless, further studies are needed to unambiguously clarify the issue of PQ observations. However, as pointed out in [100] the unsparing effort of PQ searches is not futile: *"When the dust will have settled on the issue of narrow pentaquark baryons, we will have learned a lot about the physics of hadrons, no matter what the final outcome will be"* (V. D. Burkert).

2.5   Monte Carlo Generators and QCD Models

In high energy physics (HEP), as in other fields of science, many problems cannot be solved analytically. The work around is either to simplify the problem until it is solvable or to use a stochastic description based on predictions obtained from first principle. In HEP the second approach is used. The stochastic description is implemented in so-called Monte Carlo (MC) event generators providing an approximative solution based on a simulation of the problem using pseudo random numbers [10].

In HEP, the MC generators are used to simulate the outcome of interacting particles, e.g. $e^{\pm}\,p \rightarrow X$. Therefore, the goal is to obtain generated events that mimic the true data to the highest possible level. The random character of the Monte Carlo method is used to generate events according to their probability obtained by theoretical considerations. The physics describing the transformation of the incident beam particles to the final state particles is subdivided into different parts as illustrated in figure 2.8. The different processes are treated sequentially. A comprehensive overview on MC generators that are used for the simulation of ep interactions can be found in [120]. The generated events (all final state particles) are passed through the full GEANT [121] based simulation of the H1 apparatus in order to reproduce the detector response to the generated particles. The simulation of the physical process together with the simulation of the detector response is needed to correct the data for detector effects and to study resolution effects.

Within this work, two different leading order Monte Carlo generators are used:

- The **DJANGO** [122] program simulates deep-inelastic electron - proton scattering at leading order. It generates the hard QCD $2 \rightarrow 2$ subprocesses (e.g. $\gamma^* q \rightarrow q$, $\gamma^* g \rightarrow q\bar{q}$), convoluted with the proton PDF, chosen herein to be CTEQ6L [123] or GRV94, LO [124]. The factorization and renormalisation scales are set to $\mu_f^2 = \mu_r^2 = Q^2$. Higher order QCD effects producing further hard outgoing partons are described in DJANGO using either the parton shower approach as implemented in LEPTO [125] (referred to as MEPS) or by the so-called colour dipole model approach [126, 127] available within ARIADNE [128] (referred to as CDM). In LEPTO the parton showers are ordered in the transverse momenta (k_T) of emissions, according to the leading $\log(Q^2)$ approximation (see figure 2.5). In the ARIADNE program the partons are generated by colour dipoles, spanned between the partons in the cascade. In the case of deep-inelastic ep scattering, the initial colour dipole is provided by the scattered parton and the proton remnant.

---

[10]The advantage of using pseudo random numbers is the reproducibility of the generated event sample.

The emitted gluons carry colour charge themselves and build new colour dipoles which can again radiate gluons. This process is illustrated in figure 2.20. Since the dipoles radiate independently, there is no k_T ordering. In both instances, the hadronic final state is modelled according to the LUND colour string fragmentation model [50, 51, 52] (see section 2.1.6), as implemented e.g. in the JETSET [53, 54] program. If not stated otherwise, the ALEPH-tuned JETSET parameters [72] ($\lambda_s = 0.286, \lambda_{qq} = 0.108$ and $\lambda_{sq} = 0.690$) are used.

The DJANGO program can be coupled with the HERACLES program [129] to simulate initial and final state QED radiations.

- The **PYTHIA** [130] program is the most common multipurpose simulation program. It can simulate ee, $e\gamma$, ep and pp collisions. The simulation of ep events is analogical to the DJANGO model in the LEPTO mode, i.e. it generates also the hard QCD $2 \rightarrow 2$ subprocesses, simulates initial and final state parton shower and incorporates to JETSET for the simulation of the hadronisation process.
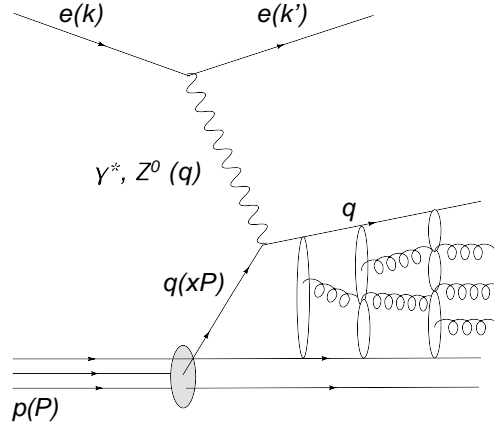

Figure 2.20: A sketch of the dipole radiation as implemented in the ARIADNE model.

2.5.1   Simulated Data Sets

For the analysis presented in the following chapters several Monte Carlo sets have been produced:

- For the correction of the data for the cross-section measurement the DJANGO (version h 1.4) generator has been used. Two sets were generated and fully simulated with GEANT, one in the ARIADNE mode with a luminosity of $260\,\mathrm{pb}^{-1}$ and one in the LEPTO mode with $\mathcal{L} = 194\,\mathrm{pb}^{-1}$ (H1-internal identification numbers 4142 and 4049, respectively). Only events with a virtuality larger than $1.8\,\mathrm{GeV}^2$ and an inelasticity within $0.05 < y < 0.7$ have been generated. In both cases only events have been kept that contain at least one K_s^0 or Λ hadron in the central part of the detector ($-1.75 < \eta < 1.75$) with a transverse momentum larger than $100\,\mathrm{MeV}$. The proton PDF set has been chosen to be GRV94, LO [124]. The JETSET parameter correspond

to the ALEPH-tuning for ARIADNE 4.08 [72]. The main properties are summarised in table 2.7. Both sets contain initial and final state photon radiations.

Table 2.7: The main properties of the two DJANGO Monte Carlo sets used for the cross-section analysis.

Generated range	$Q^2 > 1.8\,\mathrm{GeV}^2$
	$0.05 < y < 0.7$
Preselection	$p_T(K_s^0, \Lambda) > 0.1\,\mathrm{GeV}$
	$-1.75 < \eta(K_s^0, \Lambda) < 1.75$
PDF set	GRV94, leading order
JETSET	$\lambda_s = 0.286$
	$\lambda_{qq} = 0.108$
	$\lambda_{sq} = 0.69$

- For the search for new resonances the PYTHIA (version 6.2) generator is used. The new particles are generated by changing the properties of known resonances. For the simulation of the potential pentaquark states Ξ_{5q}^{--} and Ξ_{5q}^{0} the $\overline{\Delta}^{--}$ and the $\Xi(1530)^0$ resonances have been used as described in section 9.5.

Chapter 3

The H1 Experiment at HERA

The measurements presented within this work are carried out using data taken with the H1 detector at the *ep* collider HERA at DESY (**D**eutsches **E**lektronen **Sy**nchrotron) in Hamburg, Germany. The DESY laboratory was founded in 1959 and is one of the five largest accelerator centers of the world. Beside particle physics, which started in 1965 with the installation and commissioning of the DESY accelerator, other fields of physics are investigated at DESY like solid state physics, material science and molecular biology. In the late seventies of the last century the installation of the electron-positron **Do**uble **Ri**ng **S**tore (DORIS) has started and was completed in 1974. The next milestone of the development was achieved in 1978 as the construction of the 2.3 km long **P**ositron-**E**lektron **T**andem **R**ing **A**nlage (PETRA) was finished. At PETRA the physicists could observe for the first time the gluons directly. The construction of the **H**adron **E**lektron **R**ing **A**nlage (HERA) has started in 1984 and was completed eight years later. The HERA accelerator has stopped operation mid 2007. Nowadays, the DESY laboratory is involved in the LHC experiments and in the planing of a future TeV linear accelerator.

3.1 The HERA Collider

The HERA facility [131] was so far the only storage ring in the world for electrons and protons. The electrons (or positrons) and the protons were passed through several pre-accelerators (linear accelerators and synchrotrons) before being injected at HERA, where they were accelerated up to energies of 27.6 GeV and 920 GeV [1], respectively. The center-of-mass energy of 319 GeV was one order of magnitude higher than available at fixed target experiments, providing a deeper insight into the structure of the proton. A schematic overview of the accelerator is displayed in figure 3.1. Due to the significant different masses of the electrons and the protons, they were stored in two separated magnetic rings, placed in a tunnel of 6.3 km length located up to 30 m under the ground level. For the diffraction of the protons in the ring a magnetic field of 4.7 T, provided by super-conducting dipole magnets, was needed. The magnetic field was the limiting factor for the maximal proton energy. For electrons only a field of 0.165 T was needed, provided by conventional electromagnets. The energy of electrons in circular accelerators is limited by synchrotron radiation which amounted to 127 MeV per circulation at HERA. Along the tunnel, four different experiments

---

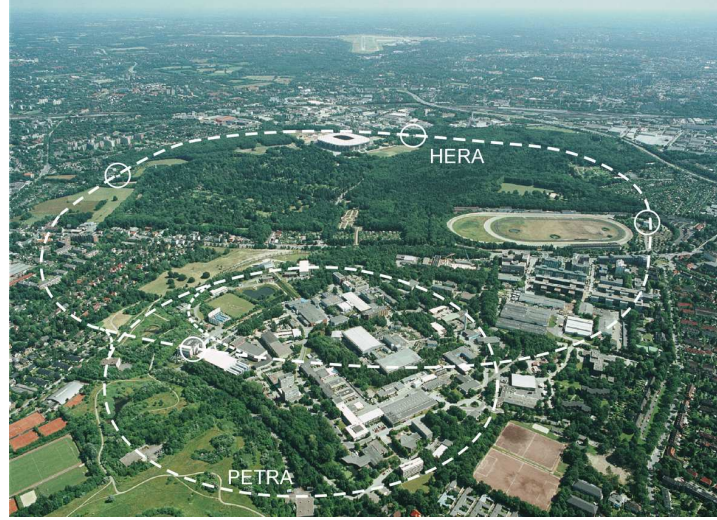[1]Before 1998 the protons were accelerated up to 820 GeV.

Figure 3.1: The HERA accelerator with the pre-accelerator PETRA. The four circles indicate the different experiments H1, HERMES, ZEUS and HERA-B (clockwise).

were located: H1, ZEUS, HERMES and HERA-B. The first two were studying the high-energy collisions of the electrons and protons while the other two were fixed target experiments using either the electron or the proton beam.

The electrons and protons were grouped in so-called bunches, each containing $10^{10} - 10^{11}$ particles. In total approximately 180 bunches were circulated in each ring, resulting in currents in the order of several tens of milliampere. The bunch crossing rate was $10.4\,\mathrm{MHz}$, corresponding to one collisions every $96\,\mathrm{ns}$. In the first data taking period (HERA I) a specific luminosity of $\mathcal{L} = 2.0 \cdot 10^{31}\,\mathrm{cm}^{-2}\mathrm{s}^{-1}$ was achieved, exceeding the design luminosity of $\mathcal{L} = 1.5 \cdot 10^{31}\,\mathrm{cm}^{-2}\mathrm{s}^{-1}$. The luminosity is given by: $\mathcal{L} = f\, n_e\, n_p\, /\, A$, where f is the bunch crossing frequency, $n_{e(p)}$ the number of electrons (protons) per bunch and A the cross section of the beams. Especially the last quantity cannot be measured with high accuracy and therefore the luminosity was determined experimentally, see section 3.2.3. The HERA I data period ended in autumn 2000. In the following break down, the focusing of the beams was improved, resulting in a roughly four times higher specific luminosity. After the luminosity upgrade, the HERA II data taking period started in 2002 and lasted until summer 2007. The luminosity accumulated by the H1 experiment is displayed in figure 3.2 for the two data taking periods of HERA I and II.

3.2   The H1 Experiment

The H1 detector was located in the North Hall and is illustrated in figure 3.3. The dimensions of the detectors were 12 x 10 x $15\,\mathrm{m}^3$ and the total wight was approximately $2800\,\mathrm{tonnes}$. H1 has used a right handed Cartesian coordinate system with the origin at the nominal ep interaction point. The proton beam direction defines the z axis of the laboratory frame, the x axis points towards the center of the ring and the y axis points upwards, see figure 3.3. Alternatively spherical coordinates (r, ϕ, θ) are used. The polar angle θ is measured with respect to the z axis and the azimuthal angle ϕ is measured with respect to the x
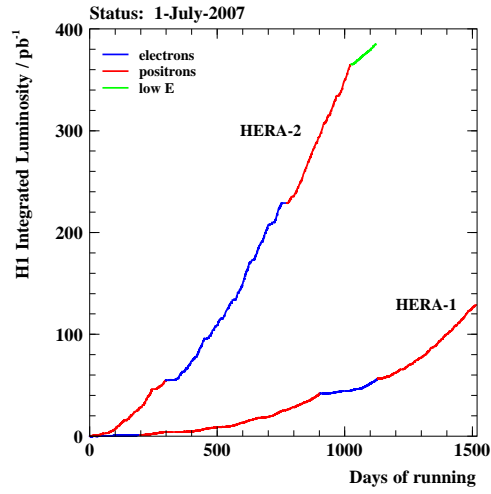
Figure 3.2: The luminosity accumulated by the H1 experiment, splited for the two data taking periods of HERA I and HERA II

axis. The pseudorapidity η is given by $\eta = -\ln\tan\frac{\theta}{2}$. Due to the different beam energies, the center-of-gravity of the electron-proton system was boosted into the direction of the incoming proton, which was accounted for by the asymmetric detector layout (more material in the positive z direction). Another important feature of the H1 detector was its almost full angular coverage. This is mainly important for events where the final state contains neutrinos which cannot be detected. The main components of the detector were the tracking system, the calorimeters and the muon chambers. A detailed description of the H1 detector can be found in [132, 133]. In the following only those detector components important for the present analysis are described. As most of the analysed data are taken during the HERA I period, only the detector setup at this time is described.

HERA Experiment H1

Size: $12 \times 10 \times 15\,\mathrm{m}^3$
Weight: 2800 t

1	Beam pipe and beam magnets
2	Central track detectors
3	Forward track detectors
4	Electromagnetic LAr calorimeter
5	Hadronic LAr calorimeter
6	Superconducting coil (1.15 T)
7	Compensating magnet

8	Helium supply for 7
9	Muon chambers
10	Instrumented iron yoke
11	Forward muon toroid
12	Backward calorimeter and drift chamber
13	PLUG calorimeter
14	Concrete shielding
15	LAr cryostat

Figure 3.3: Schematic representation of the H1 detector and the coordinate system.

3.2.1   The Tracking System

The most important part of the detector for this analysis was the tracking system of the H1 detector. All analyses presented in the following chapters are based on charged particle tracks. Three different detector techniques were used for the measurement of the tracks: Drift chambers, multi-wire proportional chambers (MWPC) and silicon detectors.

A schematic overview of the tracking system is provided in figure 3.4. The whole tracking system was contained in a magnetic field of 1.15 T produced by a super-conducting solenoid, allowing to measure the momentum of the particle track by the determination of its curvature in this field. The transverse momentum resolution is $\sigma(p_T)/p_T \simeq 0.006\,p_T\,[\text{GeV}] \oplus 0.015$ [134]. The tracking system was divided into two parts: the central track detector (CTD), covering a range of $15 < \theta < 165\,°$ and the forward track detector (FTD) covering the range $7 < \theta < 25\,°$. In this work only tracks measured in the CTD are considered and therefore only this part of the tracking system is described in the following. A detailed description of the FTD can be found in [135].
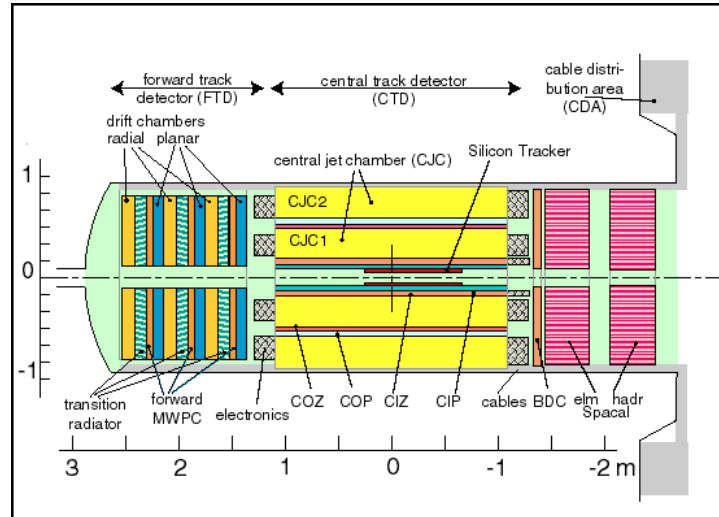
Figure 3.4: The H1 tracking system.

3.2.1.1   The Central Track Detector

The CTD consisted of several concentric parts as illustrated in figure 3.5. The innermost device was the central silicon tracker (CST), followed by the inner multi-wire proportional chamber (CIP) and the inner z chamber (CIZ). The central jet chamber was divided into two parts (CJC1 and CJC2). The outer z chamber (COZ) and the outer multi-wire proportional chamber (COP) were embedded between the two jet chambers.

The main part for the measurement of the particle tracks were the **CJC1 and CJC2** [136]. The anode wires of these drift chambers were sprung parallel to the z axis, allowing a precise measurement of the $r - \phi$ components of the trajectory of the tracks. The information of the z component of the track was obtained by sampling the currents at both ends of the chambers. However, this provided only a rudimental determination of the z position of the
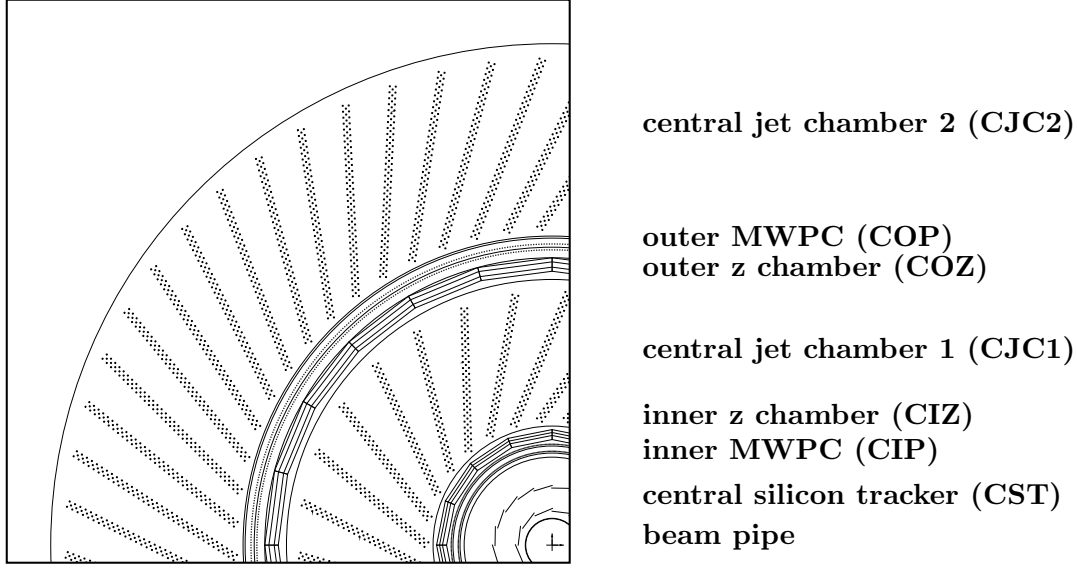
central jet chamber 2 (CJC2)

outer MWPC (COP)
outer z chamber (COZ)

central jet chamber 1 (CJC1)

inner z chamber (CIZ)
inner MWPC (CIP)

central silicon tracker (CST)

beam pipe

Figure 3.5: The H1 central track detector.

tracks. The CJC1 (CJC2) was divided into 30 (60) cells in ϕ, each cell containing 24 (32) sense wires. The different cells were tilted in radial direction, ensuring that also high momentum tracks, which have a low curvature, cross several cells. The chambers were filled with a gas mixture of approximately 49 % argon and 49 % ethane. Furthermore, ~ 1 % ethanol and ~ 0.2 % nitrogen were added. The drift velocity in this gas mixture is $50\,\mathrm{mm}\mu\mathrm{s}^{-1}$. With this drift velocity, a spatial resolution of the track position in the $r - \phi$ plane of $170\,\mu$m was achieved.

The CJC provided also a measurement of the energy loss of the particle tracks per length, dE/dx, which can be used for particle identification (see section 12.4.1).

A drawback of the drift chambers was the slow response time which complicates the usage of the CJC information for trigger purpose at the first level of the trigger farm (see section 3.2.4).

The information on the z position of the tracks was refined by the complementary information obtained by the z chambers **CIZ and COZ** [137]. The wires of these drift chambers were strung in radial direction (perpendicular to the beam axis), allowing a precise measurement of the z component of the trajectory of the tracks. The gas mixture was similar to that one in the CJC's. The CIZ had the form of a regular 16 sided polygon and was divided into 15 cells along the z direction. Each cell contained 4 sense wires. Information on the $r - \phi$ component of the tracks was gained by the charge division technique. The COZ was built very similar. It had the form of a regular 24 sided polygon and was divided into 23 cells.

The drift chambers explained so far have a good spatial resolution but a rather poor time resolution. Therefore, the tracking system was equipped with an inner and outer proportional chamber, the **CIP and COP** [138]. These chambers had an intrinsic time resolution of about 10 ns and provided information for a fast trigger decision to separate the subsequent bunch

crossings. Furthermore, these chambers provided a fast measurement of the interaction vertex which was also used for trigger purpose. The sense wires were strung parallel to the z axis. Both chambers consisted of two layers. The CIP (COP) was partitioned into 8 (16) segments along ϕ and in 60 (18) pads of a length of 36 mm (120 mm) along z. The two layers of the CIP were rotated with respect to each other by $\pi/8$. The information from the CIP and COP were not used for the final track reconstruction.

The innermost part of the tracking system was covered by the central silicon tracker **CST** [139]. The CST consisted of two cylindrical layers with 12 and 20 sensor ladders, each containing six sensors. This device provided a single hit resolution of $12\,\mu$m in the $r-\phi$ plane and $22\,\mu$m in the z plane. Therefore, the information of the CST were used to improve the parameters of the tracks determined from the hits in the CJC.

3.2.2 The Calorimeter

The H1 detector was equipped with four different calorimeters: the liquid argon calorimeter (LAr) [140] which covered the forward and the central region ($4 < \theta < 154\,°$), the backward calorimeter (SpaCal) [141] covering the backward region ($153 < \theta < 177.5\,°$), the Plug calorimeter [142] which covered the gap between the LAr and the beam pipe ($0.75 < \theta < 3.4\,°$) and the Tail catcher [143] which was situated within the return yoke of the solenoid. In this work only the SpaCal is used and described further.

3.2.2.1 The SpaCal

The SpaCal [141] was located in the backward region of the detector, see figure 3.6. Its main purpose was the detection of the scattered electron in low Q^2 DIS events ($2 < Q^2 < 120\,\mathrm{GeV}^2$). Like the LAr, it had an electromagnetic and a hadronic part. Both parts consisted of scintillating fibers embedded in a lead matrix absorber. The light, which was produced in the fibers, was guided to photon multipliers where the signal was read out. The active region in both parts was 25 cm deep and the fibers had a diameter of 0.5 mm. The electromagnetic part consisted of 1192 individual channels with a surface of 4.05 m x 4.05 m. The electromagnetic energy resolution is $\sigma_E/E \simeq 7\%/\sqrt{E/\mathrm{GeV}} \oplus 1\%$ and was determined using a test beam [144].

An additional drift chamber, the backward drift chamber (BDC) [145], was situated in front of the SpaCal. Its main purpose was to provide accurate information on the scattered electron in low Q^2 DIS events. The chamber consisted of 8 layers which were divided into octane. Each octane contained 32 drift cells with wires strung perpendicular to the beam axis to provide a good measurement of the z coordinate.

3.2.3 The Luminosity System

The luminosity is determined by the relation of the cross-section, σ, and the number of observed events, N, of a given physical process:

$$\mathcal{L} = \frac{N}{\sigma} \tag{3.1}$$

At H1 the luminosity was determined by the rate of the Bethe-Heitler process $e\,p \rightarrow e\,p\,\gamma$ [146]. The cross-section for this process can be calculated with a high precision. The electrons
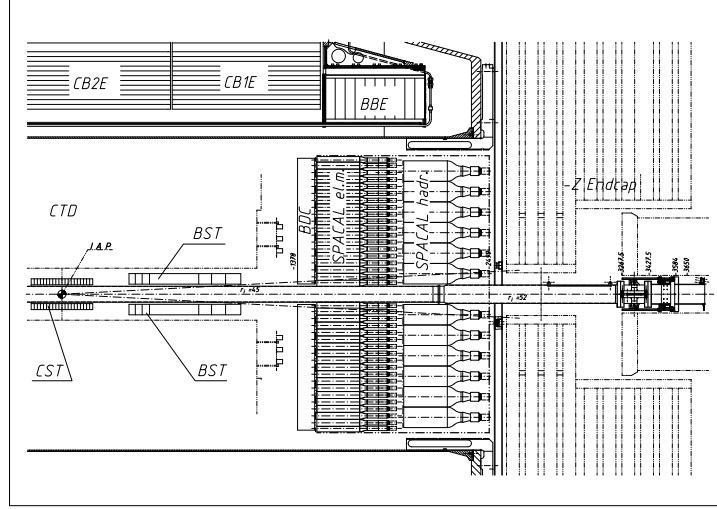
Figure 3.6: The H1 backward calorimeter SpaCal.

and photons from this process were measured with two calorimeters which formed the H1 luminosity system [147], see figure 3.7. Both detectors used Cerenkov crystal calorimeters. The electron tagger was located downstream in the tunnel at $z = -33.4\,\mathrm{m}$ and the photon tagger at $z = -102.8\,\mathrm{m}$. The luminosity for the HERA I data period was determined with an accuracy of $1.5\,\%$.
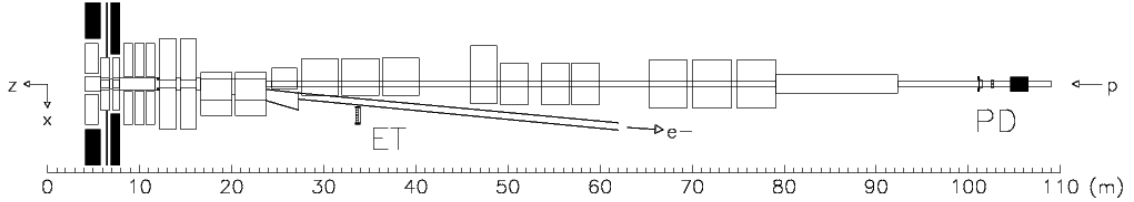

Figure 3.7: The H1 luminosity system.

3.2.4 The H1 Trigger System

A dedicated trigger system was required at H1 to reduce the high collision rate of $10.4\,\mathrm{MHz}$ to a rate of approximately $10\,\mathrm{Hz}$ which was the maximal rate with which the events could be written to tape. On the one hand, the trigger systems needed to reduce background events like beam-gas processes or synchrotron radiation as much as possible. Such background events occurred at a rate of approximately $50\,\mathrm{kHz}$. On the other hand, physical processes like photoproduction events which occurred also at high rates (20-$30\,\mathrm{Hz}$) needed to be reduced in order to ensure that rare processes are written to tape with a high efficiency.

Most of the detector components provided a trigger signal (beside the full information used to build the event off-line). These signals were evaluated in a four-level trigger system to decide whether the event was written to tape or not. The trigger system is illustrated in figure 3.8. For this analysis only two trigger levels are of relevance, the L1 and L4 level.
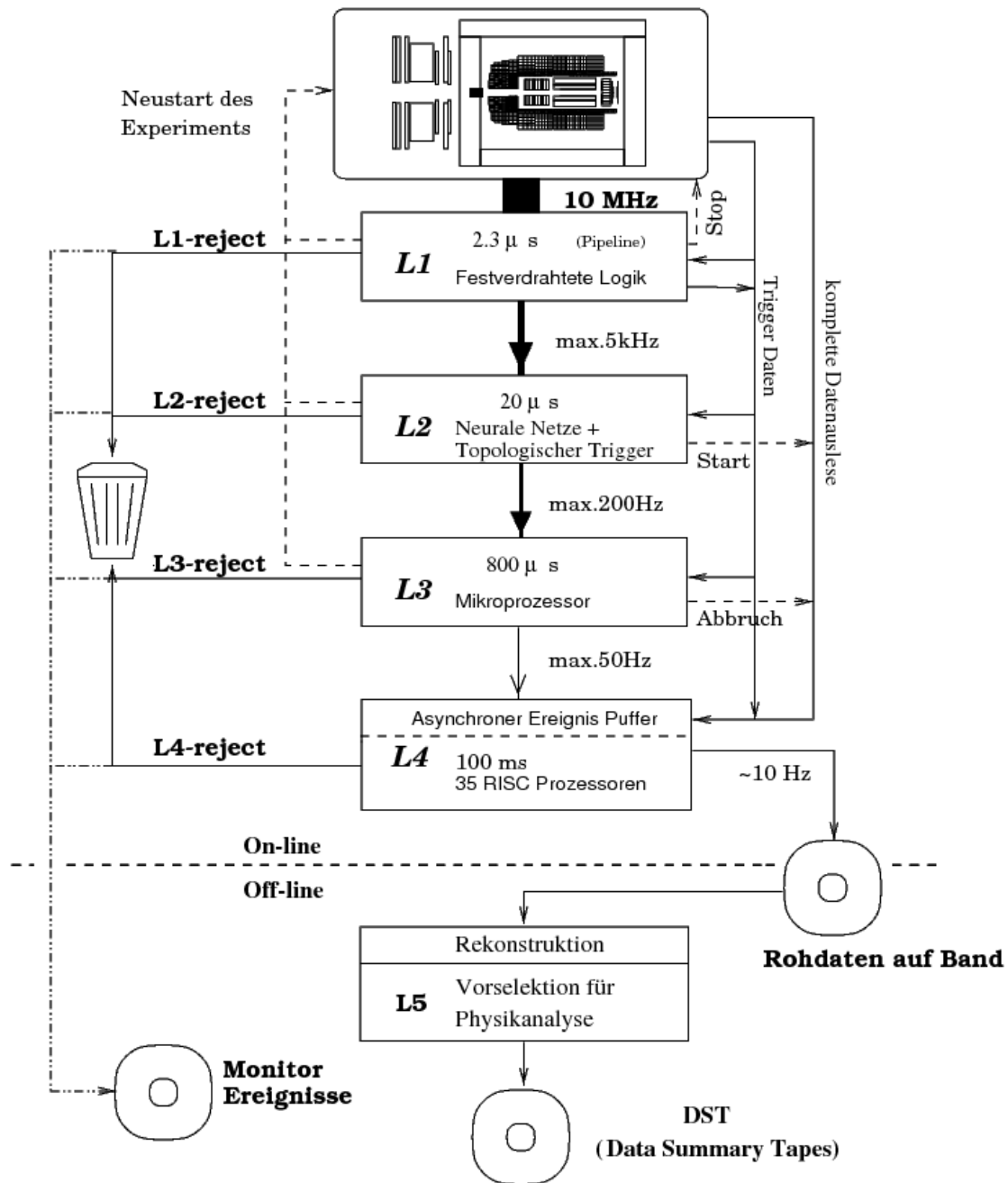
Figure 3.8: The H1 four level trigger system. The figure is taken from [76].

3.2.4.1 The Trigger Level L1

The first trigger level took a trigger decision with the bunch crossing rate of 10.4 MHz (dead-time free). All data provided by the different detector components were stored in a pipeline with a length of 25 bunch crossings. Therefore, the decision whether an event was kept or

not had to be taken within $25 \cdot 96\,\mathrm{ns} = 2.4\,\mu\mathrm{s}$. All relevant information of the event were processes within this time and so-called trigger elements were set and passed to the central trigger logic (CTL). At the CTL, subtriggers were built by logical connections of these trigger elements. The event was triggered if at least one of the 128 subtrigger conditions was fulfilled. Thereby the pipelines of the detector readout were stopped and the event that has triggered was read out. During this time no further events were processed, resulting in a so-called dead time. In order to keep this dead time below $10\,\%$, the maximal L1 trigger rate should not exceed $100\,\mathrm{Hz}$. The individual subtriggers were prescaled in order to keep the overall trigger rate below this limit. If a subtrigger had a prescale i, only every i-th event that was triggered by the corresponding subtrigger was kept.

3.2.4.2   The Trigger Level L4

For a further reduction of the rate, the events that were triggered by the previous trigger levels were passed to the fourth trigger level before being written to tape. On this trigger level the events were processed asynchronously on a PC farm where a nearly full reconstruction of the event was performed. Thereby selection criteria were applied to the reconstructed quantities, assigning the events into certain physical classes. All events that were not classified by one of the 16 L4 finders were written out only with a certain probability. The main strategy for the weighting of unclassified events was that the higher the photon virtuality of the event, the lower was the weight. This weight is in the following referred to as L4 weight.

Chapter 4

Experimental Aspects

This work consists of three related topics:

Analysis I: The measurement of the production cross-section of the strange hadrons K_s^0 and Λ as well as their ratio.

Analysis II: The search for narrow resonances decaying into $\Xi\,\pi$.

Analysis III: The investigation of $K_s^0\,\Lambda$ combinations.

The analyses I and II are carried out in deep-inelastic ep scattering data, while analysis III uses all recorded data.

The experimental aspects which are common for the three measurements are discussed in the following. In the first part the selection of the data for the different analyses is presented. The focus is put on the selection and triggering of DIS events. In the second part the technical issues relevant to the analyses are presented. This comprises the selection of well measured particle tracks, the vertex fitting routines used for the reconstruction of the long-lived strange hadrons and the discussion of the Breit frame. In the last part the so-called Armenteros-Thompson variables are introduced.

4.1 Data Selection and Event Kinematics

Here, the focus is put on the analyses I and II which are carried out in deep-inelastic ep scattering. After the selection of the run periods, the chosen subtrigger which is common for the two analyses is described. In a next step the reconstruction of the kinematic event variables and the selection criteria to extract DIS events are described. A comparison of the selected data with the predictions obtained from leading order Monte Carlo simulations is provided at the end of this section.

4.1.1 Selection of the Data Periods

For the analysis presented within this work different data periods are used:

- For the analysis I (see part I) the e^+p data from the years 1999 and 2000 are used. This data set has an integrated luminosity of $\mathcal{L} = 49.9\,\mathrm{pb}^{-1}$.

- For the analysis II (see part II) the full HERA I data set from the years 1996 to 2000 is used, corresponding to an integrated luminosity of $\mathcal{L} = 101 \, \mathrm{pb}^{-1}$.

- For the analysis III (see part III) the full 1999/2000 data set is used with an integrated luminosity of $\mathcal{L} = 78 \, \mathrm{pb}^{-1}$.

The data recorded with the H1 detector are divided in so-called runs. Each run contains data logged under almost the same condition of both, the detector and the beams. A preselection of the data is applied by rejecting certain runs. Runs with a Luminosity of less than $100 \, \mathrm{nb}^{-1}$ are rejected because this points to a technical problem during the run. The runs are classified as 'good', 'medium' or 'poor' (depending on the status of the subdetectors and on the quality of the beams). Only runs declared as 'good' or 'medium' are used. The high voltage supply of the tracking chambers was switched off for a part of the run in order to protect the chambers from high currents. Individual events of a run are rejected if at least one of the detector components relevant for the analysis is not working properly. The relevant components for this analysis are the central tracking chambers (CJC1 and 2, CIP, COP), the forward proportional chamber (FPC) [1], the calorimeters (LAr and SpaCal) as well as the backward drift chamber (BDC) and the luminosity system. The luminosity is corrected for the rejected events of a run and for satellite bunch interactions which are not considered in the data analysis. The efficiency of these run selections is in the order of $80 \, \%$.

4.1.2 Selection of Deep-Inelastic Scattering Events

The DIS events are characterised by a scattered electron in the final state. For the considered Q^2 range such events are tagged by the verification of an energy deposition in the SpaCal. Accordingly, the selected subtrigger demands a high, localised energy deposition in the SpaCal together with a high transverse momentum track in the central region of the detector. The measured properties of the scattered electron are used to reconstruct the kinematic variables of the events, see section 2.1.1. Therefore, these variables depend on the energy calibration of the electromagnetic part of the SpaCal. This calibration is verified by an independent measurement of the kinematic variables which is provided by the double angle method.

4.1.2.1 Trigger Selection

Events in the presented analysis are selected by the subtrigger S61. This subtrigger has no conditions on the second trigger level (L2) and therefore events triggered by S61 are passed directly to the fourth trigger level L4. Only events that pass the fourth trigger level are written to tape and considered further for the analysis. The fourth layer of the trigger system saves always a part of the events that have not been classified by one of the L4 finders with a corresponding weight. This weight is referred to as L4 weight. The L4 efficiency is automatically included by applying this weight event-wise to the data distributions. For this work no specific L4 finder is requested.

The subtrigger S61 requires a high transverse momentum track in the central part of the detector, a significant z-vertex position and an energy deposition in the SpaCal. The logical condition is:

$$S61 = DCRPh\_THig \wedge zVtx\_sig \wedge (SPCLe\_IET > 2 \vee SPCLe\_IET\_Cen\_3). \qquad (4.1)$$

---
[1] Some track based subtriggers use information from this system.

In addition to these main trigger elements several veto conditions are applied in order to reject non-ep background or interaction of satellite bunches. The different trigger elements are described in the following.

The track trigger: The track trigger $DCR\phi$ uses the $r - \phi$ information of the hits found in the central tracking chambers. These hit combinations are compared with different pre-defined masks ($\mathcal{O}(10'000)$) in order to find the tracks and a coarse estimation of their momenta in the transverse plane. The trigger element 'DCRPh_THig' requires at least one track with a high transverse momentum above a threshold of 800 MeV.

The z-vertex trigger: The z-vertex trigger uses the information from the CIP, the COP and the forward tracker. With this information so-called rays (particle trajectories) are reconstructed. The intersection of these rays with the z-axis is filled into a histogram ranging from z $= -43.9$ cm to z $= +43.9$ cm. For tracks originating at a common vertex, a peak at the z-position of the interaction vertex of the event is expected. The trigger element 'zVtx_sig' asks for a significant peak in this distribution.

The SpaCal trigger: SpaCal trigger elements are fired if a significant energy deposition in the SpaCal is detected. Several cells are combined and the energy depositions within these cells are summed up to build a so-called trigger tower. The element 'SP-CLe_IET>2' requires a trigger tower in the electromagnetic part with an energy larger than 5.7 GeV. The element 'SPCLe_IET_Cen_3' is set in a analogue way considering only the central region of the SpaCal.

The average prescale (see section 3.2.4) of the subtrigger S61 is 1.03 for the year 1999 and 1.19 for the year 2000. These prescales are already included in the luminosity quoted above.

Determination of the Trigger Efficiency The efficiency of the L1 trigger can be determined in two ways. Either the efficiency is determined by the simulation of the corresponding trigger or it is extracted from the data. Within this work the second way is chosen to be independent of the trigger simulation which depends for example on the Q^2 spectrum of the generated events. However, a comparison between the trigger efficiency extracted from data and simulation shows a reasonable agreement. The observed deviations are in the order of 1 %. The trigger efficiency from the data is obtained by the monitor trigger technique using a set of independent subtriggers. Unfortunately, there is no subtrigger which has gathered enough statistics and which is completely independent of S61. Therefore, the trigger efficiency of S61 has to be composed by the efficiency of its trigger elements. For the monitoring of the SpaCal part, the subtriggers S71 which uses the LAr, the track and the z-vertex trigger or the subtrigger S67 using only the LAr trigger are taken. The z-vertex element can be monitored together with the track trigger by using the monitor triggers S04 or S00 which both rely only on conditions on the SpaCal triggers. The efficiency of S61 is given by:

$$\epsilon(S61) = \prod_{TE} \frac{N_{MT \wedge TE}}{N_{MT}}, \tag{4.2}$$

where $N_{MT \wedge TE}$ denotes the number of events that are triggered by the monitor trigger and the corresponding trigger element while N_{MT} denotes the events that are triggered by the monitor trigger without additional requirements. The trigger efficiency for the K_s^0 and Λ particles is discussed in section 6.2.2.

4.1.2.2 Reconstruction of the Kinematic Variables

At fixed center-of-mass energies $\sqrt{s}$ the kinematics of deep-inelastic scattering events are characterised by three Lorentz-invariant variables Q^2, y, and x. These three quantities are related by equation 2.9 and therefore only two of the variables have to be extracted from measurable quantities (herein chosen to be Q^2 and y). In the following, two different ways for this extraction are presented.

The Electron Method For the chosen Q^2 range the scattered electron is detected in the SpaCal. This subdetector is able to measure the electron quantities (energy and polar angle) with a high precision. Therefore, the electron method (see equations 2.6 and 2.8) is used for the extraction of the kinematic variables of the DIS events. A drawback of this method is its strong dependence on the energy calibration of the SpaCal. This calibration is examined in section 4.1.4.1 and is found to be acceptable. A further drawback of the electron method is the poor resolution of the inelasticity at low values of y (see for example [148]), which is confirmed by the measurement of the resolution presented in section 6.3. This fact restricts the analysis to the region $y > 0.1$ and implies the need of a coarse binning at low values of y. As this method uses the energy of the incoming electron, the extracted quantities are measured wrongly in cases where the electron emits a photon before the interaction with the proton. However, this effect of initial and final state radiation is small and taken into account properly in the simulated events and the data are therefore corrected accordingly.

The Double Angle Method This method uses the beam energies and the scattering angle of the electron, as well as the angle of the hadronic final state and is therefore independent of the energy of the scattered electron. From the information of the hadronic final state the angle γ is calculated according to

$$\cos(\gamma) = \frac{p_{T,h}^2 - (E_h - p_{z,h})^2}{p_{T,h}^2 + (E_h - p_{z,h})^2}, \tag{4.3}$$

where E_h, $p_{T,h}$ and $p_{z,h}$ denote the total energy, the transverse momentum and the longitudinal momentum of the hadronic final state, respectively. In the QPM processes, the angle γ corresponds to the scattering angle of the struck quark. The kinematic variables are given by:

$$Q_{DA}^2 = 4E_e \cdot \frac{\sin(\gamma) \cdot (1 + \cos(\theta_e))}{\sin(\gamma) + \sin(\theta_e) - \sin(\gamma + \theta_e)} \tag{4.4}$$

$$y_{DA} = \frac{E_h}{2E_e} \cdot (1 + \cos(\gamma)) \tag{4.5}$$

$$x_{DA} = \frac{E_e}{E_p} \cdot \frac{\sin(\gamma) + \sin(\theta_e) + \sin(\gamma + \theta_e)}{\sin(\gamma) + \sin(\theta_e) - \sin(\gamma + \theta_e)}, \tag{4.6}$$

where E_e and E_p denote the beam energies and θ_e the scattering angle of the electron. The double angle method is completely independent of the energy measurement of the SpaCal and therefore provides an alternative way of determining the energy of the scattered electron:

$$E'_{e,DA} = E_e \cdot \frac{1 - y_{DA}}{\sin^2(\theta_e/2)}. \tag{4.7}$$

Beside the two method mentioned here, several other ways to determine the kinematic variables exist. A comprehensive overview is given for example in [149].

4.1.2.3 The Selection Criteria

The visible range defines the accessible phase space of the analysis and is chosen by selection criteria on the kinematic variables measured by the electron method. The cross-section measurement uses only events which fulfil the following conditions on the negative four-momentum transfer (Q^2) and the inelasticity (y):

$$2 < \quad Q^2 \quad < 100\,\text{GeV}^2 \tag{4.8}$$

$$0.1 < \quad y \quad < 0.6. \tag{4.9}$$

These boundaries imply an selection criterion on the energy of the scattered election, $E'_e \gtrsim 11\,\text{GeV}$. Events with $y < 0.1$ are excluded due to the worse resolution of the electron method in this region. For the second part of the analysis, the search for new resonances, the amount of statistic is much more important than the resolution. Therefore, the selection on y is extended to $0.05 < y < 0.7$ for analysis II.

In addition to these kinematic selection criteria defining the phase space for the DIS analysis, more technical criteria have to be introduced in order to reject non-DIS events. The main sources for this background are photoproduction events and interactions of the proton beam with rest-gas in the beam pipe[2] or with the beam pipe itself. In the photoproduction case the electron emits a quasi real photon and escape the detector unperceived through the beam pipe. It can occur that a particle from the hadronic final state enters the SpaCal and is misidentified as the scattered electron. Such fake electron candidates have usually a lower energy than real ones and are already rejected by demanding $y < 0.6$ (which corresponds to $E'_e \gtrsim 11\,\text{GeV}$).

The event vertex The z-component of the event vertex (z_{vtx}) is restricted to $-35 < z_{vtx} < 35\,\text{cm}$. This requirement rejects most of the non ep-background since such events do usually not come from the nominal interaction region of ep events. Furthermore, satellite bunch interactions are rejected by this criterion.

Cluster radius Electrons that pass through the SpaCal produce an electromagnetic shower. These showers are usually spread over different cells. All cells belonging to the shower of one particle are combined in so-called clusters. The shape of such clusters is different for electromagnetic and for hadronic showers and provides therefore a possibility to distinguish between electrons and hadrons. Therefore, the purity of the selected electron sample can be improved by a selection criterion on the cluster radius, R_{clus}, which is defined as

$$R^2_{clus} = \frac{1}{E^2_{clus}} \sum_{cells\,i} (E^2_i \cdot r^2_i), \tag{4.10}$$

where E_{clus} is the total energy of the cluster, E_i the energy measured in cell i and r_i the radial distance of cell i the the hottest cell. The cluster radius is restricted to $R_{clus} < 3.5\,\text{cm}$.

---

[2]The vacuum in the proton ring is around $1.6 \cdot 10^{-10}$ mbar.

Energy balance The energy balance is given by

$$E - p_z = (E'_e - p'_{z,e}) + \sum_{hfs}(E_i - p_{z,i}), \tag{4.11}$$

where E'_e and $p'_{z,e}$ denotes the energy and the longitudinal momentum of the scattered electron, respectively. In the second term the difference of the energy and the longitudinal momentum of all hadronic final state particles are summed up. For the initial state the energy balance is given by $E - p_z = (E_e - p_{z,e}) + (E_p - p_{z,p})$ and amounts to 55 GeV. For a perfect detector where all particles are registered the energy balance of the final state would have exactly the same value. For true DIS events the discrepancy from the nominal value is small even if some particles are leaving the detector through the beam pipe, since for such particles the energy is of similar size as the longitudinal momentum. Large deviations from this 55 GeV point to: a) missing particles in the final state (i.e. the scattered electron in photoproduction events) or b) missing electron in the initial state (i.e. beam-gas or beam-wall interactions) or c) unspotted technical problems with the detector readout or d) wrongly measured energies of hadronic final state particles. The requirement on the energy balance is $35 < E - p_z < 70$ GeV.

Central region in the SpaCal To provide a reliable energy measurement the electromagnetic shower has to be completely contained within the sensitive volume of the SpaCal which is ensured by a requirement on

$$R_\theta = |(z_{vtx} - z_{SpaCal}) \cdot tan(\theta_e)|, \tag{4.12}$$

where $z_{SpaCal} = -160$ cm denotes the z position of the SpaCal and θ_e the polar angle of the scattered electron. This expression bears the advantage that the beam tilt is taken into account properly in contrast to a requirement on the cluster position itself. The chosen selection criterion is $R_\theta > 9.1$ cm and is adapted from [76].

From Monte Carlo studies it is known that the contamination of photoproduction background after these selection criteria is below 0.1 %, see [76]. All selection criteria introduced in this section are summarised in table 4.1.

Table 4.1: The DIS selection criteria.

Type	Variable	Requirement
Kinematical	Virtuality	$2 < Q^2 < 100$ GeV^2
	Inelasticity	$0.1(0.05) < y < 0.6(0.7)$
Technical	Event vertex	$35 < z_{vtx} < 35$ cm
	Cluster radius	$R_{clus} < 3.5$ cm
	Energy balance	$35 < E - p_z < 70$ GeV
	SpaCal position	$R_\theta > 9.1$ cm

4.1.3 Re-Weighting of the Simulated Distributions

In order to minimize the known insufficiencies in the description of the data by the simulation, the Monte Carlo sets are re-weighted. This re-weighting comprises the structure functions

$F_2(Q^2, x)$ and $F_L(Q^2, x)$ as well as the distribution of the z-coordinate of the interaction point z_{vtx}. The total weight $w(Q^2, x, z_{vtz})$ is applied event-wise to the Monte Carlo distributions.

The fully simulated Monte Carlo sets of CDM and MEPS have been generated with the old proton PDF set GRV94, LO. The PDF set is used to parameterise the structure functions of the proton, F_2 and F_L (see equation 2.17), and hence the cross-section for DIS events. The structure functions parameterised by the GRV94 PDF set have a different Q^2 and x dependency as those measured at H1. Furthermore, the longitudinal structure function F_L is neglected within the GRV94 PDF set. To reflect the present knowledge of the structure functions, the Monte Carlo sets are re-weighted with the PDF set extracted from the H1 data (H1-2000 L0 PDF fit [37]) is applied. According to equation 2.14 the weight factor $w_{PDF}(Q^2, x)$ has been introduced:

$$w_{PDF}(Q^2, x) = \frac{F_2^{H1}(Q^2, x) - y^2/Y_+ \cdot F_L^{H1}(Q^2, x)}{F_2^{GRV94}(Q^2, x)}, \quad (4.13)$$

where $F_{2(L)}^{H1}$ and F_2^{GRV94} denote the structure functions from the H1-2000 and the GRV94 PDF set, respectively, and $Y_+ := 1 + (1 - y)^2$.

The H1-2000 LO PDF fit has been optimised for a higher Q^2 region ($Q^2 \gtrsim 10\,\mathrm{GeV}^2$) than used within this work. Hence, this PDF set is not optimal for the description of the low Q^2 region. A parameterisation of the structure functions for the low Q^2 region ($Q^2 \lesssim 10\,\mathrm{GeV}^2$) has been extracted from the H1 data. This parameterisation is called *fractal fit* and is given by [150]:

$$F_2^{frac}(Q^2, x) = a \cdot e \cdot \left(\frac{Q^2}{Q^2 + e}\right)^{c-1} \cdot \frac{x^{1-c}}{1 + d - b \cdot log(x)} \quad (4.14)$$
$$\cdot x^{-b \cdot log(1 + Q^2/e)} \cdot ((1 + Q^2/e)^{1+d} - 1)$$
$$F_L^{frac}(Q^2, x) = F_2^{frac} \cdot \frac{r}{1 + r}. \quad (4.15)$$

The free parameters have been determined to: $a = 0.689$, $b = 0.0550$, $c = 1.08$, $d = -1.19$, $e = 0.109$, $r = 0.579$. The fractal fit leads to an additional weight w_{frac} which is applied to the Monte Carlo distributions for the low Q^2 region:

$$w_{frac}(Q^2, x) = \begin{cases} \frac{F_2^{frac}(Q^2, x) - y^2/Y_+ \cdot F_L^{frac}(Q^2, x)}{F_2^{H1}(Q^2, x) - y^2/Y_+ \cdot F_L^{H1}(Q^2, x)} & \text{for } Q^2 \le 10\,\mathrm{GeV}^2 \\ 1 & \text{for } Q^2 > 10\,\mathrm{GeV}^2 \end{cases} \quad (4.16)$$

The structure function $F_2(Q^2, x)$ according to the fractal fit is compared with that one from the H1-2000 LO PDF fit in figure 4.1. The largest deviations from the H1-2000 LO fit is at low Q^2 and low values of x.

A last re-weighting concerns the z position of the interaction vertex. The distribution of the z-vertex position is not described correctly by the simulation. The weights are extracted by fitting the deviation of the reconstructed position in data and simulation:

$$w_{z_{vtx}}(z_{vtx}) = a + b \cdot z_{vtx} + c \cdot z_{vtx}^2 + d \cdot e^{-z_{vtx}}, \quad (4.17)$$

where $a = 0.9435$, $b = 4.562 \cdot 10^{-3}$, $c = 3.846 \cdot 10^{-4}$ and $d = 4.758 \cdot 10^{-15}$. The weight function is displayed in figure 4.2.
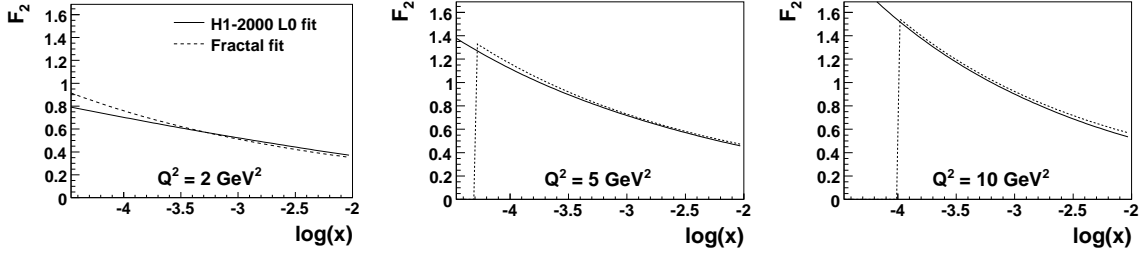
Figure 4.1: The structure function F_2 as extracted from the H1-2000 L0 PDF fit (solid line) and from the fractal fit (dashed line) as function of x for three values of $Q^2 = \{2\,\mathrm{GeV}^2, 5\,\mathrm{GeV}^2, 10\,\mathrm{GeV}^2\}$. The fall down of the fractal fit indicates the kinematic limit.
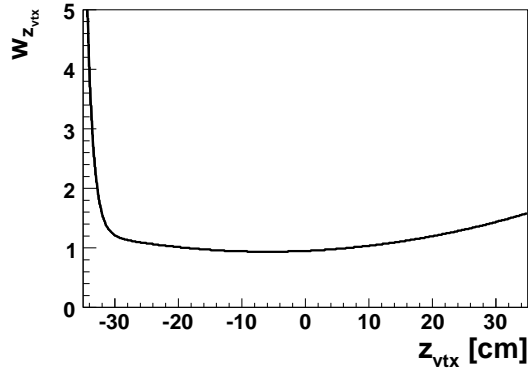
Figure 4.2: The weight function for correction of the z position of the interaction vertex.

The re-weighting of the z position is independent of the PDF weights. Therefore, the total weight w, applied event-wise to the simulated distributions, is given by:

$$w(Q^2, x, z_{vtz}) = w_{PDF}(Q^2, x) \cdot w_{frac}(Q^2, x) \cdot w_{z_{vtx}}(z_{vtx}). \tag{4.18}$$

4.1.4 Comparison of the Data Distributions with the Simulation

The distributions of the kinematic variables and of those used for the identification of the scattered electron reconstructed in the simulation are compared with those measured in the data to check the quality of the data description. For this comparison the CDM set is used and the re-weighting introduced in section 4.1.3 is applied.

In figure 4.3 the normalised distribution of the kinematic variable Q^2, y and x are shown. The Monte Carlo simulation is in general able to describe the data points. Some deviations are observed in the y distribution. These deviations are understood and related to the energy calibration of the SpaCal which is imperfect, especially for the very low Q^2 region. However, this deviation has almost no effect on the cross-section measurement and is covered by the systematic uncertainty of the measurement (see section 6.5). In the same figure the kinematic properties of the scattered electrons are displayed. The polar angle θ_e peaks in the forward region and the azimuthal angle ϕ_e is spread flatly over the range $[-\pi, \pi]$, as expected. In figure 4.4 the variables R_θ and R_{clus} (see equations 4.12 and 4.10) are illustrated. While R_θ is well reproduced by the simulation, the description of the cluster radius is rather poor. Since

a cluster radius below 3.5 cm is required, this deviation has no effect on the measurement. Furthermore, the distributions of $E - p_z$ and the z component of the interaction vertex are shown.
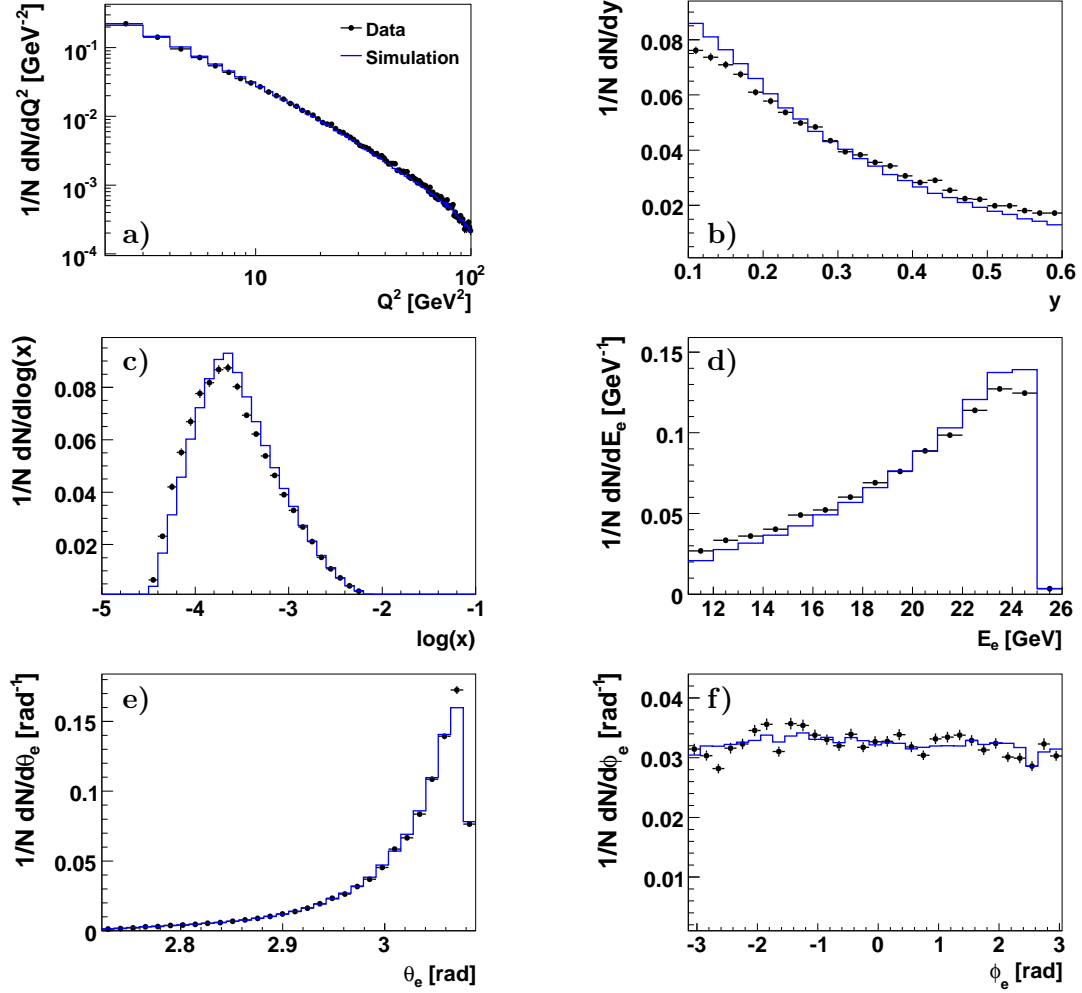
Figure 4.3: The distribution of the kinematic variables of the event, a) virtuality Q^2, b) inelasticity y, c) Bjorken variable $\log(x)$ and of the kinematic properties of the scattered electron, d) energy E_e, e) polar angle θ_e, f) azimuthal angle ϕ_e. All distributions are normalised to one. The solid points indicate the data while the histogram represents the CDM simulation.

4.1.4.1 Energy Calibration of the SpaCal

The calibration of the SpaCal is beyond the scope of this work and is provided centrally from special calibration groups within H1. Nevertheless, the calibration needs to be examined for the kinematic range under investigation within this work in order to estimate the uncertainty of the energy measurement of the SpaCal. The measurement of the electron energy with the
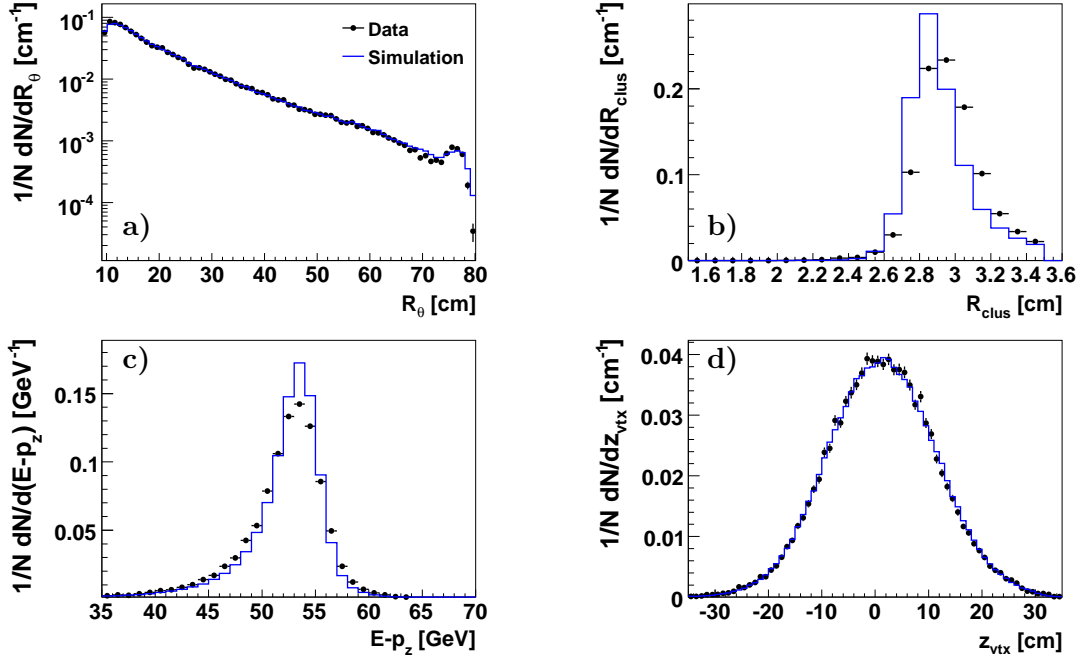
Figure 4.4: The distribution of a) R_θ, b) R_{clus}, c) $E - p_z$ and d) z_{vtx}. All distributions are normalized to one. The solid points indicate the data while the histogram represents the CDM simulation.

double angle method (equation 4.7) is used for the cross-check of the energy calibration of the SpaCal. For the calibration additional selection criteria have to be applied in order to provide a reliable measurement of the energy with the double angle method. In figure 4.5 the ratio of the energy measured in the SpaCal, $E'_{e,SpaCal}$, and that one extracted with the double angle method, $E'_{e,DA}$, is shown as a function of the electron energy, of the cluster radius R_{SpaCal}[3] and of Q^2. For this figure, the ratio of the two energies is fitted in each bin with a Gaussian function and the mean values together with their errors are filled into the histogram. If both reconstruction methods were valid for the examined range, this ratio should be equal to one. Large deviations from one are observed for low electron energies which does not point to a wrong calibration of the SpaCal but rather indicates the breakdown of the double angle method. However, for the uncertainty of the energy measurement only the difference between the data and the simulation[4] is decisive. This double ratio $R_{MC}/R_{Data} = (E'_{e,DA}/E'_{e,SpaCal})_{MC}/(E'_{e,DA}/E'_{e,SpaCal})_{Data}$ is close to one (see figure 4.5), indicating that the energy is well described by the simulation. The deviation of the double ratio from one is less than 1%, with exception of the lowest Q^2 bin ($2 < Q^2 < 2.5\,\text{GeV}^2$) where it is 2.5%. These deviations are considered for the calculation of the systematic uncertainty of the cross-sections due to the energy measurement.

---

[3]The cluster radius is defined by the radial distance of the hottest cell to the beam axis.

[4]For this comparison the CDM Monte Carlo set is used.
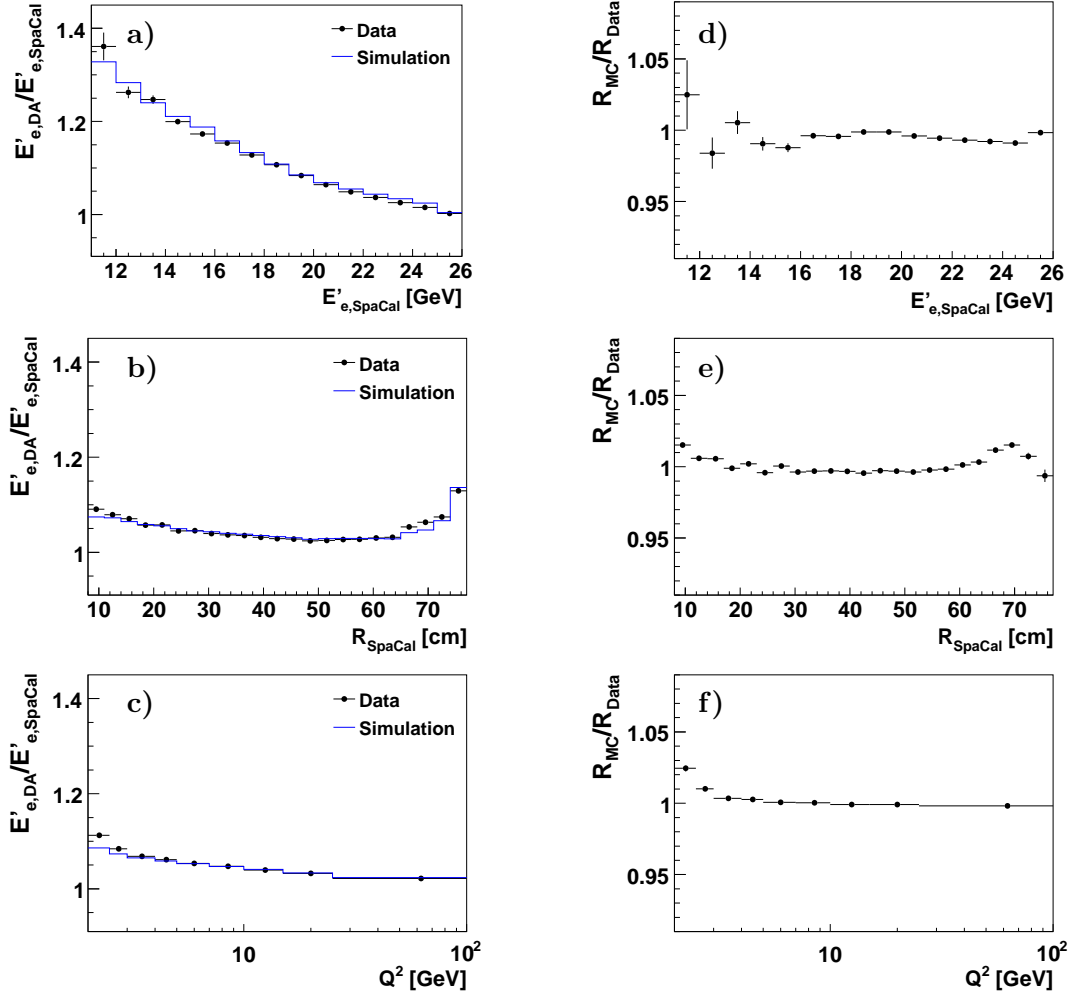
Figure 4.5: The ratio of the electron energy as measured by the double angle method and by the SpaCal as function of a) the SpaCal energy, b) the radial distance of the cluster to the beam axis and c) the virtuality. The figures d) to f) show the double ratio $R_{MC}/R_{Data} = (E'_{e,DA}/E'_{e,SpaCal})_{MC}/(E'_{e,DA}/E'_{e,SpaCal})_{Data}$ as function of the same variables.

4.2   Technical Issues

The more technical related topics relevant for the analysis presented within this work are recapitulated. This comprises the selection of well measured tracks, the introduction of the vertex fitting routines, the definition of the Breit frame and the discussion of the Armenteros-Thompson variables.

4.2.1   Track Selection

All presented analyses are based on charged particle tracks measured in the central part of the tracking detector, as discussed in section 3.2.1. The magnetic field parallel to the z axis

bends the charged particle tracks in the $r - \phi$ plane. The flight path of these particles is described by a helix trajectory (neglecting multiple scattering and energy loss). The bending radius R is related to the magnetic field strength B by $R \propto \frac{p_T}{B}$ and thus allows to measure the transverse momentum p_T of the particle. At H1 the tracks are characterised by the five parameters of the helix trajectory:

$$x(s) = (d_{ca} - \frac{1}{\kappa}) \cdot \sin(\phi_0) + \frac{1}{\kappa} \cdot \sin(\phi_0 + \kappa \cdot s) \tag{4.19}$$

$$y(s) = -(d_{ca} - \frac{1}{\kappa}) \cdot \cos(\phi_0) - \frac{1}{\kappa} \cdot \cos(\phi_0 + \kappa \cdot s) \tag{4.20}$$

$$z(s) = z_0 + s \cdot \cot(\theta), \tag{4.21}$$

where d_{ca} denotes the distance of closest approach to the origin of the H1 coordinate system [5], κ the inverse bending radius, ϕ_0 the azimuthal angle at the point of d_{ca}, z_0 the z-position at the point of d_{ca} and θ the polar angle, see figure 4.6.
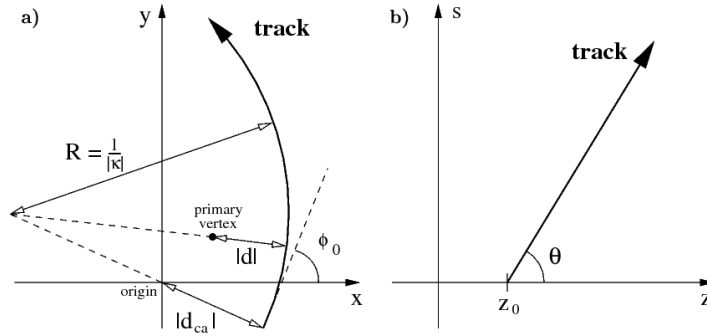
Figure 4.6: The helix trajectory in the $r - \phi$ plane (a) and in the $z - r$ plane (b). The parameters (d_{ca}, $R = \frac{1}{\kappa}$, ϕ_0, z_0, θ) are described in the text. This figure is taken from [151].

In a first step the trajectory is reconstructed using only the information provided by the CJC 1 and 2. In a second step this trajectory is extrapolated into the CST region and CST hits are assigned to this trajectory if they lie within $\pm 5 \sigma$ of the extrapolated track in the $r - \phi$ plane, see figure 4.7. The association of CST hits to the CJC-track improves the accuracy of all track parameters. In figure 4.8 the distribution of the significance $S_x = \frac{x}{\delta x}$ of the track parameters d_{ca}, κ and θ is shown. Tracks that are reconstructed in the CJC 1 only have a worse accuracy than those measured additionally in CJC 2, which explains the structure in the S_κ distribution. Due to the long lifetime of the K_s^0 and Λ hadrons, it is not necessary to apply any requirements on the number of linked CST hits because these secondary vertices are well separated from the primary one. Therefore, tracks with different resolution properties are combined for the reconstruction of the strange particles resulting in different resolution of the signal as shown in figure 4.8. For the K_s^0 reconstructed with a three-dimensional unconstraint fitting routine (see section 4.2.2) the ratio of the width of the signal where the daughter particles have both at least one CST hit to those where at least one daughter track has no CST hits is $\frac{\sigma_{CST}}{\sigma_{noCST}} = \frac{13.8 \, MeV}{26.8 \, MeV} \approx 0.5$. This value shows the enormous gain in precision of the track parameters by the additional CST information. However, for the cross-section measurement the resolution of the signal is secondary.

---

[5]In contrast, the d'_{ca} gives the distance of closest approach to the interaction vertex.
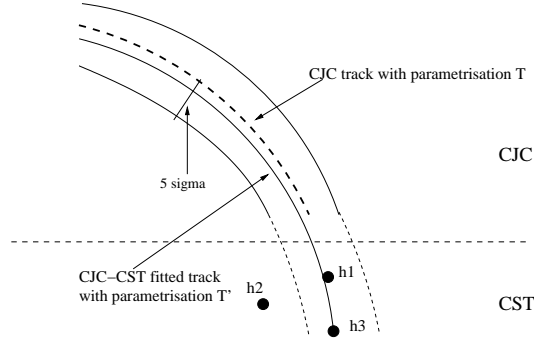
Figure 4.7: Schematic representation of the CJC-CST linking. The dashed line shows the reconstructed CJC track with parameterization T . The CST hits are denoted as h1, h2 and h3 and T' is the parameterization of the CJC-CST fitted track.
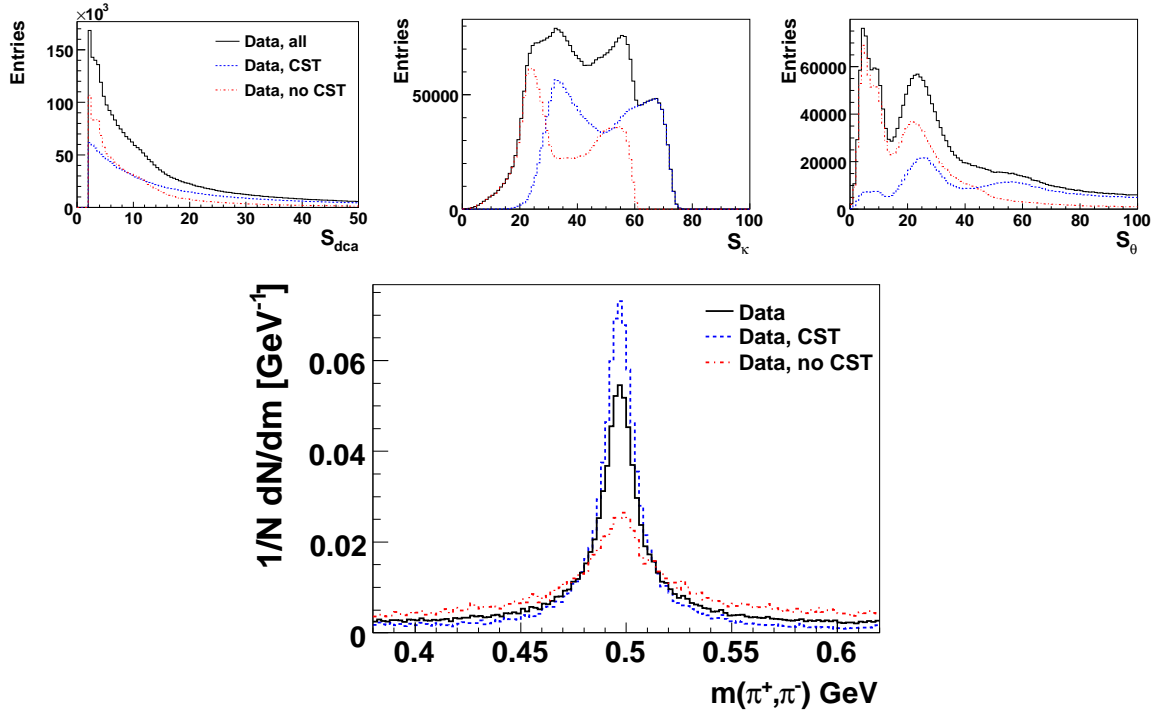
Figure 4.8: Top: The distribution of the significance of d_{ca} (left), κ (middle) and θ (right). Only tracks in the central region ($-1.5 < \eta < 1.5$) with $p_T > 0.12\,\text{GeV}$ are considered. Bottom: The mass spectrum of the selected K_s^0 candidates. The black histogram represents all selected candidates while the blue (dashed) only those where both tracks have at least one CST hit and the red (dashed-dotted) only those where at least one tracks has no CST hits.

The H1 reconstruction software provides two different kind of tracks which are referred to as *vertex fitted tracks* and *non-vertex fitted tracks*. In the first case the reconstructed track (from CJC or CJC+CST) is further constraint to the primary vertex improving the accuracy of the track parameters. Since the K_s^0 and the Λ hadrons have lifetime in the order of a few centimeters, the vertex fitted tracks cannot be used to reconstruct these particles. In

this work the vertex fitted tracks are only used for the reconstruction of the $\Xi^0(1530)$ (see section 8.3) and for the $K^\pm \Lambda$ combinations (see section 12.4.1).

4.2.1.1 The Selection Criteria

To ensure a good quality of the track, only those non-vertex fitted tracks fulfilling the following selection criteria are considered for the reconstruction of the strange particles:

- Tracks with a transverse momentum of less than $0.12\,\text{GeV}$ are excluded for two reasons: a) the cross-section for multiple interaction with the detector material increases for decreasing p_T and b) tracks with a lower p_T curl up within the CJC 1. Both effects lead to a worse accuracy of the track parameters.

- To ensure an adequate measurement, the radial length of the track [6] is required to be larger than $10\,\text{cm}$.

- The radial distance of the first CJC hit associated to the track has to be less than $35\,\text{cm}$. This requirement ensures that the track is measured within CJC 1 and thereby rejects track fragments produced in the dead material between the CJC 1 and 2 (split tracks).

- The significance of the distance of closest approach, $S_{dca} = \frac{d_{ca}}{\delta d_{ca}}$ has to be larger than four. Since most of the measured tracks are originating from the interaction vertex, this requirement rejects a significant part of the background in the strange particle spectra.

In figure 4.9 the distribution of the selection variables in data and in simulation are displayed. For the simulation the CDM generator is used. The CJC 1 subdetector has a radius of $24\,\text{cm}$, which causes the dip in the track length distribution. The track selection criteria are summarised in table 4.2.

The vertex fitted tracks are selected by a set of standard selection criteria (the so-called Lee-West selection):

- The transverse momentum of the tracks has to be larger than $0.12\,\text{GeV}$.

- The polar angle of the tracks is restricted to $20 < \theta < 160\,^\circ$.

- The track length has to exceed $10\,\text{cm}$. For the backward region ($150 < \theta < 160\,^\circ$) the requirement is relaxed to $5\,\text{cm}$.

- The radial distance of the first CJC hit associated to the track has to be less than $50\,\text{cm}$.

- The distance of closest approach of the track to the interaction vertex, dca', has to be less than $2\,\text{cm}$.

The transverse momentum distribution of the vertex fitted tracks is shown in figure 4.10 for the data and for the simulated sample. The slope in the simulated case is slightly steeper than in data. The track selection criteria are summarised in table 4.2.

---

[6]The radial length of a track is given by the radial distance of its innermost and outermost hit.
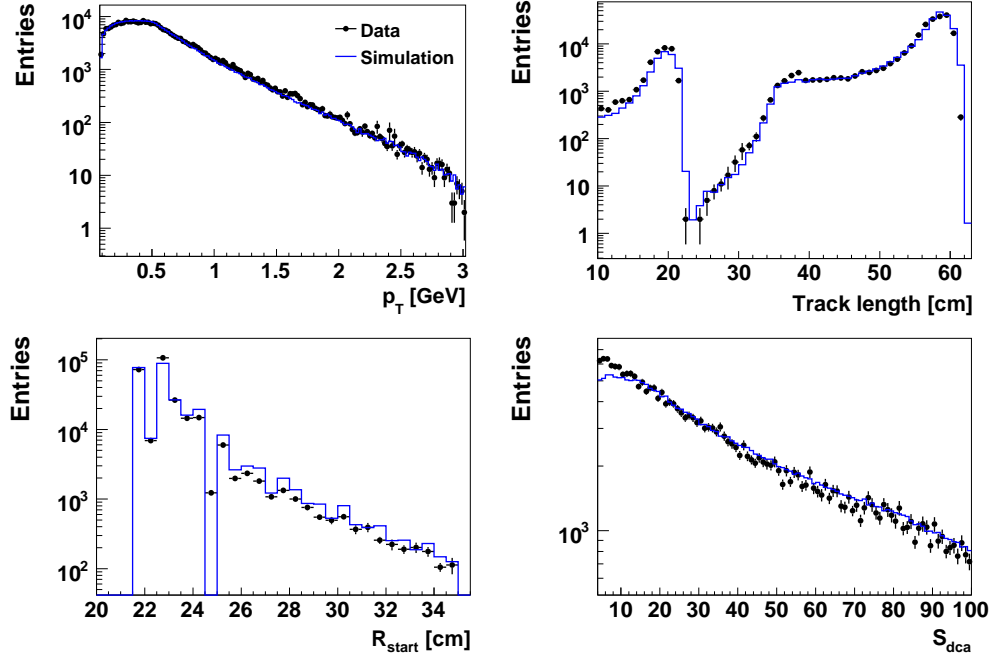
Figure 4.9: The distribution of the track-selection variables: transverse momentum (top left), track length (top right), starting radius (bottom left) and significance of the d_{ca} (bottom right). The black points represent the data, the blue histogram the simulation. The number of entries of the simulated sample has been scaled to those of the data.
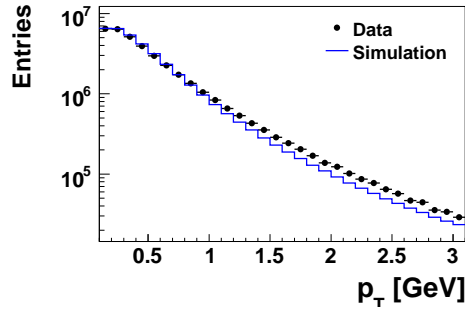
Figure 4.10: The distribution of the transverse momentum of the vertex fitted tracks. The black points represent the data, the blue histogram the simulation. The number of entries of the simulated sample has been scaled to those of the data.

4.2.2 Vertex Fitting Routines

The strange hadrons K_s^0, Λ and Ξ^- have all lifetimes $(c\,\tau)$ in the order of a few centimeters and therefore decay at secondary vertices which are usually well separated from the interaction point. For the reconstruction of these decay vertices, different vertex fitting routines have been used. All fitting routines take two non-vertex fitted tracks as input and calculate the best hypothesis for their common vertex, the secondary vertex. The programs used within this work already exist [152], but some of them had to be modified and adapted to the new

object-oriented software environment of H1. These newly imported routines are tested by reconstructing photon conversion events.

2DC The two-dimensional pointing constraint vertex fitting routine, $2DC$, uses the information of the tracks in the $r - \phi$ plane to find their common intersection point, the secondary vertex. An additional constraint is implemented by requiring that the reconstructed mother particle, which is defined by the sum of the four-momenta of the fitted tracks, is pointing back to the interaction vertex. Therefore, this routine can only be used to reconstruct particles originating at the interaction vertex and is therefore not suited for the reconstruction of Λ baryons coming form a Ξ^- decay ($c\tau(\Xi^-) = 4.9\,\mathrm{cm}$). A detailed description of this routine is given in [151].

3DU The three-dimensional unconstraint vertex fitting routine, $3DU$, uses the full three dimensional information of the tracks. Hence, this fitting routine improves also the polar angle resolution resulting in a better mass resolution of the reconstructed strange hadron with respect to the $2DC$ fitting routine by approximately 20 %, see figure 4.11. However, for the cross-section measurement of the K_s^0 and Λ this routine could not be used because it relies on a good description of the z-resolution of the tracks by the simulation. This resolution has never been tuned for the HERA I data and the z-resolution for the simulated tracks is not reliable. The systematic uncertainties on the cross-section due to the bad description of the z-resolution would roughly be 10 %.

The $3DU$ routine has been used to reconstruct the Λ baryons coming from the $\Xi^- \rightarrow \Lambda\,\pi^-$ decay for the analysis presented in part II. In that analysis only relative efficiencies are used where the effect of the non-described z-resolution cancels to a large part.

VVF The VVF fitting routine is based on the technique of the Kalman filter and is described in [153]. The advantage of this routine is that it can handle neutral "tracks". In this work the VVF routine is used to reconstruct the decay $\Xi^- \rightarrow \Lambda\,\pi^-$.

All fitting routines provide as output value the χ^2 of the fit which is related to the fit-probability $P(\chi^2, n)$ by:

$$P(\chi^2, n) = \frac{1}{\sqrt{2^n}\Gamma(\frac{n}{2})} \int_\chi^\infty e^{-\frac{t}{2}} \cdot t^{\frac{1}{2}(n-1)} dt, \tag{4.22}$$

Table 4.2: The track selection criteria.

	non-vertex fitted tracks	vertex fitted tracks
Minimal transverse momentum	$0.12\,\mathrm{GeV}$	$0.12\,\mathrm{GeV}$
Minimal track length	$10\,\mathrm{cm}$	$10\,\mathrm{cm}$ (for $20 < \theta \leq 150\,^\circ$)
		$5\,\mathrm{cm}$ (for $150 < \theta < 160\,^\circ$)
Polar angle	—	$20 < \theta < 160\,^\circ$
Maximal radial distance of first hit	$35\,\mathrm{cm}$	$50\,\mathrm{cm}$
Minimal Significance of d_{ca}	4	—
Maximal d'_{ca}	—	$2\,\mathrm{cm}$
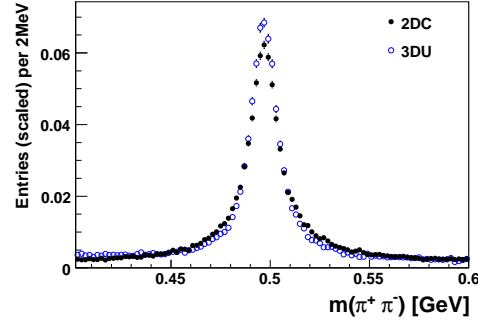
Figure 4.11: The K_s^0 mass spectrum reconstructed with the $2DC$ and the $3DU$ fitting routine. The black (solid) points show the reconstructed spectrum when the $2DC$ fitting routine is used and the blue (open) points when the $3DU$ one is used. The distributions are normalised to one.

where n denotes the number of degree of freedom ($n = 1$ for $2DC$ and $3DU$ fits with 2 tracks). The fit-probability is distributed flatly for well measured tracks that belong to the same secondary vertex. A rising edge towards zero indicates combination of tracks that do not belong to the same secondary vertex. The vertex fit-probability of the $2DC$ fitting routine is shown exemplary in figure 4.12. The distribution behaves as expected. For the simulated sample the rise towards zero is less distinct because for this sample a K_s^0 preselection is applied and therefore the fraction of tracks coming from a true secondary vertex to those not coming from a secondary vertex is higher than in data. The fit-probability for the VVF routine is discussed in section 8.2.
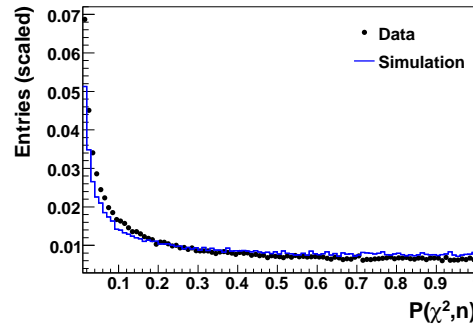
Figure 4.12: The vertex fit-probability of the $2DC$ fit. The distributions are normalised to one. The black points represents the data and the blue histogram the simulation.

4.2.2.1 Photon Conversion Events

The $3DU$ fitting routine has been tested by reconstructing photon conversion events ($\gamma \rightarrow e^- e^+$). Such events take mainly place in dense matter. Therefore, photon conversions reflect the structure of the detector. In figure 4.13 the x- and y-position of the reconstructed conversion vertex is displayed for the HERA I and HERA II detector configuration. Clearly visible are the two layers of the CST (circular shape for HERA I, elliptical for HERA II). The structures inside the first layer of the CST represent the beam pipe. The structure

observed in the HERA I figure around an azimuthal angle of $45\,^\circ$ is caused by a supply pipe for the cooling system. For the HERA II data period, more restricting selection criteria are applied[7]. In addition to the selection applied for the HERA I case, a significance of the d_{ca} of the tracks of larger than three and a significance of the decay length of larger than four is required. These additional selection criteria mainly suppress combinatorial background caused by poorly measured tracks originating from the interaction region. Therefore, in the HERA II case the central region is sparsely populated.
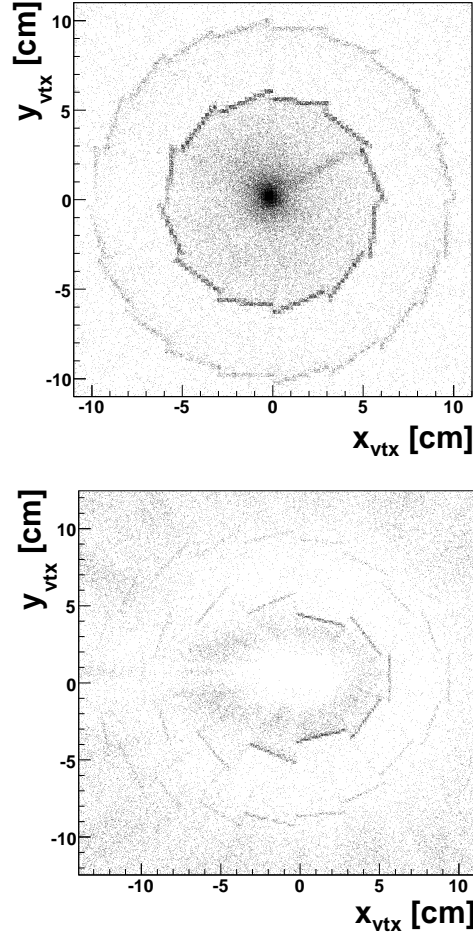
Figure 4.13: The vertex distribution of reconstructed photon conversion events for HERA I and HERA II. For the two data periods different selection criteria are applied (see text).

4.2.3   Breit Frame

The production of K_s^0 and Λ hadrons is studied in the laboratory and in the Breit frame. Frames of references where the influence of the proton boost is eliminated are better suited for the examination of the hadronic final state than the laboratory frame. Such frames are the hadronic center-of-mass frame and the Breit frame [154]. In this analysis the production of

---

[7]This is necessary since the final alignment and calibration constants were not yet available.

strange hadrons is transformed into the Breit frame, defined by $\vec{p}_\gamma + 2x \cdot \vec{p}_p = 0$, where $\vec{p}_\gamma = \vec{q}$ is the momentum of the photon emitted by the electron and $\vec{p}_p$ and x are the momentum of the incoming proton and the Bjorken scaling variable, respectively. The scattering process in the Breit frame is illustrated in figure 4.14. For QPM processes $x \cdot \vec{p}_p$ corresponds to the momentum of the struck quark. The z axis in the Breit frame is defined to coincide with the proton axis, the proton moving in the positive z direction.

No energy is transferred to the quark in the Breit frame and it behaves as if it had bounced off a brick wall. The quark that participates in the scattering process has a four-momentum of (for the QPM process) $\mathcal{P}_i = (\frac{Q}{2}, 0, 0, \frac{Q}{2})$ before and $\mathcal{P}_f = (\frac{Q}{2}, 0, 0, -\frac{Q}{2})$ after the interaction with the photon. Particles from the proton remnant are almost collinear to the incoming proton direction and therefore are populating the so-called *target hemisphere* defined by $p_z^{Breit} > 0$. On the other hand, in the QPM the struck quark populates only the *current hemisphere* given by $p_z^{Breit} < 0$. Higher order processes generate transverse momentum in the final state and may lead to particles from the hard subprocess propagating into the target hemisphere [155, 156]. This hemisphere separation is also useful in the case of baryon production, where the question of baryon number transfer arises. In the current hemisphere the mechanism of particle production should in principle resemble that of collisions without an incident proton i.e. e^+e^-. The analogy with e^+e^- collisions is extended further by introducing the fragmentation variable $x_p = \frac{|\vec{p}|}{Q/2}$, where $\vec{p}$ is the momentum of the particle in the Breit frame. In the current hemisphere the maximal available momentum is equal to $\frac{Q}{2}$ and hence $0 < x_p^{current} < 1$. This quantity corresponds to $x_p = p/p_{beam}$ in e^+e^- collider experiments. Strange quarks produced directly in the hard interaction are expected to predominantly populate the current hemisphere, which is less sensitive to non-perturbative strangeness contributions, see section 2.2.1.
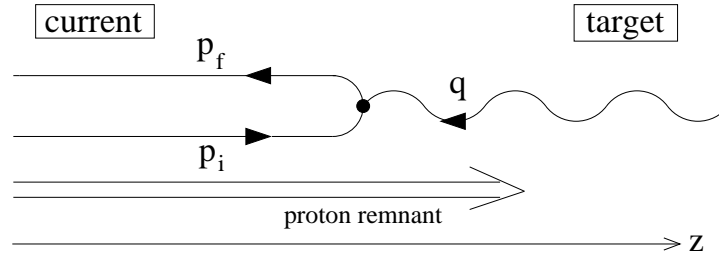
Figure 4.14: A schematic representation of the Breit frame. The variables p_i and p_f denote the incoming and outgoing quark and q the exchanged gauge boson.

4.2.4 The Armenteros-Podolski-Thompson Variable

The kinematic of a two body decay, $M \rightarrow D_1 D_2$, can be described by the variables p_T^{rel} and

$$\alpha = \frac{p_L^{rel}(D_1) - p_L^{rel}(D_2)}{p_L^{rel}(D_1) + p_L^{rel}(D_2)}, \tag{4.23}$$

where p_T^{rel} and p_L^{rel} denote the transverse and the longitudinal components of the daughter's momenta with respect to the flight direction of the mother particle [157, 158], see figure 4.15. The conservation of the momentum implies $p_T^{rel}(D_1) = p_T^{rel}(D_2)$. The two body decay is

characterised by an ellipse in the $\alpha - p_T^{rel}$ plane. The shape of this ellipse depends only on the mass of the daughter and mother particles. From four-vector conservation, the zeniths of the ellipse are calculated to [22]:

$$p_T^{rel,max} = \sqrt{\left(\frac{m(M)^2 + m(D_2)^2 - m(D_1)^2}{2m(M)}\right)^2 - m(D_2)^2} \qquad (4.24)$$

$$\alpha(p_T^{rel,max}) = \frac{\sqrt{p_T^{rel,max}(D_1)^2 + m(D_1)^2} - \sqrt{p_T^{rel,max}(D_2)^2 + m(D_2)^2}}{\sqrt{p_T^{rel,max}(D_1)^2 + m(D_1)^2} + \sqrt{p_T^{rel,max}(D_2)^2 + m(D_2)^2}}, \qquad (4.25)$$

where $m(M), m(D_{1,2})$ denote the mass of the mother and the daughter particles, respectively, and $p_T^{rel,max}(D_{1,2})$ the maximal relative transverse momentum of the daughter particles. The
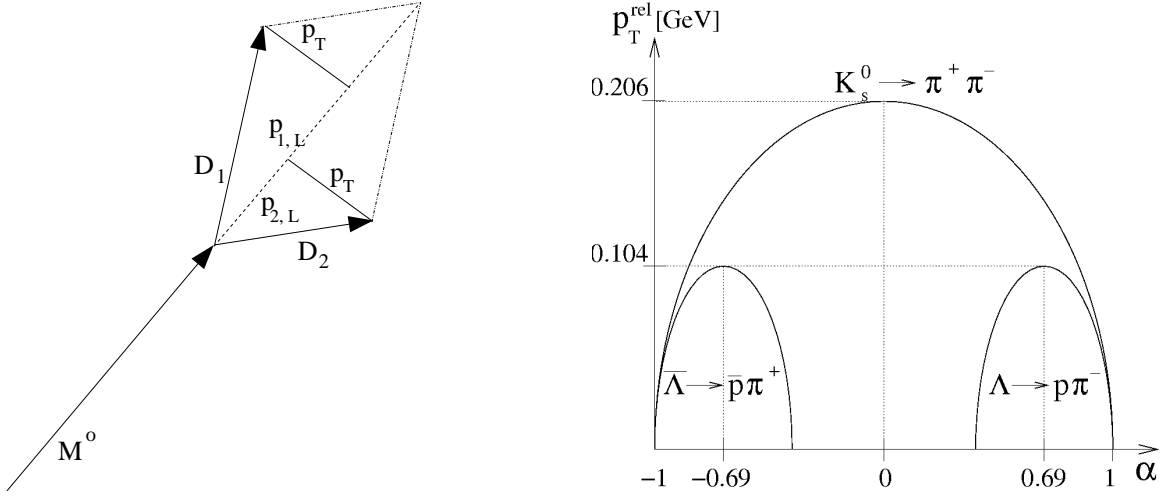
Figure 4.15: In the left part a schematic illustration of the two body decay $M \to D_1 D_2$ is shown. The right picture shows the expected ellipses in the $\alpha - p_T^{rel}$ plane for the decay of the K_s^0 and Λ hadrons into charged particles.

values of the zeniths of the ellipses for the decays of interest within this work are given in table 4.3. The predicted shape of the ellipses for these decays are shown in figure 4.15. Due to a finite resolution the measured distributions are smeared out. However, the separation of $K_s^0 \to \pi^+ \pi^-$ and $\Lambda \to p \pi^-$ remains, see figure 5.8.

Table 4.3: The values of the zeniths of the ellipses of the Armenteros-Podolski variables p_T^{rel} and α for the decay of the K_s^0 and the Λ into charged particles.

Decay	$p_T^{rel,max}$[GeV]	$\alpha(p_T^{rel,max})$
$K_s^0 \to \pi^+ \pi^-$	0.206	0
$\Lambda \to p \pi^-$	0.104	0.69
$\overline{\Lambda} \to \overline{p} \pi^+$	0.104	−0.69

Part I

Cross-Section Measurements

Chapter 5

Reconstruction of Strange Particles

The identification of the strange hadrons K_s^0 and Λ is presented[1]. The hadrons are reconstructed by their decay into charged particles according to[2]:

$$K_s^0 \;\;\rightarrow\;\; \pi^+\,\pi^- \tag{5.1}$$

$$\Lambda \;\;\rightarrow\;\; p\,\pi^-. \tag{5.2}$$

Both, the K_s^0 and Λ particles have decay length $(c \cdot \tau)$ in the order of a few centimeters leading to well separated secondary decay-vertices. In a first part the reconstruction of the strange hadron candidates by identifying these vertices is discussed. In a next step, selection criteria are introduced to suppress combinatorial background. In the last part the extraction of the signal is presented.

5.1   Reconstruction of K_s^0 and Λ Particles

The strange hadrons are reconstructed in the kinematical visible phase space given by

$$0.5 < p_T(V^0) < 3.5\,\text{GeV} \qquad |\eta(V^0)| < 1.3, \tag{5.3}$$

ensuring that the particles are well within the acceptance of the central tracking detector. The pseudorapidity η is defined by $\eta = -\ln(\tan(\frac{\theta}{2}))$, where θ is the polar angle. In a first step common vertices of the daughter tracks are identified. By choosing only non-vertex fitted tracks satisfying the track selection criteria introduced in section 4.2.1 it is ensured that only well measured tracks in the central region of the detector are considered. All possible combinations of oppositely charged tracks are fitted to their common vertex in the (x,y)-plane using the $2DC$ fitting routine (see section 4.2.2). Thereby the direction of flight of the V^0 particle is constrained to the primary event vertex. If the fit converges, the invariant mass $M_{1,2}$ of the two tracks (denotes as 1 and 2) is calculated according to:

$$M_{1,2} = \sqrt{(E_1 + E_2)^2 - (\vec{p_1} + \vec{p_2})^2}, \tag{5.4}$$

---

[1]In the following these two particles are labeled V^0.
[2]Unless explicitly mentioned, the charge conjugate states are hereafter always implicitly included.

where $E_{1/2}$ is the energy of the particle track 1 and 2, respectively. For the calculation of the energy a mass hypothesis $m_{1/2}$ for the particles 1 and 2 is needed:

$$E_{1/2} = \sqrt{m_{1/2}^2 + \vec{p}_{1/2}^{\,2}}. \tag{5.5}$$

For K_s^0 candidate reconstruction, both tracks are assumed to be pions, while for the Λ reconstruction the track with the higher momentum is assigned the proton mass and the other particle track is assumed to be the pion. The masses used within this work are $m(\pi^\pm)$ = $(139.570018 \pm 0.00035)\,\mathrm{MeV}$ and $m(p)$ = $(938.27203 \pm 0.00008)\,\mathrm{MeV}$ [26]. The mass assignment in the Λ case is feasible if the momentum of the Λ is above a certain threshold which is calculated to:

$$p(\Lambda) \gtrsim 300\,\mathrm{MeV}. \tag{5.6}$$

The detailed calculation of this threshold is provided in appendix B. For the strange hadrons considered in this work, a minimal transverse momentum of $500\,\mathrm{MeV}$ is required and therefore the condition given in equation 5.6 is always fulfilled.

5.1.1 Selection Criteria

The mass spectra of the K_s^0 and Λ candidates obtained in this way are dominated by combinatorial background and further selection criteria have to be applied in order to enhance the signal to noise ratio. The combinatorial background is mostly induced by tracks originating at the primary vertex. These combinations are suppressed by introducing a set of selection criteria for the V^0 candidates:

Decay Length The radial decay length L is given by the distance in the $r - \phi$ plane between the primary and the secondary vertex and provides a good quantity to reject combinations compatible with the primary event vertex. For both, K_s^0 and Λ candidates, it is demanded that $L > 0.5\,\mathrm{cm}$. Badly measured tracks originating from the primary vertex can lead to a secondary vertex that is separated by more than $0.5\,\mathrm{cm}$ from the primary one. Such combinations are rejected by a requirement on the significance S_L of the decay length which is given by $S_L = \frac{L}{\delta L}$, where δL denotes the error of the decay length: $S_L > 4$. The distribution of the decay length and its significance is shown in figure 5.1 for data and simulation. The distributions of the data events are reproduced by the CDM simulation. The variation of the selection criteria imply that the small discrepancies observed in the distributions are not affecting the measurement of the cross-sections.

Fit Probability The probability $P(\chi^2, n)$ of the vertex fit (see equation 4.22) is used to reject combinations of tracks that do not belong to the same vertex. The requirement is $P(\chi^2, n) > 1\,\%$. The fit probability is displayed in figure 4.12 for data and simulation.

Sign of d'_{ca} The distance of closest approach d'_{ca} of the tracks to the primary vertex is a signed number. For negative charged tracks the sign of the d'_{ca} is positive if the primary vertex is included in the circle described by the track in the $r - \phi$ plane and negative otherwise. For positive charged tracks the assignment of the sign is conversely, i.e. the sign is negative if the primary vertex is included in the circle described by the track. Tracks belonging to the same V^0 particle have opposite signs and therefore the product of the d_{ca}'s is required to be negative: $d'_{ca}(track1) \cdot d'_{ca}(track2) < 0$.

This set of selection criteria is in the following referred to as "V^0 selection criteria".
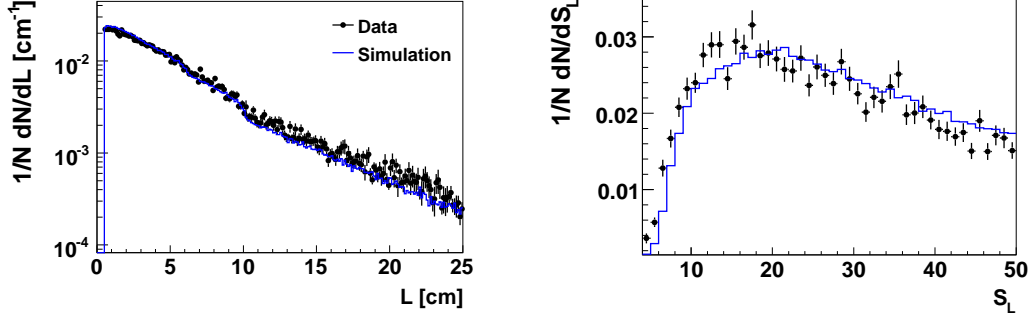
Figure 5.1: The distribution of the decay length and its significance as measured in data (black dots) and in the simulated sample (blue histogram). The distributions are scaled to one.

The mass spectra of the K_s^0 and Λ candidates after these selection criteria are displayed in figure 5.2. The K_s^0 and Λ peaks are clearly visible around the nominal mass of $0.497\,\text{MeV}$ and $1.116\,\text{MeV}$, respectively. The small enhancement near the threshold is caused by photon
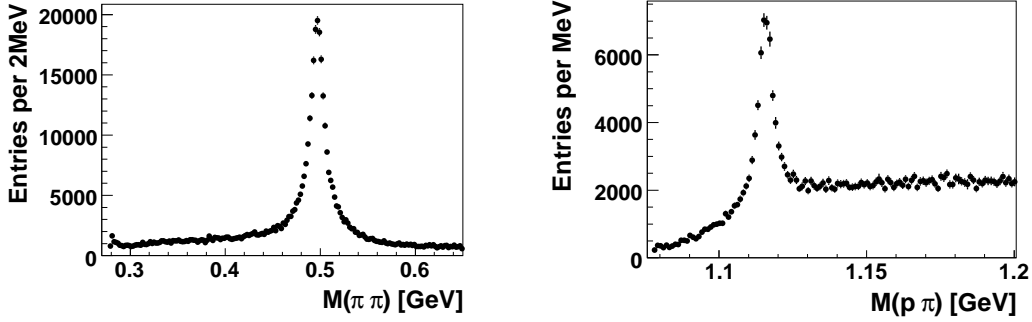
Figure 5.2: The reconstructed mass spectra of the K_s^0 (left) and Λ (right) candidates after the V^0 selection criteria.

conversion events, $\gamma \rightarrow e^+ e^-$. There is no need for special selection criteria to reject these conversion events because they are well separated in mass from the K_s^0 and Λ signal region. However, studies performed in [76] have claimed that the photon conversion might have an impact on the K_s^0 and Λ measurements. In figure 5.3 the mass spectrum of all V^0 candidates is shown, where both particle tracks are assumed to be electrons. As can be seen from the different decompositions in the simulated case, the first peak around a mass of $20\,\text{MeV}$ is caused by photons while the other two structures around $280\,\text{MeV}$ and $400\,\text{MeV}$ represent the Λ and K_s^0 particles, respectively. As already mentioned, the photon conversion events have almost no overlap with the V^0 distributions. The same behaviour is illustrated in figure 5.4. The x-axis shows the mass of the selected V^0 candidates under the pion-pion or pion-proton hypothesis while the y-axis represents the mass under the electron-electron hypothesis. Clearly visible are three clusters: The photon conversion events which are located near the threshold, the K_s^0 events around the nominal mass of $0.497\,\text{MeV}$ (upper two figures) and the Λ events around $1.116\,\text{MeV}$ (lower two figures). The quasi-elliptical structures in all
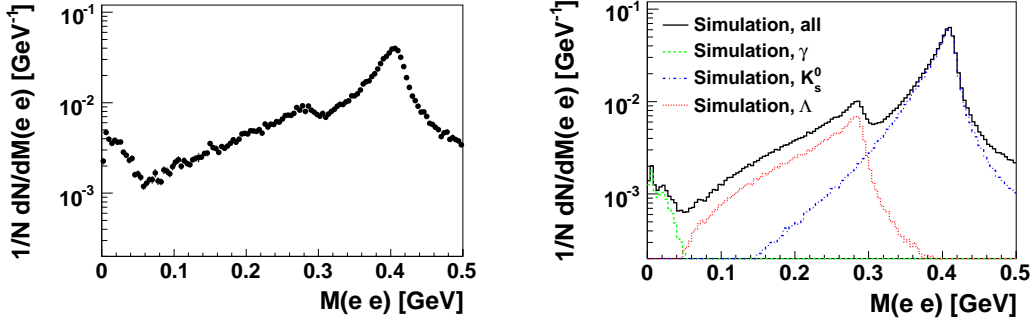
Figure 5.3: The mass spectrum of all selected V^0 candidates where for both particle tracks the electron hypothesis is used. The left figure represents the data and the right one the simulated sample. For the simulated sample the events are splited for the three different contributions of the photon, the K_s^0 and the Λ decays.

figures are caused by Λ (K_s^0) events reconstructed under the wrong particle hypothesis. The
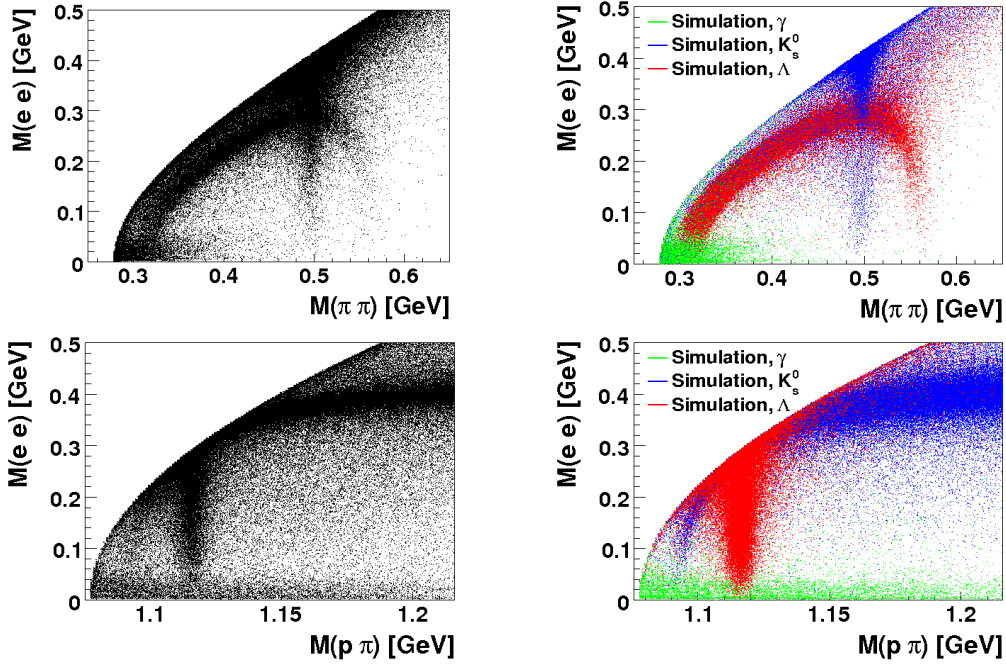
Figure 5.4: The two-dimensional representation of the selected V^0 candidates. Shown is the electron-electron hypothesis versus the pion-pion hypothesis (top row) and versus the pion-proton hypothesis (lower row).

figures 5.3 and 5.4 indicate that the reconstructed K_s^0 and Λ particles do partly overlap. The separation of these two particles is discussed in the next section.

5.1.2 Rejection of Λ (K_s^0) Contamination

In figure 5.5 the $(\pi\,\pi)$ mass hypothesis is shown versus the $(\pi\,p)$ hypothesis for all selected V^0 candidates for data and for the simulated events. For the simulated case, the events are partitioned for photon conversions, K_s^0 and Λ decays. Clearly visible are two bands around a $(\pi\,\pi)$ mass of 0.5 GeV and around a mass of 1.12 GeV from the decays $K_s^0 \to \pi\,\pi$ and $\Lambda \to p\,\pi$, respectively. These two bands do partly overlap and consequently there the Λ mass spectrum exhibits a contamination from K_s^0 decays and vice versa. This contamination is removed by a selection criteria on the invariant $\pi\,\pi$ $(\pi\,p)$ mass for the selected Λ (K_s^0) candidates. The selection criteria applied are:

$$|M(\pi\,\pi) - M_{K_s^0}| > 10\,\text{MeV} \qquad \text{for } \Lambda \text{ candidates,} \qquad (5.7)$$

$$|M(p\,\pi) - M_\Lambda| > 6\,\text{MeV} \qquad \text{for } K_s^0 \text{ candidates,} \qquad (5.8)$$

where $M_{K_s^0}$ and M_Λ are the nominal K_s^0 and Λ mass, respectively. The effect of these addi-
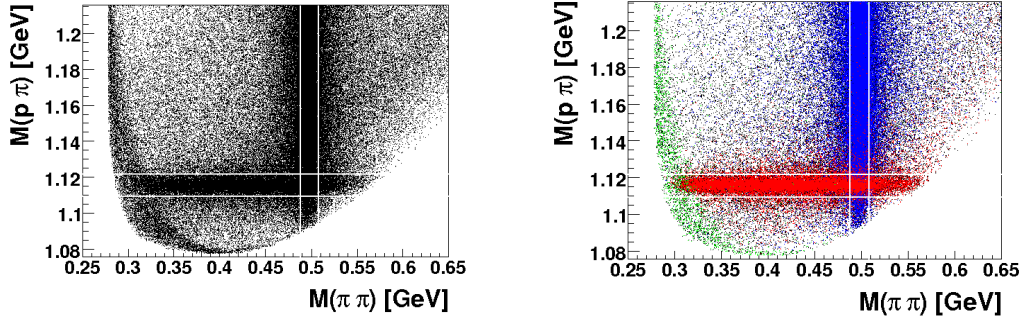
Figure 5.5: The two-dimensional representation of the selected V^0 candidates. Shown is the pion-pion hypothesis versus the pion-proton hypothesis for data (left) and for the simulated sample (right). For the simulated case, the events are partitioned for photon conversions (green), K_s^0 (blue)and Λ (red) decays.

tional requirements are displayed in figure 5.6, which shows on the left column the invariant mass of the K_s^0 and Λ candidates after this rejection and on the right column the rejected K_s^0 and Λ candidates. As expected a small fraction ($\lesssim 2\,\%$) of the K_s^0 (Λ) signal is rejected by this selection. However, the rejected events have a bad signal to noise ratio justifying the applied selection criteria.

Another possibility to reject the contamination of Λ (K_s^0) decays is provided by the Armenteros-Thompson variables introduced in section 4.2.4. Within this analysis these variables are not used to reject any events but only to cross-check the selection given by equation 5.8. In figure 5.7 the relative transverse momentum of the negative charged daughter particle, p_T^{rel}, for all selected V^0 candidates is displayed versus the variable α (see equation 4.23) for data and for the simulated sample. For visibility only a randomly chosen subsample is used. Clearly visible are three semi-ellipses with the zeniths $(\alpha(p_T^{rel,max}), p_T^{rel,max}) = \{(0, 0.21\,\text{GeV}), (\pm 0.7, 0.1\,\text{GeV})\}$, corresponding to the decays $K_s^0 \to \pi^+\,\pi^-$, $\Lambda \to p\,\pi^-$ and $\overline{\Lambda} \to \overline{p}\,\pi^+$ (see table 4.3). The effect of the rejection of the Λ (K_s^0) particles given by equation 5.8 is illustrated in figure 5.8. The Λ rejection for the K_s^0 candidates results in cutting away two small semi-ellipses, while the K_s^0 rejection for the Λ candidates overrules a significant
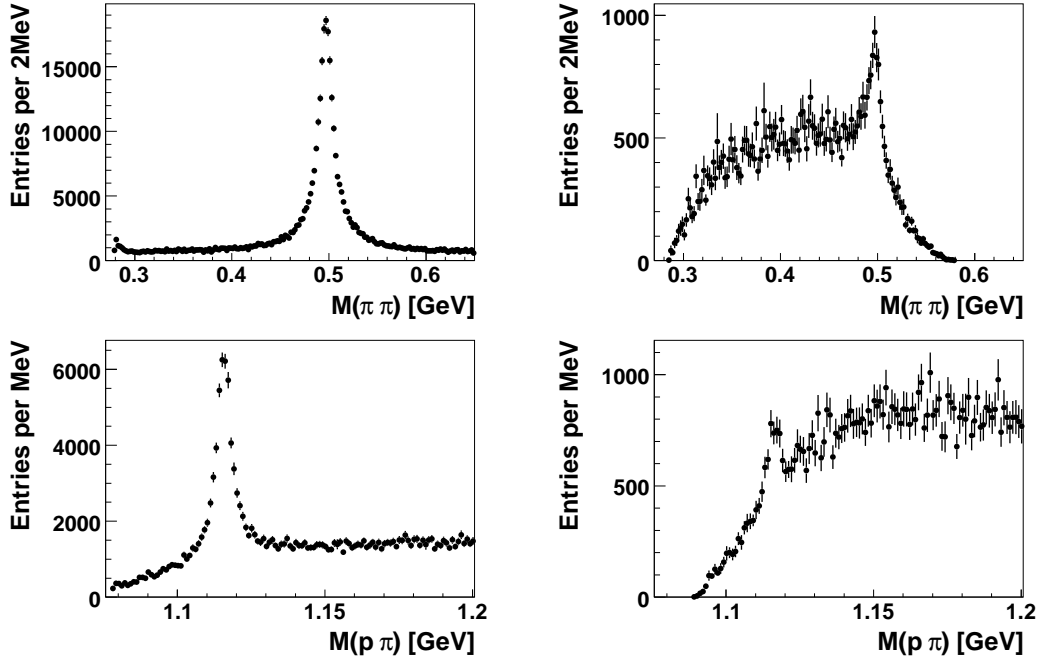
Figure 5.6: The figure shows in the left column the mass spectra of the K_s^0 (top) and Λ (bottom) candidates after the rejection given by equation 5.8 while the right column shows the rejected part of the mass spectra. For all figures the V^0 selection criteria are applied.
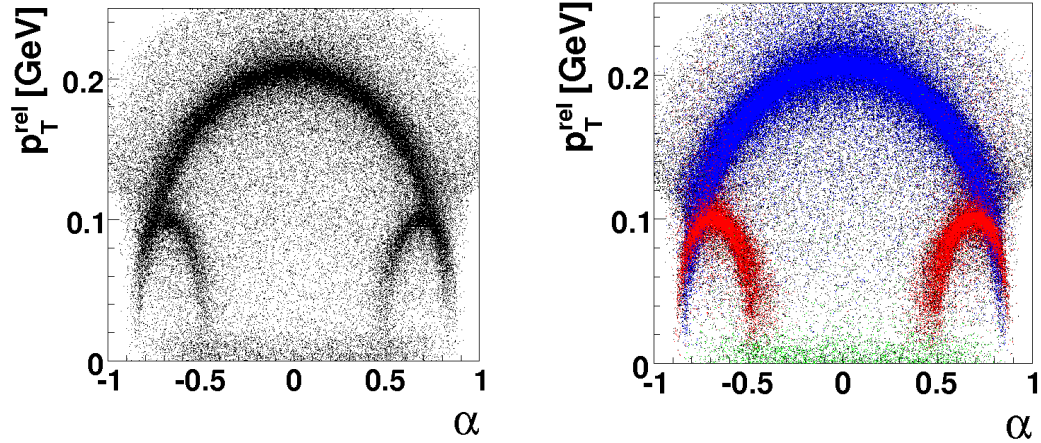
Figure 5.7: The Armenteros-Thompson figure for all selected V^0 candidates in data (left) and in the simulated sample (right). For the simulated sample the events are partitioned for photon conversions (green), K_s^0 (blue) and Λ (red) decays. For explanation see text.

part of the large semi-ellipse (upper part of the figure). Especially for the Λ candidates a part of the K_s^0 contamination remains. This contamination could be removed completely by strengthen the mass requirement. However, a significant fraction of the Λ signal would be lost and the cross-section measurement is not affected by the remaining contamination since this

is taken into account also for the simulated sample. Nevertheless, the different resolution of the signals in data and simulation imply a small systematic uncertainty on the cross-section which is estimated to be $\lesssim 2\,\% \cdot 0.1 \approx 0.2\,\%$ [3]. This uncertainty is small compared to other sources (see section 6.5) and is not considered further. The lower part of figure 5.8 shows the same distribution but only for those candidates being in the K^0_s and Λ signal region ($\pm\, 2\,\sigma$), respectively. For the Λ case the events are split into Λ (without charge conjugation) and $\overline{\Lambda}$ candidates.
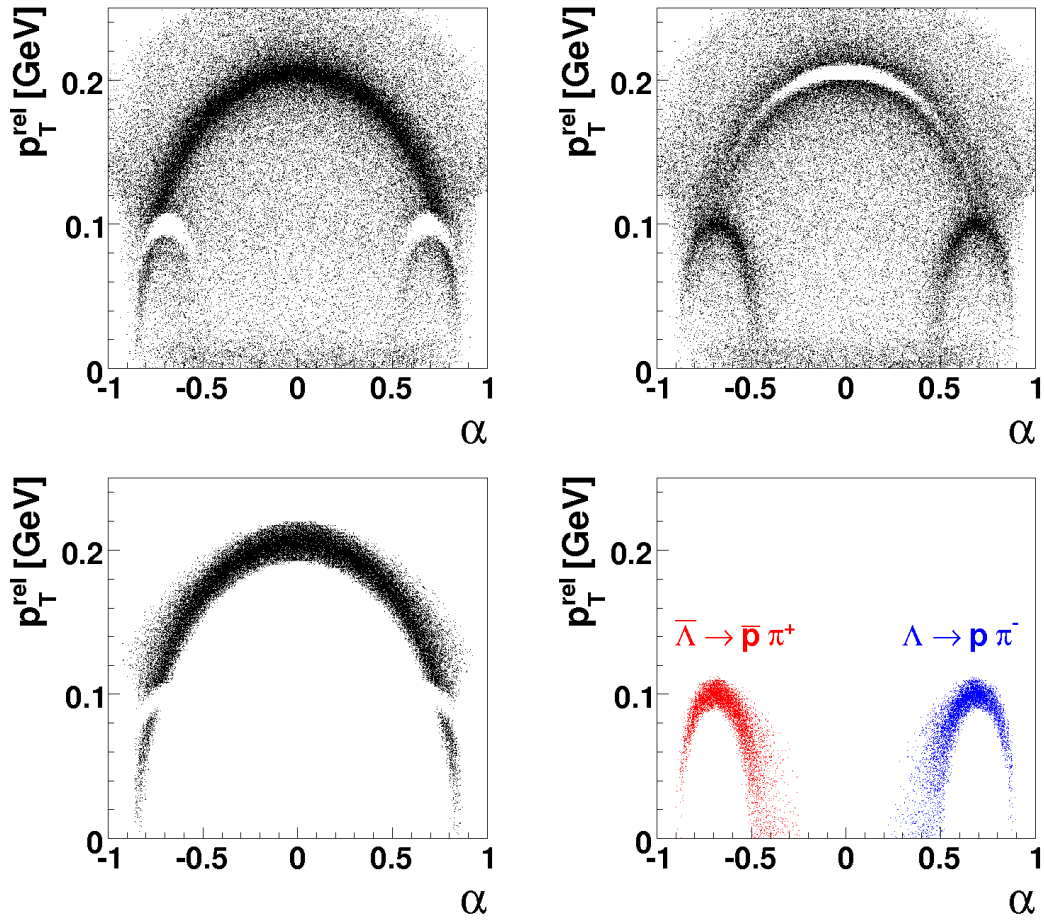
Figure 5.8: The Armenteros-Thompson figure for all selected V^0 candidates in data with removal of the Λ (K^0_s) contamination (top) and for the K^0_s (Λ) signal region (bottom). For the Λ case the events are partitioned for the $\Lambda \to p\,\pi^-$ (blue) and $\overline{\Lambda} \to \overline{p}\,\pi^+$ (red) decay.

For all following studies, the rejection of the Λ (K^0_s) contamination is applied.

---

[3]The factor of 0.1 gives the difference in the number of entries within $\pm\,2\,\sigma$ of a Gaussian function compared to the entries within $0.75 \cdot (\pm\,2\,\sigma)$. The factor of 0.75 rises because the width of the signal is underestimated in the simulation by 25 %

5.2 Signal Extraction

The number of signal entries is obtained by fitting an overall function F to the invariant mass spectra. This function is composed of a superposition of two Gaussian function $G_{1,2}$ accounting for the signal and a function $B_{K_s^0,\Lambda}$ describing the background. The function B has to be chosen separately for the K_s^0 and Λ since the background shape for these two cases is different. Due to different resolution of the reconstructed K_s^0 (Λ) particles (see section 4.2.1 and 5.2.3), the signals cannot be described by a single Gaussian function. The chosen parameterisation of the function F is given by:

$$F(M) = \alpha \cdot G_1(S_{tot}, \mu, \sigma_1) + (1 - \alpha) \cdot G_2(S_{tot}, \mu, \sigma_2) + B(M), \quad (5.9)$$

$$B_{K_s^0}(M) = P_1 + P_2 \cdot M, \quad (5.10)$$

$$B_\Lambda(M) = P_1 \cdot (M - M_\Lambda)^{P_2} \cdot e^{(1 + P_3 \cdot M + P_4 \cdot M^2)}. \quad (5.11)$$

Here, M denotes the $\pi\pi$ and the $p\pi$ invariant mass, respectively and M_Λ the nominal mass of the Λ baryon. The normalisation (S_{tot}), the central value (μ) and the widths ($\sigma_{1,2}$) of the Gaussian functions $G_{1,2}$ as well as the parameters P_i are left free in the fit. The parameter α ($0 < \alpha < 1$) represents the relative normalisation of the two signal Gaussians. The mass spectra together with the fit of the function F to these spectra is shown in figure 5.9 for the K_s^0 candidates and in figure 5.10 for the Λ candidates. Note that the whole reconstruction procedure is not optimised for best resolution but for stability of the signal which is essential for the cross-section determination.
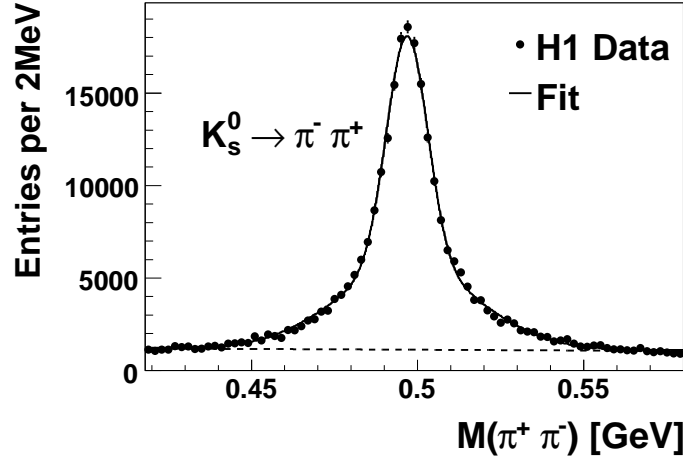
Figure 5.9: The invariant mass spectrum of all selected K_s^0 candidates. The solid line shows the result of a fit to the data using the function F as defined in equation 5.11 while the dashed line indicates the background function only.

K_s^0 case: All relevant parameters of the fit are summarised in table 5.1. The fit yields a total of approximately 213'000 reconstructed K_s^0 mesons ($\chi^2/n = 126/73$) and a mass consistent with the world average of (497.65 ± 0.02) MeV [26]. The measured widths ($\sigma_{1,2}$) of the Gaussian functions are around 6 MeV and 21 MeV, respectively and the signal is distributed nearly uniformly between the two Gaussians. To quantify the resolution of the
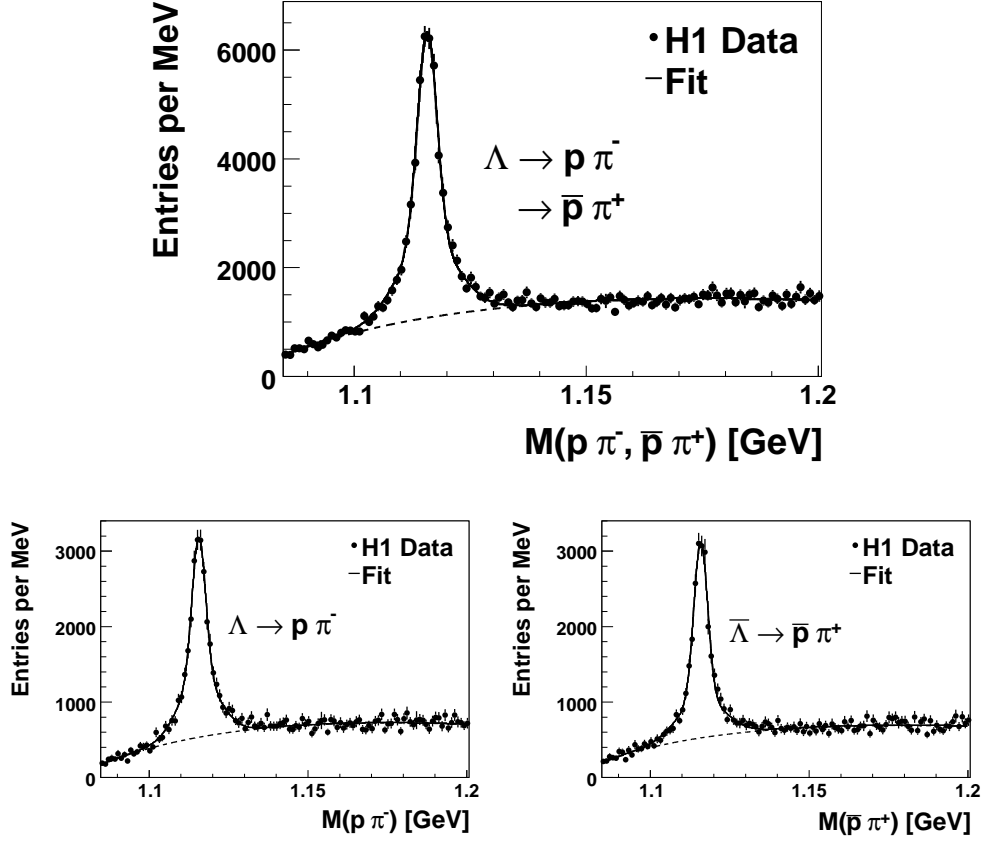
Figure 5.10: The invariant mass spectrum of all selected Λ candidates including charge conjugation (top) and excluding charge conjugation (bottom left) as well as of all $\overline{\Lambda}$ candidates (bottom right). The solid line shows the result of a fit to the data using the function F as defined in equation 5.11 while the dashed line indicates the background function only.

signal, the mean width $\overline{\sigma}$ is introduced:

$$\overline{\sigma} = \alpha \cdot \sigma_1 + (1 - \alpha) \cdot \sigma_2. \tag{5.12}$$

The fit to the K_s^0 mass spectrum reconstructed from the simulated sample (CDM) is shown in figure 5.11 and also summarised in table 5.1. The resolution of the signal in the simulated case is roughly 25 % better than in data. This effect is well known and can be traced back to an overestimated track resolution in the simulation. Concerning the cross-section measurement, the only place where the different widths of the signals in data and simulation could have an influence is the rejection of the $\Lambda(K_s^0)$ contamination. As shown in section 5.1.2 the different width leads to an uncertainty below 0.2 %. Therefore the different resolution is not investigated further.

Λ case: The properties of the fit are summarised in table 5.1. The fit yield a total of approximately 42'000 reconstructed Λ and $\overline{\Lambda}$ baryons ($\chi^2/n = 108/106$). The signal comprises 22'000 Λ (charge conjugation excluded) and 20'000 $\overline{\Lambda}$ baryons. The difference in the number of reconstructed Λ and $\overline{\Lambda}$ particles does not point to a $\Lambda - \overline{\Lambda}$ asymmetry (see figures 6.34, 6.35) but to a different reconstruction efficiency which can be explained by the nearly five times

higher absorption probability for anti-protons than for protons in the detector material for the relevant kinematic range [26]. The reconstructed Λ mass is in excellent agreement with the world average of $(1'115.683 \pm 0.006)$ MeV [26]. The fit to the individual Λ and $\overline{\Lambda}$ spectra yields a mass that is consistent with the value of the combined fit. The measured widths ($\sigma_{1,2}$) of the Gaussian functions are 2 MeV and 6 MeV. The signal is again distributed nearly uniformly between the two Gaussian functions. The fit to the Λ mass spectrum reconstructed from the simulated sample (CDM) is shown in figure 5.11 and also summarised in table 5.1. Again the simulation overestimates the resolution by $\sim 25\,\%$.

5.2.1   L4 Weights

For the extraction of the signal presented in section 5.2 the L4 weights (see section 3.2.4) have been applied event wise. The number of strange hadrons can also be extracted from the unweighted mass spectra as illustrated in this section. The chosen strategy for the cross-section measurement is to extract the number of signal entries from the unweighted mass spectra and multiply these numbers by the mean L4 weight of the distributions. For the K_s^0 case the L4 weight is independent of the mass of the candidates and the mean value is therefore calculated for all hypothesis with $0.42 < M(\pi\pi) < 0.58$ GeV. For the Λ case the L4 weight distribution has a weak dependency on the mass of the candidates and therefore the mean value $< L4 >$ is calculated for hypothesis in the signal region only $(1.109 < M(p\pi) < 1.123$ GeV). The L4 weight distribution is displayed in figure 5.12. In total, $90.5\,\%$ ($92.1\,\%$) of the reconstructed K_s^0 (Λ) candidates have passed the L4 farm (i.e. weight equal to one). The mean L4 weight is:

$$< L4(K_s^0) >= 1.587 \pm 0.005 \quad \text{and} \quad < L4(\Lambda) >= 1.503 \pm 0.014. \tag{5.13}$$

The fit to the unweighted mass spectra is displayed in figure 5.13. This fit yields a number of $134'115 \pm 621$ reconstructed K_s^0 mesons and of $28'365 \pm 307$ Λ baryons. The other properties of the fit like the mean value and the width of the signals are compatible with those extracted

Table 5.1: The result of the fit to the K_s^0 and Λ mass spectra in data and simulation. Here, N denotes the number of reconstructed signal entries, M the reconstructed mass, $\sigma_{1,2}$ the width of the signal, α the relative contribution of the two Gaussian functions and S/N the signal to noise ratio within $\pm 2\overline{\sigma}$ of the fitted mass.

	K_s^0		$\Lambda + \overline{\Lambda}$	
	Data	CDM	Data	CDM
N [k]	212.834 ± 1.866	$1'364.3 \pm 1.5$	41.988 ± 0.881	284.4 ± 0.7
M [MeV]	496.89 ± 0.07	498.259 ± 0.007	$1'115.79 \pm 0.05$	$1'115.930 \pm 0.006$
σ_1 [MeV]	6.17 ± 0.13	4.91 ± 0.01	2.08 ± 0.11	1.800 ± 0.009
σ_2 [MeV]	21.0 ± 0.4	19.00 ± 0.07	6.3 ± 0.4	5.46 ± 0.06
$\overline{\sigma}$ [MeV]	14.3 ± 0.3	10.44 ± 0.04	4.3 ± 0.3	3.21 ± 0.03
α [%]	45.5 ± 1.1	60.72 ± 0.11	48 ± 4	61.6 ± 0.4
S/N	6	16	2	6
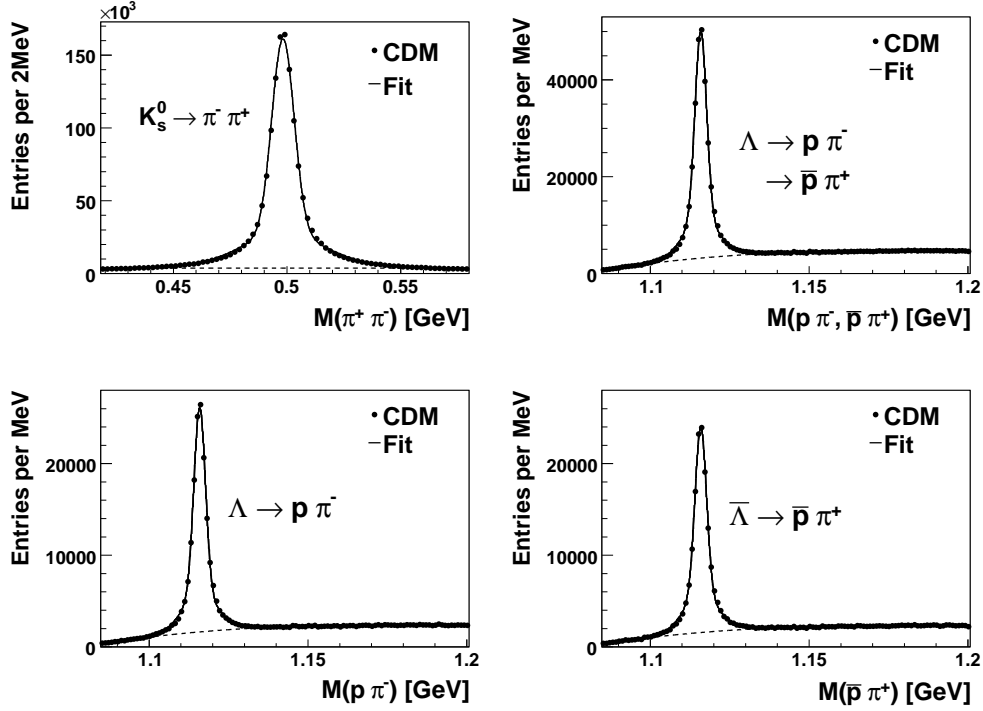
Figure 5.11: The invariant mass spectrum of all selected V^0 candidates reconstructed from the simulated (CDM) sample. Top left: K_s^0 candidates, top right: $\Lambda + \overline{\Lambda}$ candidates, bottom left: Λ candidates and bottom right: $\overline{\Lambda}$ candidates. The solid line shows the result of a fit to the data using the function F as defined in equation 5.11 while the dashed line indicates the background function only.

from the weighted distributions. The total number of strange hadrons corrected for the efficiency of the level four filter farm is therefore:

$$N(K_s^0) = N(K_s^0)_{noL4} \cdot < L4(K_s^0) > \quad = \quad 212'840 \pm 1'192 \tag{5.14}$$

$$N(\Lambda) = N(\Lambda)_{noL4} \cdot < L4(\Lambda) > \quad = \quad 42'633 \pm 609, \tag{5.15}$$

where $N(K_s^0)_{noL4}$ and $N(\Lambda)_{noL4}$ denotes the number of reconstructed K_s^0 and Λ particles without the L4 weights applied. These numbers are in good agreement with those extracted from the weighted mass spectra. Therefore, the extraction of the signal can either be done from the weighted or unweighted distributions. For the K_s^0 case the weighted distributions are chosen while for the Λ case the unweighted distributions are used. The reason for this procedure is that the differential spectra for the Λ candidates have sometimes only a small statistic and in these cases the L4 weights distort the mass spectra and the fit overestimates the signal[4]. Since the statistical uncertainty on the number of strange hadrons depends only on what is really measured, this quantity is always calculated from the unweighted mass spectra.

According to the level four strategy (see section 3.2.4), the events in different phase space regions have different weights. In figure 5.14 the mean L4 weight for the K_s^0 candidates

---

[4]In these cases there are bins in the background region where all entries have a weight equal to one. These bins have a smaller uncertainty than the neighboring bins and pull the background curve towards lower values.
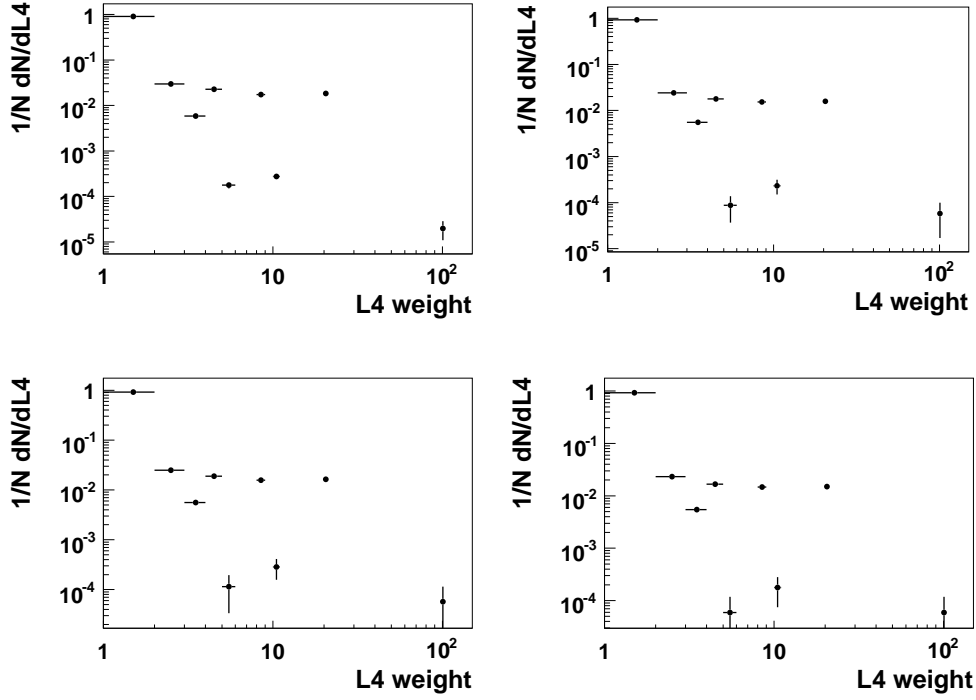
Figure 5.12: The distribution of the L4 weight for the selected K_s^0 candidates (top right), Λ candidates including (top right) and excluding (bottom left) charge conjugation as well as for the $\overline{\Lambda}$ candidates (bottom right).
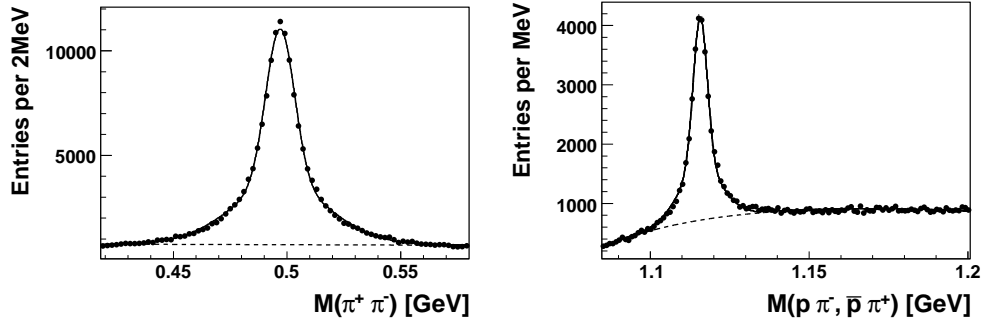
Figure 5.13: The invariant mass spectrum of all selected K_s^0 (left) and Λ (right) candidates without L4 weights. The solid line shows the result of a fit to the data using the function F as defined in equation 5.11 while the dashed line indicates the background function only.

is shown as a function of Q^2 and p_T. The mean L4 weight drops from 2.24 at the lowest Q^2 values to 1.06 at highest ones and from 1.86 for low-p_T to 1.11 for high-p_T candidates. Therefore, the level four filter farm behaves as expected and the L4 weights are taken into account properly.
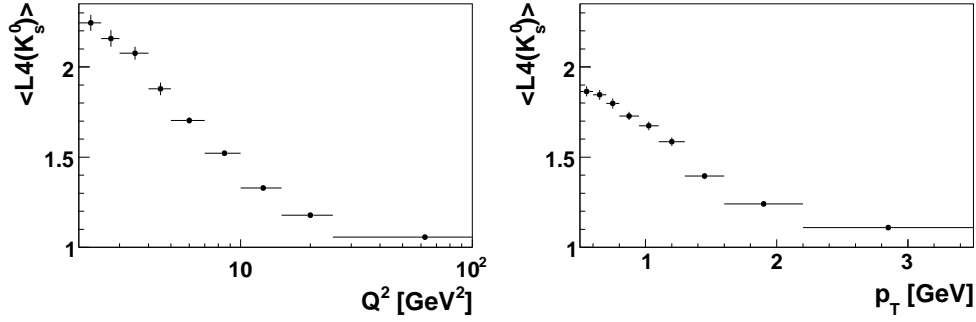
Figure 5.14: The dependency of the L4 weights on Q^2 and p_T for the K_s^0 candidates.

5.2.2 Stability of the Signal Extraction

The stability of the signal extraction is proven particularly with regard to the cross-section calculation. The cross-section has the proportionality (see section 6.1)

$$\sigma \propto \frac{N_{Data}^{rec}(V^0)}{N_{MC}^{rec}(V^0)}, \tag{5.16}$$

where $N_{Data}^{rec}(V^0)$ and $N_{MC}^{rec}(V^0)$ denote the number of reconstructed V^0 particles in data and simulation, respectively. Therefore, this ratio has to be stable under variation of the signal extraction procedure. The effect on the cross-section is stated as relative change with respect to the *standard* procedure as summarised in table 5.1:

$$\Delta\sigma_{variation,i} = \frac{|\sigma_{standard} - \sigma_{variation,i}|}{\sigma_{standard}}, \tag{5.17}$$

where $\sigma_{variation,i}$ is the cross-section under the variation i. The results are summarised in table 5.2.

Weights: The variation of the signal due to fitting the unweighted mass spectra (see section 5.2.1) is leading to a change of the cross-section compatible with the statistical uncertainty of $\Delta\sigma(K_s^0)(stat) = 0.56\,\%$ and $\Delta\sigma(\Lambda)(stat) = 1.43\,\%$.

Background: The number of strange hadrons can also be extracted by counting all entries of the mass histogram within a certain range and subtracting the background function integrated over the same range. The range is chosen to be $\pm 6\bar{\sigma}$. This variation is mainly sensitive to the description of the tails of the signal by the two Gaussian functions. Again the change in the cross-sections are of the same order as the statistical uncertainty.

Fit range: The mass range of the fit is extended for the K_s^0 candidates from $0.42 < M(\pi\pi) < 0.58\,\text{GeV}$ to $0.38 < M(\pi\pi) < 0.62\,\text{GeV}$ and for the Λ case reduced from $1.085 < M(p\pi) < 1.2\,\text{GeV}$ to $1.085 < M(p\pi) < 1.16\,\text{GeV}$. The mass spectra for data together with the fitted function for the changed mass ranges are shown in figure 5.15.
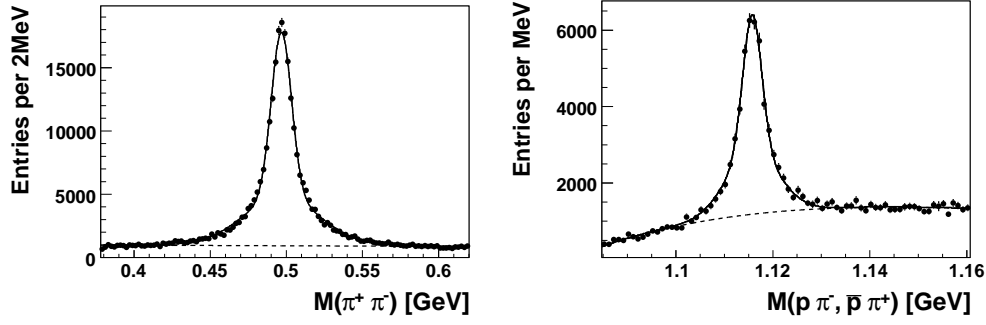
Figure 5.15: The points represent the K_s^0 and Λ mass spectra measured in data while the solid line indicates the function fitted to the changed mass range. The dashed line indicate the background function only.

Variation 4: For the Λ case the background function B_Λ has been varied. The exponential function in equation 5.11 has been exchanged by a Polynomial of degree two. This function is not able to fit the mass spectra up to high masses of the candidates. Therefore, the change in the cross-section has been calculated for the mass range $1.085 < M(p\,\pi) < 1.16\,\mathrm{GeV}$

Table 5.2: The result of the variation of the signal extracting procedure. For explanation see text.

Variation	$\Delta\,\sigma(K_s^0)\,[\%]$	$\Delta\,\sigma(\Lambda)\,[\%]$
Weights	$2.8 \cdot 10^{-3}$	1.5
Background	0.63	1.35
Fit range	2.42	2.90
Background function	—	2.31

5.2.3   Resolution of the K_s^0 and Λ Signals

In figure 5.16 the dependency of the mean width of the K_s^0 and Λ signal on the transverse momentum and on the pseudorapidity is displayed. The resolution decreases with increasing transverse momentum of the particle. The explanation is due to kinematic effects: For V^0's with low momenta the daughter particles have also a low transverse momenta. Such particle tracks have a larger curvature leading to a more accurate measurement of the transverse momentum. For the Λ, the resolution decreases below a transverse momentum of $800\,\mathrm{MeV}$ due to an increase of multiple scattering which dominates at low p_T. The distribution of the momentum of the daughter tracks is illustrated in figure 5.17 for the data and the simulated events. The pions from Λ decays peak at lower values than pions from K_s^0 decays. Therefore, the decreasing resolution at low p_T cannot be observed for the K_s^0 case. This effect is intensified by the fact that the cross-section for multiple interactions is larger for proton tracks than for pion tracks. Furthermore the energy loss is larger for protons than for pions (with the same p_T).

The dependency of the resolution on the pseudorapidity is different for the K_s^0 and Λ signal which can again be explained by the different decay kinematics. The resolution of the K_s^0 signal drops in the central part of the detector, since in this region the track length is shorter and therefore the tracks deposit less charge in the detector than tracks passing the detector more diagonally. This effect is not visible for the Λ case because the spread of the pion tracks from Λ decays is larger than in the K_s^0 case and therefore these tracks tend to leak more often into the forward or backward region of the CJC for Λ's with $\eta \sim 0$ than for K_s^0's. Furthermore the accuracy of the resolution is worse for the Λ signal than for the K_s^0 making it harder to see this effect.
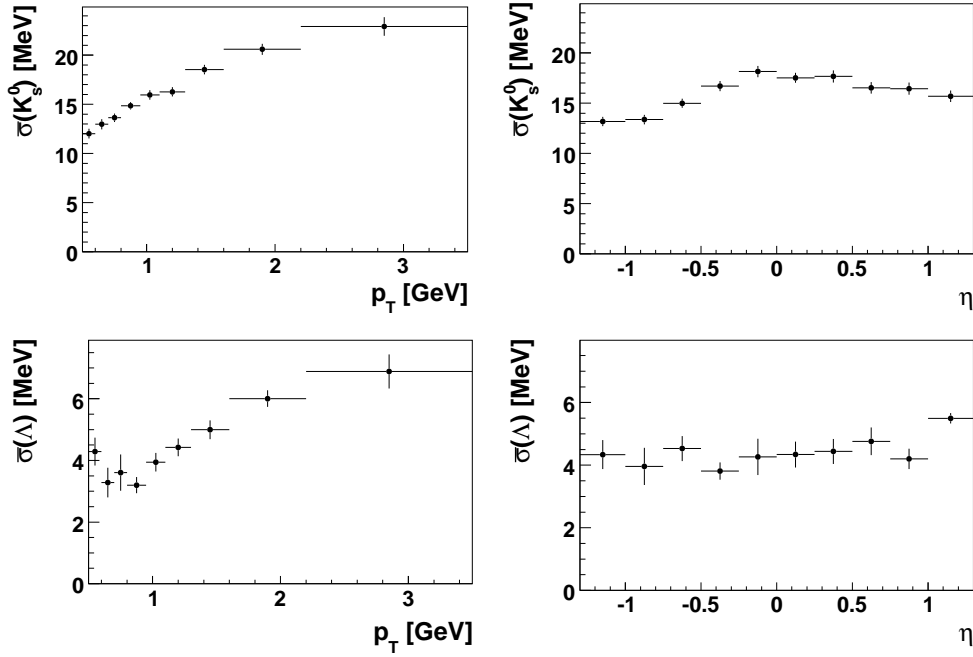
Figure 5.16: The dependency of the mass resolution of the K_s^0 (top) and Λ (bottom) signal on the transverse momentum p_T (left) and pseudorapidity η (right) for data.
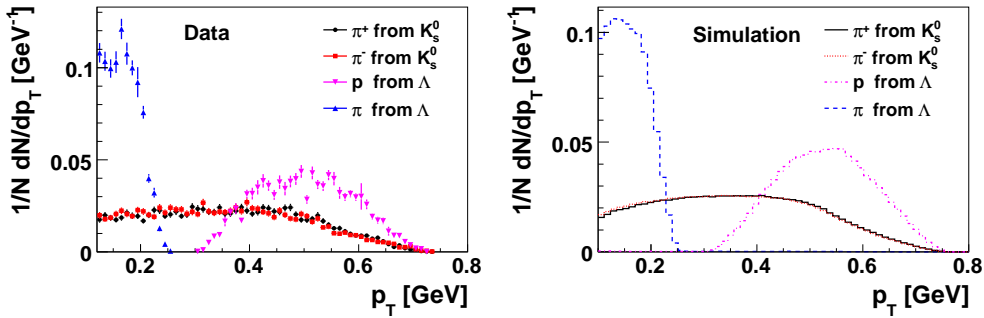
Figure 5.17: The momentum of the daughter particles of the K_s^0 and Λ for $0.5 < p_T(V^0) < 0.8\,\mathrm{GeV}$ in data (left) and simulation (right). All distributions are normalised to one.

Chapter 6

Measurement of the K_s^0 and Λ Production Cross-Sections

In this section the measurement of the cross-sections for K_s^0 and Λ production in DIS events is presented. In a first part the procedure of extracting the cross-sections from the measured K_s^0 and Λ signals is illustrated, including the correction for the detector effects, the trigger efficiency of the signals and the correction to non-radiative level. After studying the different systematic sources, the inclusive and differential K_s^0 and Λ production cross-sections and their ratios $R(\Lambda/K_s^0)$ are presented. For the differential cross-sections the variables Q^2, x, y, W, $p_T(V^0)$, $\eta(V^0)$ as well as the transverse momentum p_T^{Breit} and the momentum fraction x_p^{Breit} in the Breit frame are studied. The cross-sections are compared to leading-order Monte Carlo predictions obtained from the CDM and MEPS generator and constraints on the Lund parameter space are derived from the measured data.

6.1 Definition of the Cross-Section

The cross-section σ_{vis} is measured in the visible range defined by:

$$2 < Q^2 < 100 \, \text{GeV}^2 \qquad 0.5 < p_T(V^0) < 3.5 \, \text{GeV}$$
$$0.1 < y < 0.6 \qquad -1.3 < \eta(V^0) < 1.3 \tag{6.1}$$

and is calculated for the sum N of the observed number of V^0 particles and their antiparticles according to the formula

$$\sigma_{vis}(ep \to e'V^0 X) = \frac{N}{\mathcal{L} \cdot \epsilon \cdot BR \cdot (1 + \delta_{QED})}, \tag{6.2}$$

where $\mathcal{L}$ denotes the integrated luminosity, BR the branching ratios of the reconstructed decay channels (taken from [26]), ϵ the total efficiency and δ_{QED} the correction to Born level. The data are corrected for detector acceptance and efficiency effects using Monte Carlo event samples generated with CDM. All generated events are passed through the full GEANT [121] based simulation of the H1 apparatus and are reconstructed and analysed using the same programs as for the data. The total efficiency ϵ is given by $\epsilon = \epsilon_{rec} \cdot \epsilon_{trig}$, where ϵ_{rec} is the reconstruction efficiency including the acceptance and ϵ_{trig} is the trigger efficiency. The

trigger efficiency is extracted from the data using the monitor trigger technique introduced
in section 4.1.2.1. The number of hadrons N is taken from fitting the mass distributions. For
the differential cross-sections the fit is performed in each of the kinematical bins for any of
the variables under investigation. The correction to Born level allows the comparison of the
measured cross-sections with non-radiative Monte Carlo predictions.

6.2 Data Correction

Not all K_s^0 mesons and Λ baryons that are produced in the visible range can be measured
in the final state. The measured data are therefore corrected for detector effects to obtain
the number of produced particles. The non-measurability of such particles have plenty of
reasons. For example, not all DIS events are entering in the analysis due to the selection
criteria introduced in section 4.1.2 and the finite acceptance of the SpaCal. Other reasons
are the finite geometrical expansion of the tracking detectors implying that not all tracks
are measured, the track reconstruction itself which is not $100\,\%$ efficient or the track quality
requirements. Furthermore the suppression of background events in the V^0 mass spectra
rejects alway a part of the signal. Another reason for the correction are migration effects
due to the finite resolution of the measured quantities. This might lead to the selection of
events that are actually not within the visible range or the rejection of events that are in the
visible range. Further inefficiencies are caused by the trigger selection (see section 6.2.2). The
radiative corrections δ_{QED} are calculated using the program HERACLES [129] (see section
6.2.3).

6.2.1 Acceptance and Reconstruction Efficiency

All inefficiencies beside those caused by the triggering of the data and the radiative corrections
are calculated in one single step using the simulated event samples. Thereby, the number of
reconstructed particles passing all selection criteria is compared to those really generated in
the visible range using the simulated event samples CDM and MEPS. The correction for all
detector effects is given by:

$$\epsilon_{rec} = \frac{N_{rec}^{MC}}{N_{gen}^{MC}}, \tag{6.3}$$

where $N_{rec(gen)}^{MC}$ is the number of reconstructed (generated) V^0 particles in the visible phase
space calculated using the reconstructed (generated) values for all variables. In the following
this efficiency is referred to as reconstruction efficiency. For the determination of N_{rec}^{MC}
exactly the same selection criteria have been applied as for the analysis of the data events,
with exception that no trigger requirement is applied. The reconstruction efficiency for the
inclusive measurement are summarised in table 6.1 and amounts to $33.3\,\%$ and $19.5\,\%$ for the
K_s^0 and Λ reconstruction, respectively. The acceptance, defined as the fraction of events with
a K_s^0 (Λ) in the visible range where the daughter particles are in the central region of the
detector, amounts to roughly $80\,\%$ for the K_s^0 case and $70\,\%$ for the Λ case. This difference
can be explained by the different kinematics of the two decays. The acceptance correction
is by definition included in the numbers quoted for the reconstruction efficiencies. For the
determination of the differential cross-sections the reconstruction efficiency is calculated bin

wise for each variable under investigation and is defined in a similar way to equation 6.3:

$$\epsilon_{rec,i}(X) = \frac{N_{rec,i}^{MC}(X)}{N_{gen,i}^{MC}(X)}.$$ (6.4)

Here, $\epsilon_{rec,i}(X)$ denotes the reconstruction efficiency for V^0 particles lying in the i-th bin of the variable X. Accordingly, $N_{rec,i}^{MC}(X)$ and $N_{gen,i}^{MC}(X)$ gives the number of reconstructed and generated V^0 particles in the i-th bin of the reconstructed (generated) variable. The bin size of all variables is chosen in such a way that the number of reconstructed particles is distributed equally among the bins and that the migration effects are small, see section 6.3. The bin sizes of the different variables are listed in appendix A. The distributions of the reconstruction efficiency are displayed in figure 6.1 for the kinematic variables $p_T(V^0)$ and $\eta(V^0)$, in figure 6.2 for the event variables Q^2, x, y and W and in figure 6.3 for the variables p_T^{Breit} and x_p^{Breit} in the Breit frame. All figures show the reconstruction efficiencies extracted from the CDM sample as black, solid lines as well as those from the MEPS sample as blue, dashed lines. The difference in the efficiencies from these two models is small and is taken into account in the determination of the systematic uncertainties of the cross-section measurement, see section 6.5.
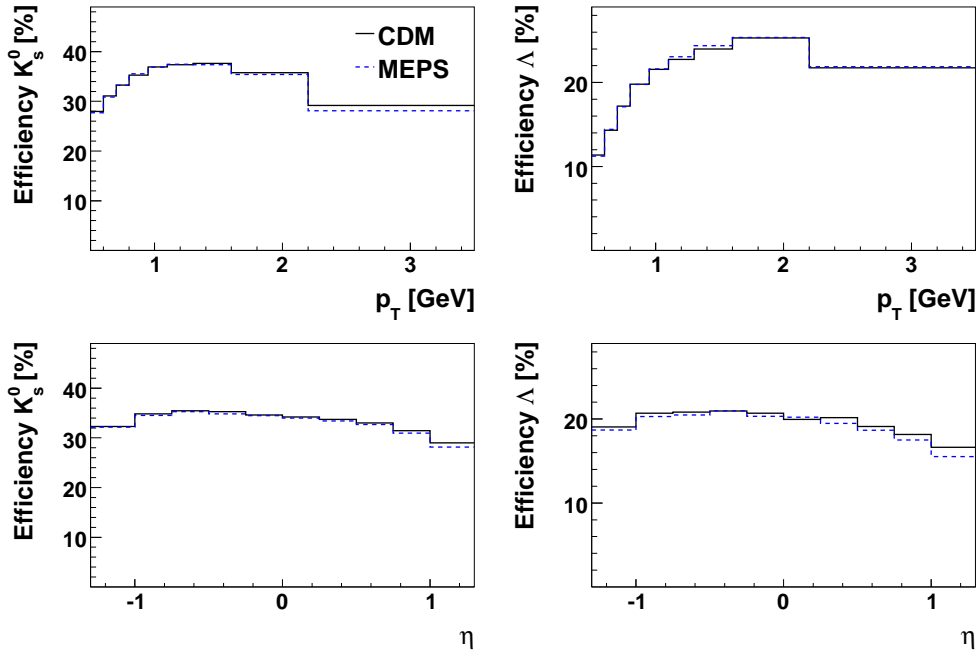
Figure 6.1: The reconstruction efficiencies ϵ_{rec} for K_s^0 mesons (left column) and Λ baryons (right column) as a function of the kinematic variables $p_T(V^0)$ and $\eta(V^0)$. Shown are the efficiencies extracted from the CDM sample (black, solid lines) and from the MEPS sample (blue, dashed lines).
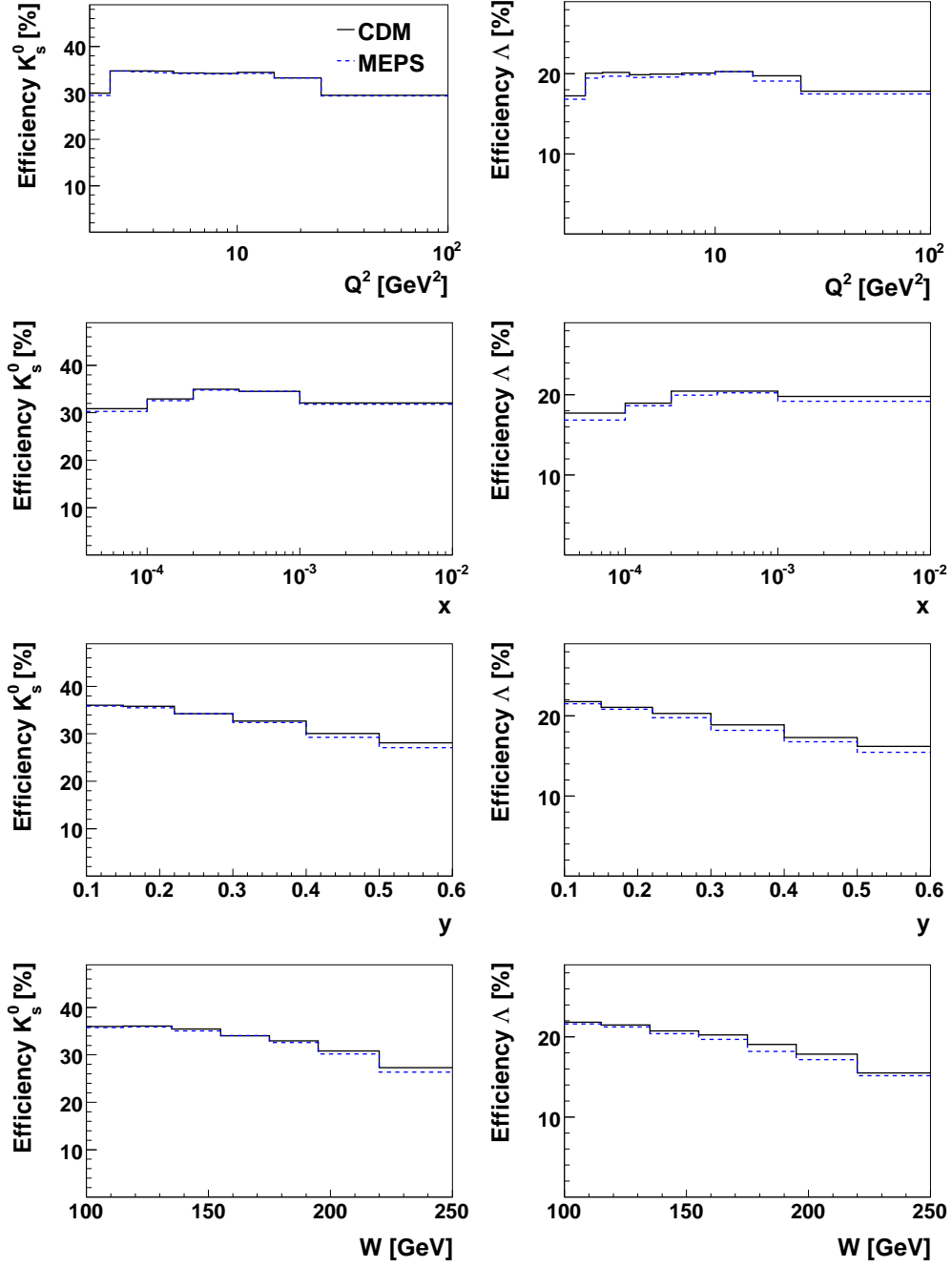
Figure 6.2: The reconstruction efficiencies ϵ_{rec} for K_s^0 mesons (left column) and Λ baryons (right column) as a function of the event variables Q^2, x, y and W. Shown are the efficiencies extracted from the CDM sample (black, solid lines) and from the MEPS sample (blue, dashed lines).
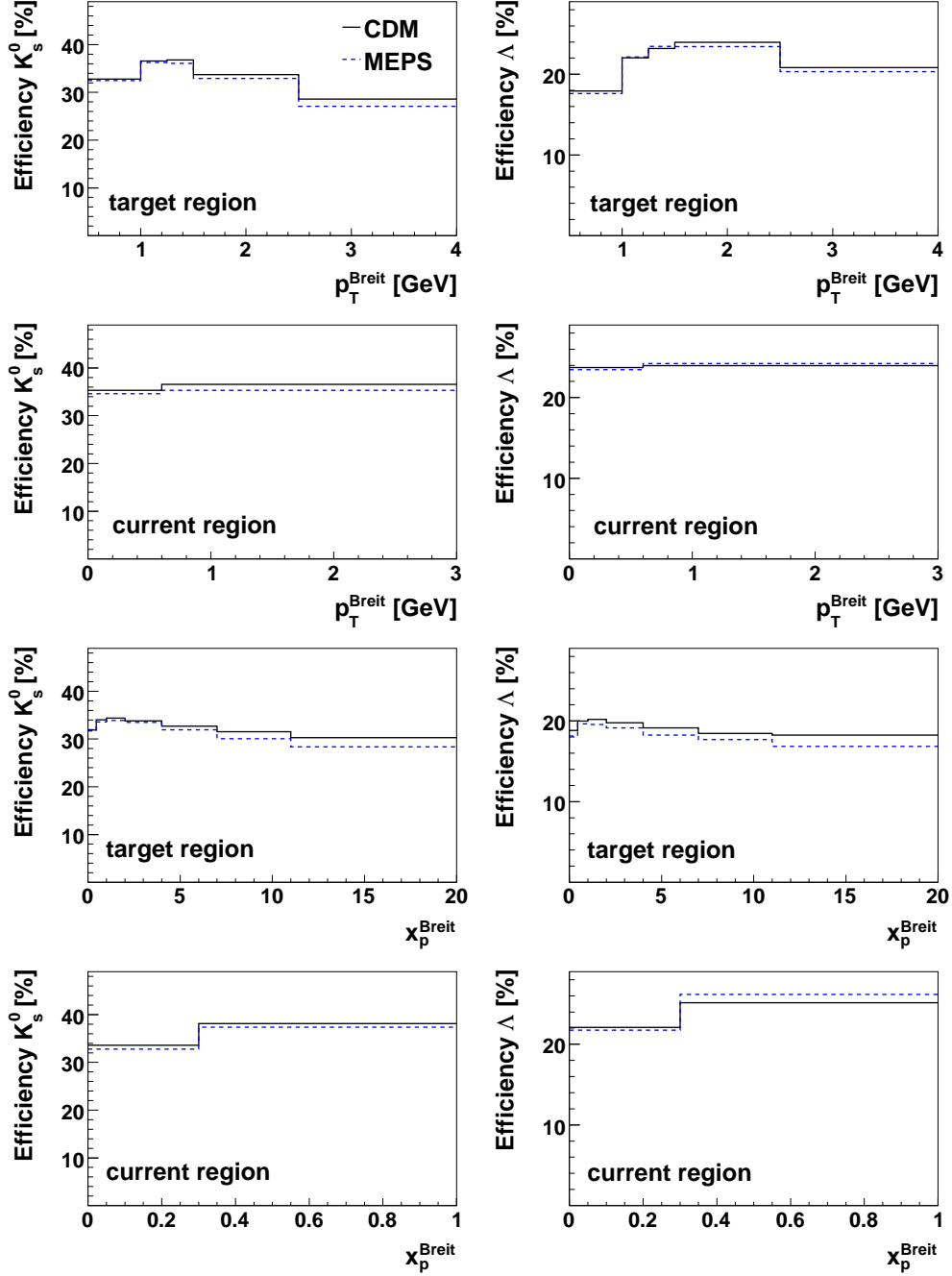
Figure 6.3: The reconstruction efficiencies ϵ_{rec} for K_s^0 mesons (left column) and Λ baryons (right column) in the Breit frame as a function of the kinematic variables p_T^{Breit} and x_p^{Breit} in the target and current hemisphere. Shown are the efficiencies extracted from the CDM sample (black, solid lines) and from the MEPS sample (blue, dashed lines).

6.2.2 Trigger Efficiency

The trigger efficiency is extracted from the data distributions according to the technique introduced in section 4.1.2.1. The monitor triggers S04 and S71 are used for the determination of ϵ_{trig} while the monitor triggers S0 and S67 are used for cross-checks only. The trigger efficiency for the inclusive sample amounts to $81.84\,\%$ and $83.66\,\%$ for the K_s^0 and the Λ case, respectively. The higher efficiency for the triggering of the Λ baryons with respect to the K_s^0 mesons can be traced back to a higher efficiency of the trigger elements $DCR\phi$. The probability that the proton from the Λ decay fires this element is larger than for the pions from the K_s^0 decays because the proton takes the larger fraction of $p_T(V^0)$. The distributions of the trigger efficiency of S61, as well as the contributions from the different trigger elements, is displayed for all variables in the figure 6.4 to 6.6. The SpaCal trigger element is nearly $100\,\%$ efficient for the selected events, while the $DCR\phi$ and the z-vertex elements are roughly $90\,\%$ efficient. The dependency of the $DCR\phi$ efficiency on $p_T(V^0)$ shows the anticipated behaviour: For high p_T candidates it reaches nearly $100\,\%$ and the rise with increasing $p_T(V^0)$ is steeper for Λ baryons than for K_s^0 mesons which can again be explained by the different decay kinematics.
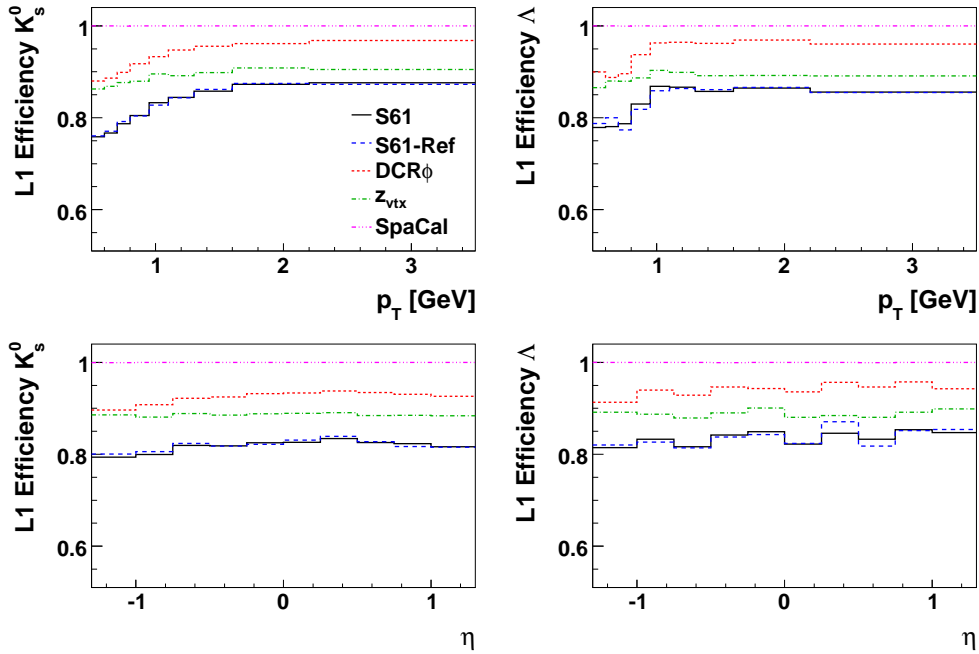
Figure 6.4: The trigger efficiencies ϵ_{trig} for K_s^0 mesons (left column) and Λ baryons (right column) as a function of the kinematic variables $p_T(V^0)$ and $\eta(V^0)$. Shown are the total efficiencies for the two monitor sets (S04, S71), labeled "S61" and (S0, S67), labeled "S61-Ref" and the contributions from the different trigger elements.
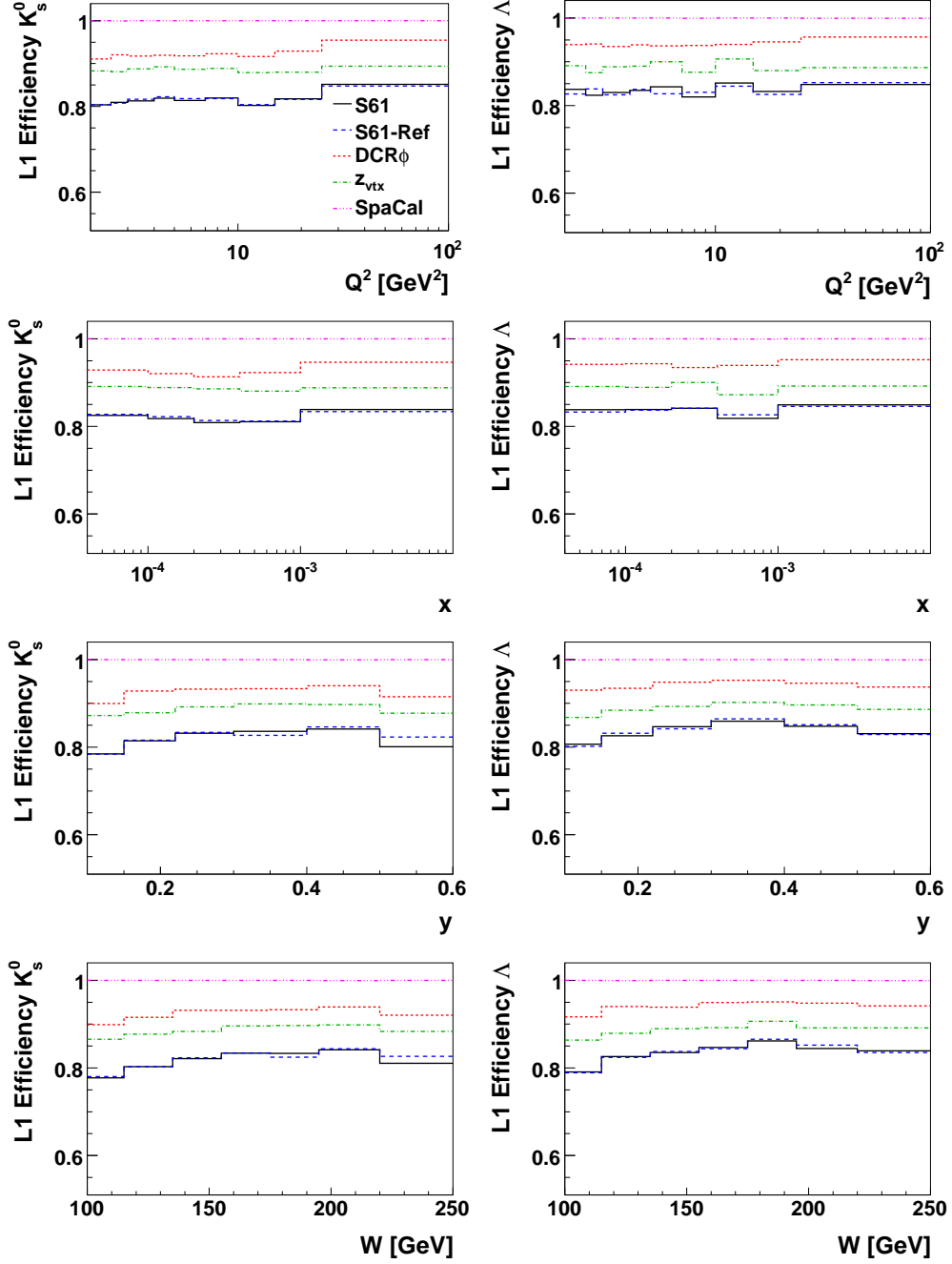
Figure 6.5: The trigger efficiencies ϵ_{trig} for K_s^0 mesons (left column) and Λ baryons (right column) as a function of the event variables Q^2, x, y and W. Shown are the total efficiencies for the two monitor sets (S04, S71), labeled "S61" and (S0, S67), labeled "S61-Ref" and the contributions from the different trigger elements.
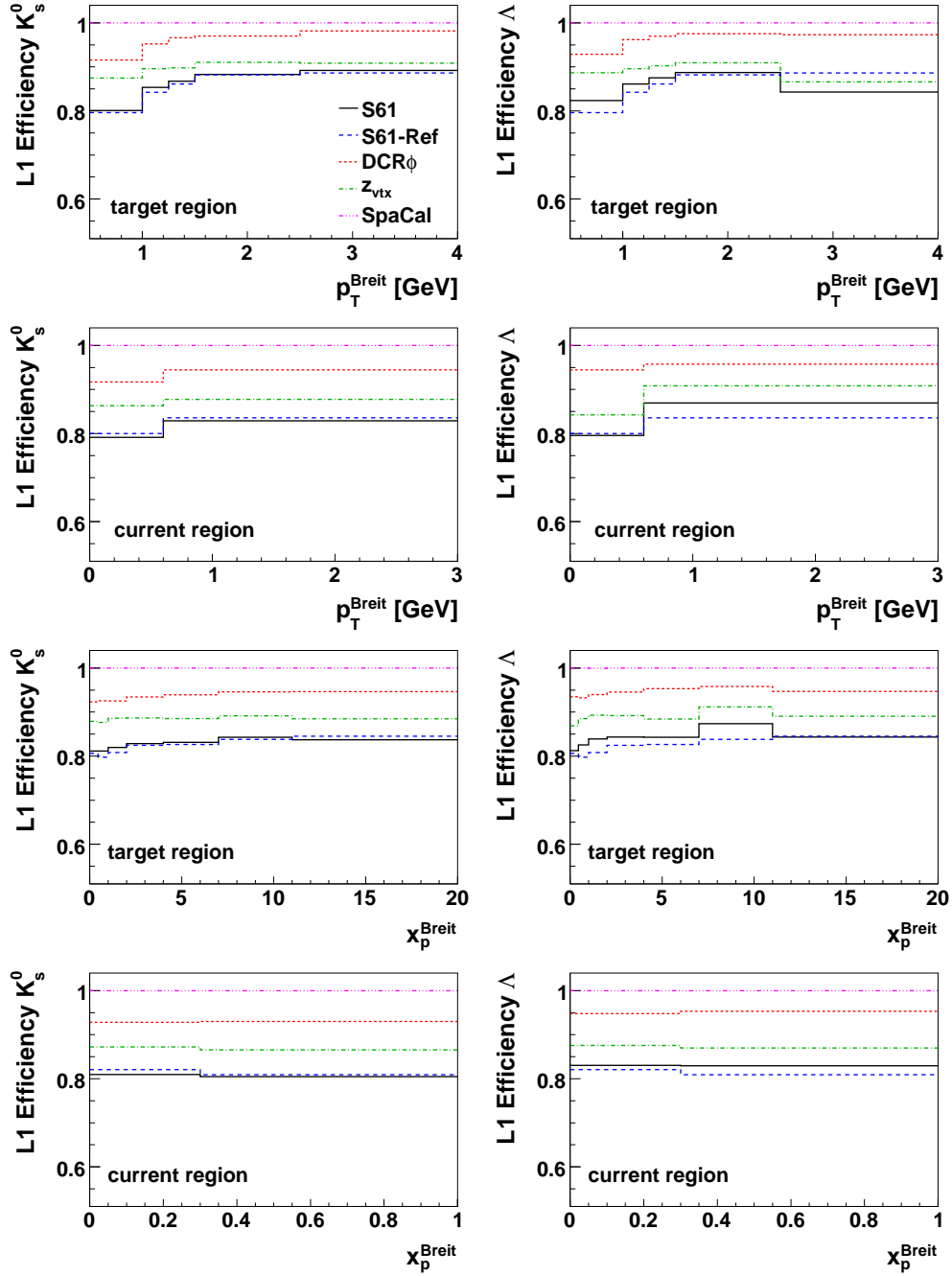
Figure 6.6: The trigger efficiencies ϵ_{trig} for K_s^0 mesons (left column) and Λ baryons (right column) in the Breit frame as a function of the kinematic variables p_T^{Breit} and x_p^{Breit} in the target and current hemisphere. Shown are the total efficiencies for the two monitor sets (S04, S71), labeled "S61" and (S0, S67), labeled "S61-Ref" and the contributions from the different trigger elements.

6.2.3 Correction to Born Level

For events with initial or final state radiation, the reconstructed energy and momentum of the scattered electron are possibly shifted. This leads for example to events being reconstructed in the wrong bin. The cross-sections are corrected for these effects by introducing the factor:

$$1 + \delta_{QED} = \frac{N_{gen}(V^0)^{rad}}{N_{gen}(V^0)^{non-rad}} \cdot \frac{\mathcal{L}^{non-rad}}{\mathcal{L}^{rad}}, \tag{6.5}$$

transforming the measured cross-sections to non-radiative level. Here, $N_{gen}(V^0)^{rad(non-rad)}$ denotes the number of generated V^0 particles from a simulated sample where radiative corrections are included (excluded) and $\mathcal{L}^{rad(non-rad)}$ the luminosity of the simulated samples. The radiative correction factors are determined from the CDM and from the MEPS samples. For the inclusive measurements the correction amounts to 6.6 % and 4.1 % for the K_s^0 and Λ case, respectively (see also table 6.1). For the differential cross-sections this factor is calculated for each bin. The correction factors δ_{QED} are displayed in figure 6.7 to 6.9 for all variables under investigation. Shown are the predictions from the CDM and the MEPS samples.
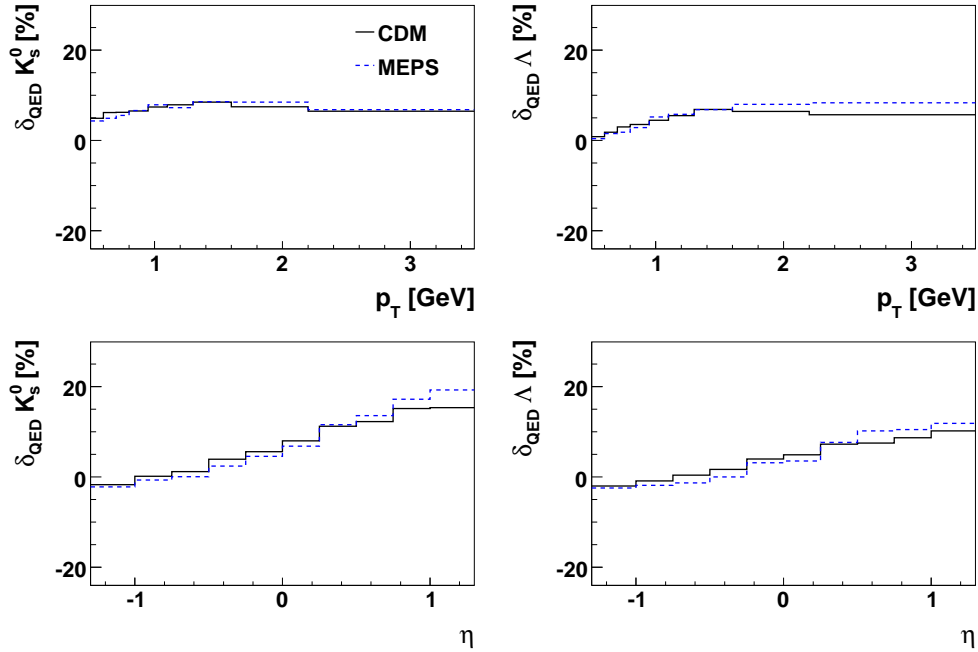
Figure 6.7: The radiative correction factors δ_{QED} for K_s^0 mesons (left column) and Λ baryons (right column) as a function of the kinematic variables $p_T(V^0)$ and $\eta(V^0)$.
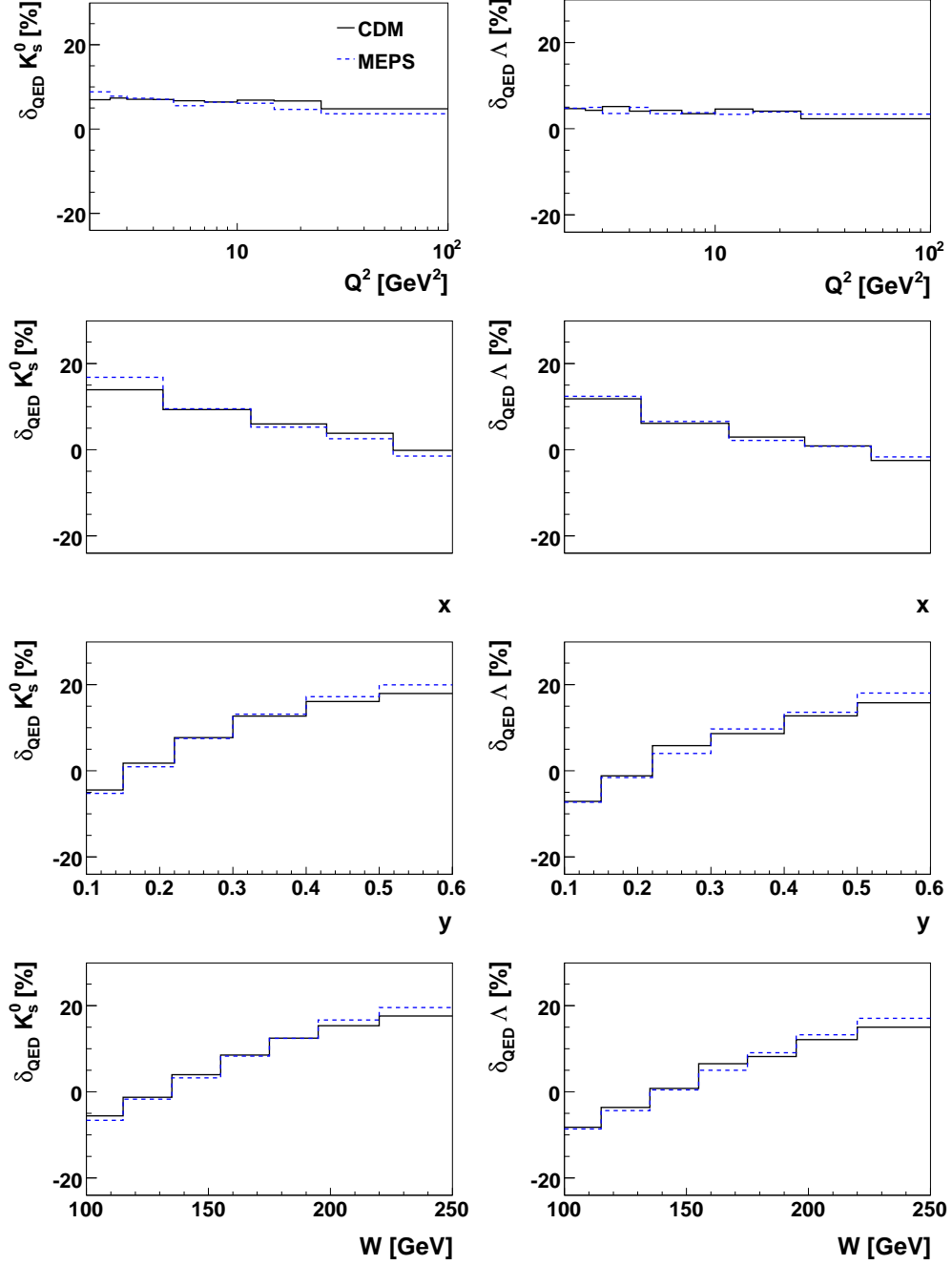
Figure 6.8: The radiative correction factors δ_{QED} for K_s^0 mesons (left column) and Λ baryons (right column) as a function of the event variables Q^2, x, y and W.
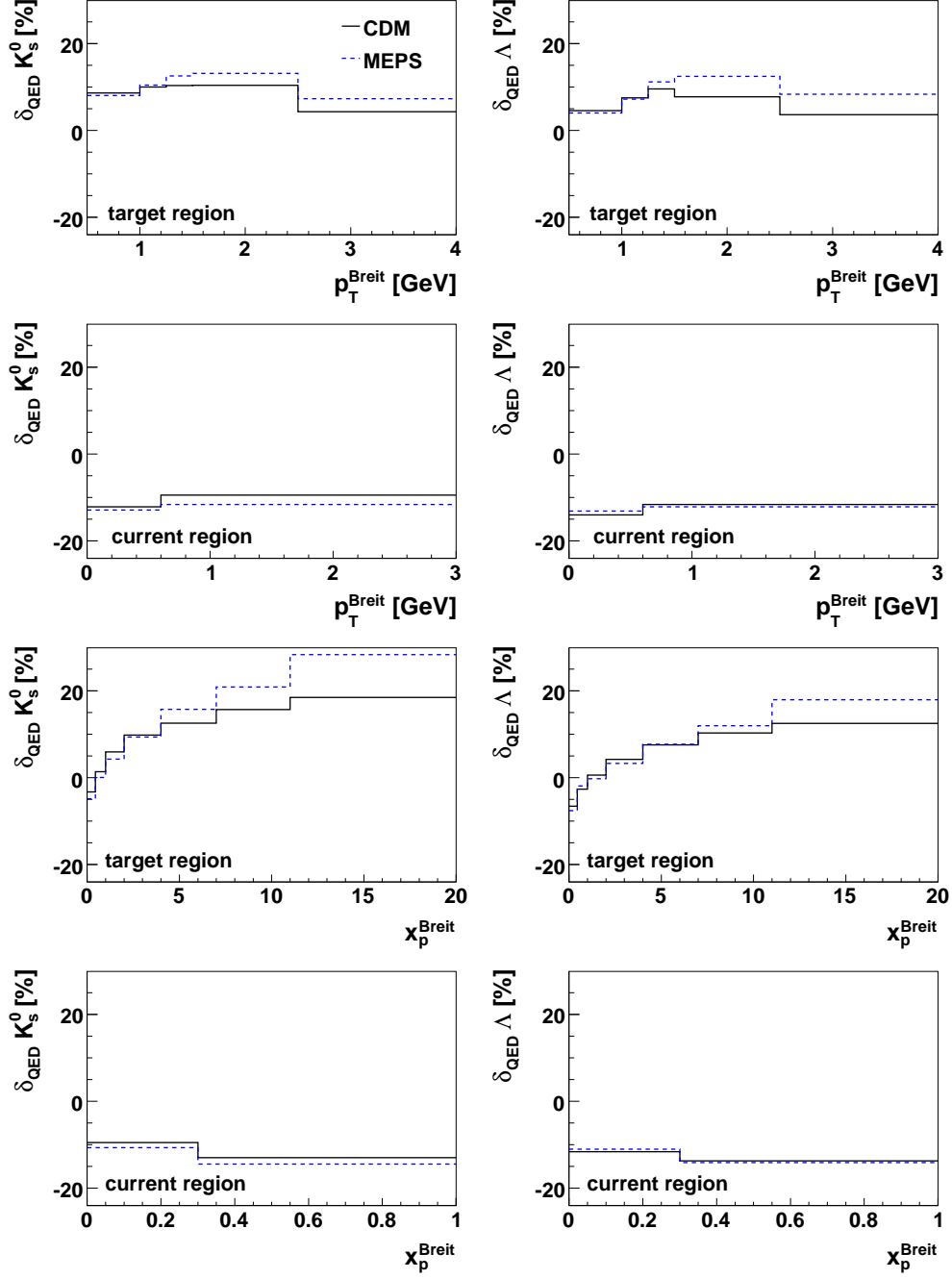
Figure 6.9: The radiative correction factors δ_{QED} for K_s^0 mesons (left column) and Λ baryons (right column) in the Breit frame as a function of the kinematic variables p_T^{Breit} and x_p^{Breit} in the target and current hemisphere.

Table 6.1: The correction factors used for the measurement of the inclusive K_s^0 and Λ cross-sections. Quoted are the reconstruction efficiency (ϵ_{rec}) and the radiative corrections (δ_{QED}) obtained from the CDM and the MEPS simulation and the trigger efficiency (ϵ_{trig}) as extracted from the data.

	K_s^0		Λ	
	CDM	MEPS	CDM	MEPS
ϵ_{rec} [%]	33.3	33.1	19.5	19.1
δ_{QED} [%]	6.6	6.2	4.1	3.9
ϵ_{trig} [%]	81.8		83.7	

6.3 Migration Effects

For the measurement of the differential cross-sections the continuous spectra of a variable is divided into discrete bins. Thereby events can be reconstructed in the wrong bin because of the finite resolution of the detector or for example because of QED effects as described above. This effect is called migration. The correction of the data which is done bin-wise (see section 6.2) corrects for such effects. Nevertheless, for a reliable measurement these migration effects have to be kept small, which is ensured by choosing an appropriate bin size: the larger the bin size, the smaller are the migration effects. On the other hand, the differential cross-sections should be measured in as many bins as possible. The bin size of all variables is chosen to fit these two conflicting requirements as well as possible.

The migration effects are kept small if the bin size is significantly larger than the resolution of the corresponding variable. The resolution of a variable X is defined as the width of the distribution of:

$$R = \frac{X_{rec} - X_{gen}}{X_{gen}}, \tag{6.6}$$

where X_{rec} and X_{gen} denotes the reconstructed and the generated value of the variable X, respectively and is obtained by a Gaussian fit to this distribution. The resolution of all variables are shown in figure 6.10 and 6.11. In the present work the resolution is in general better than 10 %. Worse resolutions are observed for the low y and therefore also for the low W region which can be explained by the properties of the electron method for the reconstruction of the events variables, see section 4.1.2.2. This effected is accounted for by a larger bin size for the first y-bin. The resolution properties are very similar for the K_s^0 and Λ particles with exception of the p_T dependency which reflects the different decay kinematics: at low transverse momenta, the resolution of the Λ baryons is worse because in this region the pion tends to reach very low p_T and therefore experience more multiple interactions than the pions form the K_s^0 decays.

The migration effects are controlled by the distribution of the purity (P) and the stability
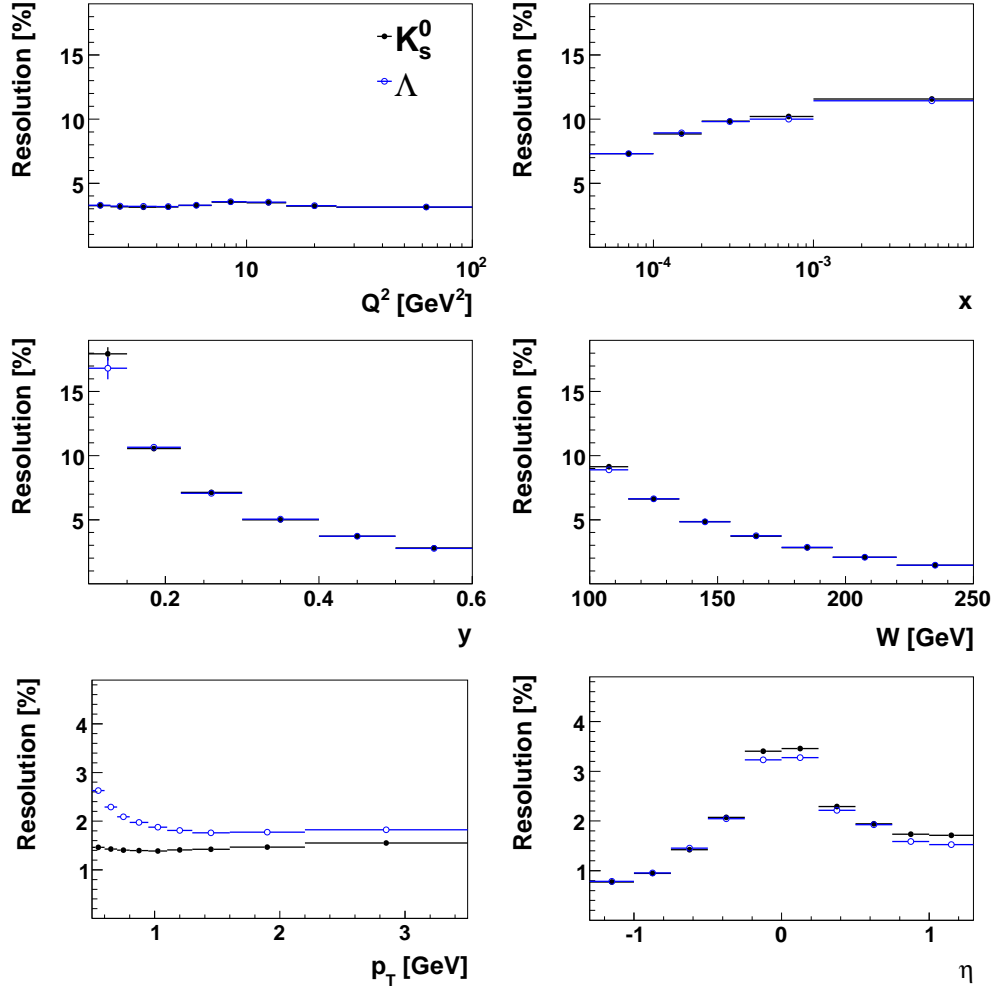
Figure 6.10: The resolution of the event variables Q^2, x, y and W as well as of the kinematic variables $p_T(V^0)$ and $\eta(V^0)$. The black (solid) circles shows the resolution for the K_s^0 mesons while the blue (open) circles represents the Λ baryons.

(S), given by:

$$P \quad = \quad \frac{N_{rec\&\&gen}^{MC}(i)}{N_{rec}^{MC}(i)} \tag{6.7}$$

$$S \quad = \quad \frac{N_{rec\&\&gen}^{MC}(i)}{N_{gen}^{MC}(i)}, \tag{6.8}$$

where $N_{rec\&\&gen}^{MC}(i)$ denotes the number of events that are generated and reconstructed in the same bin i while $N_{rec(gen)}^{MC}(i)$ are the number of events that are reconstructed (generated) in bin i but possibly generated (reconstructed) in another bin $j \neq i$. The migration into (out of) the bin is therefore given by P (S). The corresponding distributions are presented in figure 6.12 to 6.14. The purity and stability is extracted from the CDM sample. In general they are well above $80\,\%$ confirming that migration effects for the chosen bin sizes are small.
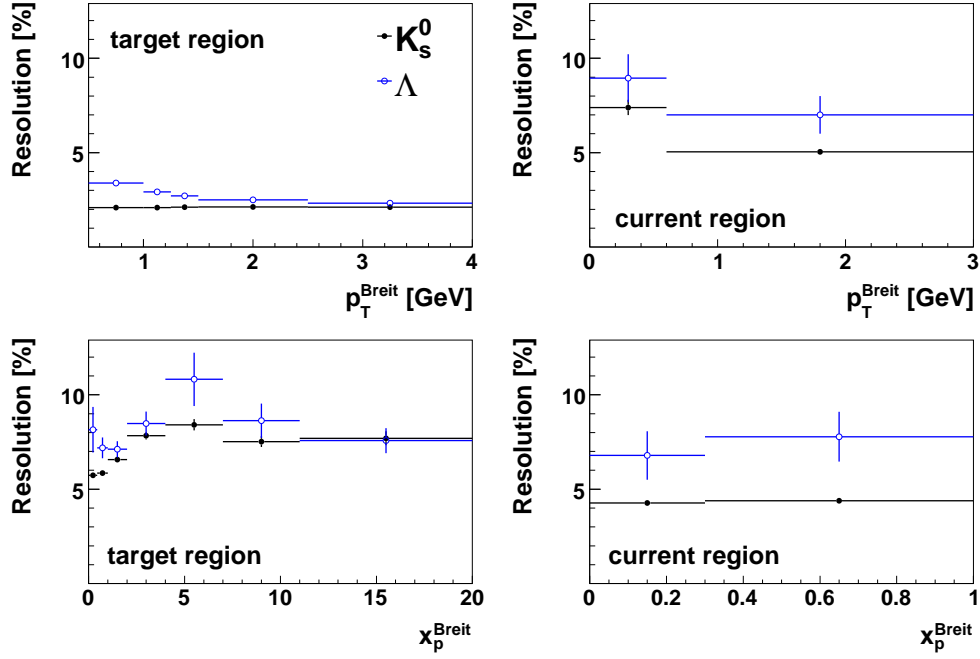
Figure 6.11: The resolution of the Breit frame variables p_T^{Breit} and x_p^{Breit}. The black (solid) circles shows the resolution for the K_s^0 mesons while the blue (open) circles represents the Λ baryons.
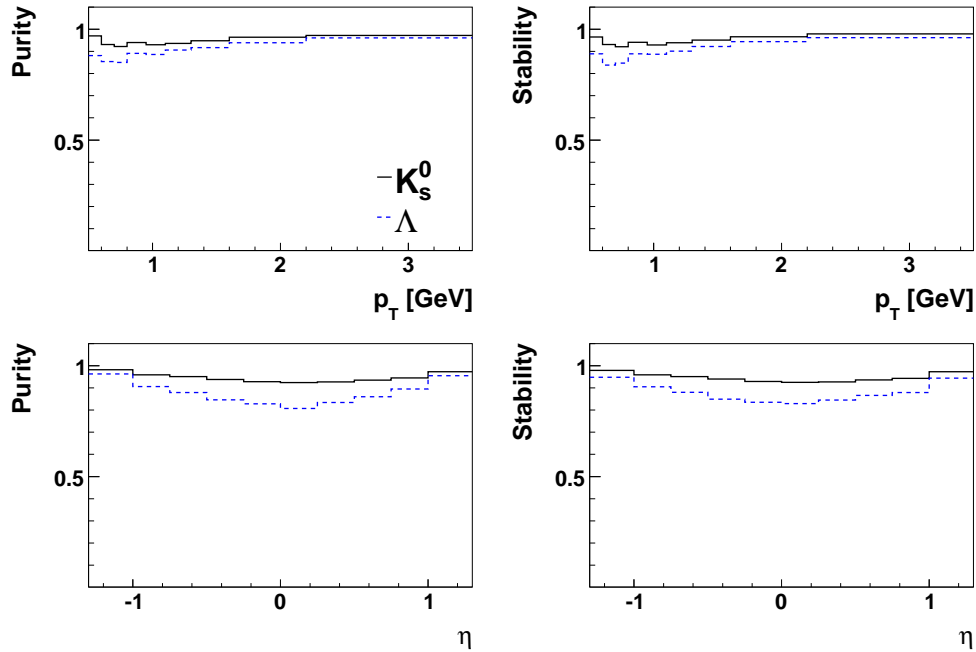
Figure 6.12: The purity (left column) and stability (right column) for K_s^0 mesons (black, solid line) and Λ baryons (dashed, blue line) as a function of the kinematic variables $p_T(V^0)$ and $\eta(V^0)$.
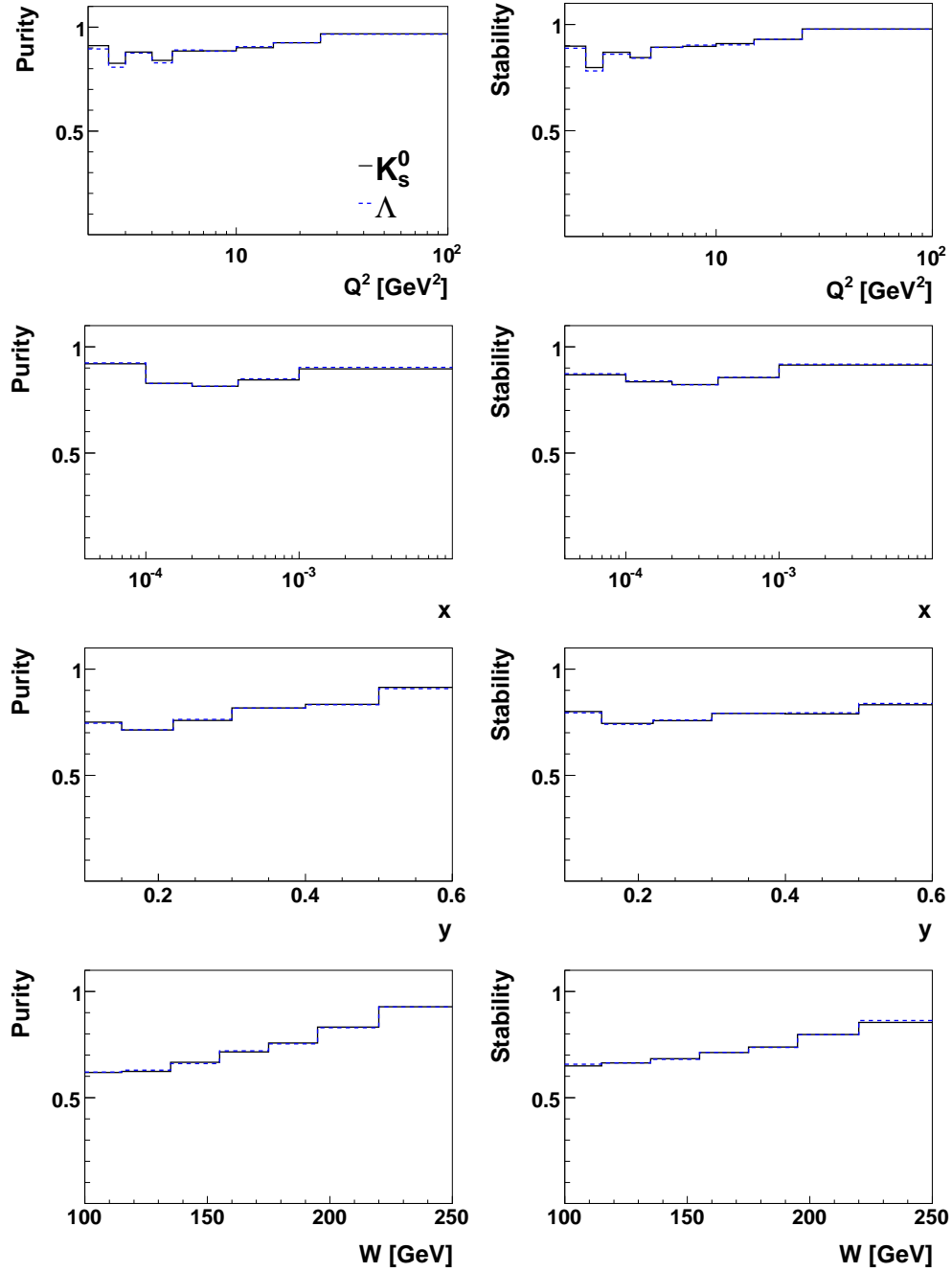
Figure 6.13: The purity (left column) and stability (right column) for K_s^0 mesons (black, solid line) and Λ baryons (dashed, blue line) as a function of the event variables Q^2, x, y and W.
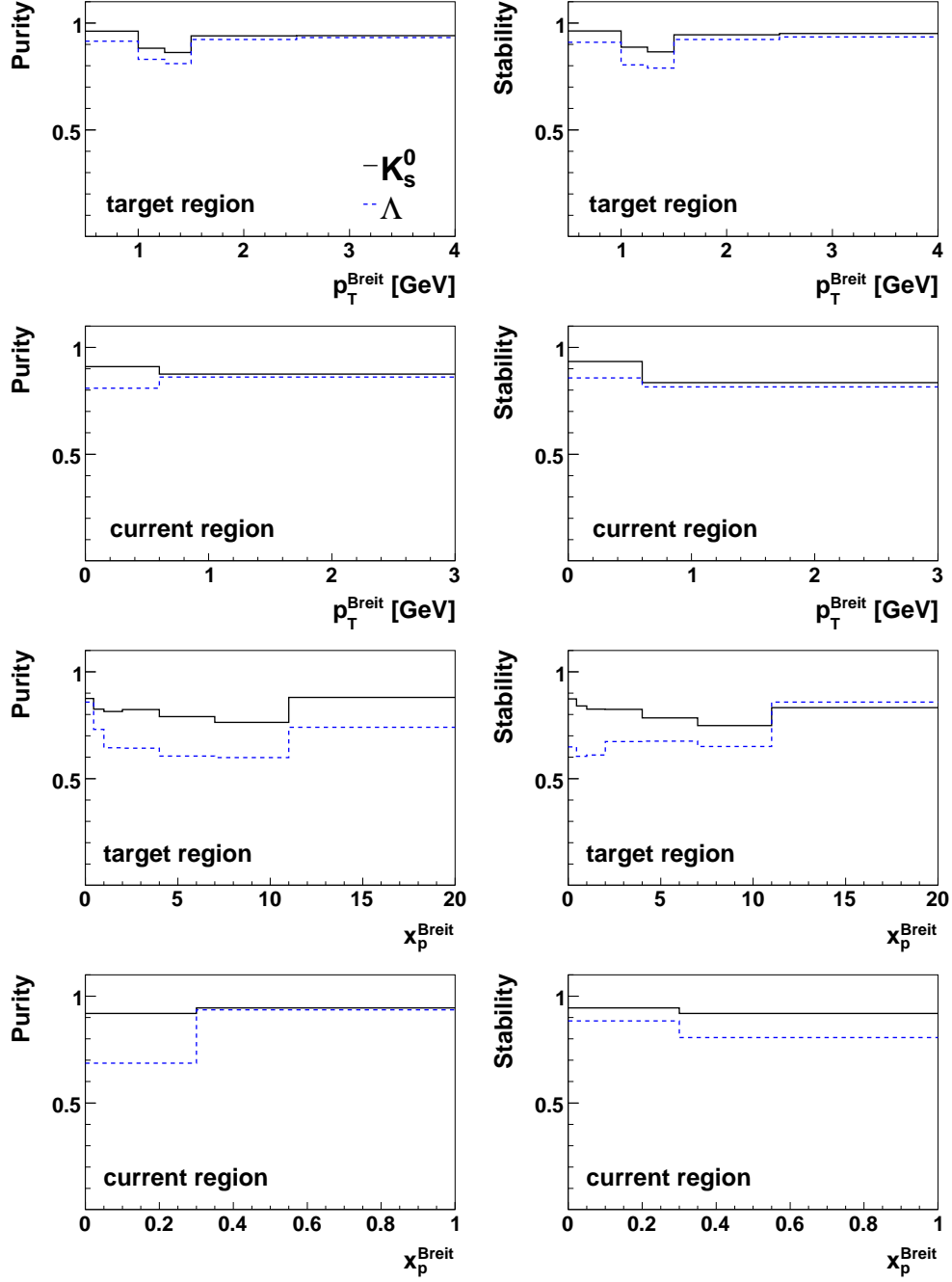
Figure 6.14: The purity (left column) and stability (right column) for K_s^0 mesons (black, solid line) and Λ baryons (dashed, blue line) as a function of the kinematic variables p_T^{Breit} and x_p^{Breit} in the target and current hemisphere.

6.4 Control Distributions

The distributions obtained from the simulated sample should describe the data as well as possible. However, since the corrections are applied bin wise, a perfect agreement is not a prerequisite for the extraction of the cross-sections.

The distributions of all variables used for the investigation of the K_s^0 and Λ production are compared to the predictions obtained from the CDM and the MEPS Monte Carlo samples (see section 2.5.1). In order to be independent of the background, the number of V^0 particles is obtained by a fit with the function F defined in equation 5.11 to the mass spectra in each bin. All distributions within this section show the uncorrected number of V^0 particles, i.e. no correction of detector effects is applied. For all figures the total number of V^0 particles is normalised to one in order to compare the shapes. Overlaid to the data points are the distributions from the CDM and MEPS sample after the reweighting (see section 4.1.3). For the CDM sample the spectra are also shown for the raw distributions (i.e. without the re-weighting).

In figure 6.15 the distributions for the kinematic variables p_T and η of the V^0 particles is shown. The transverse momentum is predicted softer than measured in data by both generators for the K_s^0 as well as for the Λ particles. The general features of the pseudorapidity distribution are well reproduced for the K_s^0 mesons while the rise towards the forward region in the Λ case is not described by the simulation. This could point to interesting, so far not understood aspects of the Λ production. In general, the CDM generator describes the kinematic variables of the V^0 particles better than the MEPS generator. As expected, the re-weighting of the Monte Carlo sample in (Q^2, x, z_{vtx}) has no effect on these spectra.

In figure 6.16 the distributions for the event variables Q^2, x, y and W are presented. After re-weighting, both generators are able to describe the Q^2 and x spectra. The discrepancies in describing the data is below 10% and is due to the energy calibration of the SpaCal. The effect of the re-weighting is most distinct at low values of Q^2 where it is as large as 50%. The y and W spectra are not well reproduced by the simulation which can again be traced back to deficits in describing the energy spectrum of the scattered electron. It seems that the re-weighting is even amplifying this effect. However, as shown in section 6.5 the cross-section measurement is not affected by the poor description of the data in certain regions of the phase space.

Finally, in figure 6.17 the distributions of the kinematic variables in the Breit frame are displayed. The spectra are well reproduced by both simulations. Nevertheless, the transverse momentum is again predicted too softly by both simulations and small deviations are especially observed in the x_p distribution in the current hemisphere for the Λ production while the K_s^0 production is described quite well.

Due to the bin-wise correction of the data, the deviations between the simulated and the measured spectra in certain regions of the phase space have only a very small effect on the cross-sections measurement, see section 6.5. This effect is accounted for in the systematic uncertainties.
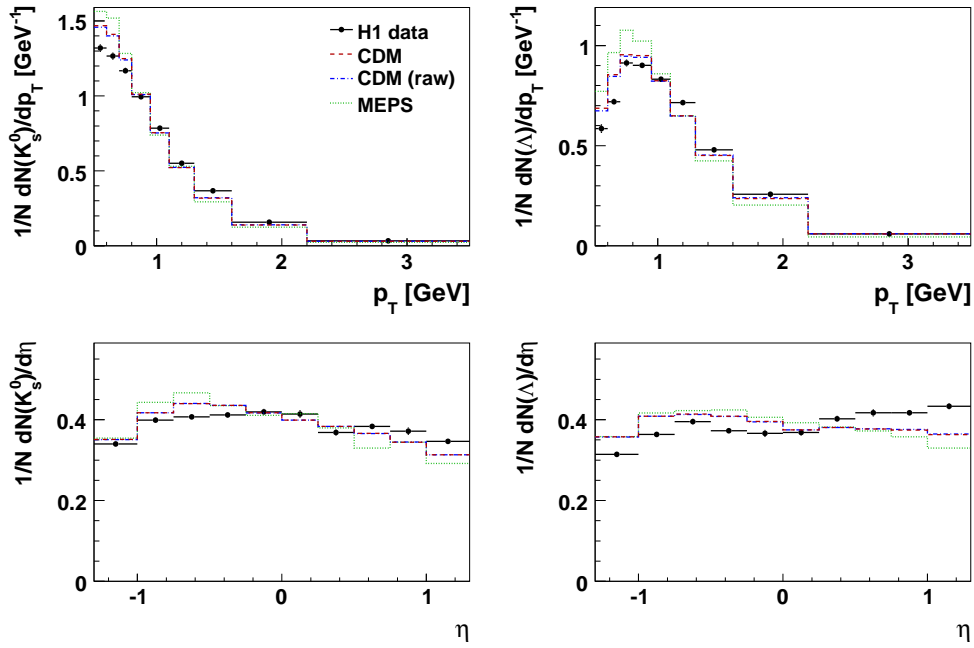
Figure 6.15: The reconstructed p_T (upper row) and η (lower row) spectra of the K_s^0 mesons (left column) and Λ baryons (right column) in data and simulation. Shown are the predictions from the CDM sample before (blue, dashed-dotted lines) and after (red, dashed lines) the re-weighting and from the MEPS sample with the re-weighting applied (green, dotted lines).
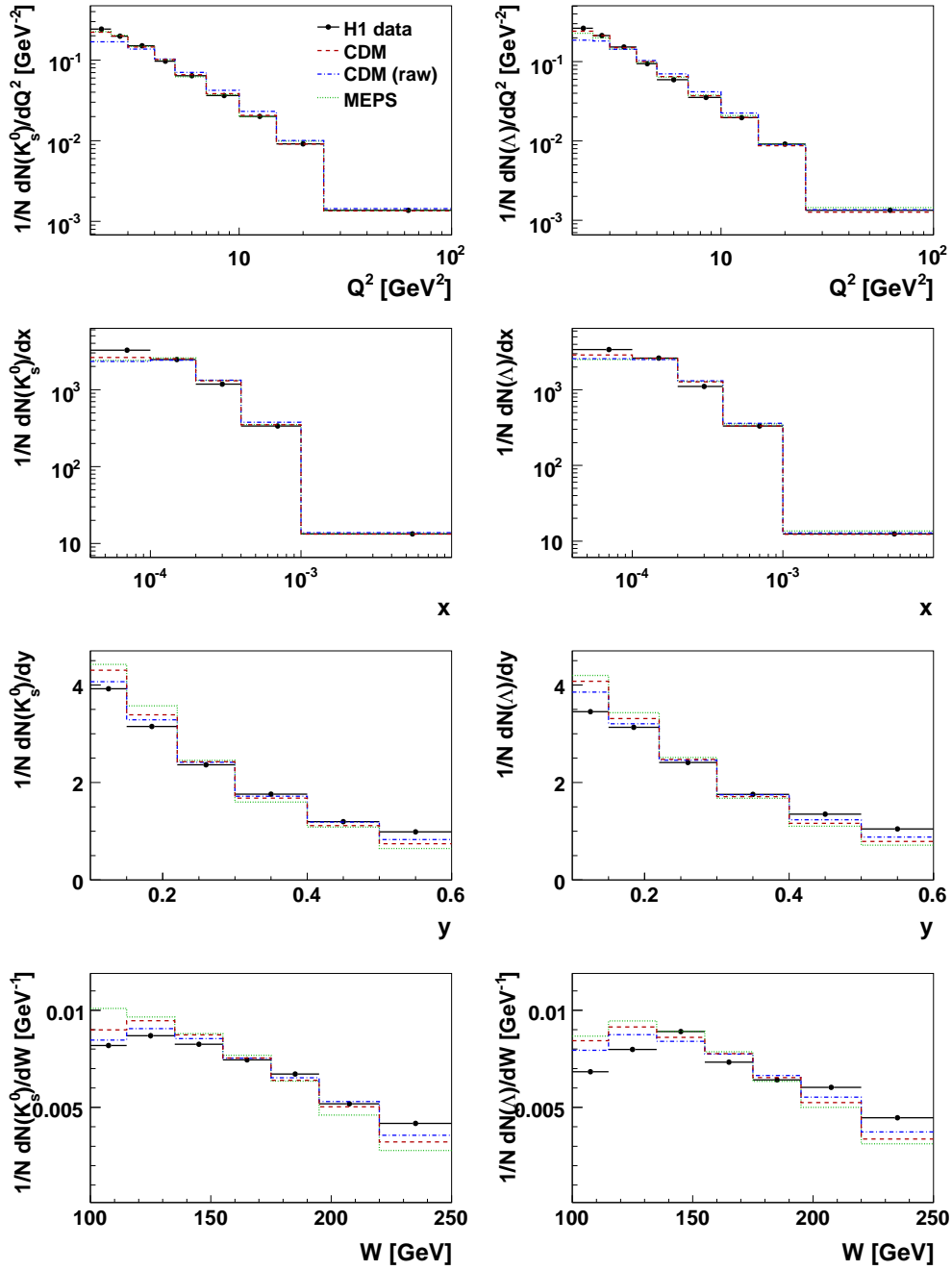
Figure 6.16: The reconstructed Q^2, x, y and W spectra of the K_s^0 mesons (left column) and Λ baryons (right column) in data and simulation. Shown are the predictions from the CDM sample before (blue, dashed-dotted lines) and after (red, dashed lines) the re-weighting and from the MEPS sample with the re-weighting applied (green, dotted lines).
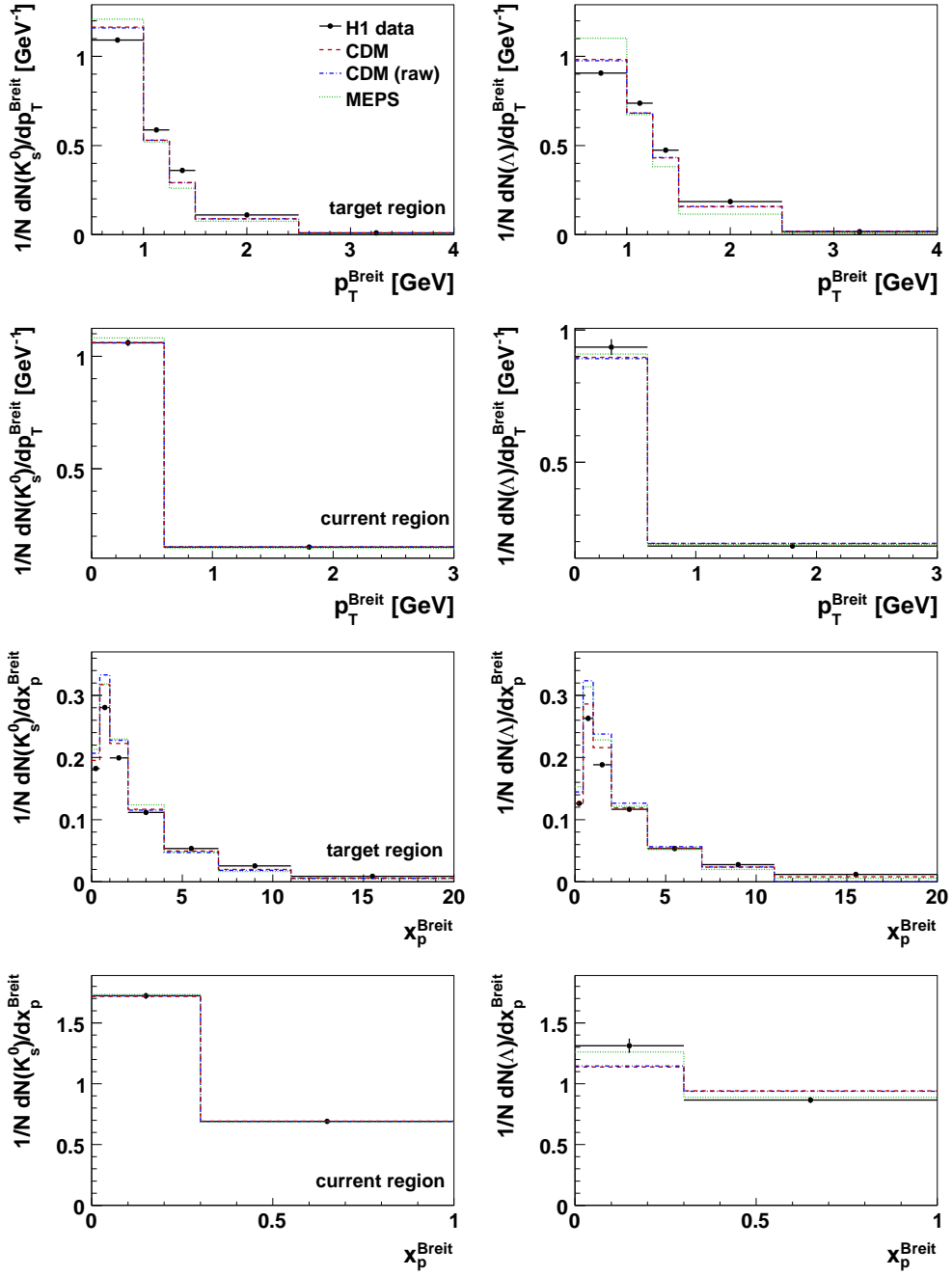
Figure 6.17: The reconstructed p_T^{Breit} and x_p^{Breit} spectra of the K_s^0 mesons (left column) and Λ baryons (right column) in the Breit frame for data and simulation. Shown are the predictions from the CDM sample before (blue, dashed-dotted lines) and after (red, dashed lines) the re-weighting and from the MEPS sample with the re-weighting applied (green, dotted lines).

6.5   Systematic Uncertainties

The effect on the cross-section measurement of the different systematic sources is stated as relative change in the cross-section by the corresponding variation V_i:

$$\Delta\,\sigma(V_i) = \frac{\sigma - \sigma(V_i)}{\sigma}, \tag{6.9}$$

where σ is the measured cross-section and $\sigma(V_i)$ the cross-section with the variation of condition V_i. If not stated otherwise, the systematic uncertainties are studied with the CDM Monte Carlo simulation. A summary of all effects on the inclusive cross-sections is given in table 6.2. For the differential cross-sections, the systematic uncertainties are taken into account bin wise and are displayed exemplarily in figure 6.20 as a function of $p_T(V^0)$. The corresponding figures for the other variables are given in appendix C.

The variation of all V^0 and track selection criteria within a reasonable range are studied. The change in the cross-sections implied by these variations are found to be negligible with respect to the statistical uncertainty and are not considered further.

6.5.1   Energy Measurement of the Scattered Electron

The energy scale in the SpaCal measurements is known to $1\,\%$, except for the lowest Q^2 bin $(2 < Q^2 < 2.5\,\mathrm{GeV}^2)$ where the uncertainty on the energy measurement is $2.5\,\%$ (see section 4.1.4.1). The change of the energy scale by $+1\,\%$ $(-1\,\%)$ changes the inclusive K_s^0 cross-section by $-3.5\,\%$ $(+3.3\,\%)$ and the Λ cross-section by $-3.1\,\%$ $(+2.8\,\%)$. Therefore, the ratio of the Λ to the K_s^0 production cross-section, $R(\Lambda/K_s^0)$, is in first order insensitive to this variation. This holds also for the differential cross-sections, see figure 6.20.

6.5.2   Measurement of the Polar Angle of the Scattered Electron

The systematic uncertainty in the measurement of the polar angle of the scattered electron is 1 mrad. The resulting uncertainty on the inclusive K_s^0 cross-section is $\pm 1.4\,\%$ and on the Λ cross-section $\pm\,1.5\,\%$. The uncertainty on $R(\Lambda/K_s^0)$ is therefore negligible.

6.5.3   Branching Ratios

The branching ratios (see equation 6.2) are only known with a finite precision [26]:

$$BR(K_s^0 \to \pi^+\,\pi^-) = (0.6920 \pm 0.0005)\,\% \tag{6.10}$$
$$BR(\Lambda \to p\,\pi) = (0.639 \pm 0.005)\,\% \tag{6.11}$$

The resulting uncertainty on the K_s^0 and Λ cross-section is therefore $0.07\,\%$ and $0.78\,\%$, respectively. For the differential cross-sections these uncertainties are negligible with respect to all other errors and are not considered.

6.5.4   Luminosity Measurement

The luminosity measured with the Bethle-Heitler process is known with a precision of $1.5\,\%$ [147]. For the production ratio this uncertainty cancels entirely.

6.5.5 Signal Extraction

The uncertainty in the signal extraction is discussed in section 5.2.2: For the inclusive cross-section measurements this amounts to $0.6\,\%$ and $1.4\,\%$ for the K_s^0 and Λ case, respectively. For the differential cross-sections this uncertainty is typically in the order of $2-3\,\%$ for the K_s^0 reconstruction and $3-4\,\%$ for the Λ reconstruction. However, in certain bins where the determination of the background is more complicated (like the low p_T region), it may vary up to $7\,\%$ and therefore become the main source of systematic uncertainties for those bins. For the ratio $R(\Lambda/K_s^0)$, these uncertainties are assumed to be independent.

6.5.6 Determination of the Correction Factors

The correction factors comprises the reconstruction efficiency, the trigger efficiency and the correction for QED effects as described in section 6.2.

For the uncertainty due to the *reconstruction efficiency and the QED correction*, $50\,\%$ of the difference of $\epsilon_{rec} \cdot (1 + \delta_{QED})$ extracted from the CDM and the MEPS simulation is taken [1]. For the inclusive K_s^0 and Λ cross-section this amounts to $\pm 0.35\,\%$ and $\pm 1.16\,\%$, respectively. For the differential cross-sections this is typically below $2\,\%$, see figure 6.20 and appendix C. For the ratio $R(\Lambda/K_s^0)$ these two uncertainties are considered to be independent and therefore added in quadrature.

The uncertainty due to the *trigger efficiency* (which is determined from data) is taken to be the difference in the efficiency predicted by the two different monitor trigger sets (see section 6.2.2). For the determination of this uncertainty the difference of the two monitor sets is not taken into account bin-wise but a fit of this deviation in the variables Q^2, y, p_T and η with a Gaussian function is applied [2], see figure 6.18. This method ensures that the (statistical) fluctuations in certain bins are not taken into account and that the statistical uncertainties of the measurement are not considered twice. The uncertainty related to the trigger efficiency is given by the mean value (μ) and the width (σ) of the fitted Gaussian function: $\mu \pm \sigma$. For the K_s^0 case this amounts to $-0.39\,\%$ $+0.85\,\%$ and for the Λ case to $-1.39\,\%$ $+1.04\,\%$. For the ratio $R(\Lambda/K_s^0)$ these two uncertainties are treated independently and therefore added in quadrature [3].

The uncertainty due to charged particle *track reconstruction* is $2\,\%$ per track for the kinematic range considered. This number is provided centrally (like the luminosity) and is estimated by looking at tracks that curl up within the CJC. The total uncertainty on the K_s^0 and Λ cross-section is therefore $4\,\%$ and is applied as a constant factor to the differential cross-sections. For the ratio $R(\Lambda/K_s^0)$ the uncertainty caused by the pion track appearing in both decays is assumed to cancel. The systematic uncertainty on the ratio is therefore taken to be $2.0\,\%$.

6.5.7 Re-Weighting of the Simulated Distributions

The Monte Carlo distributions are re-weighted (see section 4.1.3) in order to achieve a better description of the data. The full differences in the cross-sections when using the re-weighted distributions instead of the bare ones are taken as systematic uncertainties. The re-weighting

---

[1] The uncertainty of the reconstruction of the single tracks is here not included and discussed separately.

[2] Here it is assumed that the trigger efficiencies in these variables are independent.

[3] This is a conservative approach since some effects of the trigger should cancel in the ratio.
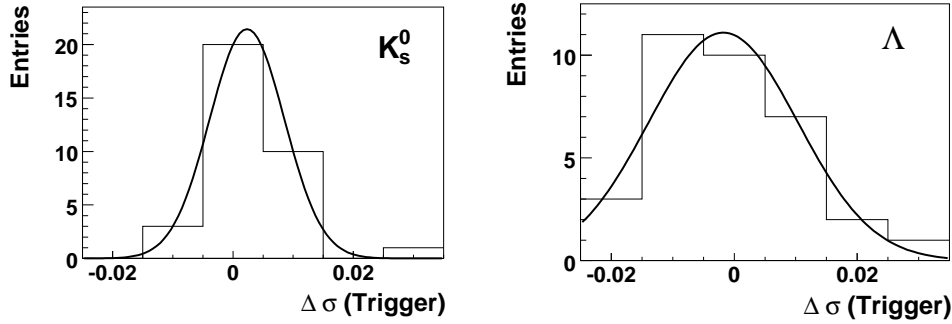
Figure 6.18: The uncertainty on the K_s^0 cross-section (left) and on the Λ cross-section (right) due to different monitor trigger sets. Shown is the relative deviation in the cross-section by exchanging the monitor trigger set for the variables Q^2, y, p_T and η. Overlaid on the data points are the results of a Gaussian fit to the distributions.

affects only the shape of the distributions and not the normalisation and has therefore no impact on the inclusive cross-sections but only a small one on the differential measurements, typically below 1 %.

6.5.8 Application of the L4 Weights in the Λ Case

The number Λ signal entries is extracted from the mass spectra where the L4 weights are not applied but multiplied by the mean L4 weight (see section 5.2.1). For the differential distributions, the latter one is the mean values of the L4 weights of all Λ candidates in the corresponding bin. Due to the trigger level four strategy the distribution of the L4 weights should have a well defined shape[4]. But as they are extracted from statistically limited data, fluctuations can occur. In order to be independent of these fluctuations, the distribution of the L4 weights is fitted with smooth functions which are subsequently used to correct the data. The distribution of the L4 weights is shown in figure 6.19 together with the fitted functions. The distributions in the current hemisphere which have only two bins are not fitted.

This procedure implies an additional uncertainty on the Λ cross-sections which is taken to be the full difference of the measured L4 weights and the values extracted from the fit. They are typically below 2 %.

---

[4]They should for example be monotonically decreasing with Q^2 and also with $p_T(\Lambda)$.
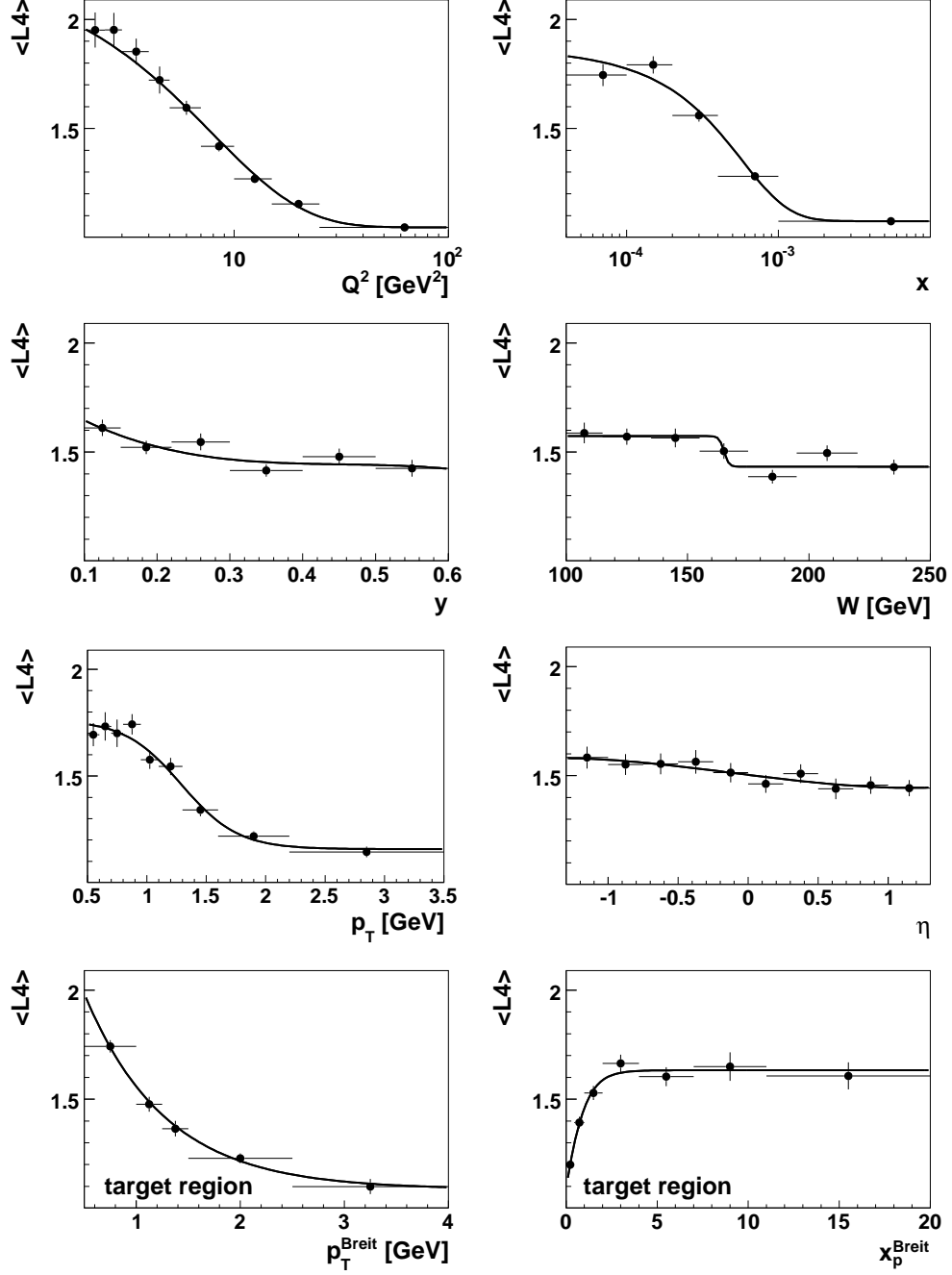
Figure 6.19: The distribution of the mean L4 weights for all relevant variables. Shown are the data points (full dots) and the result of the fit (solid lines).

6.5.9   Summary of the Systematic Uncertainties

A summary of all systematic effects relevant for the inclusive cross-section measurement are given in table 6.2. For the comparison of the differential cross-sections with theory predictions the uncertainties are divided into two sets. One contains all uncertainties that depend on any of the variables under investigation. This comprises the uncertainty due to the energy and angle measurement of the electron, the signal extraction, the model dependency, the re-weighting of the simulated distributions and the application of the L4 weights in the Λ case. This set of uncertainties is referred to as "correlated". These uncertainties are shown exemplarily in figure 6.20 as a function of the transverse momentum of the particles. The uncertainties being common for all bins comprises the branching ratios, the trigger efficiency, the luminosity measurement and the track reconstruction. They are referred to as "uncorrelated" and shown as bands in the result section.

Table 6.2: The different systematic sources, their variation and their effect on the inclusive cross-sections as well as on the ratio. All numbers are given in %.

Source	Variation	$\Delta\sigma(K_s^0)$	$\Delta\sigma(\Lambda)$	$R(\Lambda/K_s^0)$
E_e'	$\pm 1\%$	$-3.5 + 3.3$	$-3.1 + 2.8$	$-$
θ_e	$\pm 1\,\mathrm{mrad}$	± 1.4	± 1.5	$-$
signal extraction	$\frac{N^{fit} - N^{count}}{N^{fit}}$	± 0.6	± 1.4	± 1.5
model	$0.5 * \frac{\epsilon_{rec}^{CDM} - \epsilon_{rec}^{MEPS}}{\epsilon_{rec}^{CDM}}$	± 0.4	± 1.2	± 1.2
trigger efficiency	$\frac{\epsilon_{trig}^{MTset1} - \epsilon_{trig}^{MTset2}}{\epsilon_{trig}^{MTset1}}$	$-0.4 + 0.9$	$-1.4 + 1.0$	$-1.6 + 1.1$
track reco	$2.0\,\%$ per track	± 4.0	± 4.0	± 2.0
luminosity		± 1.5	± 1.5	$-$
branching ratio		$< \pm 0.1$	± 0.8	± 0.8
Total systematic uncertainty		$-5.8 + 5.6$	$-6.0 + 5.8$	$-3.3 + 3.1$
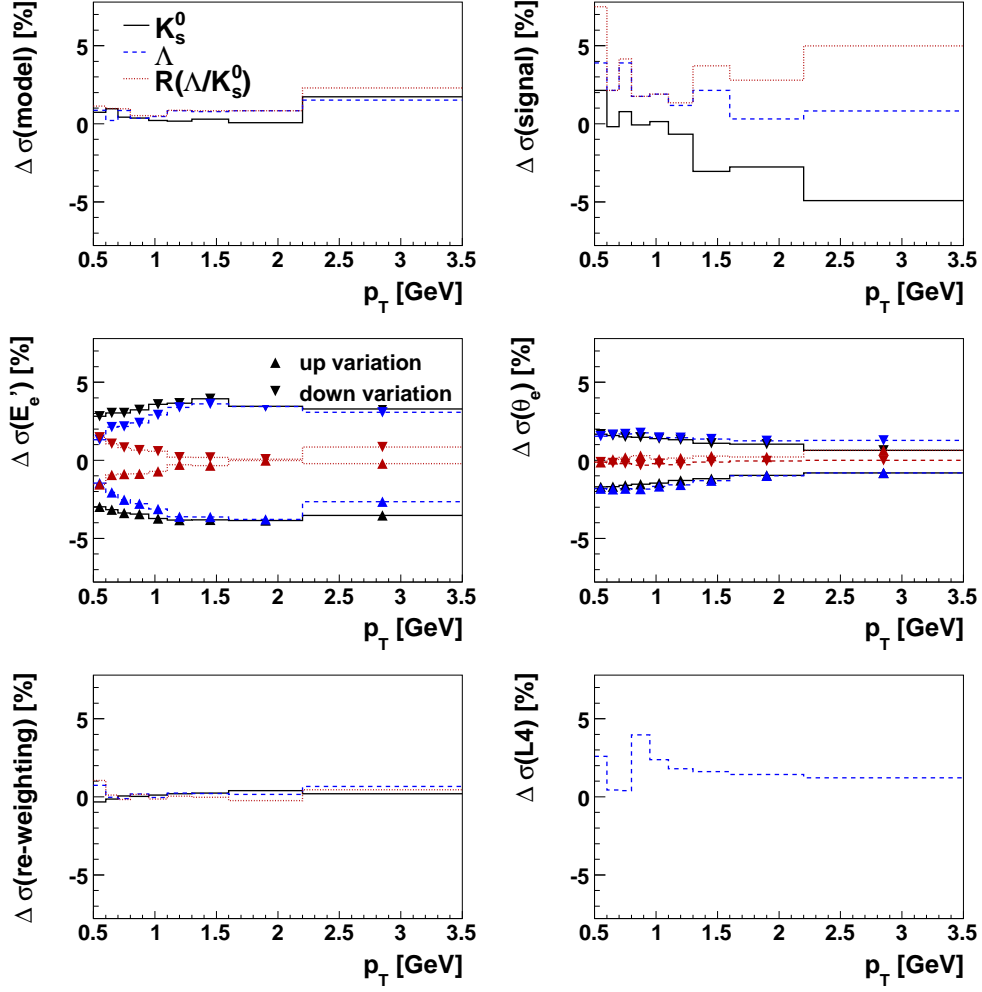
Figure 6.20: The effect of the different systematic sources on the differential cross-sections in p_T for the K_s^0 mesons (solid, black lines) for the Λ baryons (blue, dashed lines) and for the ratio Λ/K_s^0 (red, dotted lines). For further explanation see text.

6.6 Results of the Inclusive Cross-Section Measurements

The inclusive K_s^0 and Λ production cross-sections σ_{vis} are measured in the experimentally accessible kinematic region given by $2 < Q^2 < 100\,\mathrm{GeV}^2$ and $0.1 < y < 0.6$, for the ranges $0.5 < p_T(V^0) < 3.5\,\mathrm{GeV}$ and $|\eta(V^0)| < 1.3$. The K_s^0 cross-section is found to be

$$\sigma_{vis}(ep \rightarrow e'K_s^0 X) = 21.18 \pm 0.09(\text{stat.})^{+1.19}_{-1.23}(\text{syst.})\ \mathrm{nb}. \qquad (6.12)$$

The measurement is in good agreement with the expectation of $\sigma = 21.77$ nb [5] obtained from leading order Monte Carlo simulation.

The production of the sum of Λ and $\overline{\Lambda}$ baryons is measured in the same kinematical region and is found to be

$$\sigma_{vis}(ep \rightarrow e'[\Lambda + \overline{\Lambda}]X) = 7.88 \pm 0.10(\text{stat.})^{+0.45}_{-0.47}(\text{syst.})\ \mathrm{nb}, \qquad (6.13)$$

in agreement with the expectation of $\sigma = 7.94$ nb from the CDM generator.

The individual Λ and $\overline{\Lambda}$ production rates (here the charge conjugated states are explicitly excluded) are measured to be

$$
\begin{aligned}
\sigma_{vis}(ep \rightarrow e'\Lambda X) &= 3.96 \pm 0.06(\text{stat.})^{+0.23}_{-0.24}(\text{syst.})\ \mathrm{nb} \\
\sigma_{vis}(ep \rightarrow e'\overline{\Lambda} X) &= 3.94 \pm 0.07(\text{stat.})^{+0.23}_{-0.24}(\text{syst.})\ \mathrm{nb}
\end{aligned}
\qquad (6.14)
$$

and are therefore found to be consistent with each other within the statistical accuracy. The measurement is also in agreement with the CDM predictions of $\sigma = 3.97$ nb for both of the individual Λ and $\overline{\Lambda}$ cross-sections.

The ratio of the inclusive baryon to meson production is determined to

$$\frac{\sigma_{vis}(ep \rightarrow e'[\Lambda + \overline{\Lambda}]X)}{\sigma_{vis}(ep \rightarrow e'K_s^0 X)} = 0.372 \pm 0.005(\text{stat.})^{+0.011}_{-0.012}(\text{syst.}), \qquad (6.15)$$

in agreement with the prediction of 0.365 of the CDM model.

All measured cross-sections values are summarised and compared to further theory predictions in table 6.3.

6.7 Constraints from the Inclusive Measurements on the LUND Parameters

In this section the reduction of the Lund parameters λ_s, λ_{qq} and λ_{sq} (see equations 2.23, 2.24 and 2.25) by the measured data is illustrated. A complete determination of these parameters is only possible with a global fit to more redundant input data (see for example [72]) and is beyond the scope of this work. Nevertheless, the data presented within this work can be used as a main ingredient for such a combined study.

The parameters that affect the K_s^0 and Λ production are the strangeness suppression factor λ_s, the diquark suppression factor λ_{qq} and the strange diquark suppression factor λ_{sq}.

---

[5]If not stated otherwise, theory predictions are obtained by the CDM generator with the ALEPH-tuned JETSET parameters and with the CTEQ6L PDF set.

Table 6.3: Summary of the measured inclusive cross-sections together with theory predictions for different values of the strangeness suppression factor λ_s. For all theory predictions the CTEQ6L PDF set has been used.

	Data	CDM			MEPS		
λ_s	$---$	0.22	0.286	0.3	0.22	0.286	0.3
$\sigma_{vis}(K_s^0)$ [nb]	$21.18 \pm 0.09^{+1.19}_{-1.23}$	19.00	21.77	22.31	21.05	23.91	25.74
$\sigma_{vis}(\Lambda + \overline{\Lambda})$ [nb]	$7.88 \pm 0.10^{+0.45}_{-0.47}$	6.83	7.94	8.12	6.95	7.96	8.60
$\frac{\sigma_{vis}(\Lambda+\overline{\Lambda})}{\sigma_{vis}(K_s^0)}$	$0.372 \pm 0.005^{+0.011}_{-0.012}$	0.359	0.365	0.364	0.330	0.333	0.334

Table 6.4: Summary of the measured inclusive cross-sections together with theory predictions for different PDF sets (see text). For all theory predictions the ALEPH-tuned JETSET parameters have been used (i.e. $\lambda_s = 0.286$).

	Data	CDM($\lambda_s = 0.286$)			MEPS($\lambda_s = 0.286$)		
$PDF set$	$---$	GRV	$CTEQ$	$H1$	GRV	$CTEQ$	$H1$
$\sigma_{vis}(K_s^0)$ [nb]	$21.18 \pm 0.09^{+1.19}_{-1.23}$	21.87	21.77	20.49	22.61	23.91	21.62
$\sigma_{vis}(\Lambda + \overline{\Lambda})$ [nb]	$7.88 \pm 0.10^{+0.45}_{-0.47}$	7.76	7.94	7.53	7.43	7.96	7.29
$\frac{\sigma_{vis}(\Lambda+\overline{\Lambda})}{\sigma_{vis}(K_s^0)}$	$0.372 \pm 0.005^{+0.011}_{-0.012}$	0.355	0.365	0.367	0.329	0.333	0.337

For this study 25 additional Monte Carlo sets have been generated with different values of λ_{qq} and λ_{sq} [6]:

$$\lambda_{qq} = \{0.05, 0.08, 0.1, 0.12, 0.15\}$$
$$\lambda_{sq} = \{0.2, 0.5, 0.6, 0.7, 0.9\}. \tag{6.16}$$

For all these sets the CDM generator was used with the PDF set CTEQ6L. In addition, several sets have been generated with CDM and MEPS using different values of λ_s. In both cases the other parameters are set to the values obtained by the ALEPH collaboration [72].

The dependency of the predicted K_s^0 and Λ cross-section on the parameters mentioned above is shown in figure 6.21 and confronted with the measurement. The main observations are:

1. The predicted K_s^0 and Λ cross-sections depend linearly on λ_s and the slope is approximately the same for both cases.

2. For the K_s^0 production the MEPS generator favours a lower λ_s than the CDM generator.

---

[6] Every of the λ_{qq} values is combined with each of the λ_{sq} values in order to form a Monte Carlo set.

3. The dependency of the predicted cross-sections on the PDF set is very similar for K_s^0 mesons and Λ baryons.

4. The predicted K_s^0 cross-section falls linearly with λ_{qq} while the Λ cross-section rises linearly with λ_{qq}.

5. The predicted K_s^0 cross-section is independent on the choice of λ_{sq} while the Λ cross-section rises linearly in λ_{sq}.
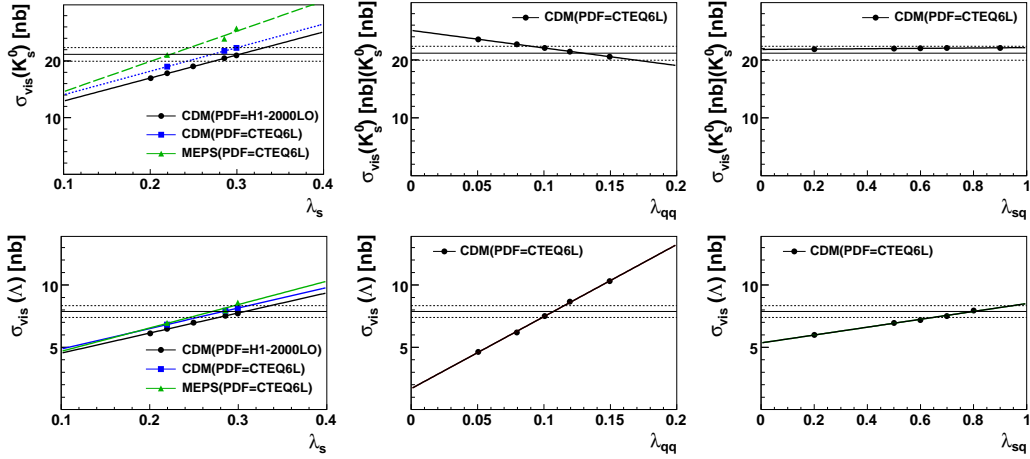
Figure 6.21: The dependency of the predicted K_s^0 (upper row) and Λ (lower row) cross-sections on: the parameter λ_s for the two models CDM and MEPS with the PDF set CTEQ6L and H1-2000LO (left column), the parameter λ_{qq} (for the CDM model, middle column) and the parameter λ_{sq} (for the CDM model, right column). For all other parameters the ALEPH-tune has been used. The vertical lines indicate the measured cross-section together with its total uncertainty (dashed lines).

6.7.1 Constraints implied by the Ratio $R(\Lambda/K_s^0)$

The points 1 and 3 in above list imply that the ratio of the Λ to the K_s^0 cross-section is independent of the strangeness suppression factor λ_s and also of the PDF set. This is also confirmed by the values presented in tables 6.3 and 6.4. Therefore this ratio provides data that can be used to constrain the other two parameters λ_{qq} and λ_{sq}. The dependency of the ratio (Λ/K_s^0) on the parameter λ_{qq} is enhanced with respect to λ_{sq} because of the opposed slopes in the K_s^0 and Λ case. All studies presented in the following are carried out for the CDM generator only. The ratio $\sigma_{vis}(ep \to e'\Lambda X)/\sigma_{vis}(ep \to e'K_s^0 X)$ predicted by the CDM generator is shown in figure 6.22 as a function of λ_{sq} for different values of λ_{qq}. The measured value and its uncertainty is indicated by the vertical lines. For a given λ_{qq} value, the λ_{sq} value and its uncertainty is determined by the intersection of the predicted curves with the data band. The resulting relation between λ_{sq} and λ_{qq} is displayed in figure 6.23 and summarised in table 6.5.

The point from the ALEPH-tune fits nicely into this distribution, indicating that the Lund parameters tuned from e^+e^- data are also applicable to ep data. The JETSET default value
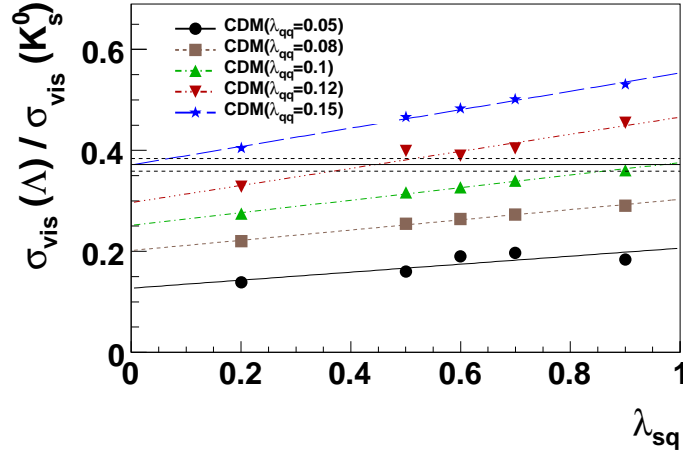
Figure 6.22: The ratio $R(\Lambda/K_s^0)$ as a function of the parameter λ_{sq} for different values of λ_{qq}. The measured ratio is indicated by the solid line and the total uncertainty by the dashed lines.
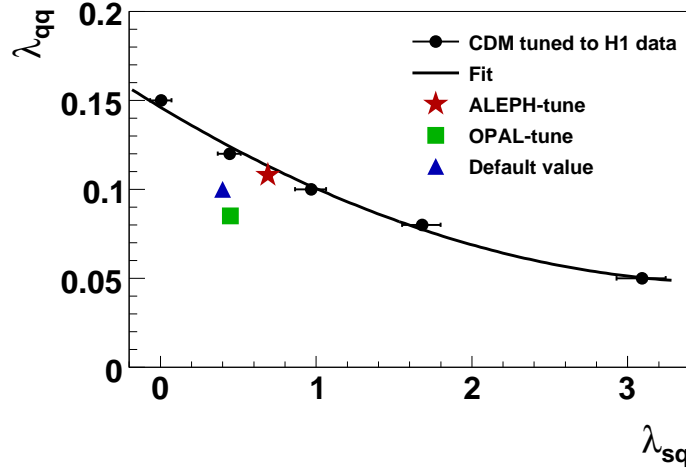
Figure 6.23: The points represent the $(\lambda_{qq}, \lambda_{sq})$ values extracted from a fit of the CDM model to the data. Overlaid to the points is the result of fit with a Polynomial of degree two. The value from the ALEPH-tune is indicated by a red star, the JETSET default value by a blue triangle and the OPAL-tune by a green square.

Table 6.5: The $(\lambda_{qq}, \lambda_{sq})$ points extracted from a fit of the CDM model to the data.

λ_{qq}	0.05	0.08	0.1	0.12	0.15
λ_{sq}	$3.09^{+0.15}_{-0.16}$	$1.68^{+0.12}_{-0.13}$	$0.97^{+0.10}_{-0.10}$	$0.45^{+0.07}_{-0.08}$	$0.00^{+0.06}_{-0.07}$

and the value extracted by the OPAL collaboration are not compatible with the H1 data. A

polynomial fit to the $(\lambda_{qq} - \lambda_{sq})$ points yields:

$$\lambda_{qq} = 0.146 - 0.053 \cdot \lambda_{sq} + 0.07 \cdot \lambda_{sq}^2. \tag{6.17}$$

These results are independent of the choice of the PDF set and also of the parameter λ_s. However, they are only valid for the CDM generator. With the conservative expectation, $0 \leq \lambda_{sq} \leq 1$ [7], the parameter λ_{qq} can be constraint by this measurement to:

$$\lambda_{qq} \in [0.101, 0.146]. \tag{6.18}$$

Earlier experiments (ALEPH, OPAL, L3 and HRS, see section 2.3) imply that a reasonable range for the parameter λ_{sq} is: $0.4 \leq \lambda_{sq} \leq 0.93$. Using this constraint, the λ_{qq} parameter has to take values within:

$$\lambda_{qq} \in [0.103, 0.126] \tag{6.19}$$

in order to be compatible with the H1 data.

6.7.2 Constraints implied by the K_s^0 Cross-Section

The measured K_s^0 cross-sections can be used to constrain the $\lambda_s - \lambda_{qq}$ parameter space. As the predicted cross-section for the K_s^0 production depends on the choice of the PDF set the following study is only valid for one PDF set, herein taken to be CTEQ6L. The predicted K_s^0 cross-section for different values of λ_s and λ_{qq} is shown in figure 6.24. To keep the amount
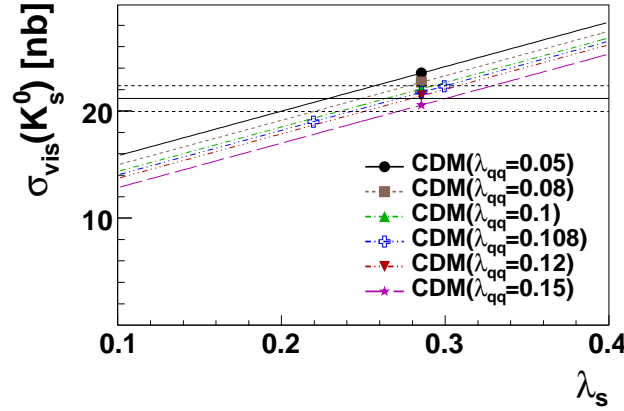
Figure 6.24: The dependency of $\sigma_{vis}(K_s^0)$ on the parameter λ_s for different values of λ_{qq}. The cross-section measured in data is indicated by the solid line and the total uncertainty by the dashed lines.

of generated Monte Carlo data in a reasonable range, the assumption is made that the two dependencies on λ_s and λ_{qq} are uncorrelated, i.e. that the slope in λ_s is the same for all λ_{qq} values. This slope is determined form the points predicted for a given value of $\lambda_{qq} = 0.108$. The extraction of the parameters λ_s and λ_{qq} is done in complete analogy the $\lambda_{sq} - \lambda_{qq}$ case. The results are displayed in figure 6.25 and summarised in table 6.6 [8]. Again, the point from

---

[7]This range is confirmed by all available measurements from other experiments.

[8]All points in this table have the same uncertainty due to the assumption of equal slopes.
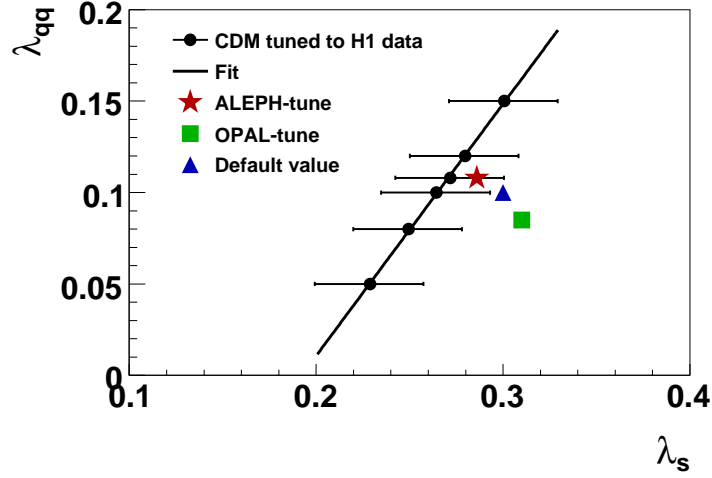
Figure 6.25: The points represent the $(\lambda_s, \lambda_{qq})$ values extracted from a fit of the CDM model to the data. Overlaid to the points is the result of fit with a Polynomial of degree one. The value from the ALEPH-tune is indicated by a red star, the JETSET default value by a blue triangle and the OPAL-tune by a green square.

the ALEPH-tune fits nicely into this measurement while the JETSET default value as well as the point from the OPAL-tune are not compatible with the measurement. A fit to the $(\lambda_s - \lambda_{qq})$ points yields:

$$\lambda_{qq} = -0.265 + 1.377 \cdot \lambda_s. \tag{6.20}$$

With the result of equation 6.18, the parameter λ_s can be constrained to:

$$\lambda_s \in [0.266, 0.298]. \tag{6.21}$$

With the more reasonable range for the diquark suppression factor given in equation 6.19, the parameter λ_s can be constraint further by this single measurement to:

$$\lambda_s \in [0.267, 0.284]. \tag{6.22}$$

Table 6.6: The $(\lambda_s, \lambda_{qq})$ points extracted from a fit of the CDM model to the data.

λ_{qq}	0.05	0.08	0.1	0.108	0.12	0.15
λ_s	$0.229^{+0.029}_{-0.030}$	$0.249^{+0.029}_{-0.030}$	$0.264^{+0.029}_{-0.030}$	$0.272^{+0.029}_{-0.030}$	$0.280^{+0.029}_{-0.030}$	$0.301^{+0.029}_{-0.030}$

6.8 Differential Cross-Section Measurements

The differential distributions are investigated in the event variables Q^2, x, y and W and in the kinematic variables $p_T(V^0)$, $\eta(V^0)$, $p_T^{Breit}(V^0)$ and $x_p^{Breit}(V^0)$ in the laboratory as well as in the Breit frame. To facilitate the interpretation of the results, the contributions of the different production processes to the strange particle production are investigated. The results extracted from the H1 data are compared to the predictions of the CDM and the MEPS models with two values of the strangeness suppression factor $\lambda_s = \{0.22, 0.3\}$ and to the values published by the ZEUS collaboration. Furthermore, the Λ asymmetry, measured with the same variables, is presented. Finally the constraints provided by the differential cross-section on the Lund parameter space are investigated.

6.8.1 Contribution from the Different Production Processes

The contributions of the different processes (see section 2.2.1) to the K_s^0 and Λ production are investigated. For the separation of the different subprocesses, the flavour of the quark participating in the hard interaction is studied (i.e. that one absorbing the photon emitted by the electron). The relative fraction of the different quarks are listed in table 6.7 for events where a K_s^0 or a Λ is produced in the visible range (see equation 6.1). The fractions are given for the laboratory frame as well as for the target and current regions of the Breit frame. All presented results are obtained by the CDM model with the ALEPH-tuned JETSET parameters and the PDF set CTEQ6L.

If an up or a down quark participates in the hard interaction, the strange particle is produced by the hadronisation process which is roughly the case for 60 % of all K_s^0 and 65 % of all Λ particles. In the current hemisphere of the Breit frame this fraction is reduced significantly. The remaining fraction is related directly to the hard subprocess; either to an strange quark participating in the hard interaction or to an charm quark with an subsequent decay into a strange quark. The fraction of particles from a bottom quark is negligible. According to the predictions, 38 % of all K_s^0 and 31 % of all Λ particles are produced in the

Table 6.7: The relative fraction of the different quarks participating in the hard interaction where a K_s^0 (Λ) particle is produced in the visible range. Shown are the values for the laboratory frame ('Lab') and for the target and current regions of the Breit frame. The results are obtained by the CDM model with the ALEPH-tunes JETSET parameters and the CTEQ6L PDF set. All numbers are given in percentage.

Quark flavour	K_s^0			$\Lambda + \overline{\Lambda}$		
Frame	Lab	Target	Current	Lab	Target	Current
up	48.5	49.7	36.3	54.9	55.4	43.5
down	13.0	13.2	11.7	13.8	13.9	11.2
strange	14.4	14.1	18.0	14.9	14.6	22.4
charm	23.8	22.9	33.2	16.3	16.0	22.4
bottom	0.3	0.2	0.8	0.1	0.1	0.5
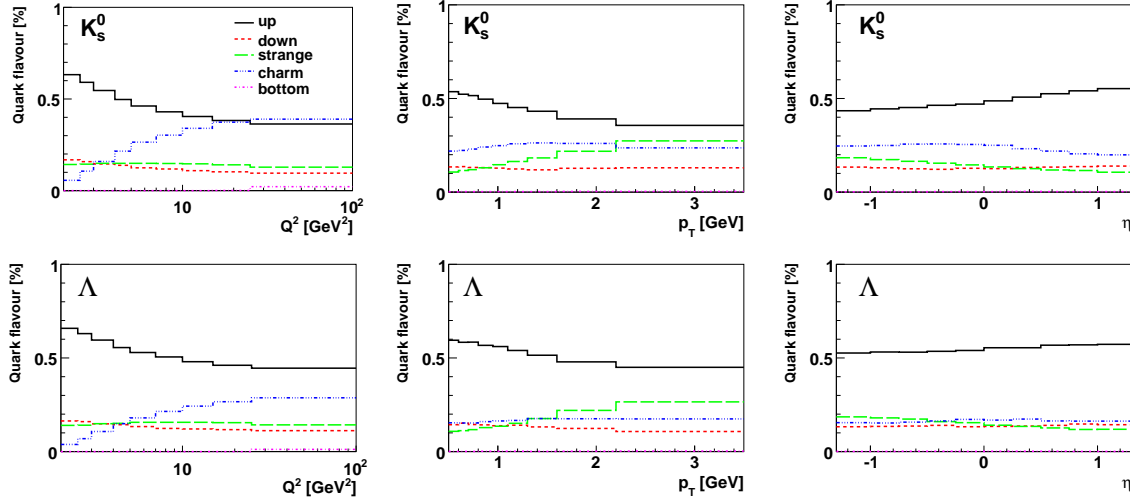
Figure 6.26: The relative fraction of the different quarks participating in the hard interaction for the events where a K_s^0 (upper row) or a Λ (lower row) is produced in the visible range. The fractions are shown as a function of Q^2, p_T and η.

hard interaction (i.e. s, c or b quarks). In the current region of the Breit frame this fraction is enhanced to 52 % and 45 %, respectively.

These fractions significantly change in different regions of the phase space. The relative fraction of the different quarks is presented as a function of Q^2, p_T and η in figure 6.26. The fraction of strange particles produced in the hard interaction is clearly enhanced for the high Q^2 region where it reaches values above 50 %. Especially the charm fraction is enriched in this region of the phase space. Furthermore, events with a K_s^0 in the visible range have a larger charm fraction than those with a Λ particle. A similar effect can be observed for the high p_T region. In this region particularly the strange fraction is enhanced allowing to tag events where a strange quarks participates in the hard interaction. Therefore, the measurement of strange hadrons with large p_T bears the potential of extracting the structure function F_s [9]. This is particularly interesting with regard to strange hadron physics at the LHC. In the forward region the sensitivity to particles produced in the hard interaction is reduced. The relative fractions are shown in figure 6.27 as a function of the transverse momentum p_T^{Breit} in the Breit frame. The influence of the hadronisation process is reduced in the current hemisphere and the charm fraction is constantly high, otherwise the distributions behave similarly as those in the laboratory frame. Furthermore, the composition of the different processes behave in an similar way for all variables shown in figures 6.26 and 6.27.

6.8.2   Differential K_s^0 and Λ Cross-Sections

The measurement of the differential cross-sections is restricted to the same visible range as for the inclusive case, see equation 6.1. The differential visible cross-sections are calculated

---

[9]The s quark fraction reaches values up to 50 % for $p_T(V^0) \sim 10\,\mathrm{GeV}$.
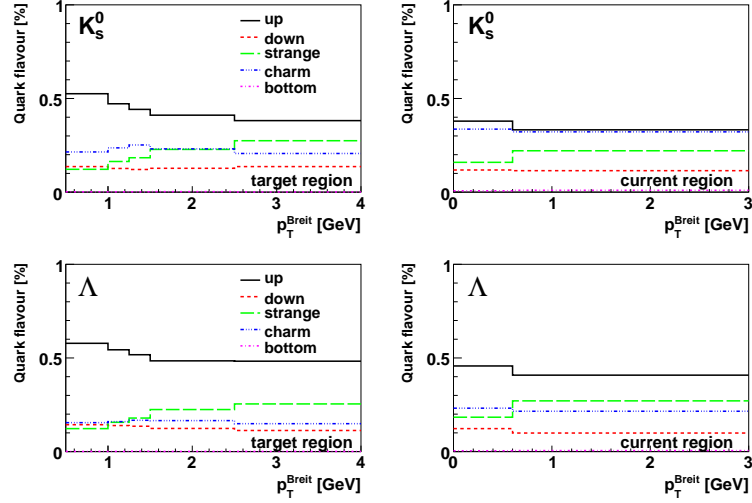
Figure 6.27: The relative fraction of the different quarks participating in the hard interaction for the events where a K_s^0 (upper row) or a Λ (lower row) is produced in the visible range. The fractions are shown as a function of the transverse momentum p_T^{Breit} in the Breit frame.

in analogy to equation 6.2:

$$\frac{d\sigma_{vis}(ep \rightarrow e'V^0X)}{dY} = \frac{N(\Delta Y)}{\mathcal{L} \cdot \epsilon(\Delta Y) \cdot BR \cdot (1 + \delta_{QED}(\Delta Y)) \cdot \Delta Y}, \tag{6.23}$$

where ΔY is the bin width of the investigated variable Y and $N(\Delta Y)$ is the number of reconstructed V^0 particles in this bin. The efficiency for the V^0 reconstruction, $\epsilon(\Delta Y)$, and the correction to non-radiative level, $\delta_{QED}(\Delta Y)$, are calculated for each bin, see section 6.2. All cross-section values and their uncertainties are tabulated in appendix A.

6.8.2.1   Distribution of the Event Variables

The differential cross-sections of the K_s^0 and Λ production in the event variables Q^2, x, y and W are presented in figures 6.28 and 6.29. All following figures show in the upper part the measured cross-sections together with the predictions of the CDM model with $\lambda_s = 0.3$. The values shown in the distributions are bin averaged and no bin-center corrections are applied. In the lower part the predictions of CDM and MEPS models with the two values of λ_s are displayed as a ratio to the data distributions. For this ratio only the uncorrelated uncertainties (see section 6.5.9) are included in the error bars, while the correlated uncertainties are shown as a yellow band.

The cross-sections decrease rapidly with Q^2 and x and smoothly with y and W as expected from the DIS kinematics. The general features of the distributions are well reproduced by the simulation. The shape of the distributions is slightly better described by the CDM model compared to the MEPS model. The theory over data distributions show that CDM favours a higher strangeness suppression factor around 0.3 for both, the K_s^0 and Λ production while the MEPS model favours a λ_s around 0.22 for the description of the K_s^0 production and a

value between 0.22 and 0.3 for the Λ description. These conclusions are in line with the observations form the inclusive measurements, see table 6.3.

The predictions of the K_s^0 and Λ cross-sections as a function of Q^2 for different PDF sets are shown in figure 6.30. For these predictions the ALEPH-tune was used (i.e. $\lambda_s = 0.286$). A distinct dependency of the cross-sections on the PDF set is observed. The shape of the Q^2 spectrum is best described by the CTEQ6L set. The GRV set delivers a completely different shape, while the H1-2000 PDF describes the data quite well for $Q^2 \gtrsim 4 \, \text{GeV}^2$. This behaviour is understood in terms of the input data used for the different sets. The choice of the CTEQ6L set is therefore justified and the deficits in the description of the data by the models are more likely related to a deficit in the models themselves and not in the PDF set.
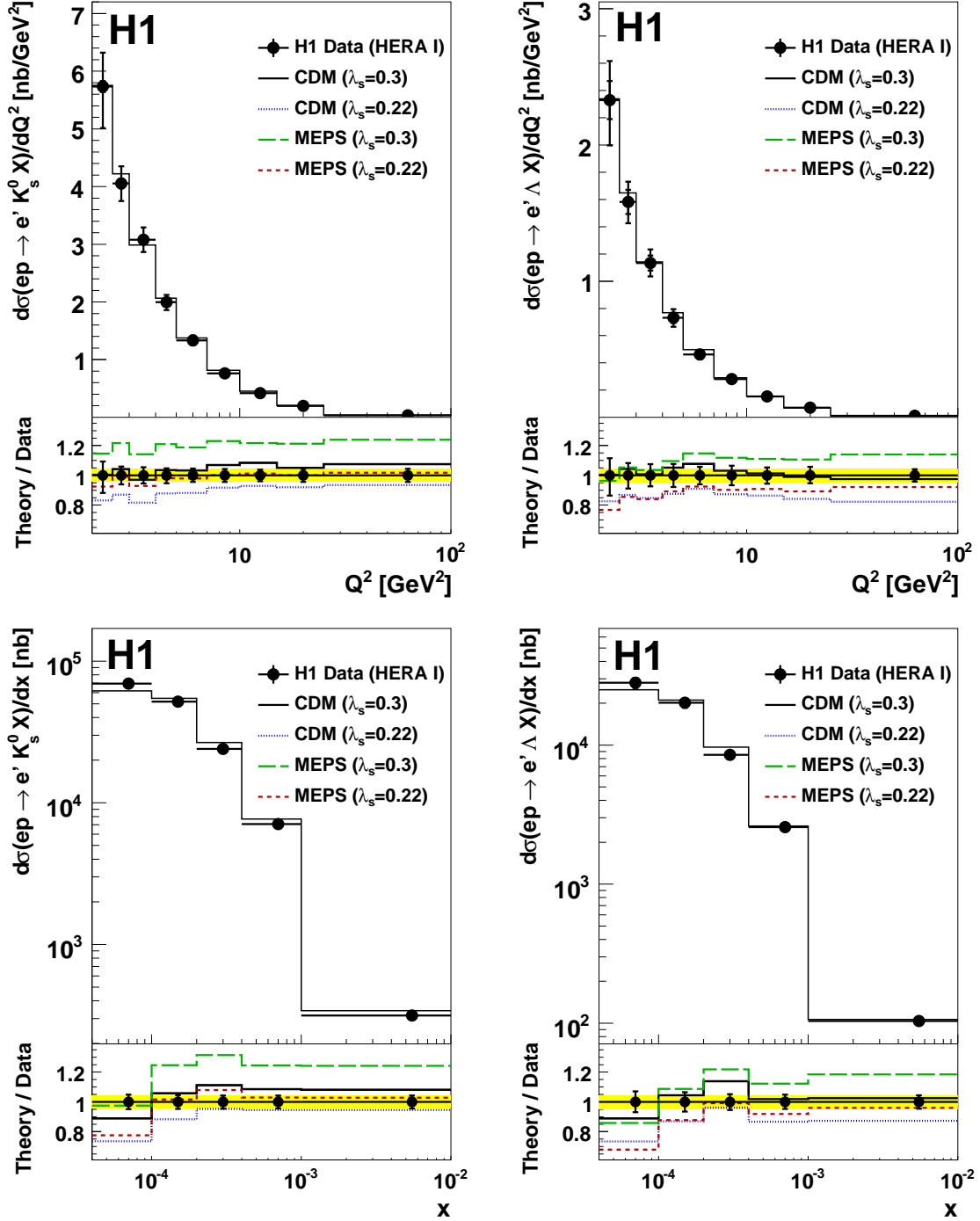
Figure 6.28: The differential production cross-sections for K_s^0 (left column) and Λ (right column) in the laboratory frame as a function of the photon virtuality squared Q^2 (upper row), and the Bjorken variable x (lower row). The error bars show the statistical (inner) and total (outer) errors. On the bottom of each figure, the ratios of "Theory/Data" are appended for different LO Monte Carlo predictions (see text). In these "Theory/Data" ratios, only the uncorrelated systematic uncertainties are included. The size of the correlated systematic uncertainties is indicated by the yellow band.
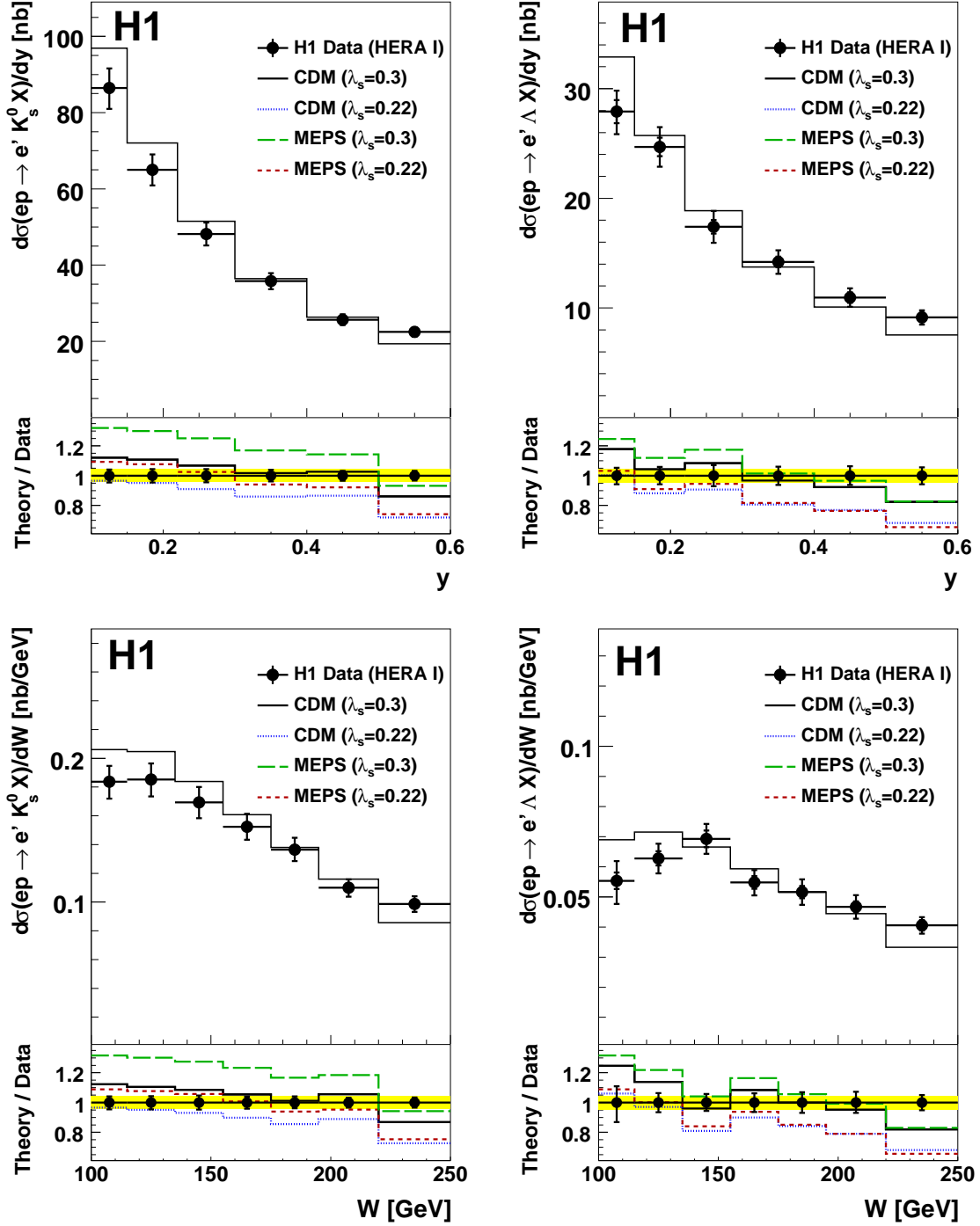
Figure 6.29: The differential production cross-sections for K_s^0 (left column) and Λ (right column) in the laboratory frame as a function of y (upper row) and W (lower row). See also caption of figure 6.28.
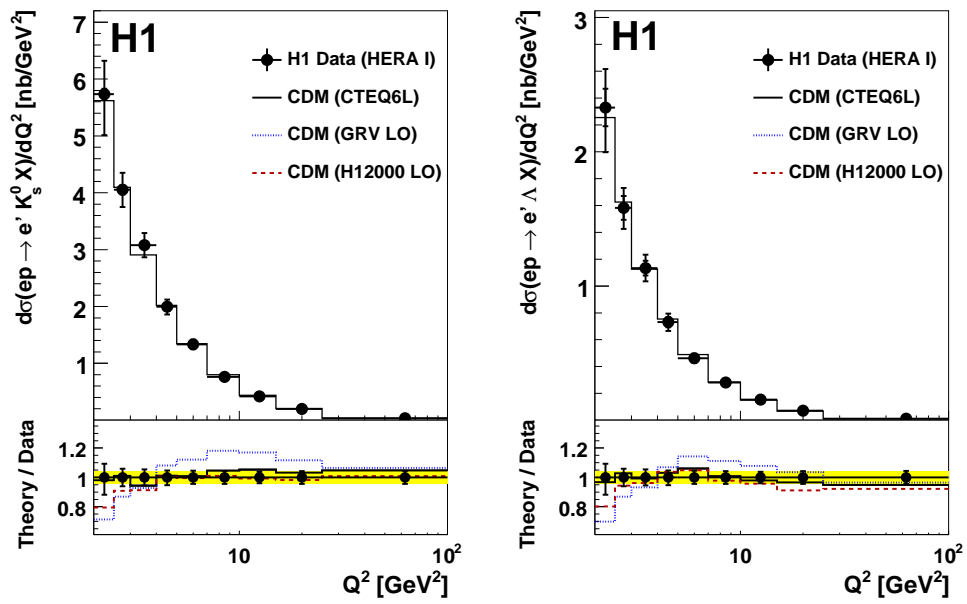
Figure 6.30: The differential production cross-sections for K_s^0 (left) and Λ (right) in the laboratory frame as a function of Q^2 for three different PDF sets. See also caption of figure 6.28.

6.8.2.2 Distribution of the Kinematic Variables

The differential distributions in the kinematic variables of the V^0 are presented and compared to the CDM and MEPS model predictions for the two values of λ_s.

The Laboratory Frame of Reference The production cross-sections are shown in figure 6.31 as a function of $p_T(V^0)$ and $\eta(V^0)$. The cross-sections are steeply falling with p_T and flat in η for the K_s^0 production while for the Λ production a rise in the forward region is observed. Both models predict softer p_T spectra than measured in data for both, K_s^0 mesons and Λ baryons. The CDM model describes the shape of the p_T distribution better than the MEPS model. The shape of the distribution is insensitive to the choice of the strangeness suppression factor λ_s. The CDM model favours a higher λ_s values around 0.3 while the MEPS model prefers a value around 0.22 for the description of the data. This is a general effect and is observed for all spectra. The CDM model describes the η spectrum quite well for the K_s^0 case with $\lambda_s \approx 0.3$ while the rise in the Λ case is not described by the model. For the MEPS case, the η spectrum of the K_s^0 is only well described for $\eta \lesssim 0.5$ and a lower suppression factor of $\lambda_s \approx 0.22$. For the forward region, where the influence of the hadronisation process is enlarged, a higher suppression factor is needed. Therefore, the MEPS model is not able to describe the whole η spectrum of the K_s^0 mesons with one single value of λ_s. For the Λ case the MEPS predictions are quite similar to the CDM ones. The shape of the p_T and η distributions do not show any dependency on the choice of the PDF set.

The Breit Frame of Reference The production of strange hadrons is investigated in the Breit frame of reference by examining the distribution of the transverse momentum, p_T^{Breit}, and the momentum fraction x_p (see section 4.2.3). These variables are studied in the target and current hemisphere separately. The strange particles produced directly in the hard interaction are expected to predominately populate the current hemisphere (see section 6.8.1). However, the statistic in the current hemisphere is strongly limited: only $\sim 8\,\%$ ($\sim 4\,\%$) of all K_s^0 (Λ) are reconstructed in this hemisphere. Therefore, in the current hemisphere only two bins are used.

The cross-sections are shown in figure 6.32 differentially in p_T^{Breit} for the target and current hemispheres. In the target hemisphere, the predicted transverse momentum of both particles is softer than in data. The CDM model provides a better description of the shape of the transverse momentum distribution than the MEPS model. In the current hemisphere, where the influence of the hadronisation process is reduced, the predictions of the two models are very similar and both models provide a reasonable description of the K_s^0 meson and fail in describing the Λ baryon. However, due to the limited statistics in the current hemisphere, the drawing of concrete conclusions is ambiguous.

The cross-sections as a function of x_p in the target and current hemispheres are displayed in figure 6.33. In the target hemisphere the x_p spectrum is predicted softer than measured in data. Again the CDM model provides a slightly better description of the shape than the MEPS model. In the current hemisphere the predictions of the two models are very similar (as already observed for the p_T^{Breit} distribution) and they provide a reasonable description of the K_s^0 meson and fail in describing the Λ baryon.
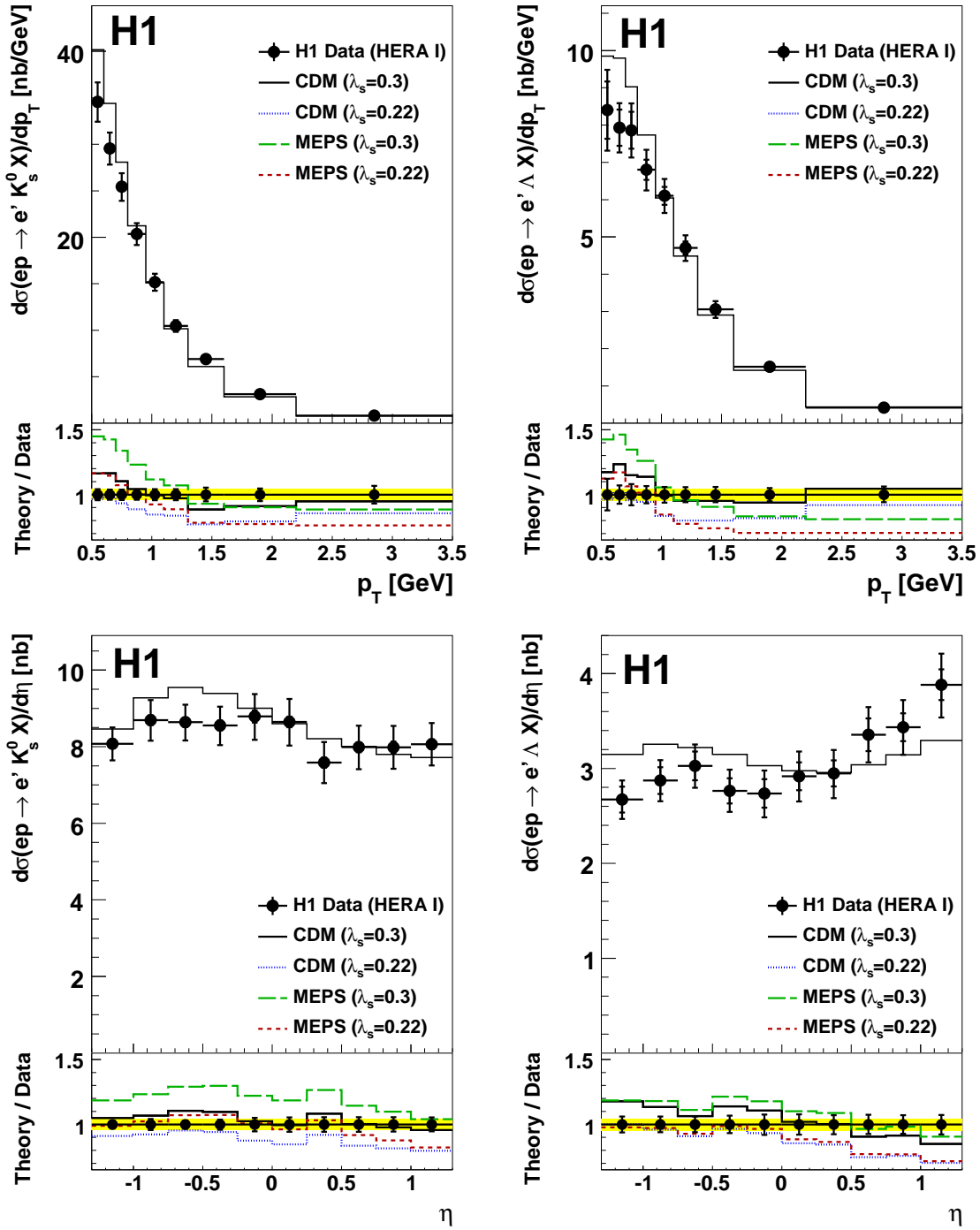
Figure 6.31: The differential production cross-sections for K_s^0 (left column) and Λ (right column) in the laboratory frame as a function of the transverse momentum (upper row), and the pseudorapidity (lower row). See also caption of figure 6.28.
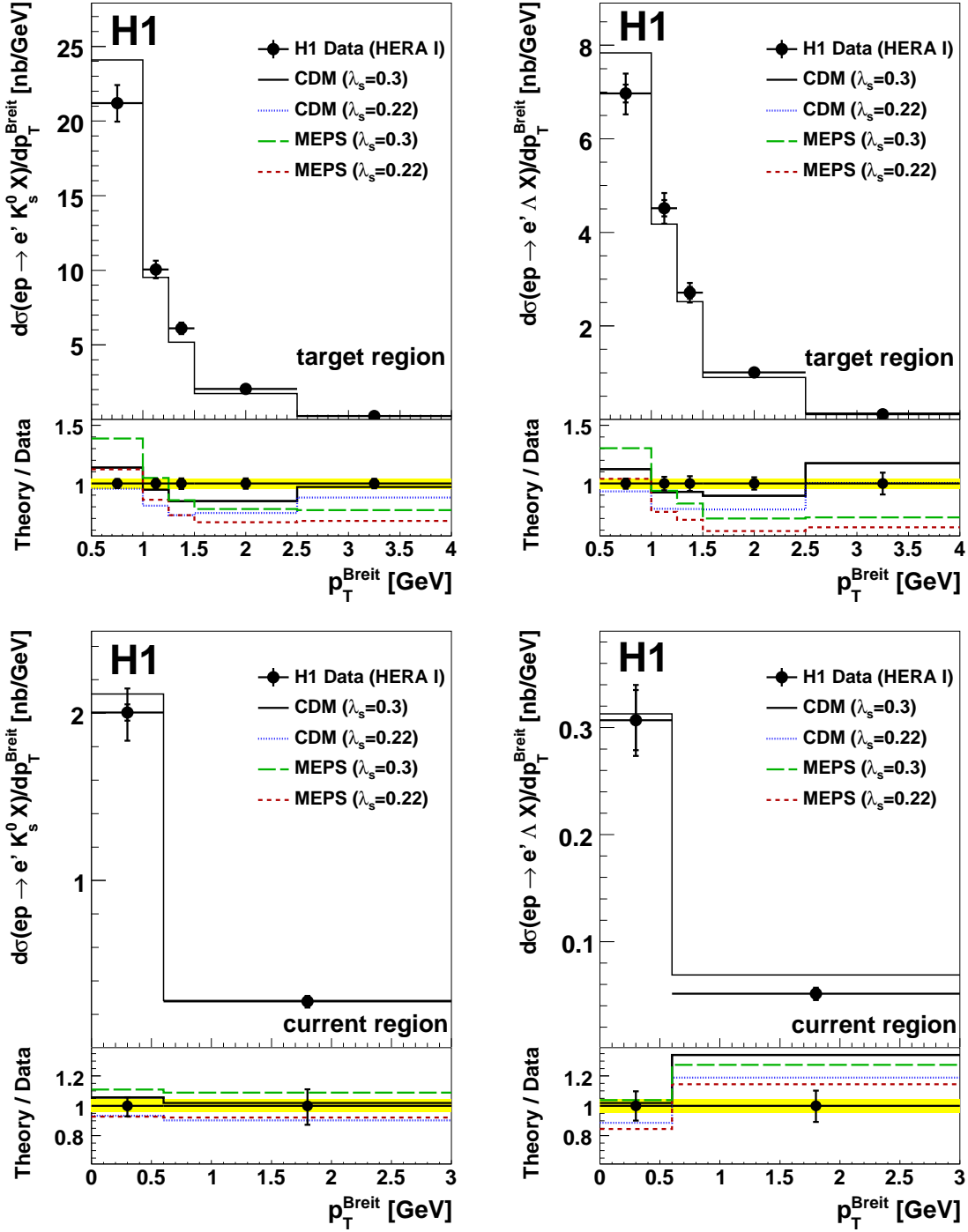
Figure 6.32: The differential production cross-sections for K_s^0 (left column) and Λ (right column) as a function of the transverse momentum in the Breit frame in the target (upper row) and in the current (lower row) hemisphere. See also caption of figure 6.28.
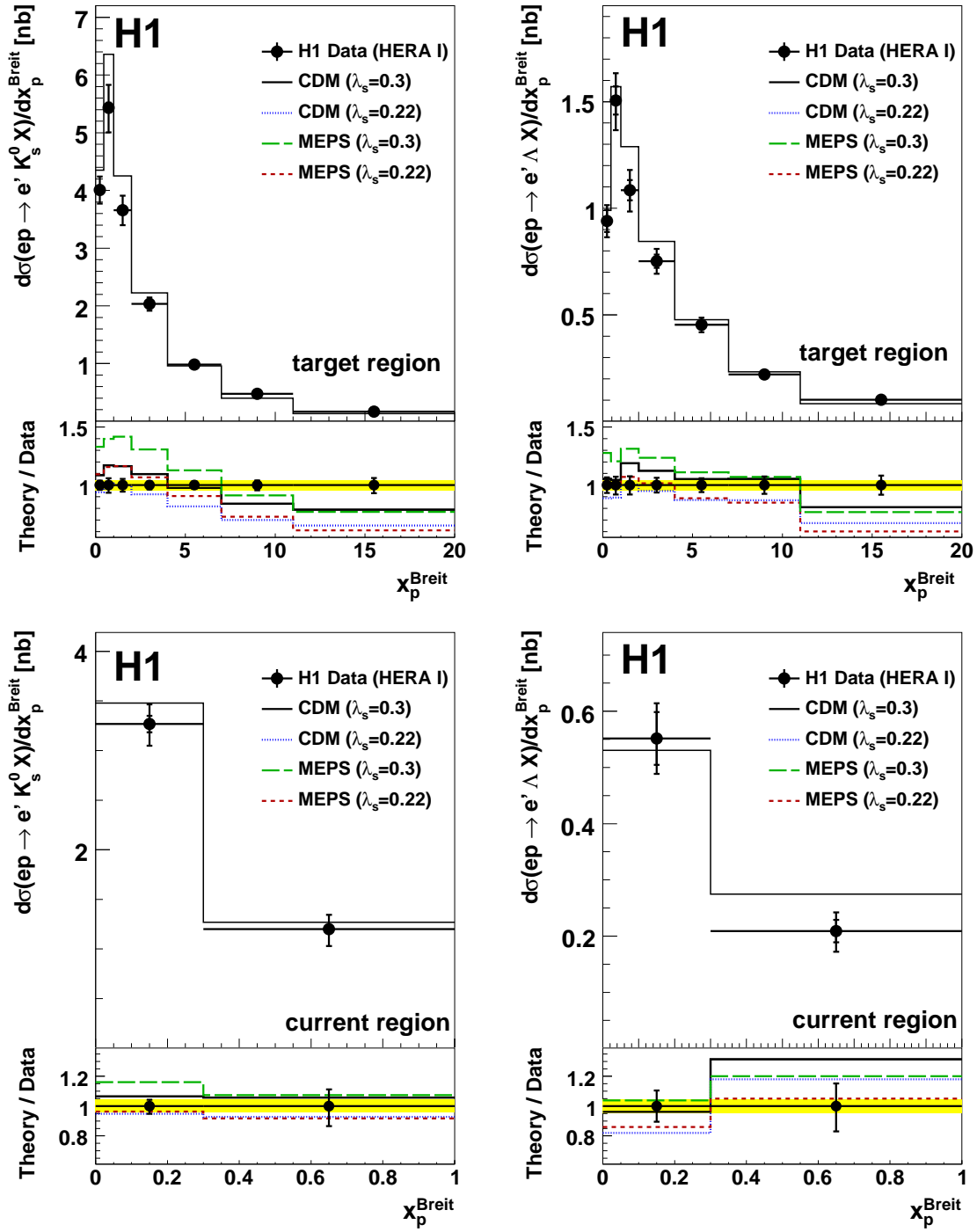
Figure 6.33: The differential production cross-sections for K_s^0 (left column) and Λ (right column) as a function of x_p in the Breit frame in the target (upper row) and in the current (lower row) hemisphere. See also caption of figure 6.28.

6.8.2.3   Summary of the Observations on the Differential Cross-Sections

In general, both models provide a reasonable description of the data. The CDM generator describes the data slightly better than the MEPS one, except for the current hemisphere where the predictions of both models are very similar [10]. The CDM model prefers a higher value of the strangeness suppression factor λ_s around 0.3 while the MEPS model favours a value around 0.22. In conclusion, the CDM model with the ALEPH-tuned JETSET parameters provides a reasonable description of all data distributions.

6.8.3   The $\Lambda - \overline{\Lambda}$ Asymmetry

Different mechanisms could produce a $\Lambda - \overline{\Lambda}$ asymmetry in the central region of the detector. On the one hand, the baryon number of the incoming proton could flow over the rapidity gap between the incident proton and the measured final state [159]. On the other hand a non-vanishing baryon asymmetry in the proton sea could exist [160] and lead to an observable asymmetry in the final state. This asymmetry is predicted to be approximately $7\,\%$ for $x < 5 \cdot 10^{-4}$. As pointed out in [160], the production of Λ relative to $\overline{\Lambda}$ at HERA energies provides an interesting quantity to study the asymmetry.

The asymmetry in the production of Λ with respect to $\overline{\Lambda}$ is measured by the variable [11]:

$$A_\Lambda = \frac{\sigma_{vis}(ep \to e'\Lambda X) - \sigma_{vis}(ep \to e'\overline{\Lambda}X)}{\sigma_{vis}(ep \to e'\Lambda X) + \sigma_{vis}(ep \to e'\overline{\Lambda}X)}. \tag{6.24}$$

A significant $\Lambda - \overline{\Lambda}$ asymmetry would indicate a substantial transfer of the baryon number from the proton beam to the strange particles. The resulting distributions are shown in figure 6.34 in the laboratory frame and in figure 6.35 in the Breit frame. All distributions are observed to be compatible with zero within errors. Thus, no evidence of baryon number transport is visible in the measured data, including the low x region.

---

[10]This behaviour in the current region is expected since the hard interaction, which is the dominant production process in this hemisphere, is described similarly for both models but only the implementation of the hadronisation is different.

[11]Here charge conjugation is explicitly excluded.
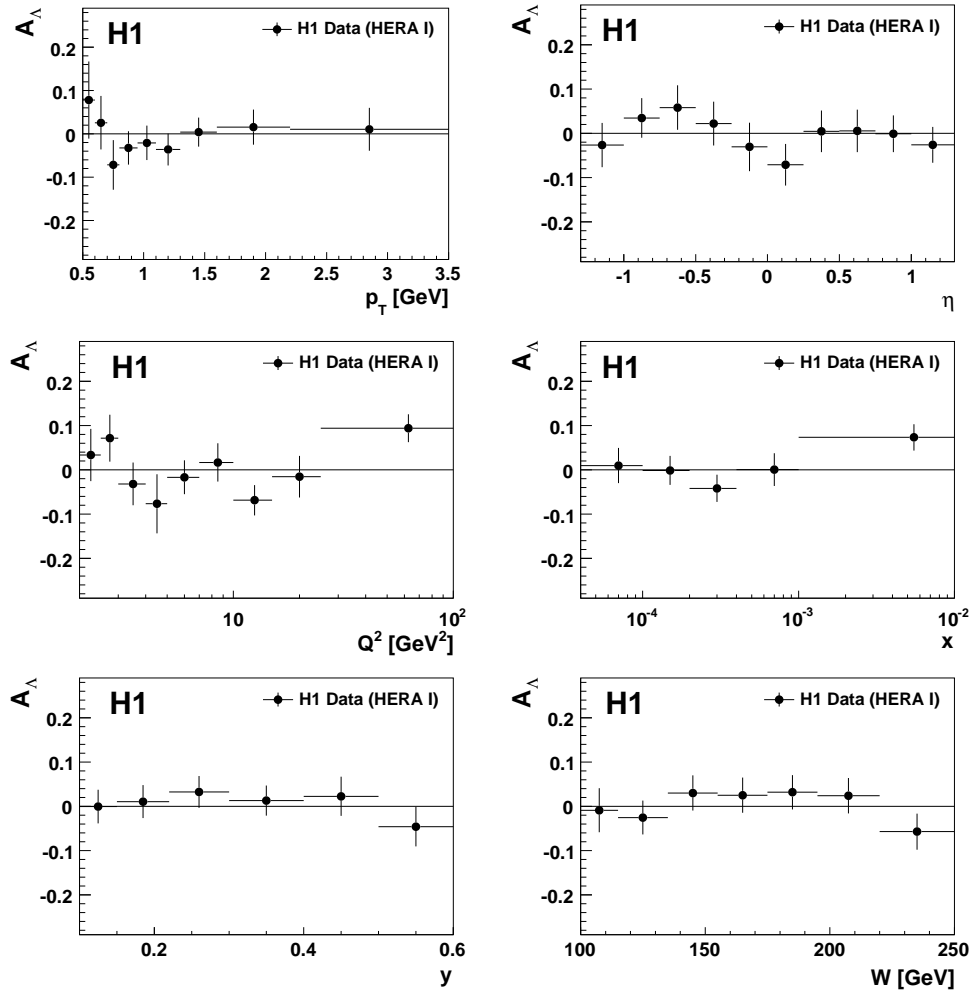
Figure 6.34: The asymmetry A_Λ of the differential production cross-sections in the laboratory frame as a function of the transverse momentum p_T, the pseudorapidity η, and of the event variables Q^2, x, y and W. The error bars show the statistical uncertainty.
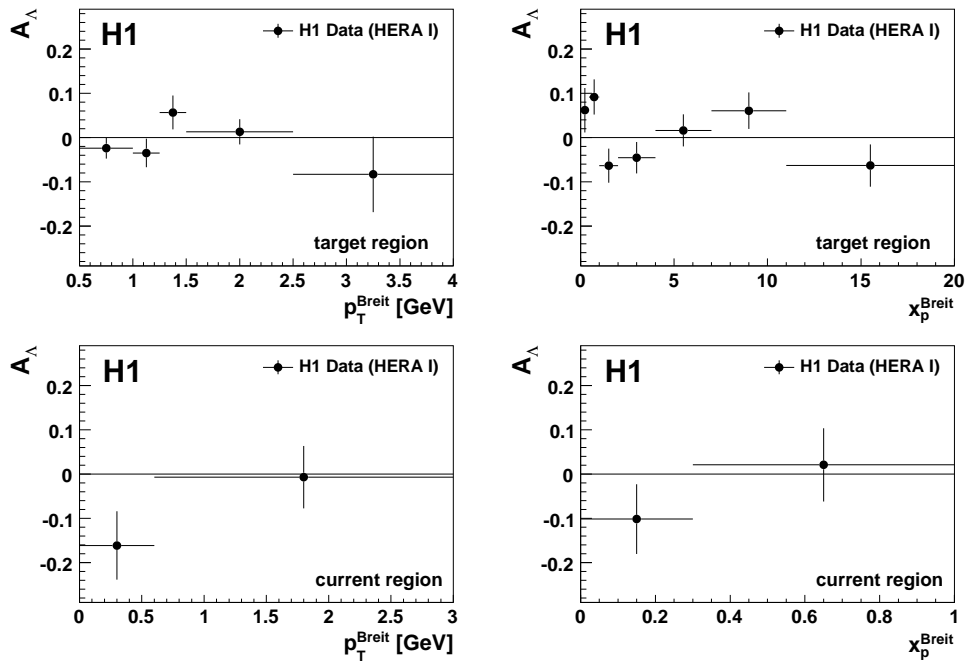
Figure 6.35: The asymmetry A_Λ of the differential production cross-sections in the Breit frame as a function of the transverse momentum p_T^{Breit} and the variable x_p^{Breit}. The error bars show the statistical uncertainty.

6.8.4 Ratio of the Differential K_s^0 and Λ Cross-Sections

Certain aspects of strangeness production can be studied by looking at the ratio of the differential Λ and K_s^0 production cross-sections. A significant fraction of the systematic uncertainties on the cross-sections cancels and also the theory uncertainties are reduced. The ratio $R(\Lambda/K_s^0)$ of the differential Λ and K_s^0 production cross-sections is given by:

$$R(\Lambda/K_s^0) = \frac{d\sigma_{vis}(ep \to e'[\Lambda + \overline{\Lambda}]X)}{d\sigma_{vis}(ep \to e'K_s^0 X)}. \tag{6.25}$$

This ratio exhibits only a significantly reduced dependency on the choice of the PDF set and also on the value of the strangeness suppression factor λ_s as can be seen in figure 6.36. This ratio provides therefore a sensitive quantity to study the diquark suppression factors λ_{qq} and λ_{sq}, which is discussed in section 6.8.5.
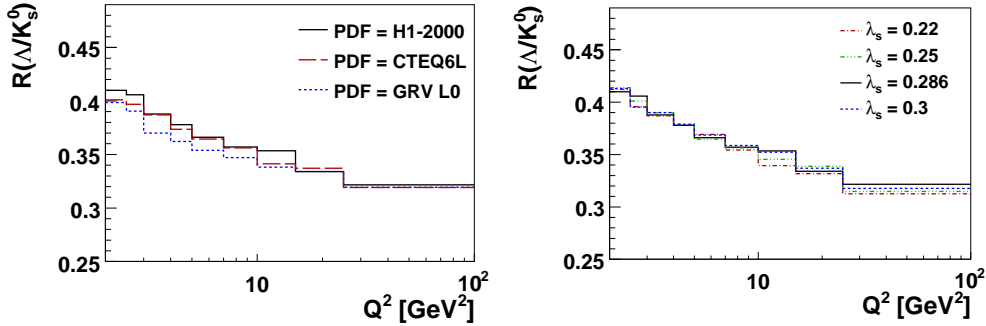
Figure 6.36: Predictions of the ratio $R(\Lambda/K_s^0)$ for different PDF sets (left) and different λ_s values (right). All predictions are obtained with the CDM generator.

The ratio $R(\Lambda/K_s^0)$ is shown in figure 6.37 as a function of the event variables Q^2, x, y and W together with the predictions by the CDM and MEPS models for two values of λ_s (0.22 and 0.3). At high values of Q^2 and x the number of Λ baryons decreases with respect to the K_s^0 mesons and increases with rising y. The CDM implementation provides a reasonably good description of the data in all four variables, although systematic deviations are seen for $Q^2 \gtrsim 10\,\text{GeV}$. The MEPS predictions describe neither the shape nor the normalisation of the distributions. The MEPS model predicts throughout lower values of the ratio $R(\Lambda/K_s^0)$ than measured in data.

The dependency of the ratio R on the kinematic variables p_T and η in the laboratory frame is displayed in figure 6.38. The number of produced Λ baryons relative to K_s^0 mesons increases rapidly with p_T as expected from the different kinematic properties of these two particles (i.e. their mass). The ratio increases also for the forward region ($\eta \gtrsim 0.5$) due to the Λ production. In contrast to the individual cross-sections where both models predict a softer spectrum than in data, the p_T distribution of the ratio is reasonably well described by both models due to cancellation of the insufficient description. The MEPS model describes the distribution more accurately at low p_T while the CDM model gives a better description of the high p_T region. The increase of the ratio in the forward direction cannot be reproduced
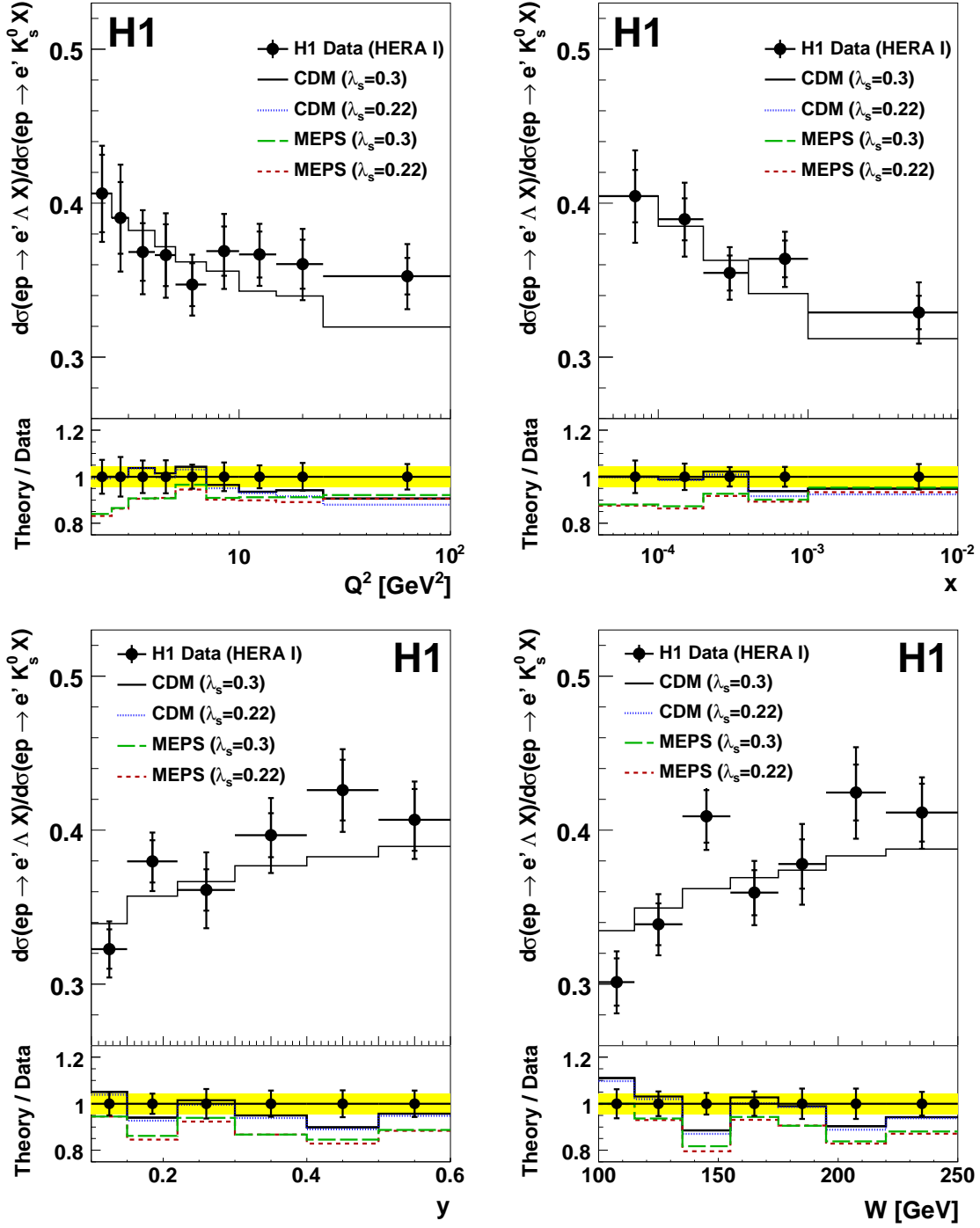
Figure 6.37: The ratio R(Λ/K_s^0) of the differential production cross-sections as a function of the event variables Q^2, x, y and W. The error bars show the statistical (inner) and the total (outer) errors. The lines show the predictions of the LO Monte Carlo programs. (See also caption of figure 6.28).
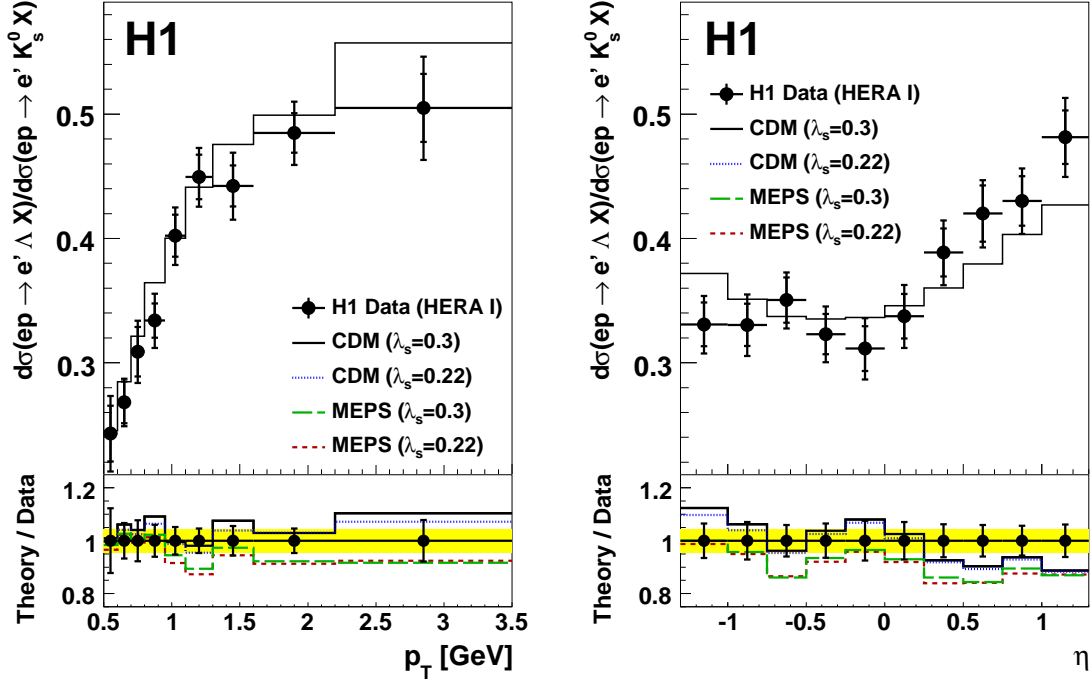
Figure 6.38: The ratio R(Λ/K_s^0) of the differential production cross-sections as a function of the kinematic variables p_T and η in the laboratory frame. The error bars show the statistical (inner) and the total (outer) errors. The lines show the predictions of the LO Monte Carlo programs. (See also caption of figure 6.28).

by any of the models. Nevertheless, the CDM model provides a better description of the η distribution. The χ^2, calculated as a sum over all bins, is a factor of two better for the CDM model with respect to the MEPS model.

The p_T^{Breit} and x_p^{Breit} spectra in the Breit frame are shown in figure 6.39. In the target hemisphere the ratio increases for large p_T^{Breit} and x_p^{Breit} values, while in the current hemisphere the ratio remains almost constant within the uncertainty. The main effects are reasonably well described by both models. However, it should be noted that in the current hemisphere of the Breit frame the predictions are less sensitive to the model implementation (CDM or MEPS) and that the statistic is rather poor.

In conclusion , the CDM model provides a better description of ratio R(Λ/K_s^0) than the MEPS model. Therefore, the mechanism implemented in the colour dipole radiation model seems to better describe the baryon to meson ratio than those implemented in the parton shower.

6.8.5 Extraction of the Diquark Suppression Factors

The differential distributions of the cross-section ratios are used to constrain the diquark suppression factors λ_{qq} and λ_{sq} of the Lund string model. The main interest of this investiga-
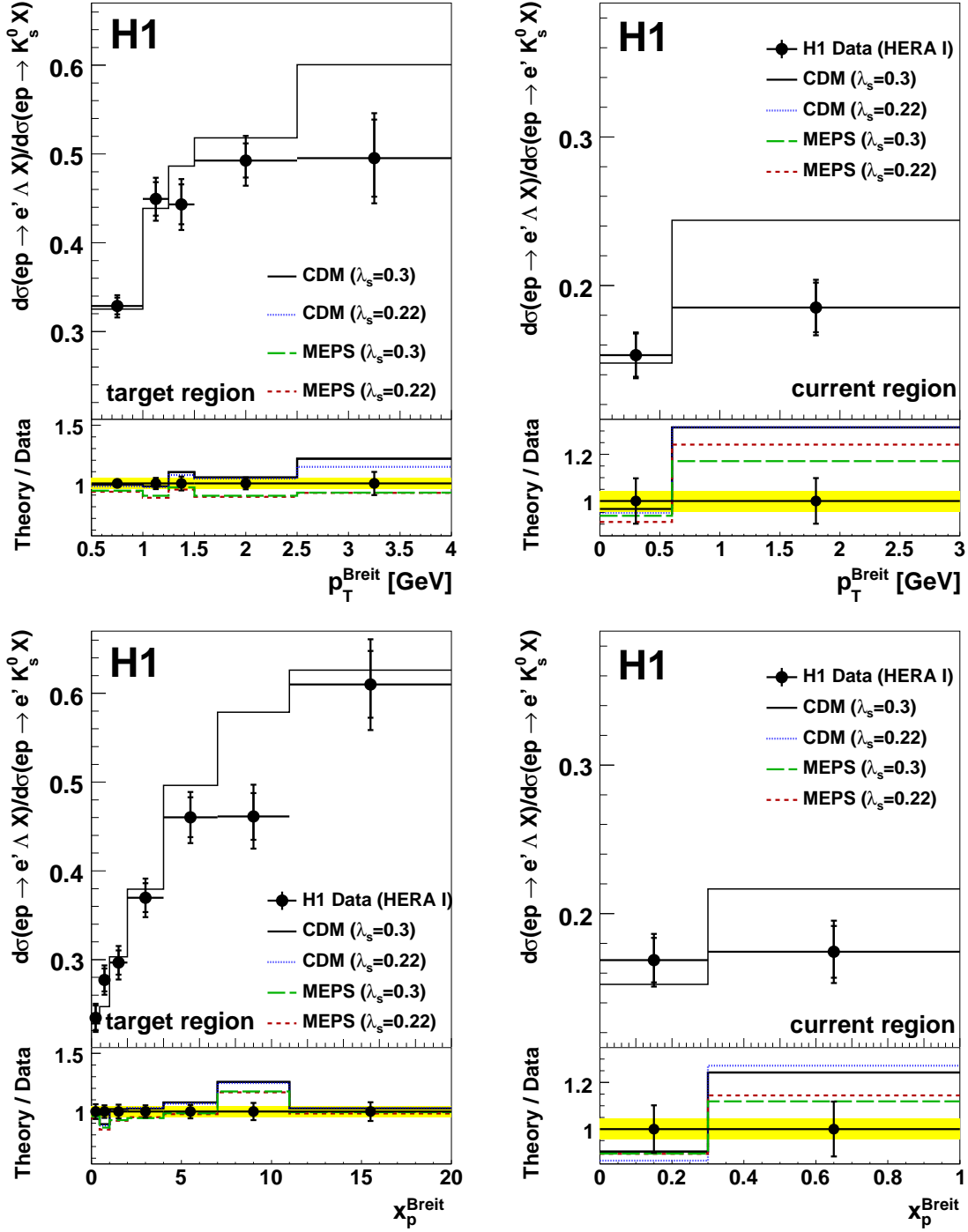
Figure 6.39: The ratio $R(\Lambda/K_s^0)$ of the differential production cross-sections as a function of the kinematic variables p_T^{Breit} and x_p^{Breit} in the Breit frame. The error bars show the statistical (inner) and the total (outer) errors. The lines show the predictions of the LO Monte Carlo programs. (See also caption of figure 6.28).

tion is to study whether the results obtained from the inclusive measurement are confirmed by the differential distributions. In the following a slightly different approach than the one introduced in section 6.7.1 is used: For each variable and for each $(\lambda_{qq}, \lambda_{sq})$ Monte Carlo set (see section 6.7) a χ^2 value is calculated according to:

$$\chi^2(\lambda_{qq}, \lambda_{sq}) = \sum_i \frac{(R_{Data}(i) - R_{MC(\lambda_{qq}, \lambda_{sq})}(i))^2}{\delta(R_{Data}(i))^2}, \qquad (6.26)$$

where the sum loops over all bins i of the variable under investigation. Here, $R_{Data}(i)$ denotes measured the value of the ratio $R(\Lambda/K_s^0)$ in bin i, $R_{MC(\lambda_{qq}, \lambda_{sq})}(i)$ as extracted from the simulated sample with parameters $(\lambda_{qq}, \lambda_{sq})$ and $\delta(R_{Data}(i))$ the total uncertainty of the measurement. The χ^2-distribution obtained from the differential distribution in Q^2 is shown as an example in figure 6.40. A distinguished valley of minima is observed. Therefore, only a relation between the two parameters can be extracted (as already seen in section 6.7.1) which is given by the valley of minimal χ^2-values. In order to find a parameterisation of this valley, the χ^2-distribution is fitted with a two-dimensional function $F(\lambda_{qq}, \lambda_{sq})$ parameterised by:

$$F(\lambda_{qq}, \lambda_{sq}) = a(\lambda_{sq}) + b(\lambda_{sq}) \cdot \lambda_{qq} + c(\lambda_{sq}) \cdot \lambda_{qq}^2, \qquad (6.27)$$

where a, b and c are Polynomial functions of degree two in the variable λ_{sq}. The function fitted to the χ^2-distribution obtained from the differential ratio in Q^2 is also shown in figure 6.40. The relation between the two diquark suppression factor is extracted by a minimisation of the fitted function F for given values of λ_{sq}.
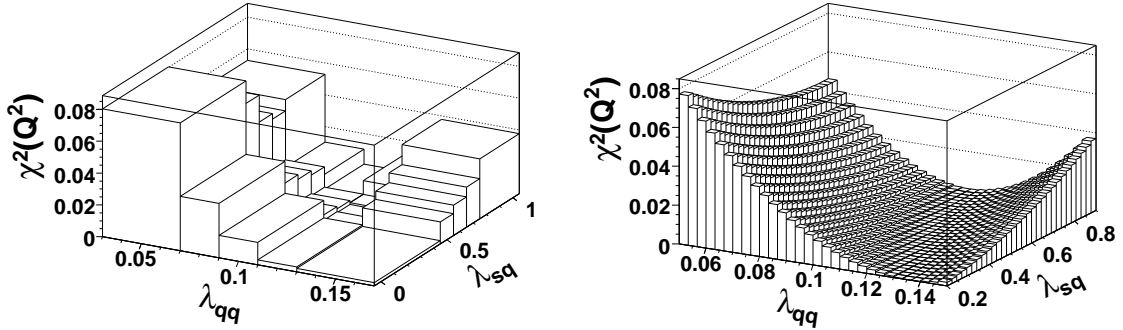
Figure 6.40: Left: The χ^2-distribution (see equation 6.26) obtained from the differential production cross-section ratio in Q^2. Right: The result of the fit using the function F as defined in equation 6.27. For explanation see text.

In order to show the compatibility of this method with the one used for the inclusive cross-section measurement, the parameterisation of the valley of minimal χ^2-values is extracted with this method from the inclusive cross-section ratio. In this case the χ^2 is defined analogue to equation 6.26 (without the sum). The resulting relation between λ_{qq} and λ_{sq} extracted with the method described in this section ("new method") is shown in figure 6.41 together with the parameterisation obtained in section 6.7.1 ("old method"). The two results are in good agreement, implying that the two methods are compatible.
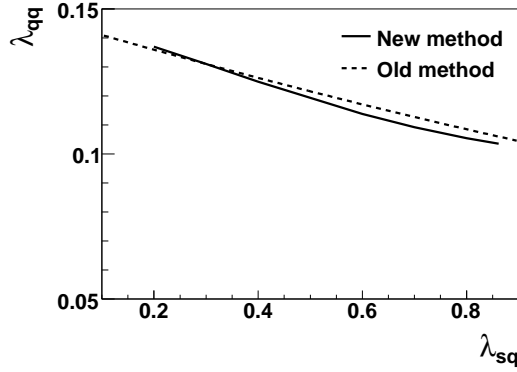
Figure 6.41: The relation between the parameters λ_{qq} and λ_{sq} as extracted with the method introduced in this section ("new method"). Overlaid is the result obtained in section 6.7.1 ("old method").

In figure 6.42 the $(\lambda_{qq}, \lambda_{sq})$ values providing the best description of the differential cross-section ratios in Q^2, x, p_T and η are shown. All spectra are described by nearly the same $(\lambda_{qq}, \lambda_{sq})$ parameterisation. The ALEPH-tuned value provides a good description of all differential spectra, while the OPAL-tune and the JETSET default value are not able to describe the data.
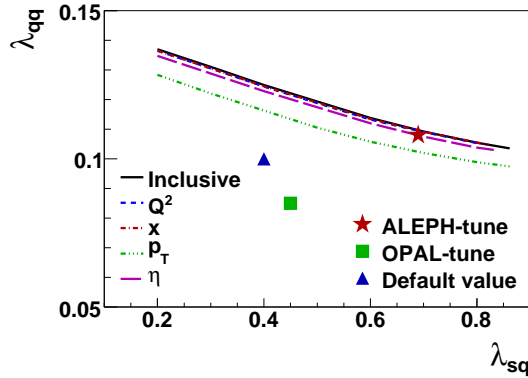
Figure 6.42: The relation between the two diquark suppression factors λ_{qq} and λ_{sq} as extracted from the measured differential cross-section ratios in the variables Q^2, x, p_T and η.

In conclusion, the studies made within this work indicate that the ALEPH-tune from e^+e^- collisions pretty well describes the overall data features also in ep collisions. Therefore it can be speculated that this tune is also able to describe pp collisions (LHC).

6.8.6   Comparison to the ZEUS Measurement

The ZEUS collaboration has recently measured the production cross-sections of the K_s^0 mesons and Λ baryons in a phase space region different to that one used in this analysis.

Especially the Q^2 range is substantially reduced with respect to this work. The cross-sections as a function of p_T and η obtained in this work are compared to those published by the ZEUS collaboration. The difference in the phase space selections are summarised in table 6.8. All selection criteria beside the y range are adapted for the comparison. For y this is not possible due to different detector acceptances and therefore an extrapolation of the results is needed.

Table 6.8: The phase space selection used in this work and in the ZEUS publication.

	This work	ZEUS range
$Q^2[\mathrm{GeV}^2]$	$2 - 100$	$5 - 25$
y	$0.1 - 0.6$	$0.02 - 0.95$
$p_T[\mathrm{GeV}]$	$0.5 - 3.5$	$0.6 - 2.5$
η	$-1.3 - 1.3$	$-1.2 - 1.2$
δ_{QED}	yes	no

In figure 6.43 the generated y spectrum of the V^0 particles is shown for the visible range of the ZEUS analysis. This spectrum is obtained by the CDM generator with the H1-2000 PDF set and is used for the extrapolation of the cross-sections. The range that needs to be extrapolated is quite large and includes the steeply falling edge of the spectrum at low values of y. Thus, a significant (and unknown) contribution to the uncertainty of the extrapolated cross-sections is expected. The extrapolation factor CF used for the correction of the measured cross-section is given by the number of K_s^0 (Λ) particles within $0.1 < y < 0.6$ to those with in $0.02 < y < 0.95$:

$$CF_{K_s^0(\Lambda)} = \frac{N_{K_s^0(\Lambda)}(0.1 < y < 0.6)}{N_{K_s^0(\Lambda)}(0.02 < y < 0.95)}.\tag{6.28}$$

Since the η (and also the p_T) distribution is correlated with the y distribution, the extrapolation factor is determined for each bin of interest and displayed in figure 6.44 for the K_s^0 and Λ particles. In the forward region the cross-sections needs to be extrapolated by a factor of almost two.

The extrapolated K_s^0 and Λ cross-sections and their ratio are shown in figure 6.45 as a function of p_T and η together with the values measured by the ZEUS collaboration. The lower part of each figure shows the ratio of the two cross-sections. In general the cross-sections as well as the ratio are in agreement at the $5\,\%$ level. Taking the large uncertainty of the extrapolation into account, the two measurements are in good agreement with each other.

The comparison of the cross-section with the results of the ZEUS collaboration shows that the two analyses delivers results that are compatible.
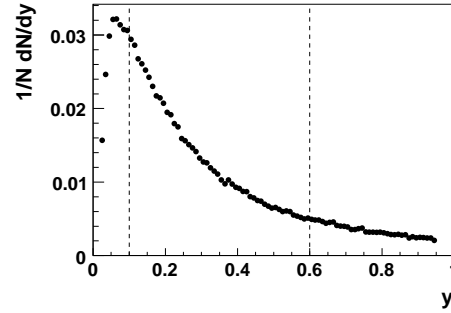
Figure 6.43: The generated y spectrum for the visible range used by ZEUS. The spectrum is obtained from the CDM simulation with the H1 2000 PDF set. The dashed lines indicated the measured region.
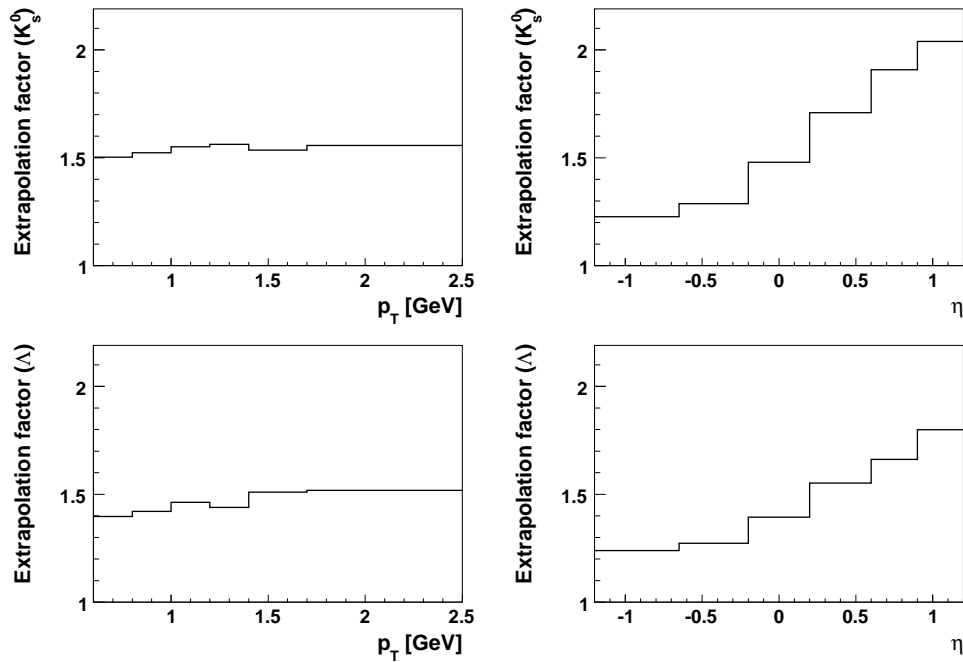
Figure 6.44: The extrapolation factors for the K_s^0 (top) and Λ (bottom) cross-sections as a function of p_T (left) and η (right).
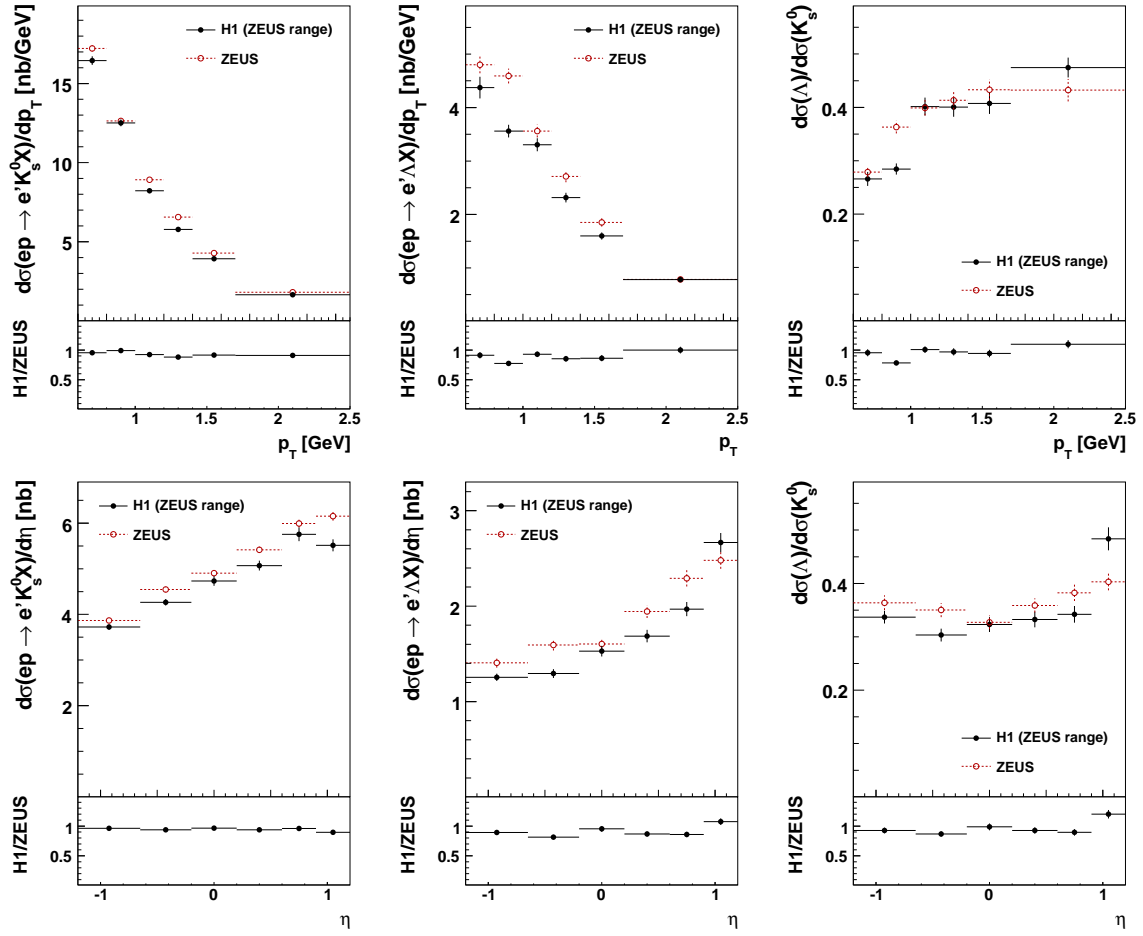
Figure 6.45: The extrapolation K_s^0 (left) and Λ (middel) cross-sections as well as their ratio (right) as a function of p_T (upper row) and η (lower row) measured in the visible range used by ZEUS. On the bottom of all figure, the ratios of the two analyses are appended.

Part II

Search for Exotic Baryonic Resonances Decaying into $\Xi\pi$

Chapter 7

Introduction

Various experiments have reported evidence for narrow signals that can be interpreted as a candidate for the strange pentaquark state Θ^+, see section 2.4. Such states are expected to occur as a flavor antidecuplet within various theoretical models. Therefore, if the state mentioned above is indeed a pentaquark, several other states are expected to exist. Among them, two are expected to decay predominantly into a Ξ baryon and a π meson. In this part of the thesis the search for such states using the H1 data is presented.

7.1 The Decay Channel

This analysis describes a search for the predicted pentaquark states [1] Ξ_{5q}^{--} and Ξ_{5q}^0 (see figure 2.16) in the decay channel $\Xi^-\pi^\pm$. The $\Xi^-(\overline{\Xi}^+)$ particles are identified by their decay into $\Lambda\pi^-(\overline{\Lambda}\pi^+)$, see figure 7.1. The decay chain under investigation is:

$$X^0 \to \Xi^-\,\pi^+ \to (\Lambda\,\pi^-)\,\pi^+ \to ((p\,\pi^-)\,\pi^-)\,\pi^+ \equiv p\,\pi_1^-\,\pi_2^-\,\pi_3^+ \tag{7.1}$$

$$X^{--} \to \Xi^-\,\pi^- \to (\Lambda\,\pi^-)\,\pi^- \to ((p\,\pi^-)\,\pi^-)\,\pi^- \equiv p\,\pi_1^-\,\pi_2^-\,\pi_3^- \tag{7.2}$$

In the neutral decay channel (7.1) the standard (three quark) excited baryonic state $\Xi(1530)^0$ is expected to occur.

7.2 Selection of the Data and the DIS Events

The analysis is performed using 101 pb^{-1} of deep inelastic ep scattering data taken in the years 1996/97 and 1999/2000 (HERA I). The selection of the data events is performed in the same way as discussed in section 4.1, including the selection of the DIS events which is summarised in table 4.1. The only difference with respect to the selection presented in that section is the different y requirement: $0.05 < y < 0.7$. The y range is enlarged because for the search of new resonances, the amount of statistic is more important than the resolution which drops for low y values (electron method). For the same reason of enlarged statistics, events are accepted if they are triggered by any of the subtriggers S0, S1, S2, S3 or S61 which all demand a significant energy deposition in the SpaCal.

---

[1]This includes a search for any other narrow state decaying into $\Xi^-\pi^\pm$.
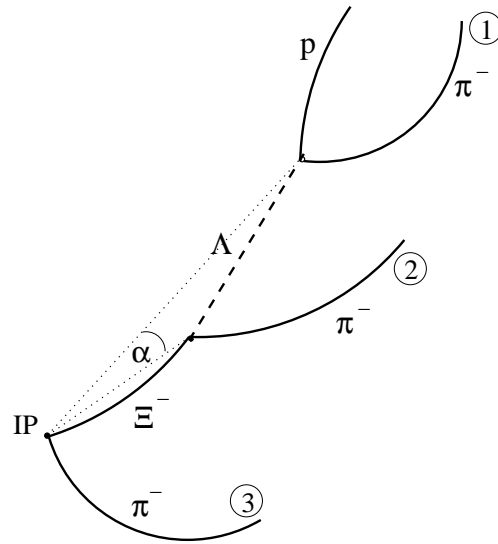
Figure 7.1: The cascade decay of the X^{--}, see equation (7.2). Here, "IP" denotes the interaction point and α the angle between the lines connecting the IP with the Λ and with the Ξ^- decay vertex.

Chapter 8

Reconstruction of the Strange Particles

The strange baryons Λ and Ξ^- are reconstructed and subsequently combined with an additional charged track to form the $X^{0,--}$ candidates (see equation 7.1 and 7.2). The main difference in the selection strategy compared to the measurement of the cross-sections is that the selection criteria for the Λ baryons are opened for more statistics and that no pointing constraint is applied in the vertex fit. The reconstruction of tertiary vertices, which is done for the first time at H1, is cross-checked by measuring the lifetime of the selected Λ and Ξ^- baryons.

8.1 Reconstruction of the Λ Candidates

For the Λ reconstruction (see also section 5) all possible combinations of oppositely charged tracks are fitted to a common vertex. For this analysis the vertex fit is performed in three dimensions using the 3DU routine (see section 4.2.2). Hereby, no constraints on the flight direction of the reconstructed Λ candidates are applied. This is essential since the Λ particles from the Ξ^- decay originate at a vertex that is well separated from the primary interaction vertex ($c\tau_0(\Xi^-) = 4.9\,\mathrm{cm}$). For this reconstruction, only well measured, non-vertex fitted tracks as defined in section 4.2.1 are considered. Again, for the reason of high statistics the selection requirement on the significance of the d_{ca} is weakened to $S_{dca} > 2$. The Λ candidates are retained if the following selection criteria apply:

- Fit probability $P(\chi^2, n) > 1\,\%$,

- $p_T(\Lambda) > 0.3\,\mathrm{GeV}$,

- Radial decay length (in the $r - \phi$ plane) larger than $0.75\,\mathrm{cm}$.

The contamination from $K_s^0 \to \pi^- \pi^+$ decays are rejected by a mass exclusion cut (see section 5.1.2): $|M(\pi^+, \pi^-) - M_{K_s^0}| > 10\,\mathrm{MeV}$. The resulting mass spectra are shown in figure 8.1 for all combinations and for the $p\,\pi^-$ ($\bar{p}\,\pi^+$) combinations separately. Again, more Λ than $\bar{\Lambda}$ particles are reconstructed due to the lower reconstruction efficiency for the $\bar{\Lambda}$ case (higher absorption probability of anti-protons than of protons in the detector material, see also section 5.2). Here, the Λ candidates are an intermediate step in the reconstruction chain allowing

to apply a weak selection (in contrast to the analysis presented in part I). The background in the Λ mass spectrum is reduced by applying selection criteria on the Ξ^- candidates [1] (see section 8.2.3).
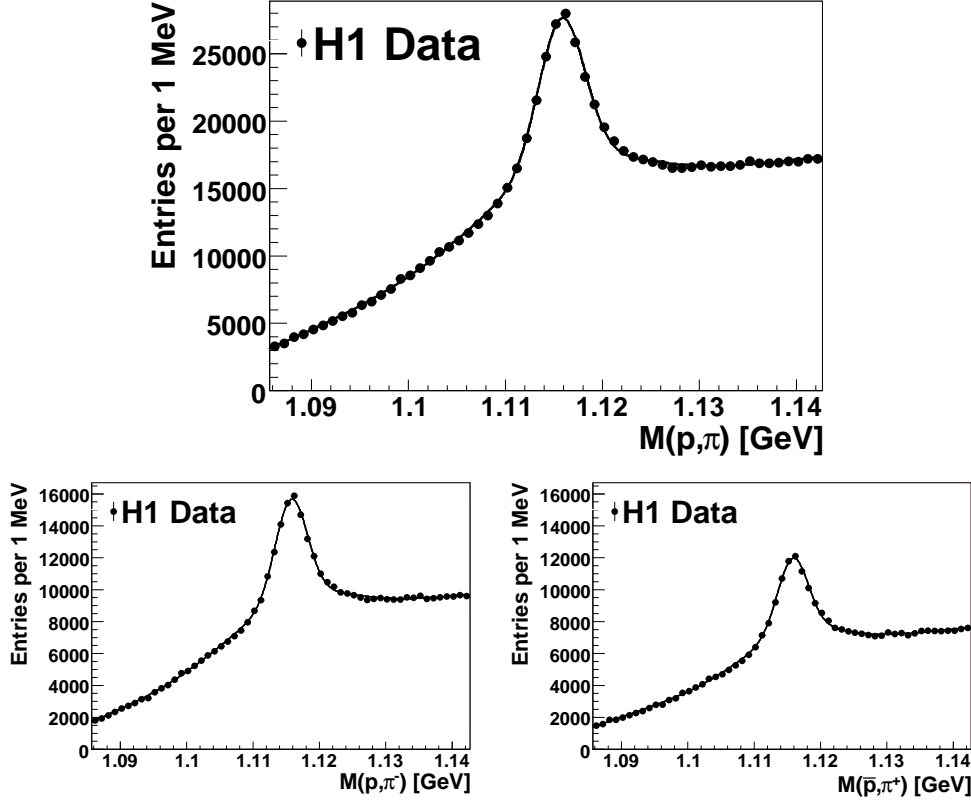
Figure 8.1: The invariant mass spectrum used for the reconstruction of the Ξ^- baryons of all selected Λ candidates including charge conjugation (top) and excluding charge conjugation (bottom left) as well as of all $\overline{\Lambda}$ candidates (bottom right). The solid lines indicate the result of a fit to the data using the function F as defined in equation 5.11.

8.2   Reconstruction of the Ξ^- Candidates

The Ξ^- candidates are formed by fitting the Λ candidates taken within $\pm 8\,\mathrm{MeV}$ of the nominal Λ mass (corresponding to roughly two sigma) with negatively charged tracks assumed to be pions to a secondary vertex using the VVF routine (see section 4.2.2). The vertex fit probability $P(\chi^2, n)$ and the χ^2 distributions are shown in figure 8.2. The fit probability is distributed flat for $P(\chi^2, n) \gtrsim 0.1$, indicating that the fit of the neutral particle candidates with a charged track works appropriately.

The mass spectrum of all Ξ^- candidates is displayed in Figure 8.3. The structure around a mass of $1.28\,\mathrm{GeV}$ is caused by Ξ^- candidates where the same track is used twice, as implied

---

[1]The goal of this analysis is not to extract a clean Λ signal but to maximize the number of reconstructed Ξ^- baryons.
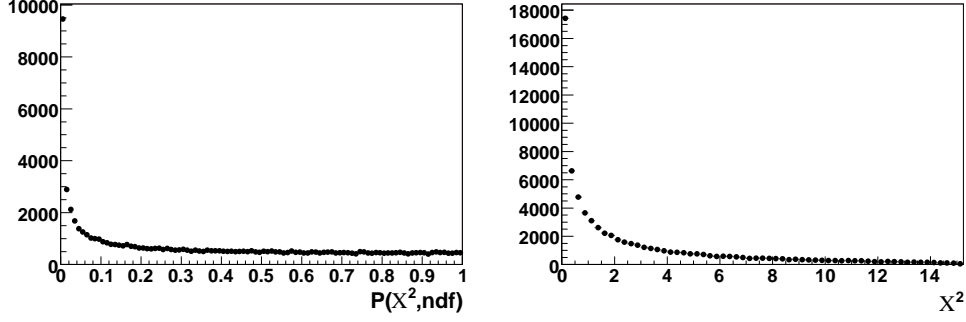
Figure 8.2: The vertex fit probability $P(\chi^2, n)$ and the χ^2 distributions for the fit of the Λ candidates with charged tracks.
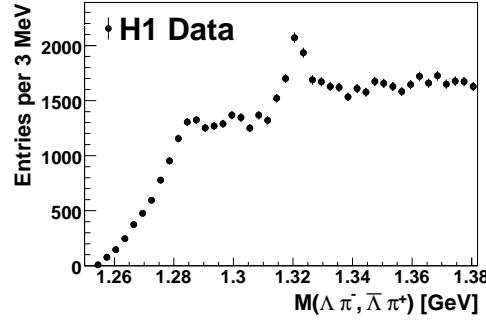
Figure 8.3: The mass spectrum of all $\Lambda \pi^-$ combinations. A signal from the Ξ^- baryon is expected around a mass of 1.32 GeV.

by the two-dimensional distribution of $\Delta_{i,j}(p_T) := p_T(track_i) - p_T(track_j)$ versus $\Delta_{i,j}(\phi) := \phi(track_i) - \phi(track_j)$ (see figure 8.4). A clear clustering around $(\Delta_{i,j}(p_T), \Delta_{i,j}(\phi)) \approx (0,0)$ for like signed tracks contributing to the mass region around 1.28 GeV is observed, whereas for unlike signed tracks or track combinations contributing to the signal region no clustering is observed. These (wrong) Ξ^- candidates are rejected by demanding the $\Delta_{i,j}(p_T)$ and $\Delta_{i,j}(\phi)$ of the like signed track in the Ξ^- decay (i.e. track 1 and 2 in figure 7.1) to lie outside the ellipse with the half-axes 0.025 GeV and 0.23 rad (0.025 GeV and 0.15 rad) centered around 0 GeV, 0.12 rad (0 GeV, -0.12 rad) for the Ξ^- ($\overline{\Xi}^+$) candidates, as indicated in figure 8.4. In figure 8.5 the influence of this elliptical rejection is shown. No signal is lost while the structure around the mass of 1.28 GeV disappears. In the following this requirement against double counting of tracks is applied.

Only Ξ^- candidates fulfiling the following criteria are retained for the further analysis:

- Vertex fit probability: $P(\chi^2, n) > 0.1 \%$,

- Distance of closest approach to the interaction point: $|d'_{ca}(\Xi^-)| < 2.5$ mm

- Angle α (see figure 7.1): $\alpha < 0.6$ rad

These selection criteria are chosen to optimize the $\Xi(1530)^0$ signal. All variables used for the Ξ^- selection are displayed in figure 8.6 together with the corresponding effect on the invariant
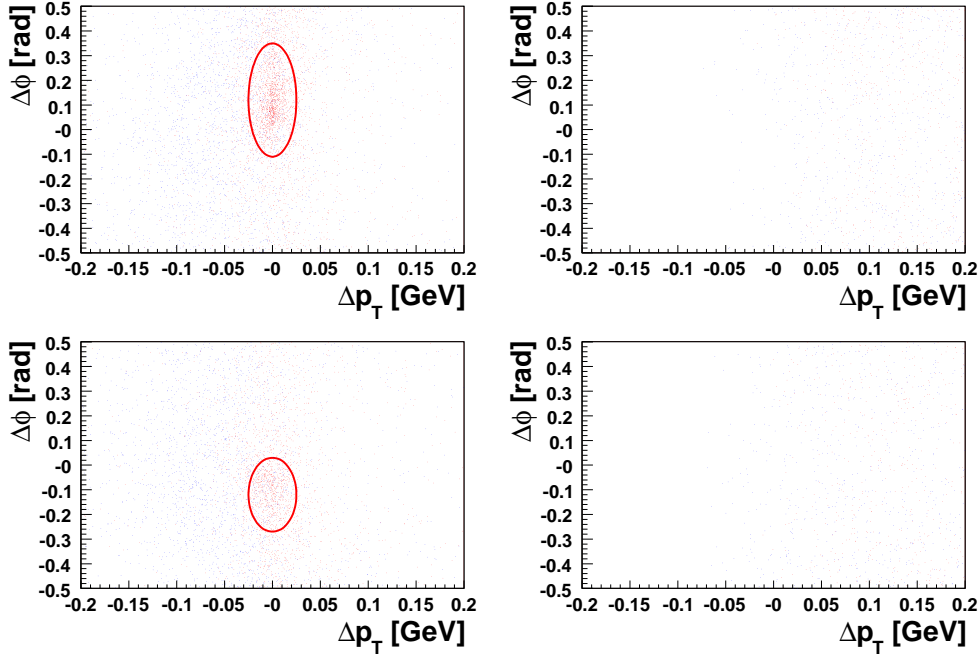
Figure 8.4: The two-dimensional distribution of $\Delta_{i,j}(p_T)$ and $\Delta_{i,j}(\phi)$. Top: for the Ξ^- candidates (charge conjugation excluded) and bottom: for the $\overline{\Xi}^+$ candidates. The left column shows the distribution for like signed tracks and the right one for unlike signed tracks. In red the contribution from candidates with a mass $M \in [1.275\,\mathrm{GeV}, 1.295\,\mathrm{GeV}]$ is shown and in blue from those in the signal region $M \in [1.312\,\mathrm{GeV}, 1.332\,\mathrm{GeV}]$. The ellipses indicate the exclusion region to prevent from double counting.
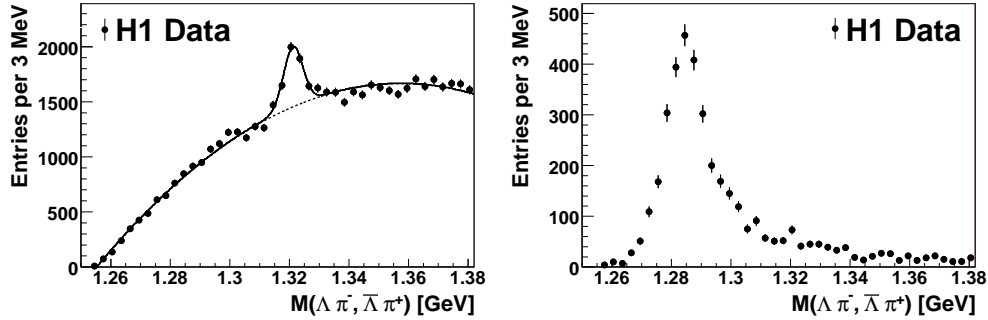
Figure 8.5: The influence of the selection criteria against double counting of tracks on the invariant mass spectrum. Left: the mass spectrum after the rejection and right: the rejected candidates. The solid line in the left figure indicates the result of a fit using the background function defined by equation 8.1 and a Gaussian for the Ξ^- signal.

mass spectrum of the Ξ^- candidates. The mass spectrum of all selected Ξ^- candidates is shown in figure 8.7. For these mass spectra only right charge combinations, i.e. $\Lambda\,\pi^-$ and $\overline{\Lambda}\,\pi^+$ are taken into account. The number of Ξ^- baryons is obtained by fitting an overall function F to the invariant mass spectrum. This function is composed by a Gaussian function
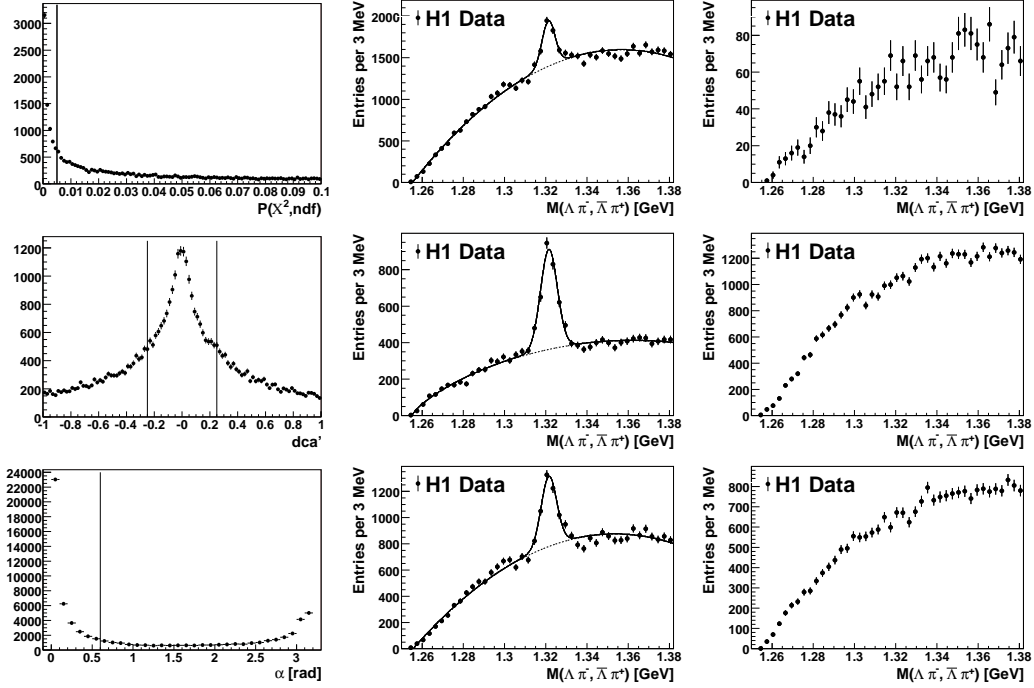
Figure 8.6: Left row: the three variables used for the Ξ^- selection, middle row: the influence of the corresponding selection on the mass spectra and right row: the mass spectra of the rejected candidates. The solid line shows the result of a fit using a superposition of a Gaussian for the Ξ^- signal and the background function defined by equation 8.1.

accounting for the signal and the background function B(M) parameterised by:

$$B(M) = P_1 \cdot (M - M_\Lambda - M_\pi)^{P_2} \cdot (1 + P_3 \cdot M + P_4 \cdot M^2). \tag{8.1}$$

Here, M denotes the invariant $\Lambda\,\pi$ mass and M_Λ (M_π) the nominal Λ (π) mass. This fit yield a total of 1874 ± 64 reconstructed Ξ^- and $\overline{\Xi}^+$ baryons ($\chi^2/n = 62/34$). The signal comprises 1018 ± 48 Ξ^- (charge conjugation excluded) and 835 ± 44 $\overline{\Xi}^+$ baryons. The ratio of Ξ^- to $\overline{\Xi}^+$ is described correctly by the simulation (see section 8.2.1) within the uncertainty. The reconstructed mass of $(1'321.6 \pm 0.2)\,\text{MeV}$ is in good agreement with the world average of $(1'321.31 \pm 0.13)\,\text{MeV}$ [26]. The fit to the individual Ξ^- and $\overline{\Xi}^+$ mass spectra yields a mass that is consistent with the value of the combined fit. The measured width of the Gaussian function is found to be $(4.3 \pm 0.2)\,\text{MeV}$. As expected, the wrong charge combinations $\Lambda\,\pi^+$ and $\bar{\Lambda}\,\pi^-$ do not show any signal (see figure 8.8).
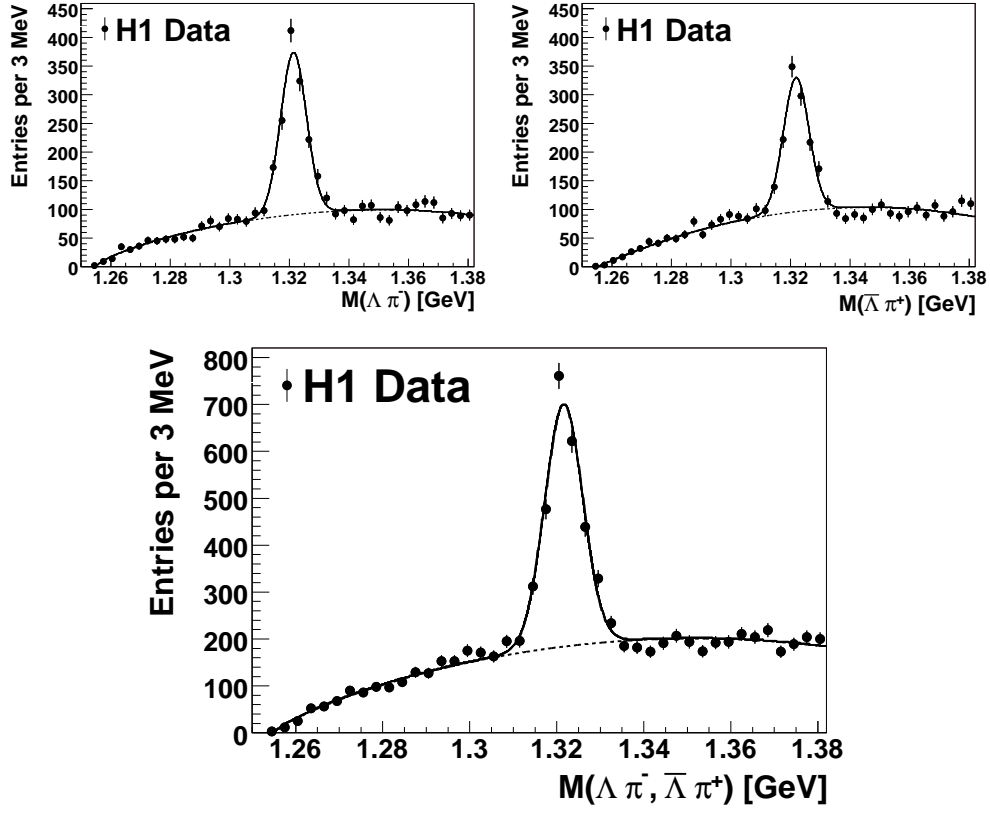
Figure 8.7: The reconstructed mass spectra of the selected Ξ^- candidates. Top left: Only $\Lambda\pi^-$ combinations, top right: Only $\bar{\Lambda}\pi^+$ combinations and bottom: $\Lambda\pi^-$ and $\bar{\Lambda}\pi^+$ combinations. The solid line shows the result of a fit using a superposition of a Gaussian and the background function defined by equation 8.1.
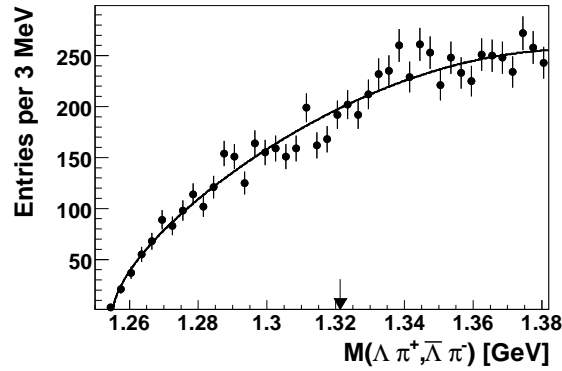
Figure 8.8: The mass spectrum of the wrong charge combinations $\Lambda\pi^+$ and $\bar{\Lambda}\pi^-$. The solid line shows the result of a fit using the background function defined by equation 8.1. The arrow indicates the nominal Ξ^- mass.

8.2.1 Simulation of the Ξ^- Baryons

In order to study resolution and efficiency effects a signal Monte Carlo for the Ξ^- baryon is generated. The simulation uses the PYTHIA generator (see section 2.5.1) in the subprocess 10 (f + f' → f + f'). The reconstructed width of the Ξ^- baryons is 3.7 MeV. Therefore, the width observed in data is described by the simulation at the 10 % level. The reconstructed mass of 1321.5 MeV is PDG compliant. The ratio of Ξ^- to $\overline{\Xi}^+$ is 1.08.

The simulated sample is used to estimate the efficiency of each single selection criteria which is given by the number of reconstructed Ξ^- baryons in DIS events before the corresponding requirement is applied to the number afterwards[2]. The results are listed in table 8.1 ("dc" denotes the cut against double counting). They are all well above 90 %.

Table 8.1: The efficiency of each single Ξ^- selection criterion.

selection criteria	efficiency [%]
dc	98.6
angle	97.6
dca	93.1
prob	98.1

A comparison of the p_T and η spectrum of the Ξ^- candidates between data and simulation is shown in figure 8.9. In order to be independent of the background the mass spectra are fitted in each bin. The simulated sample describes the data reasonably well. In the same figure the width of the Ξ^- signal as a function of p_T and η is shown.

8.2.2 Lifetime of the Ξ^- Baryons

The lifetime of the selected Ξ^- candidates is estimated as a cross check that true Ξ^- baryons are selected. For the lifetime determination the Ξ^- candidates shown in fig 8.7 are divided into bins of $c \cdot \tau$ and a fit to each of the resulting mass spectra is applied, see figure 8.10. The lifetime is determined by the equation

$$l = \gamma \cdot \beta \cdot c \cdot \tau = \frac{p}{m \cdot c} \cdot c \cdot \tau, \tag{8.2}$$

where l denotes the 3-dimensional decay length and $p = |\vec{p}|$ the momentum of the Ξ^- candidates. The Ξ^- candidates are supposed to be produced at the primary vertex. Therefore the separation of the reconstructed Ξ^- decay vertex and the interaction point is used for the calculation of the decay length l.

The generated and reconstructed lifetime of the Ξ^- particles as obtained by Monte Carlo simulation (see section 8.2.1) is shown in figure 8.11. The lifetime extracted from the simulated sample is in agreement with the world average, indicating that the extraction procedure works appropriate. From these two spectra the efficiency as a function of $c\tau$ is extracted according to

$$\epsilon(c\tau) = \frac{N_{allcuts}^{rec}(c\tau)}{N_{Q^2,y}^{gen}(c\tau)}, \tag{8.3}$$

---

[2]All other Ξ^- selection criteria are not applied.
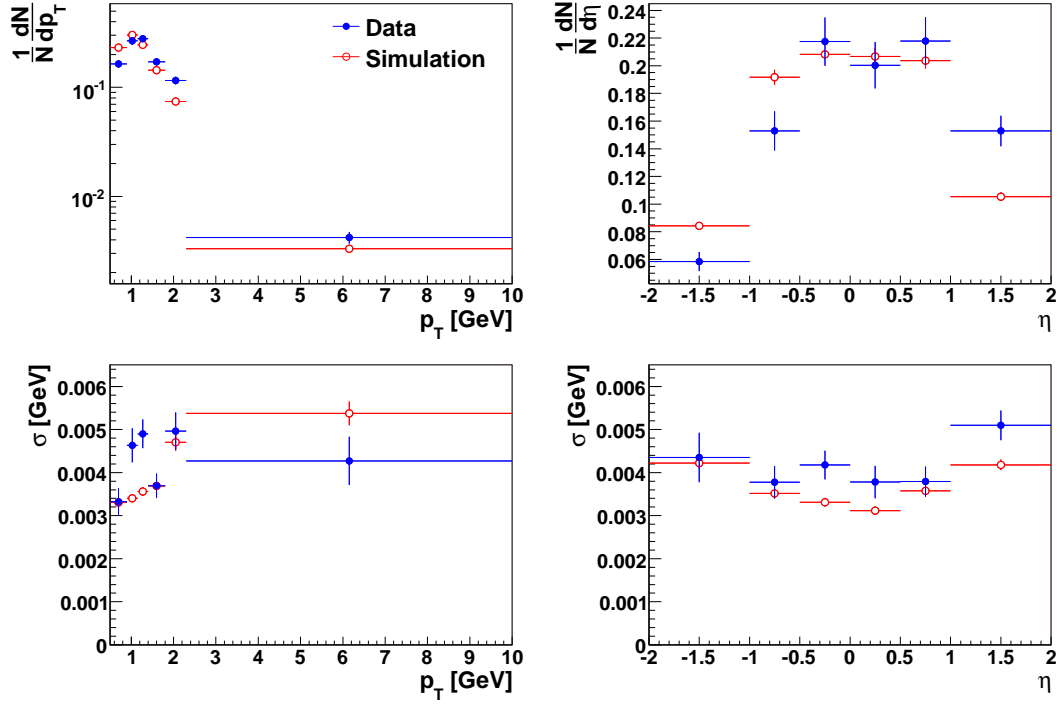
Figure 8.9: Top: The p_T and η spectra of the reconstructed Ξ^- in simulation (red, open circles) and in data (blue, full circles). Bottom: The width of the signal as a function of $p_T(\Xi^-)$ and $\eta(\Xi^-)$.

where $N_{allcuts}^{rec}$ denotes the number of reconstructed Ξ^- applying all selection criteria introduced in previous sections and $N_{Q^2,y}^{gen}$ denotes the number of generated Ξ^- particles in the range $2 < Q^2 < 100\,\mathrm{GeV}^2$ and $0.05 < y < 0.7$. This efficiency factor is applied bin-wise to the data. The reconstructed lifetime spectrum of the selected Ξ^- baryons is shown in figure 8.12. The lifetime of the Ξ^- baryons is extracted by an exponential fit to this spectrum ($\chi^2/n = 33.9/17$) and amounts to:

$$c\,\tau|_{data} \;=\; (5.16 \pm 0.35)\,\mathrm{cm} \tag{8.4}$$

$$c\,\tau|_{PDG} \;=\; (4.91 \pm 0.05)\,\mathrm{cm}. \tag{8.5}$$

Therefore, the measured lifetime is well compatible with the world average. The agreement of the measured lifetime with the PDG value strongly indicates that the selected particles are indeed real Ξ^- particles coming from the interaction point.

8.2.3   The Λ Candidates Contributing to the Ξ^- Signal Region

To ensure that the Ξ^- signal is formed by proper Λ baryons, the mass spectrum of the Λ candidates contributing to the Ξ^- signal is shown in figure 8.13. These Λ candidates are reconstructed backwards from the Ξ^- signal region and show a clean Λ signal justifying the weak Λ selection introduced in section 8.1. The Armenteros-Thompson plot (see section 4.2.4) for the Λ candidates contribution to the Ξ^- signal region is shown in figure 8.13. For this
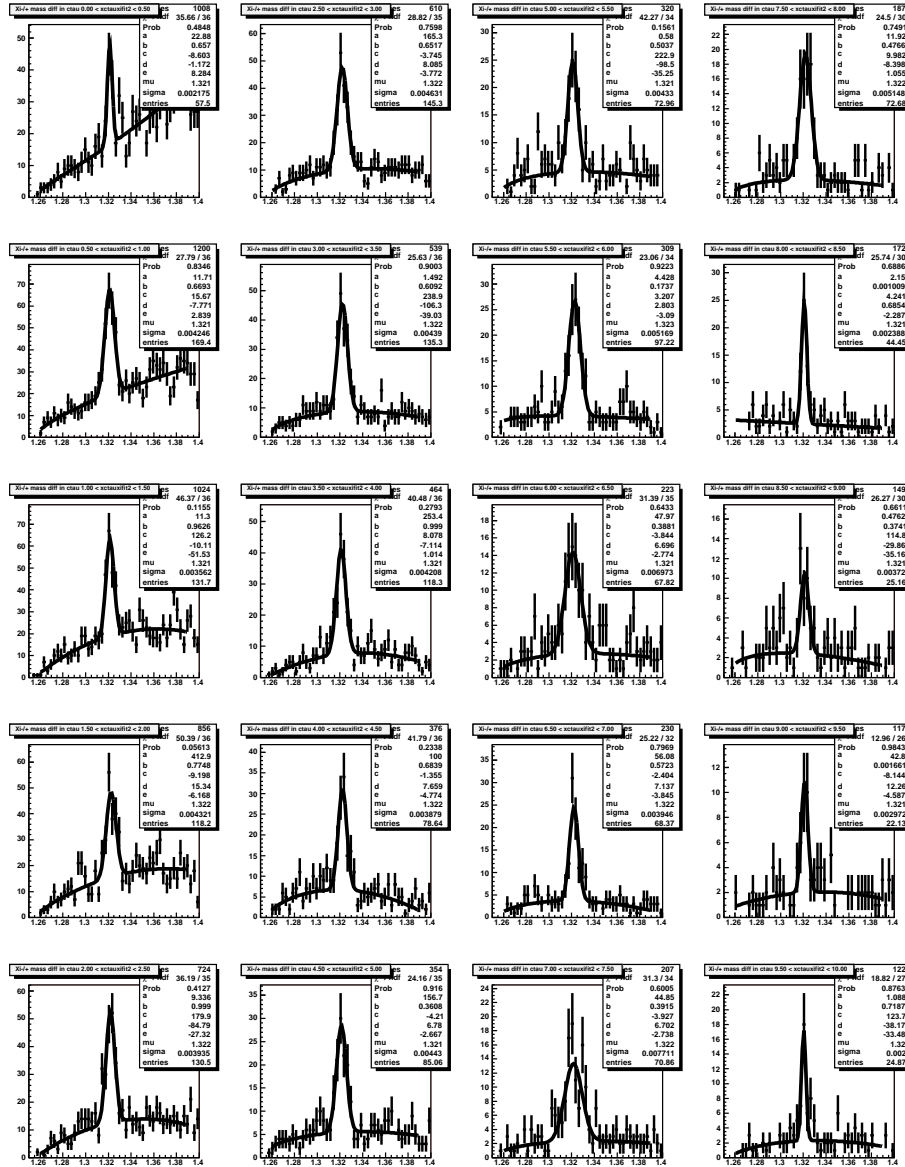
Figure 8.10: The Ξ^- mass spectra in bins of $c \cdot \tau$ (column wise in $0.5\,\mathrm{cm}$ steps for $c \cdot \tau = 0\,\mathrm{cm}$ to $10\,\mathrm{cm}$). The solid line shows the result of a fit using a superposition of a Gaussian and the background function defined by equation 8.6.

figure Λ candidates are selected within $\pm 8\,\mathrm{MeV}$ of their nominal mass. The two semi-ellipses representing the decays $\Lambda \rightarrow p\,\pi^-$ and $\overline{\Lambda} \rightarrow \overline{p}\,\pi^+$ are clearly visible without background. The zeniths are in good agreement with the expectation ($\alpha = \pm 0.69$ and $p_T^{rel} = 0.104\,\mathrm{GeV}$, see table 4.3). No indication for any $K_s^0 \rightarrow \pi\pi$ contamination, which would appear as a semi-ellipse centered at $\alpha = 0$ with maximal $p_T^{rel} = 0.206\,\mathrm{GeV}$, is visible. Therefore, the K_s^0 rejection works appropriately.
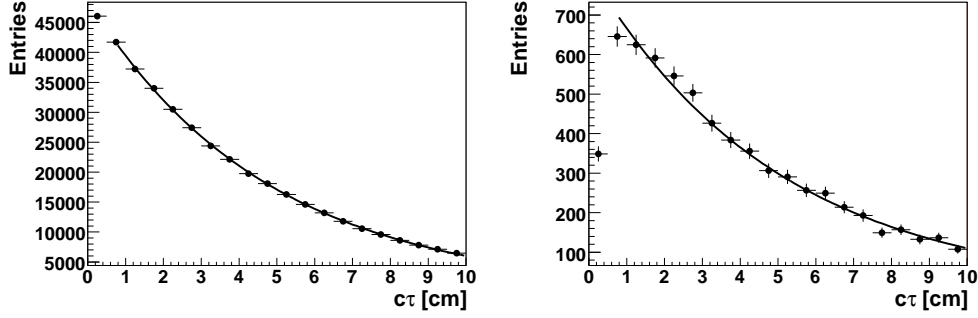
Figure 8.11: The lifetime of the Ξ^- baryons obtained from the simulated sample (left: generated, right: reconstructed).
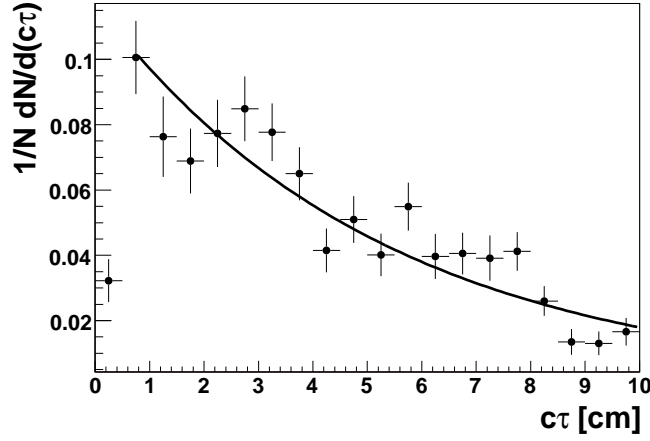
Figure 8.12: The efficiency corrected (bin-wise) number of reconstructed Ξ^- baryons as a function of $c \cdot \tau$. The solid line shows the result of the fit using an exponential function. The errors are purely statistical and are obtained from the fit of the Ξ^- mass spectra.

8.2.3.1   The Lifetime of the Λ Baryons from the Ξ^- Decay

To ensure that real Λ baryons contribute to the signal of the Ξ^- baryon and that the vertex reconstruction of the Λ and Ξ^- decay vertices works appropriate, the lifetime of the Λ candidates from the Ξ^- signal region is determined. Since these Λ's are supposed to be produced at the Ξ^- decay vertex the lifetime calculation provides a test of the vertex separation, see figure 7.1. The lifetime is determined in the same way as for the Ξ^-, see section 8.2.2. For the decay length the 3-dimensional separation of the Ξ^- and the Λ vertex is used.

The efficiency corrected lifetime is shown in figure 8.14. A fit of an exponential function to this spectrum ($\chi^2/n = 17.3/15$) yields a lifetime of $c \cdot \tau (\Lambda) = (7.6 \pm 0.9)$ cm, in agreement with the world average of 7.9 cm. Nevertheless, not all Λ baryons are really related to a Ξ^- decay as can be seen by the number of backwards reconstructed Λ baryons. In total, approximately 2'200 Λ baryons contribute to the Ξ^- signal region while only approximately 1'800 Ξ^- particles are reconstructed. However, the agreement of the measured lifetime with the world average provides a clear indication that the selected particles are indeed real Λ
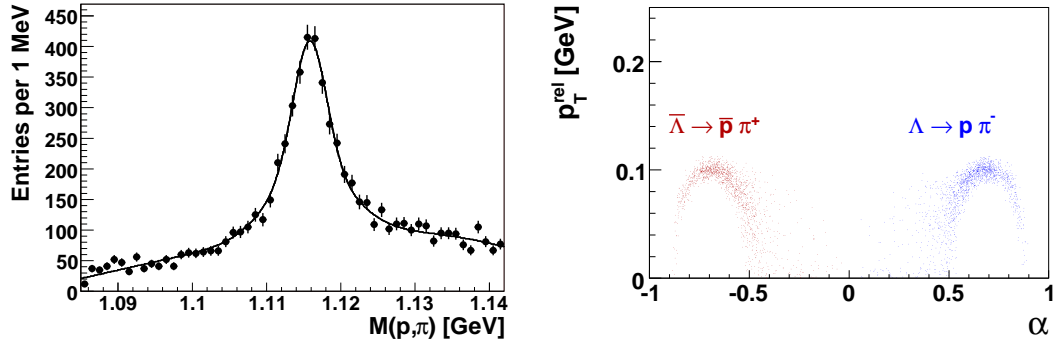
Figure 8.13: Left: The reconstructed mass of the Λ candidates from the Ξ^- signal region (± 10 MeV). All Ξ^- selection criteria are applied, see section 8.2. The solid line shows the result of a fit using a superposition of two Gaussians with a background function defined according to equation 8.1 (with M_Λ exchanged by M_p). Right: The Armenteros-Thompson figure for the selected Λ candidates. The red points represent the contribution from the $\overline{\Lambda}$ candidates and the blue ones those from the Λ candidates.

baryons and that the separation of the Λ and Ξ^- decay vertex is understood.
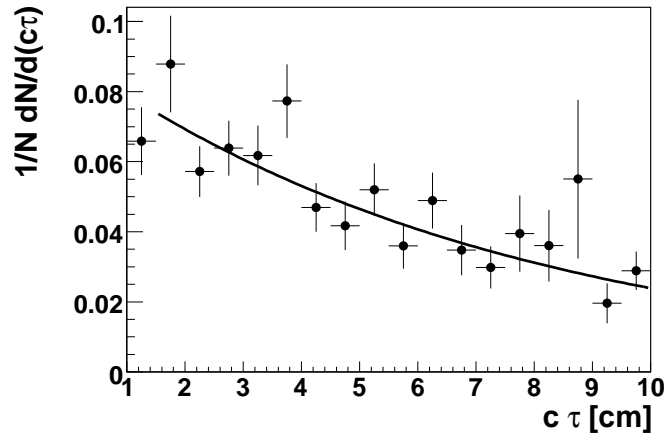
Figure 8.14: The efficiency corrected (bin wise) number of reconstructed Λ baryons from the Ξ^- signal region as a function of $c \cdot \tau$. The solid line shows the result of a fit using an exponential function. The errors are purely statistical and are obtained from the fit of the Λ mass spectra.

8.3   The $\Xi^- \pi^\pm$ Combinations

The $X^{0,--} \rightarrow \Xi^- \pi^\pm$ candidates are obtained by combining the Ξ^- candidates within $\pm 15\,\mathrm{MeV}$ of the nominal mass with an additional track assumed to be a pion. For this additional track only well measured vertex fitted tracks (see section 4.2.1.1) are considered. Furthermore, the significance of the d_{ca} of this track has to be smaller than four. Only $\Xi^- \pi^\pm$ candidates with a transverse momentum larger than $1\,\mathrm{GeV}$ are retained for the further analysis. The mass spectra of all selected $\Xi^- \pi^\pm$ candidates are shown in figure 8.15. The left figure shows the neutral combinations, i.e. $\Xi^- \pi^+$ (including $\overline{\Xi}^+ \pi^-$) whereas the right one shows the charged combinations $\Xi^- \pi^-$ (including $\overline{\Xi}^+ \pi^+$). In the neutral combinations the signal of the well known $\Xi(1530)^0$ baryon [26] is clearly visible as a peak at a mass of $1.53\,\mathrm{GeV}$.
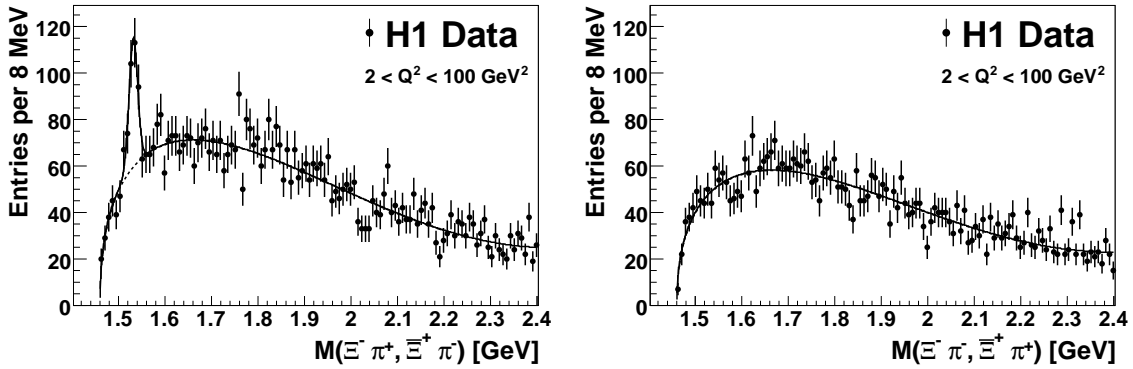
Figure 8.15: Left: The mass spectrum of the reconstructed $\Xi\pi$ candidates for neutral combinations, i.e. $\Xi^- \pi^+$ and $\overline{\Xi}^+ \pi^-$, right: for the charged combinations, i.e. $\Xi^- \pi^-$ and $\overline{\Xi}^+ \pi^+$. The solid line shows the result of a fit using a superposition of a Gaussian (for neutral combinations only) and the background function defined by equation 8.6.

A fit to the neutral mass spectrum with a superposition of a Gaussian for the signal of the $\Xi(1530)^0$ baryon and the background function B(M) parameterised by:

$$B(M) = P_1 \cdot (M - m_{\Xi^-} - m_\pi)^{P_2} \cdot (1 + P_3 \cdot M + P_4 \cdot M^2), \qquad (8.6)$$

where M is the $\Xi\pi$ invariant mass, m_{Ξ^-} and m_π are the nominal Ξ^- and π masses, respectively, and P_i are free parameters. This fit yields a total of 158 ± 25 reconstructed $\Xi(1530)^0$ baryons. The reconstructed mass of $(1532 \pm 2)\,\mathrm{MeV}$ is in perfect agreement with the world average of $(1531.8 \pm 0.3)\,\mathrm{MeV}$. The measured width of $(9.2 \pm 1.5)\,\mathrm{MeV}$ is consistent with the detector resolution and is correctly described by the simulation (see section 9.5). The fit has a $\chi^2/n = 112/110$.

The four possible charge combinations of $\Xi\,\pi$ $(^{-+},^{+-},^{--},^{++})$ are shown separately in figure 8.16. A clear signal representing the $\Xi(1530)^0$ baryon can be observed in both neutral combinations ($\Xi^- \pi^+$ and $\overline{\Xi}^+ \pi^-$) and no signal is seen in the charged combinations.

The neutral and charged combinations are shown in figure 8.17 for different Q^2 ranges [3]:

- $2 < Q^2 < 5\,\mathrm{GeV}^2$

---

[3]This splitting is provided to be sensitive to the existence of a resonance in the different regions of the phase space.
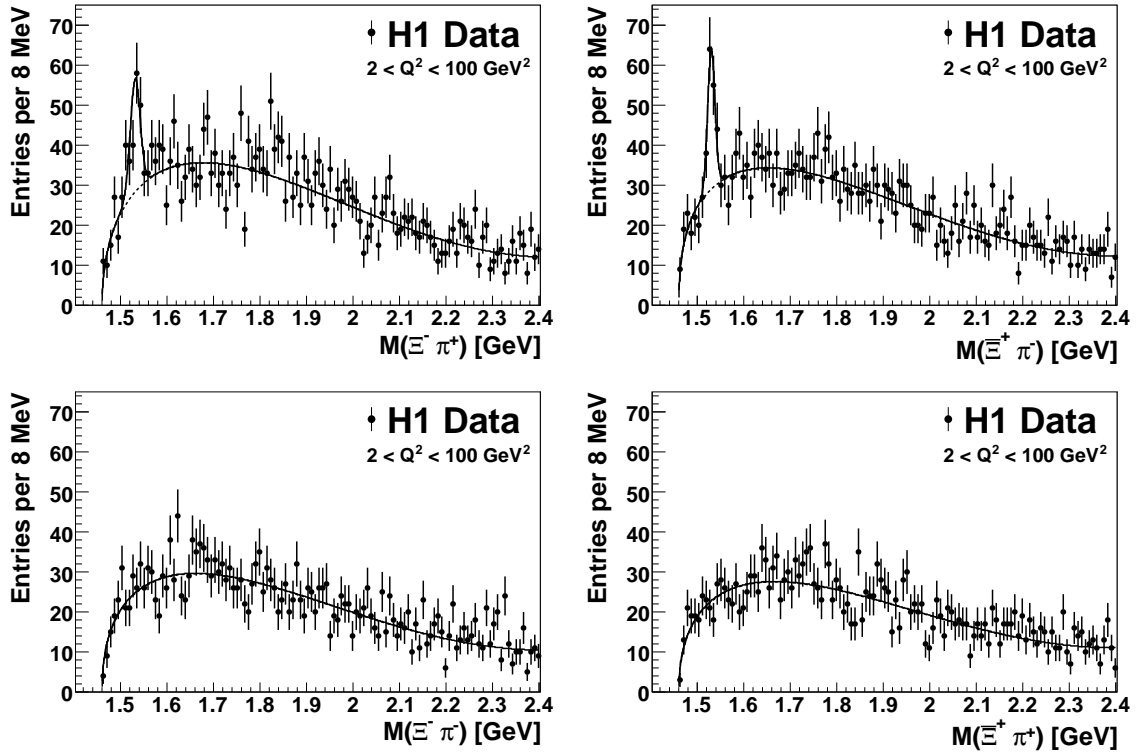
Figure 8.16: The mass spectra of the reconstructed $\Xi\pi$ candidates. Top: neutral combinations (left: $\Xi^-\pi^+$ (charge conjugated states are excluded), right: $\overline{\Xi}^+\pi^-$. Bottom: charged combinations (left: $\Xi^-\pi^-$ only, right: $\overline{\Xi}^+\pi^+$ only). The solid line shows the result of a fit using a superposition of a Gaussian (for neutral combinations only) and the background function defined by equation 8.6.

- $5 < Q^2 < 20\,\mathrm{GeV}^2$

- $20 < Q^2 < 100\,\mathrm{GeV}^2$

The signal of the $\Xi(1530)^0$ baryon becomes marginal for $Q^2 > 20\,\mathrm{GeV}^2$.

Beside the $\Xi(1530)^0$ no significant signal is observed in any of the four possible charge combinations and in any of the Q^2 bins. Therefore the signal reported by the NA49 Collaboration cannot be confirmed with the H1 data.
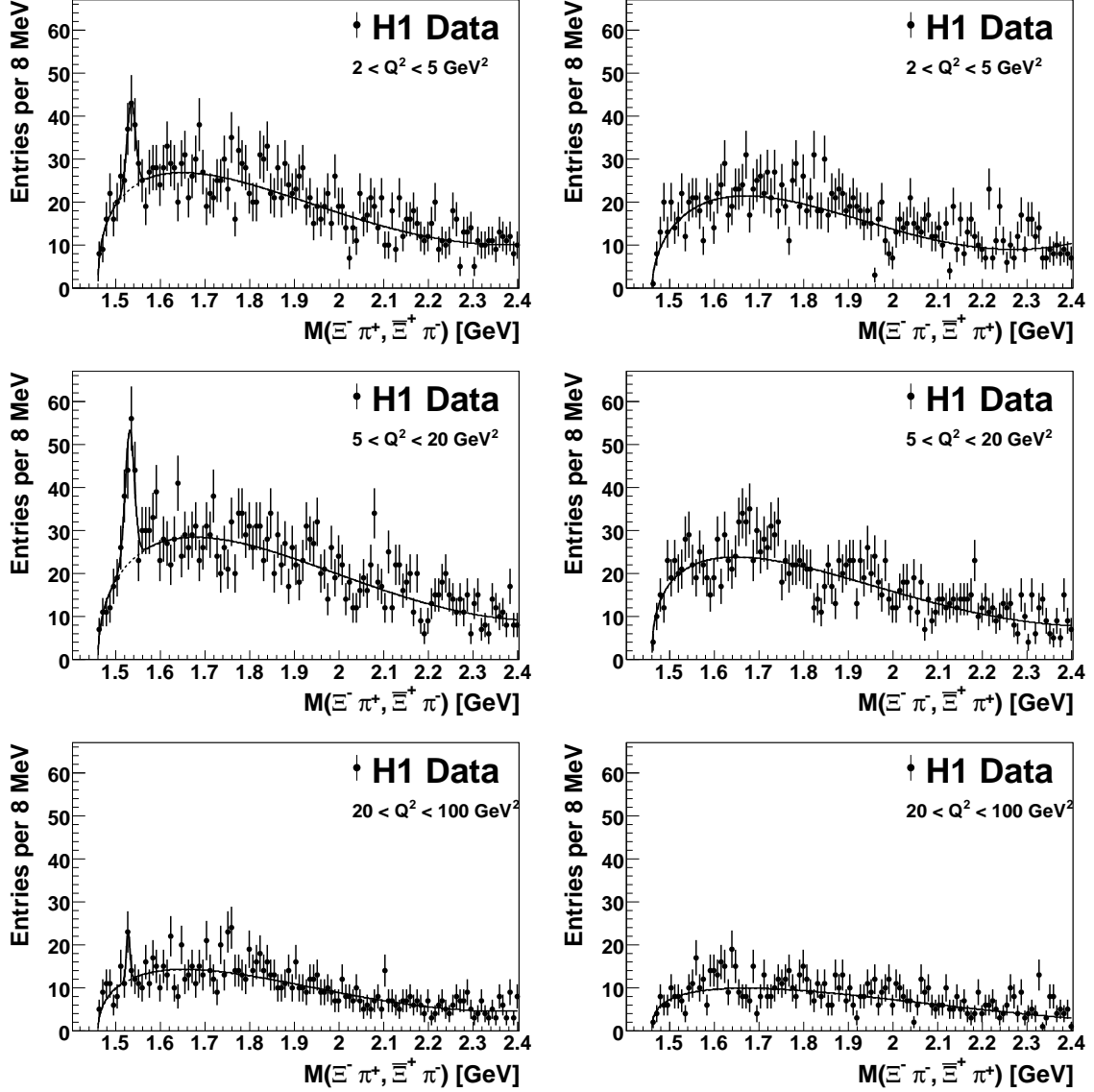
Figure 8.17: The mass spectra of the reconstructed $\Xi\pi$ candidates in Q^2 bins: $2 < Q^2 < 5\,\mathrm{GeV}^2$ (top row), $5 < Q^2 < 20\,\mathrm{GeV}^2$ (middle row) and $20 < Q^2 < 100\,\mathrm{GeV}^2$ (bottom row). The solid line shows the result of a fit using a superposition of a Gaussian and the background function defined by equation 8.6.

Chapter 9

Extraction of the Upper Limit

Because none of the $\Xi\pi$ mass spectra show any prominent structure beside the established $\Xi(1530)^0$ resonance, upper limits are set on the production of new states decaying to $\Xi^-\pi^\pm$ in the mass range $1.6 - 2.3\,\mathrm{GeV}$ for the kinematic region $0.05 < y < 0.7$ and $2 < Q^2 < 100\,\mathrm{GeV}^2$. The procedure of the limit calculation is discussed in section 9.1. After explaining the method, the different components of the limit calculation are extracted and the systematic sources are elaborated (section 9.2 to 9.6). The results of the limit calculation are presented in section 9.7. The chapter ends with a comparison of the results to the ZEUS measurement and a study of the HERA II data.

9.1   Calculation of the Upper Limit

For the limit calculation, the resonance search is performed relative to the number of observed $\Xi(1530)^0 \rightarrow \Xi^- \pi^+$ decays using the ratio R given by:

$$R(M) = \frac{N^{res}(M,q)}{N(\Xi(1530)^0)} \cdot \frac{\epsilon(1530,0)}{\epsilon(M,q)}, \tag{9.1}$$

where $N(\Xi(1530)^0)$ represents the number of observed $\Xi(1530)^0 \rightarrow \Xi^- \pi^+$ and $\overline{\Xi}(1530)^0 \rightarrow \overline{\Xi}^+ \pi^-$ decays. $N^{res}(M,q)$ describes the estimated number of resonance decays depending on the mass M and the charge q of the final state, which is derived from the difference between the observed spectrum and the expected background contribution. The mass M of the $\Xi\pi$ combinations varies from 1.6 to $2.3\,\mathrm{GeV}$. The background distribution is taken to be the fitted function given by equation 8.6. For the calculation of N^{res}, the mass distribution of the signal is assumed to be a Gaussian function with a mean M and a mass-dependent width $\sigma(M)$ corresponding to the experimental mass resolution. This width $\sigma(M)$ varies from 6.8 to 22.8 MeV in the mass range considered here, as obtained from the Monte Carlo simulation, see section 9.5. The term $\epsilon(M,q)$ describes the reconstruction efficiency of the $\Xi\pi$ final state as determined by Monte Carlo simulation, and it depends on the $\Xi\pi$ invariant mass M and on the charge q of the final state. Correspondingly, $\epsilon(1530,0)$ represents the reconstruction efficiency for the neutral $\Xi(1530)^0$ baryon. The ratio of efficiencies in equation 9.1 compensates for the small difference in the reconstruction efficiencies of the $\Xi(1530)^0$ baryon and of a hypothetical baryon state. This factor is discussed in section 9.5.

The ratio $R(M)$ is presumed to be sensitive to the existence of new states, because of the clean signal observed for the established $\Xi(1530)^0$. The ratio also has the advantage that the systematic effects of the acceptances and the reconstruction efficiencies mostly cancel, making it insensitive to detector effects and thus providing a robust method for the limit determination.

An upper limit at the 95% confidence level (C.L.) on $R(M)$, denoted as $R_{u.l.}(M)$, is obtained from the observed spectra using a modified frequentest approach based on likelihood ratios [161]. Each bin of the mass spectrum is treated as a statistically independent counting search providing a uniform representation of the data and is assumed to consist of s_i signal entries and b_i background entries. The confidence level is computed as the ratio of CL_{s+b}, being the probability assuming the presence of both, signal and background at their hypothesised levels to CL_b, which is the probability obtained by assuming the presence of background only. The number of signal entries s_i is varied to achieve the 95 % C.L. These probabilities are calculated using probability distribution functions (PDFun). The PDFun for the signal is assumed to be a Gaussian with a (fixed) mean M and a width corresponding to the experimental mass resolution at that mass M according to the Monte Carlo simulations (see section 9.5.2). This mass M is varied from 1.6 to 2.3 GeV in 8 MeV steps and defines the range where the limit is calculated. The background distribution is modelled according to equation (8.6), see also section 9.4. The systematic uncertainties in the signal $\{s_i\}$ and background $\{b_i\}$ estimations is taken into account by a generalisation of the method of Cousins and Highland [162]. When forming the list of the probabilities of a possible outcome for a certain bin, each entry is affected by the systematic uncertainties on the signal and background estimations. The estimation of the different systematic sources are discussed in section 9.6.

9.2 L4 Weights

The limit calculation works only properly if the input data events are not weighted [1]. Therefore, the limit calculation is carried out with the unweighted mass spectra. Since only the ratio $R(M)$ is determined, the L4 weights cancel each other, as long as they have the same values for the charged and neutral combinations and do not depend on the $\Xi\pi$ mass. As shown in figure 9.1 and in table 9.1 the weights are the same, within errors, for the charged and neutral combinations [2].

Table 9.1: The L4 weights for charged and neutral combinations for different Q^2 ranges.

	$\Xi^- \pi^+$	$\Xi^- \pi^-$
$2 < Q^2 < 100\,\text{GeV}^2$	1.305 ± 0.024	1.272 ± 0.022
$2 < Q^2 < 5\,\text{GeV}^2$	1.545 ± 0.060	1.470 ± 0.054
$5 < Q^2 < 20\,\text{GeV}^2$	1.198 ± 0.015	1.192 ± 0.016
$20 < Q^2 < 100\,\text{GeV}^2$	1.062 ± 0.013	1.054 ± 0.014

---

[1]Using weighted data events in the limit calculation is not correct, because weighted events are not Poisson distributed.

[2]One event with weight 100 (not shown) is observed in the lowest Q2 bin for the neutral combination.
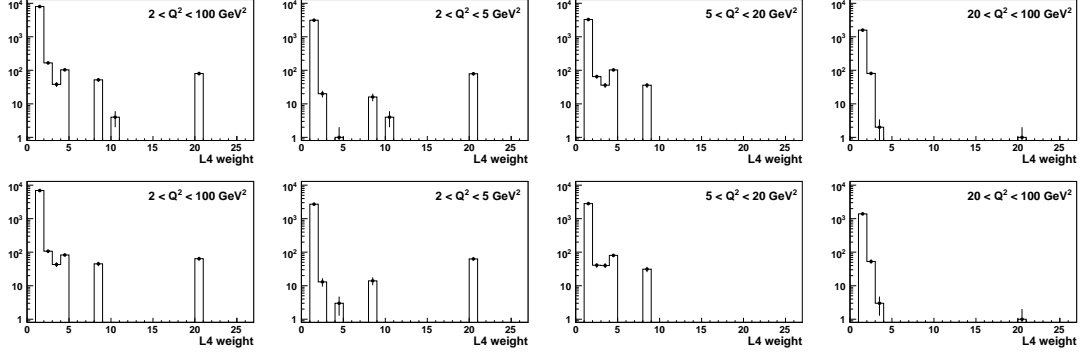
Figure 9.1: The L4 weight distribution for the neutral combinations (upper row) and for the charged combinations (lower row) for different Q^2 ranges. The x-axis shows the weight and the y-axis the number of hypotheses.

The L4 weights are shown in figure 9.2 as a function of the $\Xi\pi$ mass. They are flatly distributed within errors. The lines indicate a fit with a constant function to this distribution. The results of these fits are compatible with the values quoted in table 9.1. Furthermore,
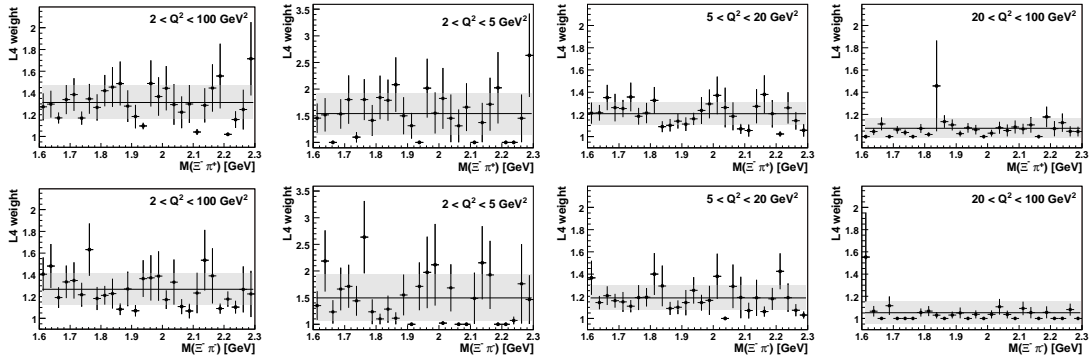
Figure 9.2: The L4 weight distribution as a function of the $\Xi\pi$ mass for the neutral combinations (upper column) and for the charged combinations (lower column) for different Q^2 ranges.

in figure 9.3 the L4 weights normalised to the value obtained from the mass bin containing the $\Xi(1530)^0$ state is displayed. A fit with a Polynomial of degree one gives a slope that is consistent with zero within the uncertainty [3], implying that the L4 weights can indeed be dropped for the limit calculation.

---

[3]The value of the slopes are -0.13 ± 0.15 for the neutral and -0.17 ± 0.16 for the charged combinations.
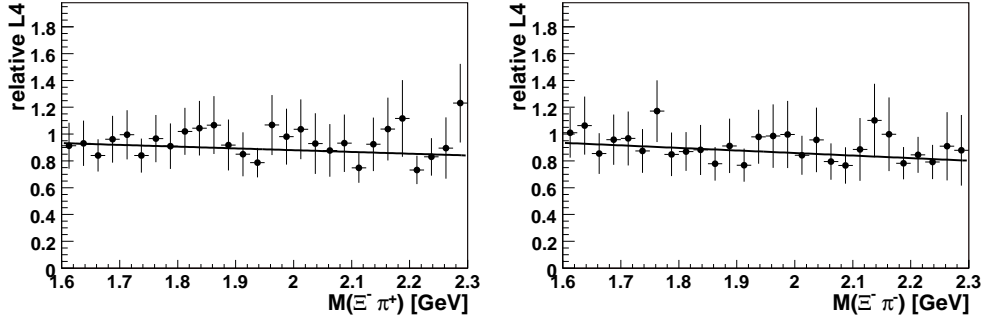
Figure 9.3: The relative L4 weight distribution as a function of the $\Xi\pi$ mass for the neutral combinations (left) and for the charged combinations (right). Shown are the average L4 weight per mass bin of 25 MeV, normalized to the L4 weight of the bin containing the $\Xi(1530)^0$

9.3   Extraction of the $\Xi(1530)^0$ Signal

The ratio of the neutral to the charged combinations is displayed in figure 9.4. This ratio appears to be reasonably flat in the mass region above the $\Xi(1530)^0$ state. Therefore, the utilisation of both mass spectra for a simultaneous background determination is justified, providing a more stable determination of the background contribution. For this simultaneous fit the $\Xi^-\,\pi^-$ mass spectra is artificially shifted by 1.2 GeV and a relative normalization factor for the two mass spectra is introduced. According to equation 8.6 the fit function used is:

$$f(M) = \begin{cases} G(M) + B(M) & (1.461 < M \leqslant 2.4\,\text{GeV}) \\ 0 & (2.4 < M \leqslant 2.66\,\text{GeV}) \\ P \cdot B(M - 1.2) & (2.66 < M \leqslant 3.6\,\text{GeV}) \end{cases} \qquad (9.2)$$

where G(M) denotes a Gaussian and B(M) the background function defined in equation 8.6. The result of this fit is shown in figure 9.5. The normalization factor 'P' is determined to 1.19 ± 0.02, comparable with the value observed in the ratio, see figure 9.4. The fit has a $\chi^2/n = 232/227$. The number of reconstructed $\Xi(1530)^0$ according to this fit is 163 ± 24, with a width of $(9.4 \pm 1.4)\,\text{MeV}$. As expected these values are very similar to the ones obtained by considering only the neutral combinations, see section 8.3. In the following the values
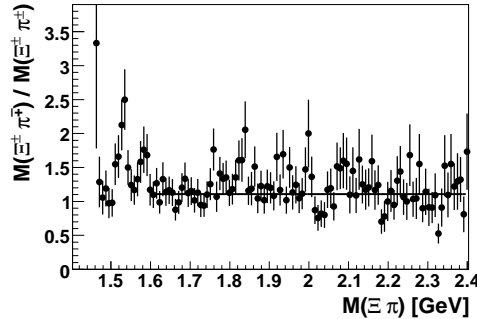
Figure 9.4: The ratio of the $\Xi^-\,\pi^+$ to the $\Xi^-\,\pi^-$ mass spectra. Overlayed is the result of a fit with a constant function.
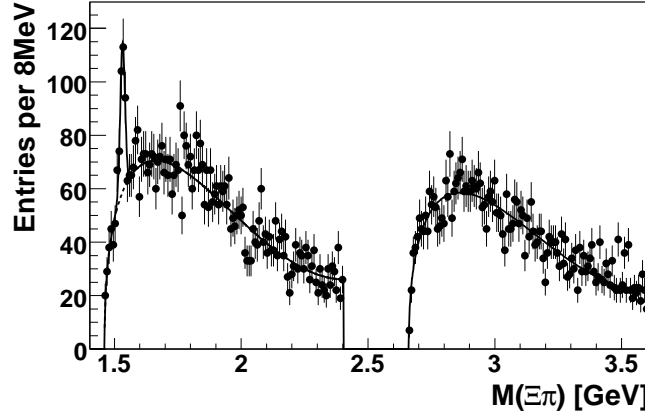
Figure 9.5: The background determination using the simultaneous fit to both mass spectra as described in equation 9.2. The doubly charged mass spectra is artificially shifted by 1.2 GeV.

obtained from the simultaneous fit are used.

9.3.1 Breit-Wigner Fit to the Mass Distributions

The $\Xi(1530)^0$ has an intrinsic Breit-Wigner width of 9.2 MeV which is of the same order as the detector resolution (see section 9.5). Therefore a fit to the mass spectra with a convolution of a Breit-Wigner (for the intrinsic width) and a Gaussian (for the detector resolution) is examined. For this fit the Gaussian G from equation 9.2 is exchanged by the convolution of a Breit-Wigner BW and a Gaussian $\widetilde{G}$:

$$G \Longleftrightarrow \int \widetilde{G}(M') \cdot BW(M - M')dM', \qquad (9.3)$$

where the Breit-Wigner function is given by:

$$BW(M) = \frac{N}{2\pi} \cdot \frac{\Gamma_{BW}}{(M - \mu_{BW})^2 + (\Gamma_{BW}/2)^2}. \qquad (9.4)$$

Here N is a normalization constant, μ_{BW} is the mean value of the peak and Γ_{BW} its width. The integral in equation 9.3 is not analytically solvable and is evaluated as a "Riemann-Sum". For the fit with the convolution function the width of the BW is fixed to the PDG value and the normalization of the Gaussian G is set to one. The free parameters of the fit are therefore $P_1 - P_4$ from the background function (equation 8.6) and the normalization N of the BW as well as the mass of the $\Xi(1530)^0$ and the width of the Gaussian G. These parameters are determined to: $M = (1532.3 \pm 1.6)$ MeV, $N = 182 \pm 27$ and $\sigma = (6.6 \pm 1.8)$ MeV. The detector resolution (width of the Gaussian) obtained by this fit is in good agreement with the value obtained by the Monte Carlo simulation which amount to 5.2 MeV, see section 9.5. The result of the fit to the mass spectra with the convolution function is displayed in figure 9.6. The difference between the convolution and the Gaussian fit comes mainly from the tails of the signal peak. In the same figure the fit to the neutral combinations only (as introduced in section 8.3) is shown. The background determination does not depend on the function used for the $\Xi(1503)^0$ signal and therefore the limit calculation not on the
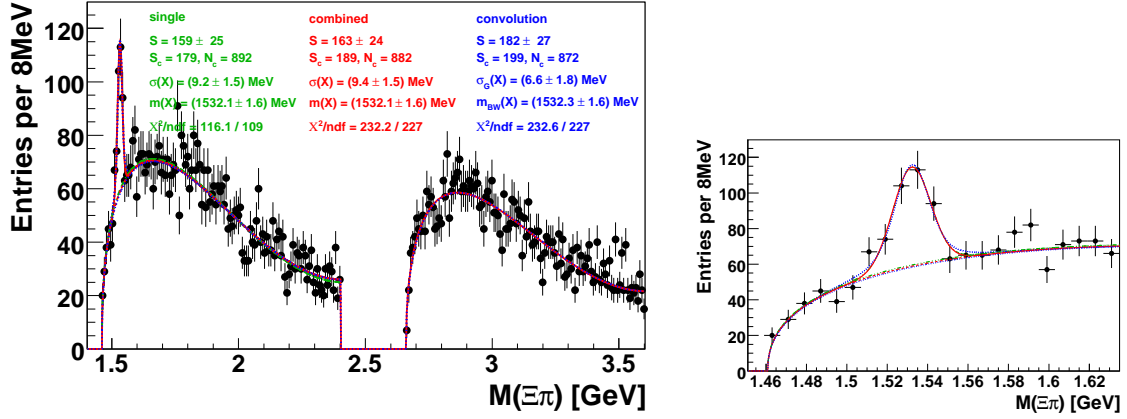
Figure 9.6: The comparison of the different fit functions. Shown are the results obtained from the fit with the Gaussian function for the signal to the neutral mass spectrum only (green dashed line) and to the combined mass spectra (red full line). Furthermore the results from the fit with the convolution function for the signal to the combined mass spectra is displayed (blue dotted line). The figure in the right shows a zoom to the $\Xi(1503)^0$ signal region.

choice of this function. Only the normalisation changes slightly. In the following the values obtained by the simultaneous fit with the Gaussian for the $\Xi(1530)^0$ signal are used in the limit calculation.

9.4 Stability of the Background and the $\Xi(1530)^0$ Signal.

The background shape is a key ingredient for the limit calculation. It is preferably extracted from the data distributions. In order to estimate the quality of the background extraction, the fit to the mass spectra is carried out with different functions and fitting options. The simultaneous fit with a Gaussian for the $\Xi(1530)^0$ signal as described in section 9.3 is referred to as "*standard fit*". The changes in the background shape are quantified by comparing the number of background events within $\pm 3\sigma$ of the considered mass between the standard fit and the variations listed below:

$$\frac{\Delta N_{BG}}{N_{BG}}(M_i) = \frac{N_{BG}^{standard}(M_i) - N_{BG}^{test}(M_i)}{N_{BG}^{standard}(M_i)} \cdot 100,$$

$$N_{BG}(M_i) = \int_{M_i-3\sigma_i}^{M_i+3\sigma_i} f_{BG}(m)dm \tag{9.5}$$

Here M_i is the considered $\Xi\pi$ mass and grows in 8 MeV-steps from 1.6 to 2.3 GeV and $\sigma_i = \sigma(M_i)$ is the resolution of the possible resonance at the mass M_i as obtained by the Monte Carlo simulation.

The following variations V_i to the standard fit are studied:

- **V_1**: Use only one mass spectrum (neutral or doubly charged combinations) at the time.

- **V_2**: Use the convolution of a Gaussian and a Breit-Wigner for the $\Xi(1530)^0$ signal.

- **V_3**: In the standard fit the data points within $\pm 3\sigma$ around the considered mass are excluded.

- **V_4**: An additional Gaussian is added to the standard fit function with a mean value corresponding to the considered mass and a fixed width corresponding to the detector resolution at the given mass. This additional Gaussian accounts for a possible new signal.

- **V_5**: Use in the standard fit the integral of the fit function over the bin instead of the value in the bin center.

- **V_6**: Use an exponential function in the background parameterization instead of the Polynomial of degree 2 (see equation 8.6).

The change in the number of background events according to these variations is displayed in in figure 9.7 for the background in the neutral and doubly charged combinations separately. The relative change in the number of background events is in general less than $2\,\%$. This number is taken into account in the systematic uncertainty used for the limit calculation, see section 9.6.

The influence of the variation of the fit function on the number of reconstructed $\Xi(1530)^0$ baryons is summarised in table 9.2. The variation number in this table correspond to the numbers in the list above. Beside the results obtained by the Breit-Wigner fit, the number of $\Xi(1530)^0$ is well consistent within the statistical uncertainty with the value obtained by the standard fit.

Table 9.2: The change in the number of reconstructed $\Xi(1530)^0 \rightarrow \Xi^- \pi^+$ decays for the six variations investigated. The statistical uncertainty of all numbers is roughly 25.

Variation	$N(\Xi(1530)^0)$
V_1	158
V_2	182
V_3	161 - 167
V_4	163 - 167
V_5	160
V_6	156
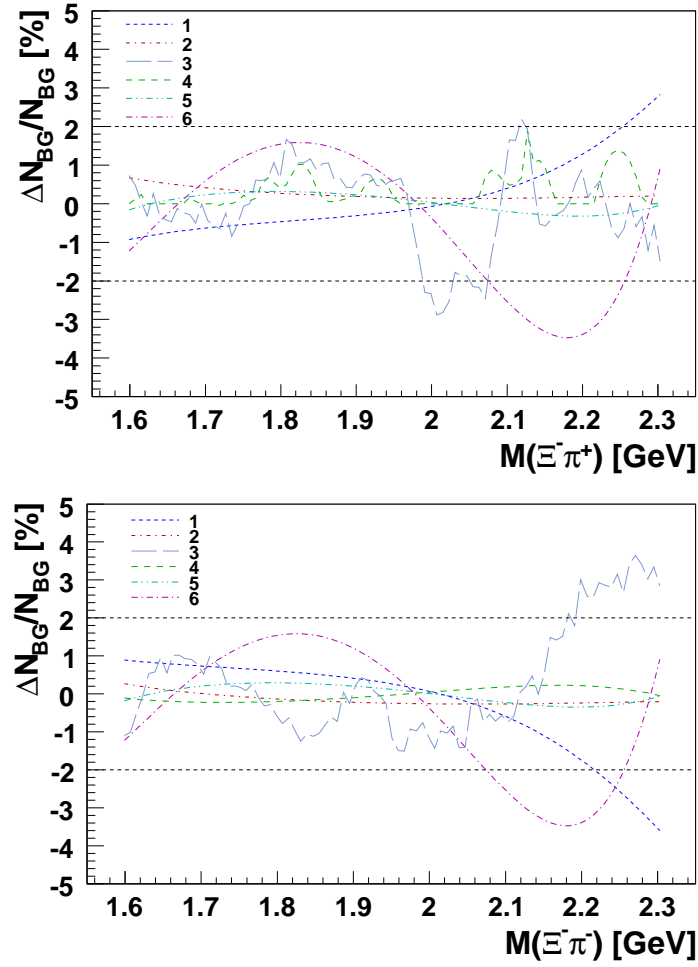
Figure 9.7: The relative change in the number of background events around $\pm 3\sigma_i$ of the $\Xi\pi$ mass M_i for the six variations $V_1 - V_6$ investigated, shown for neutral (top) and for the charged (bottom) combinations. For explanation see text.

9.5 $\Xi^- \pi^\pm$ Combinations in Simulation

To estimate the resolution and the ratio of the efficiencies of the hypothetical pentaquark state and the $\Xi(1530)^0$ baryon, a Monte Carlo simulation based on the PYTHIA 6.2 generator in the subprocess 10 (f + f' →f + f') is used. The hypothetical pentaquark state is simulated for a variety of different masses, widths, types and charge settings to study the following dependencies:

- *Mass dependence:* For the neutral combinations the $\Xi(1530)^0$ state is used. This state has an intrinsic Breit Wigner width of 9.2 MeV. The mass is set to 1.53, 1.6, 1.86 and 2.1 GeV, respectively, keeping the width of 9.2 MeV fixed.

- *Charge dependence:* For the charged combinations the $\overline{\Delta}^{--}$ state is used. The resonance is forced to decay into $\Xi^- \pi^-$. The intrinsic width of this state is set to zero and the mass to 1.53, 1.6, 1.86 and 2.1 GeV, respectively. The use of the $\overline{\Delta}^{--}$ resonance is chosen for technical reasons only (PYTHIA always demands charge conservation).

- *Dependence on the intrinsic width:* A $\Xi(1530)^0$ state with intrinsic width of zero was simulated at a mass of 1.53 GeV in order to study the efficiency dependence on the intrinsic width by comparison with the $\Xi(1530)^0$ with a width of 9.2 MeV .

From these studies the efficiency is found to be independent of the intrinsic width of the simulated particle, which is of particular interest since the width of the possible pentaquark candidates is not precisely known [4]. Furthermore the production mechanism of the pentaquark candidates is also not known. Therefore it is *assumed* that the pentaquark candidates are produced with the same p_T and η spectra as that one of the $\Xi(1530)^0$. To simulate this assumption, the spectra obtained from the $\overline{\Delta}^{--}$ simulation are re-weighted, using a two-dimensional (p_T, η) grid.

9.5.1 Re-Weighting of the $\overline{\Delta}^{--}$ Monte Carlo

The re-weighting is used to estimate the dependence of the efficiency on the p_T and η distributions of the simulated events which is found to be negligible. The re-weighting of the $\overline{\Delta}^{--}$ MC is shown for the mass of 1860 GeV only. Figure 9.8 shows the generated p_T and η spectrum of the $\overline{\Delta}^{--}(1860)$ (red, open circles) and of the $\Xi^0(1860)$ (blue, full circles), both normalized to one. The small differences observed in this figure is leveled out by applying a p_T and η dependent weight factor w_{ij} to the $\overline{\Delta}^{--}$ MC. The index i corresponds to the 11 non equidistant p_T bins (1, 1.25, 1.5, 1.75, 2, 2.25, 2.5, 2.75, 3, 3.5, 4, 6 GeV) and the index j to the 8 equidistant η bins (ranging from -2 to 2), leading to 88 p_T/η bins. The weights are defined by:

$$w_{ij} = \frac{N_{\Xi^0}(p_T^i, \eta^j)/N_{\Xi^0}^{tot}}{N_{\overline{\Delta}^{--}}(p_T^i, \eta^j)/N_{\overline{\Delta}^{--}}^{tot}} (i = 1, 11 \quad j = 1, 8), \tag{9.6}$$

where $N_{\Xi^0(\overline{\Delta}^{--})}(p_T^i, \eta^j)$ denotes the number of generated $\Xi^0(\overline{\Delta}^{--})$ in the i-th p_T and j-th η bin and $N_{\Xi^0(\overline{\Delta}^{--})}^{tot}$ denotes the total number of generated $\Xi^0(\overline{\Delta}^{--})$. The k-th p_T/η bin

---

[4]The width of the pentaquarks is expected to be small. For the Θ^+, measurements and theory suggest $\sigma \lesssim$ 1 MeV.
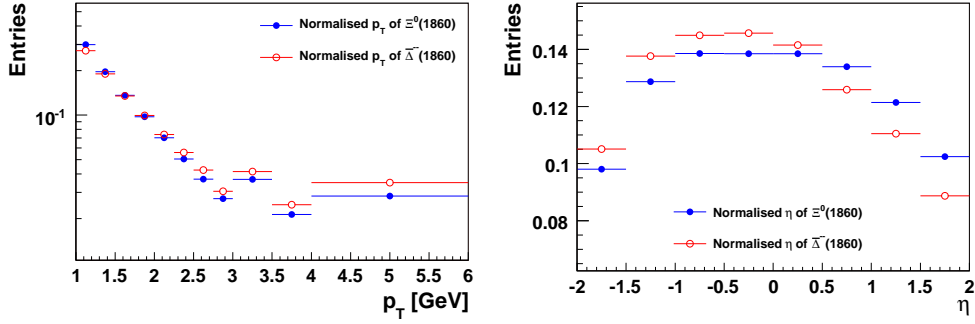
Figure 9.8: The generated p_T and η spectrum of the $\overline{\Delta}^{--}(1860)$ (red, open circles) and the $\Xi^0(1860)$ (blue, full circles) normalized to one.
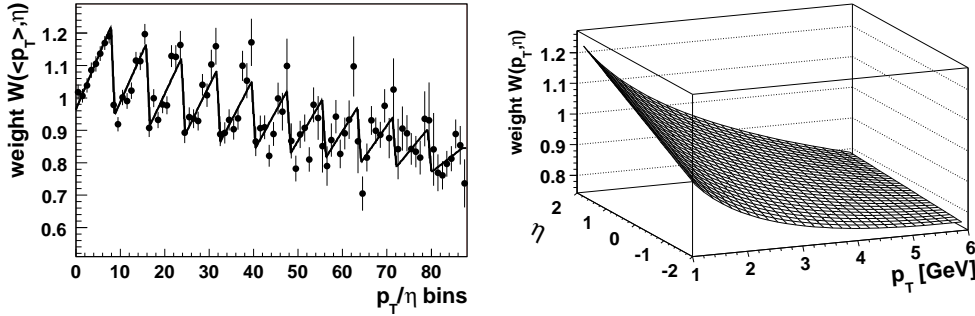
Figure 9.9: Left: The weights in p_T/η bins. The solid line represents the result of the fit using the weight function $W(<p_T>, \eta)$, see equation 9.7. Right: The 2-dimensional weight function $W(p_T, \eta)$.

corresponds to $(i-1) \cdot N_j + j$, where N_j ($=8$) denotes the number of η bins. This numbering scheme is used in figures 9.9 and 9.11. The distribution of the weights is described by a function of the form:

$$W(p_T, \eta) = P_1 + P_2 \cdot \eta + (P_3 + P_4 \cdot \eta) \cdot p_T + P_5 \cdot p_T^{P_6}, \qquad (9.7)$$

where P_i are free parameters. These parameters are determined by a fit to the data (88 p_T/η bins) with the weight function $W(<p_T>, \eta)$, where $<p_T>$ is the mean value of p_T in a given p_T bin ($\chi^2/n = 118/82$), see figure 9.9. For the correction of the $\overline{\Delta}^{--}$ MC the full weight function $W(p_T, \eta)$ is used. This function is also displayed in figure 9.9.

To cross-check the re-weighting procedure, the p_T and η distributions before and after the re-weighting are compared in figure 9.10. The two figures on the top show the distributions after the reweighting (green triangles). Overlaid on the same figure is the distribution of these variables before the reweighting for the $\overline{\Delta}^{--}(1860)$ (red, open circles) and for the $\Xi^0(1860)$ (blue, full circles). The re-weighted distributions of the $\overline{\Delta}^{--}(1860)$ are much closer to those of the $\Xi^0(1860)$ than the original ones, indicating that the re-weighting works properly. This is confirmed by the two figures on the bottom of figure 9.10 where the weights as a function of p_T, $w(p_T)$ (integrated over η) and as a function of η $w(\eta)$ (integrated over p_T) are displayed.
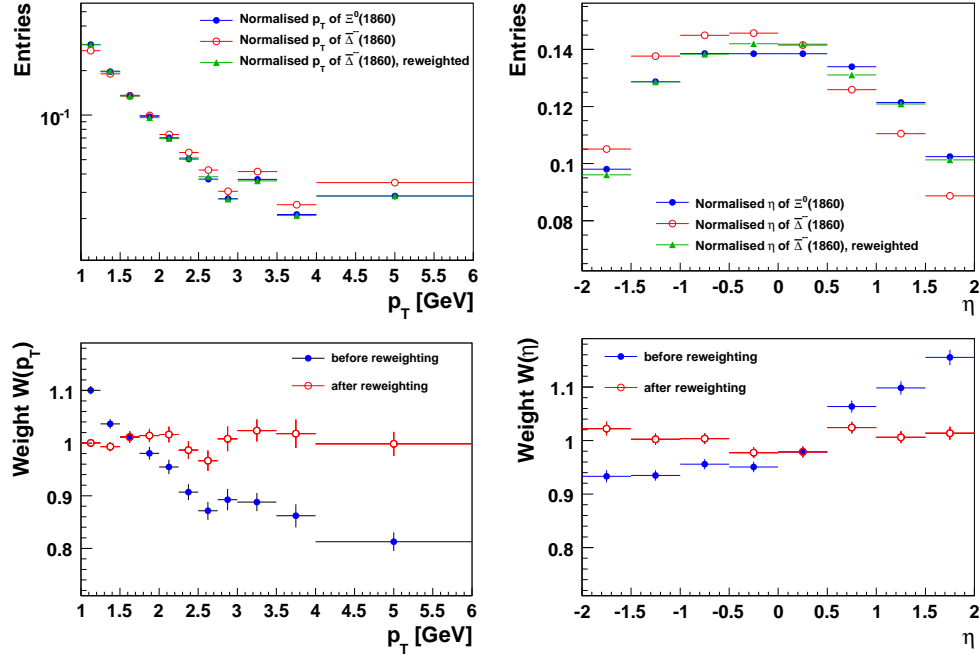
Figure 9.10: Top: The generated p_T and η spectrum of the $\overline{\Delta}^{--}(1860)$ (red, open circles) and the $\Xi^0(1860)$ (blue, full circles) as well as of the reweighted $\overline{\Delta}^{--}(1860)$ (green, full triangles). All distributions are normalised to one. Bottom: The weights in p_T (left) and in η (right) for the mass of 1860 GeV before (blue, full circles) and after (red, open circles) the re-weighting.

After the reweighting these weights are distributed flatly around one[5].

The weight function $\mathrm{W}(<p_T>, \eta)$ is displayed in figure 9.11 for all four masses and show only a weak dependence on the mass.

However, the change in the number of reconstructed particles (and therefore in the efficiency) due to the reweighting is very small. It amounts to roughly 1 %.

9.5.2 Dependence of the Resolution on the Mass

For the estimation of the width of the possible pentaquark signal the simulation with the $\overline{\Delta}^{--}$ (intrinsic width zero) is used. The reconstructed mass spectra are shown in figure 9.12 and the resulting dependence of the width on the mass is shown in figure 9.13. To parameterize this dependency a fit using a polynomial of degree one is performed. The resulting function is:

$$\sigma(M) = -29.7\,\mathrm{MeV} + 0.0228 \cdot M\,[\mathrm{MeV}], \tag{9.8}$$

where M is the mass of the hypothetical pentaquark state. This function enters the limit calculation.

---

[5]For a perfect reweighting the ratio should be exactly one for all p_T and η values.
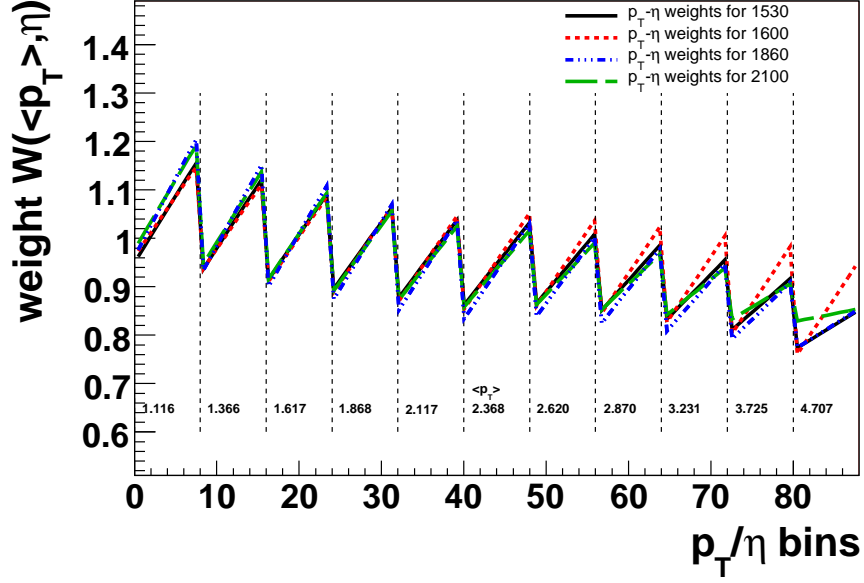
Figure 9.11: The 2-dimensional weight function $W(< p_T >, \eta)$ for the four masses. The numbers quoted at the bottom of the figure are the mean p_T values for the 11 p_T bins, given in GeV.
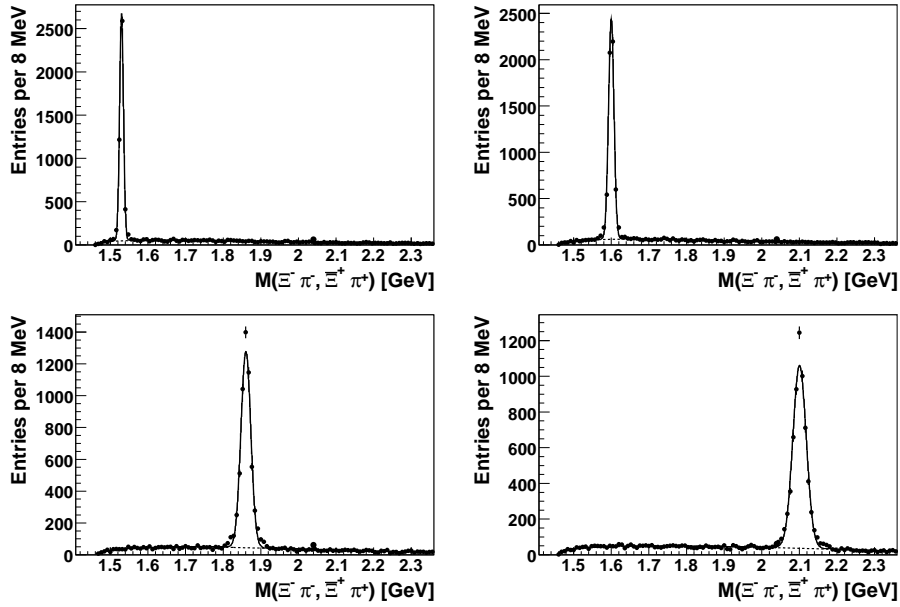
Figure 9.12: The reconstructed $\Xi^- \pi^-$ mass in the simulation for the four generated masses. For these figures the reweighting is applied.
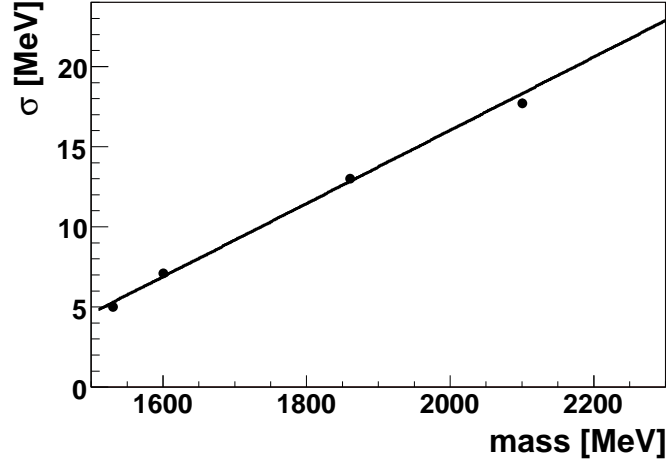
Figure 9.13: The mass dependent resolution of the possible pentaquark signal obtained from the $\overline{\Delta}^{--}$ Monte Carlo simulation. The error on the individual points is of the order of 2 %.

9.5.3 Determination of the Efficiency

The efficiency, which is used in equation 9.1, is determined in the kinematical visible range:

$$\epsilon(M,q) = \frac{N_{allcuts}^{rec}(M,q)}{N_{(p_T^{gen}>1\,GeV,|\eta^{gen}|<2)}^{gen}(M,q)}, \tag{9.9}$$

where q denotes the total charge of the $\Xi\,\pi$ final state and M its mass. Thus, the efficiency is determined for the neutral and charged combinations separately. As mentioned in section 9.5.1 the number of reconstructed $\Xi^-\,\pi^-$ is re-weighted in p_T and η. The reconstructed mass spectra for the neutral and charged combinations (before and after the re-weighting) are shown in figure 9.14 for the generated mass of 1860 MeV.

As fit function a superposition of one or two Gaussian [6] with the background function defined by equation 8.6 is used. Although the double Gaussian fit gives better results, the single Gaussian fit is used for the efficiency determination in order to be compatible with the limit calculation where a possible signal is described by a single Gaussian. Furthermore the uncertainty on the efficiency is small compared to the most dominant source which is the statistical uncertainty of the $\Xi(1530)^0$ signal (see section 9.6). The overall uncertainty on the number of reconstructed particles has 2 components: a) A statistical one which is just the uncertainty obtained by the Gaussian fit and the difference of the number of reconstructed particles from the Gaussian fit and b) the number obtained by counting all entries within $\pm$ 64 MeV around the nominal mass and subtracting the integrated (over the same range) background function. The efficiencies for the charged ($\epsilon(M,--)$) and neutral ($\epsilon(M,0)$) combinations are shown in figure 9.15. The uncertainty of the efficiencies varies from 2.7 to 7.5 %. To parameterize the mass and charge dependencies of the efficiency a fit using a

---

[6]As a cross-check also a double Gaussian fit is applied. The result of this fit is also shown in figure 9.14, right column.
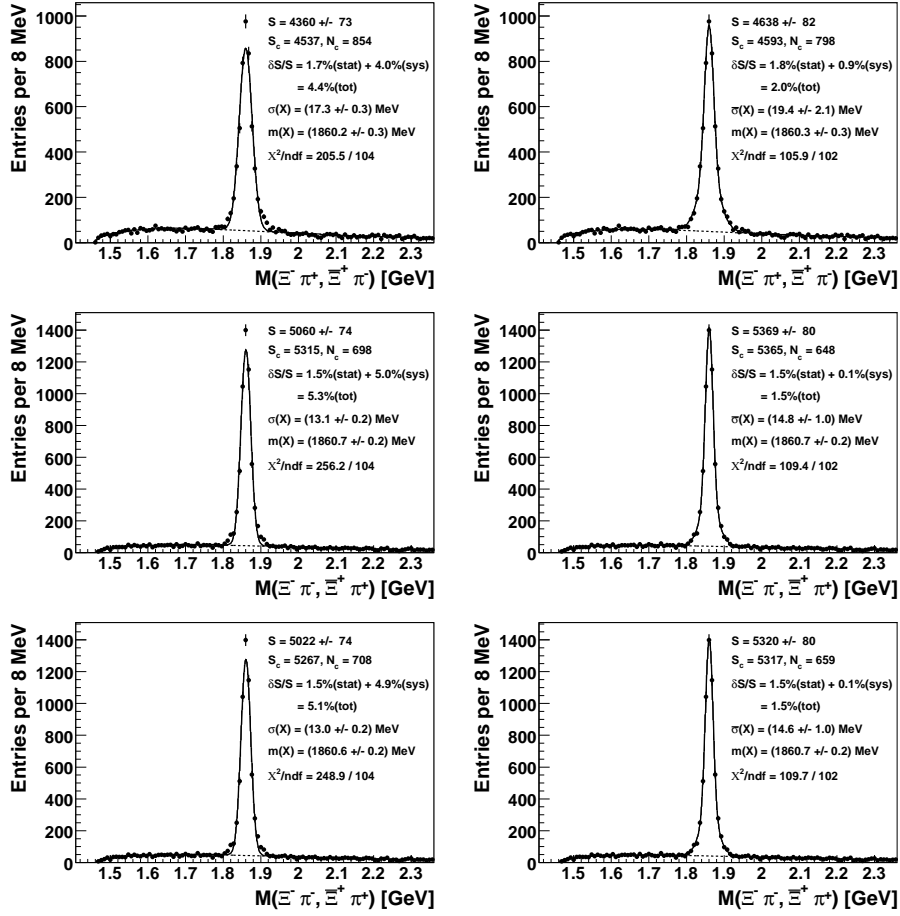
Figure 9.14: The reconstructed mass spectra for the generated mass of 1860 GeV in the simulation for the neutral combinations (upper row), for the charged combinations before (middle row) after (lower row) the re-weighting. The left column shows the results obtained by a single Gaussian fit and the right one for a double Gauss fit. S_c denotes the number of reconstructed particles by counting all entries within $\pm$ 64 MeV of the reconstructed mass and subtracting the integrated (over the same range) background function and $\delta S/S$ the uncertainty on the signal. The systematic uncertainty takes the difference in the number of reconstructed particles obtained by the counting method and the Gaussian fit into account.

polynomial of degree one is performed. The resulting functions shown in figure 9.15 are:

$$\epsilon(\Xi\,\pi|M,0) = 4.388 + 0.898 \cdot M \,[\text{GeV}] \tag{9.10}$$

$$\epsilon(\Xi\,\pi|M,--) = 5.005 + 0.696 \cdot M \,[\text{GeV}], \tag{9.11}$$

where M is the mass of the hypothetical pentaquark state. These functions are used for the efficiency correction, see equation 9.1.
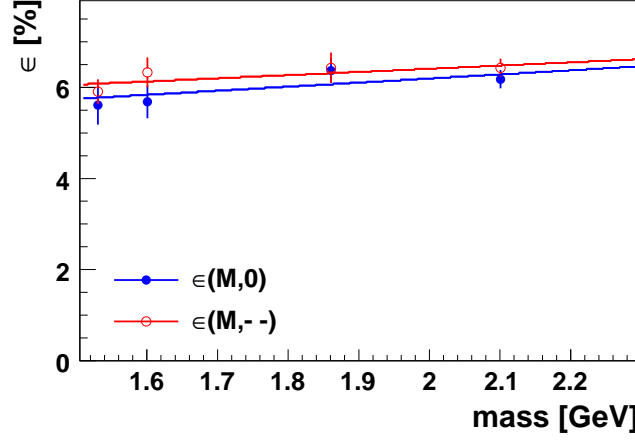
Figure 9.15: The reconstruction efficiency $\epsilon(M, 0)$ for the neutral combinations (blue, full circles) and $\epsilon(M, --)$ for the charged combinations (red, open circles).

9.6   Systematic Uncertainties

The final results are represented as an upper limit $R_{u.l.}$ on the ratio R introduced in equation 9.1. Since $R_{u.l.}$ denotes the 95 % C.L. upper limit on the ratio R of the number of resonant $\Xi\pi$ combinations to the number of observed $\Xi(1530)^0$ baryons, the systematic uncertainties in the measurement enters only through the 95 % C.L. upper limit of observed resonant $\Xi\pi$ combinations ($N^{res}(M, q)$) [7].

The systematic uncertainties for the $R_{u.l.}$ calculation comprises the following contributions:

- **Number of $\Xi(1530)^0$**: for the uncertainty on the overall number of $\Xi(1530)^0$ baryons the statistical uncertainty derived from the fit of **16 %** is used, see section 8.3.

- **Reconstruction efficiency**: The uncertainty of the reconstruction efficiency $\epsilon(M, q)$ is smaller than 7.5 % for all masses considered in this analysis. Therefore a total systematic uncertainty of **7.5 %** for the ratio $\frac{\epsilon(1530,0)}{\epsilon(M,q)}$ is taken. The two different efficiencies $\epsilon(1530, 0)$ and $\epsilon(M, q)$ appearing in the ratio are of course strongly correlated and therefore adding the uncertainties of these two efficiencies would be too conservative. Due to this correlation, even the 7.5 % is a conservative approach.

- **Width of the possible signal**: The uncertainty due to the width of the possible signal has two components: a) the uncertainty determined in the simulation, which is below 2 % for the masses considered here and b) a possible difference of the width between simulation and data. This difference is assumed to be the same as that of the $\Xi(1530)^0$ baryon. The width of the $\Xi(1530)^0$ baryon in simulation is (9.5 ± 0.2) MeV, whereas in data it is (9.2 ± 1.4) MeV. The uncertainty on the width in data is already taken into account in the uncertainty of the number of $\Xi(1530)^0$. Thus, applying the uncertainty in the reconstructed width of the $\Xi(1530)^0$ in data as a systematic uncertainty for the width of the possible signal is too conservative. Therefore, the relative difference

---

[7]Otherwise $R_{u.l.}$ would not denote an 95 % C.L. limit anymore.

between data and simulation from the $\Xi(1530)^0$ studies is used as estimation of the pentaquark width uncertainty. This is $\frac{9.5-9.2}{9.2} \simeq 4\,\%$. The resulting total uncertainty of the width of the possible signal is $\sqrt{2\,\%^2 + 4\,\%^2} \simeq \mathbf{5\,\%}$.

- **Background uncertainty**: The uncertainty on the background distribution is assessed by performing the fit under different assumptions, see section 9.4. The differences are found to be in general less than 2%.

- The uncertainties due to the inclusive DIS event selection and the trigger efficiency are assumed to cancel in the ratio.

The limit calculation distinguishes between uncertainties applied on the possible signal and uncertainties applied on the background. The first three points mentioned above contribute to the uncertainty of the signal. The contributions on the signal are added in quadrature and the resulting total systematic uncertainty of 18 % enters the limit calculation. The uncertainty on the background of 2 % enters the limit calculation separately.

9.7 Results of the Limit Calculation

The final results are displayed in terms of upper limits $R_{u.l.}$ on the ratio R defined by equation 9.1. All uncertainties summarized in section 9.6 are taken into account for the limit calculation. The results are presented in figure 9.16 and 9.17, showing in the upper part the $\Xi\pi$ mass spectrum for the charged and neutral combinations, respectively (same spectra as displayed in figure 8.15). In the lower part, the 95% C.L. upper limit $R_{u.l.}(M)$ is given; it varies from 0.12 to 0.45 in the mass range 1.6 - 2.3 GeV for the charged combinations and from 0.1 to 0.5 for the neutral ones.

These limits are quoted for the kinematic region $2 < Q^2 < 100\,\mathrm{GeV}^2$, $0.05 < y < 0.7$, $p_T(\Xi\,\pi) > 1\,\mathrm{GeV}$ and $-1.5 < \eta(\Xi\,\pi) < 1.5$. Furthermore, the limits are derived under the assumption that the new resonant states are produced by a similar mechanism as the $\Xi(1530)^0$, that they decay into $\Xi^-\,\pi^\pm$ with a 100 % branching ratio and that their intrinsic widths are small (i.e. below detector resolution).

If the signal extraction of the $\Xi(1530)^0$ is performed by a convolution of a Gaussian and a Breit-Wigner function (see section 9.3.1, the limits would be 10 % lower. Since the systematic uncertainty in the number of reconstructed $\Xi(1530)^0$ baryons is left unchanged by this variation (16 %), the calculation of the upper limit is not affected at all by the change of the signal function, but only the normalisation changes.

9.7.1 Cross-Check of the Limit Calculation

Without a signal, the upper limit should follow the statistical fluctuations of the background. Therefore, the comparison of these two quantities provide a cross-check of the limit calculation The upper limit on R for the doubly charged and neutral combinations shifted by its mean value is displayed in figure 9.18 as a dotted curve. In addition, the weighted deviation of the data points from the background function given by $\frac{N_{Signal}^{weighted}(M_i)}{N_{BG}^{weighted}(M_i)} - 1$, where M_i grows in 8 MeV steps from 1.6 to 2.3 GeV is overlaid. Since the possible signal in the limit calculation is assumed to be Gaussian, the deviation from the background at point M_i counts more than
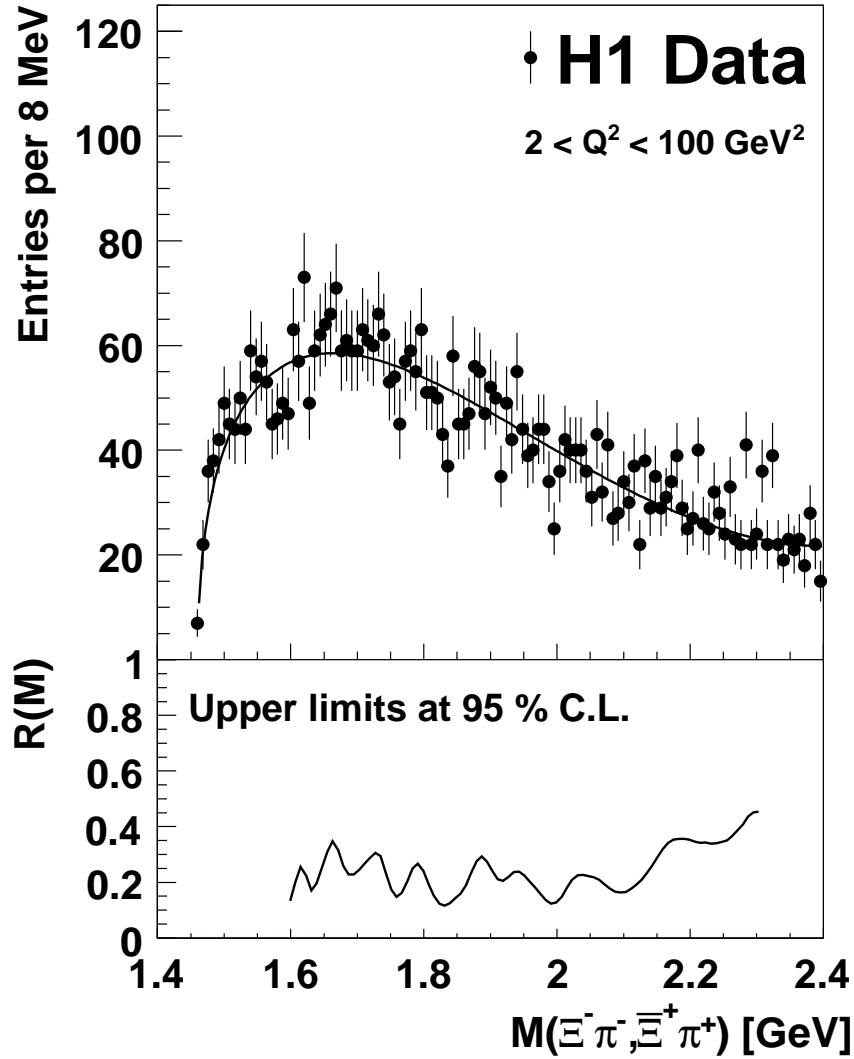
Figure 9.16: Top: the $\Xi^- \pi^-$ mass spectrum as shown in figure 8.15 together with the fitted background function (see equation 8.6). Bottom: the upper limit $R_{u.l.}(M)$ on the ratio R at 95 % C.L. for the charged combinations.

that one in the neighboring bins. Therefore, the deviation shown in the figure 9.18 is weighted with a Gaussian with a width corresponding to the resolution at the mass M_i:

$$N_{Signal}^{weighted}(M_i) = \sum_{bins j} N_{Signal}(M_j) \cdot G_{\sigma_i, M_i}(M_j), \tag{9.12}$$

where G_{σ_i, M_i} denotes a Gaussian with a mean value of M_i and a width $\sigma_i = \sigma(M_i)$ as used in the limit calculation. The same weighting is also applied for the number of background events, $N_{BG}^{weighted}$. The two curves in figure 9.18 are indeed strongly correlated, indicating that the limit calculation is reliable.
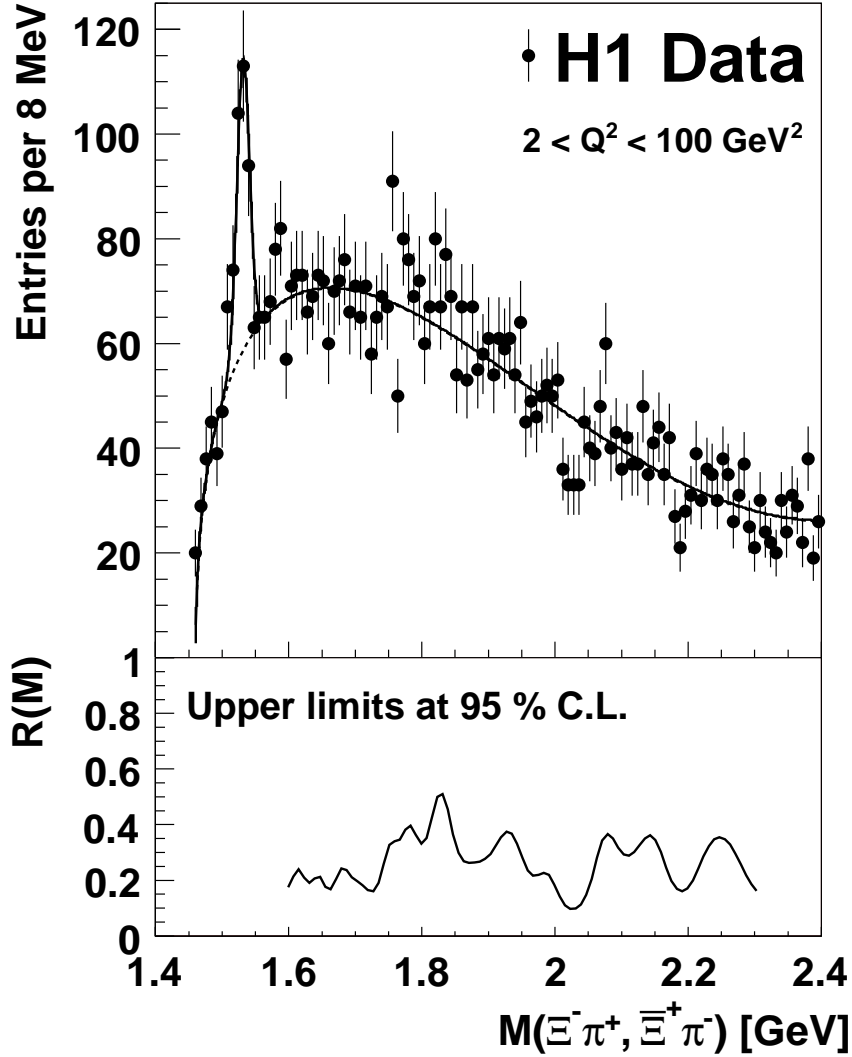
Figure 9.17: Top: the $\Xi^- \pi^+$ mass spectrum as shown in figure 8.15 together with the fitted background function (see equation 8.6). Bottom: the upper limit $R_{u.l.}(M)$ on the ratio R at 95 % C.L. for the neutral combinations.

9.7.2   Separate and Combined Limits of the four Charge Assignments

The limit calculation is carried out for all four possible charge combinations separately, which is of interest for the case that only the Pentaquark but not its anti-particle (or vice versa) is produced in ep collisions. The limits on $\Xi^- \pi^+$ and $\Xi^- \pi^-$ resonant decays are normalized to the number of reconstructed $\Xi(1530)^0$ (charge conjugation excluded) states, while that ones on $\overline{\Xi}^+ \pi^-$ and $\overline{\Xi}^+ \pi^+$ are normalized to the number of $\overline{\Xi}(1530)^0$. For the signal extraction the width of the $\Xi(1530)^0$ and of the $\overline{\Xi}(1530)^0$ are fixed to the value obtained by the fit to all mass spectra (see section 9.3). The result of this fit is shown in Figure 9.19. In total 74 ± 15 $\Xi(1530)^0$ (charge conjugation excluded) baryons and 95 ± 16 $\overline{\Xi}(1530)^0$ anti-baryons are
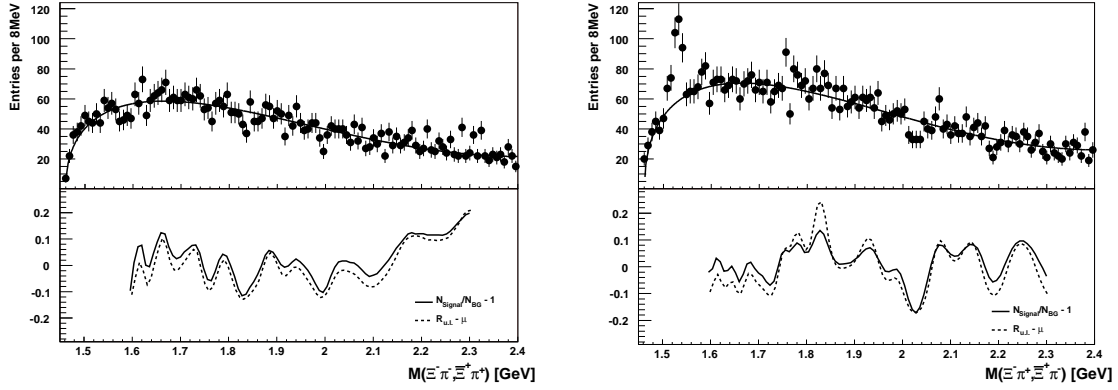
Figure 9.18: Cross-check of the upper limit for the charged (top) and neutral (bottom) combinations. For explanation see text.

reconstructed.

The upper limits on R for the four possible charge combinations are presented in figure 9.20. The change in the systematic uncertainty due to the reduced number of reconstructed $\Xi(1530)^0$ ($\overline{\Xi}(1530)^0$) are taken into account in the limit calculation. As expected, the upper limits on R takes higher values due to the reduced statistic compared to the combined limits. In the Ξ^- case they vary typically between 0.2 and 0.8 and in the $\overline{\Xi}^+$ case between 0.15 and 0.6. The peak in the upper limit in the $\Xi^- \pi^+$ case is at a mass of 1.83 GeV and not at 1.86 GeV which is the mass of the pentaquark candidates observed by the NA49 Collaboration. This enhancement is not visible in any of the other charge combinations and therefore most likely due to a statistical fluctuation.

Finally figure 9.21 shows the mass spectrum and upper limit for the combination of all possible charge assignments ($\Xi^- \pi^-$, $\Xi^- \pi^+$, $\overline{\Xi}^+ \pi^+$, $\overline{\Xi}^+ \pi^-$). In this case a simultaneous fit is no longer possible. For the extraction of the signal and the background parameterisation, a fit to this mass spectrum using a superposition of a Gaussian for the $\Xi(1530)^0$ signal and the background function defined by equation 8.6 is applied. For this fit the width of the Gaussian is again fixed to 9.4 MeV. The fit yields a number of 159 ± 27 reconstructed $\Xi(1530)^0$, which is used for the normalization in the ratio R. The change in the systematic uncertainty is taken into account in the limit calculation. The efficiency $\epsilon(M, q)$ appearing in equation 9.1 is taken to be the average of the efficiency for the neutral combinations and of the charged ones: $\epsilon(M) = \frac{1}{2} \cdot (\epsilon(M, 0) + \epsilon(M, --))$. The upper limit on R varies between 0.16 and 0.57.
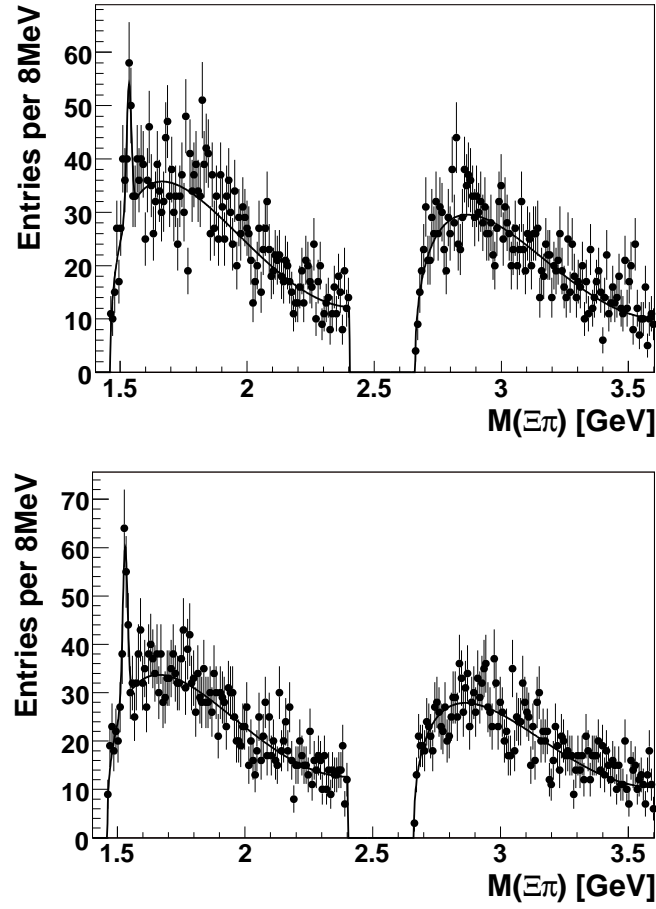
Figure 9.19: Background determination using the simultaneous fit to both mass spectra, as described in equation 9.2. The doubly charged mass spectra is artificially shifted by $1.2\,\text{GeV}$. The figure on the top shows the mass spectra $\Xi^-\,\pi^+$ and $\Xi^-\,\pi^-$ (charge conjugation excluded) while that one on the bottom shows $\overline{\Xi}^+\,\pi^-$ and the $\overline{\Xi}^+\,\pi^+$.
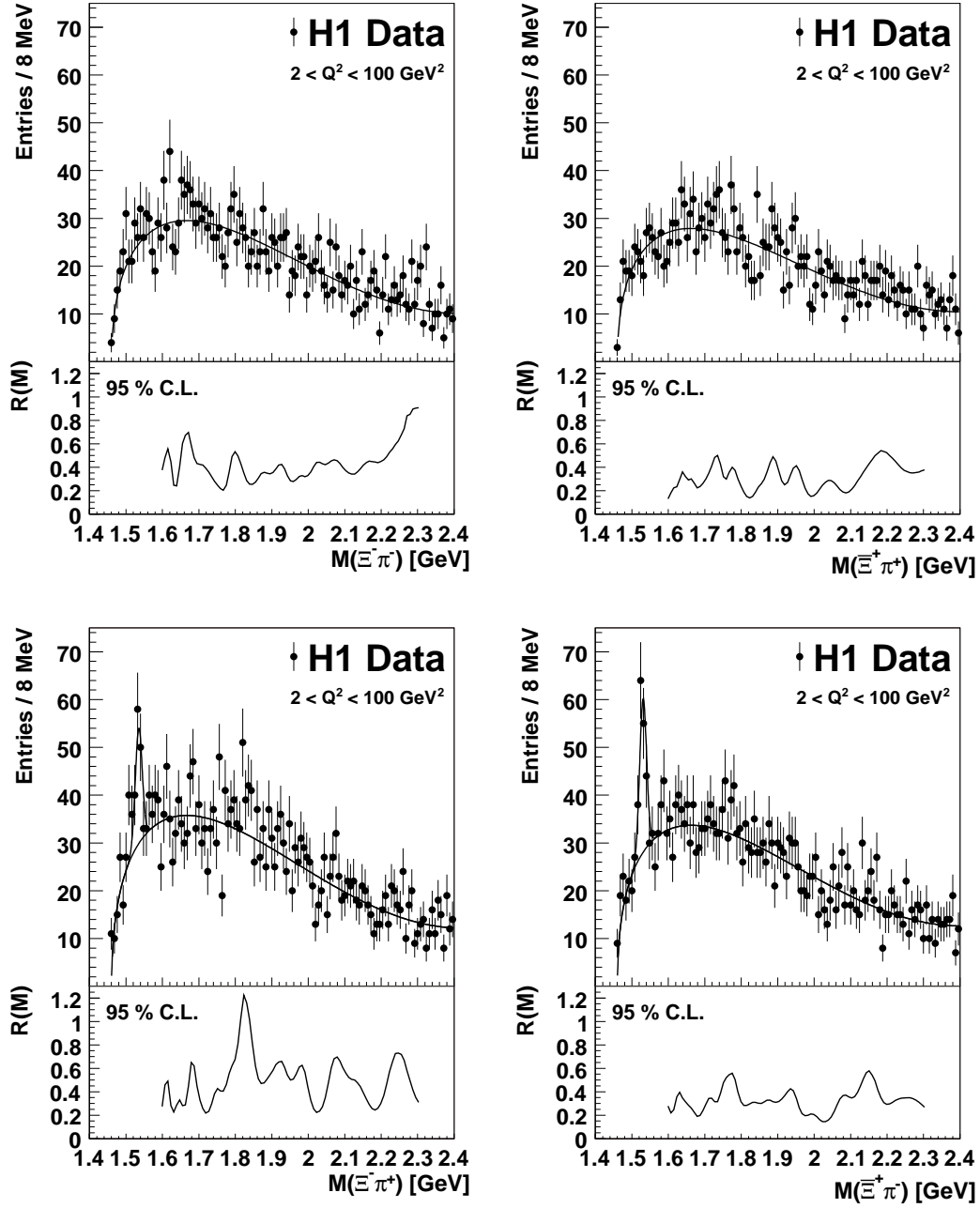
Figure 9.20: The $\Xi^- \pi^-$ mass spectrum (top left, charge conjugation excluded) together with the fitted background function (see equation 8.6) and the upper limit on R at 95 % CL for resonant $\Xi^- \pi^-$ decays. The same is shown for the $\overline{\Xi}^+ \pi^+$ combinations (top right), for the $\Xi^- \pi^+$ combinations (bottom left) and for the $\overline{\Xi}^+ \pi^-$ combinations (bottom right).
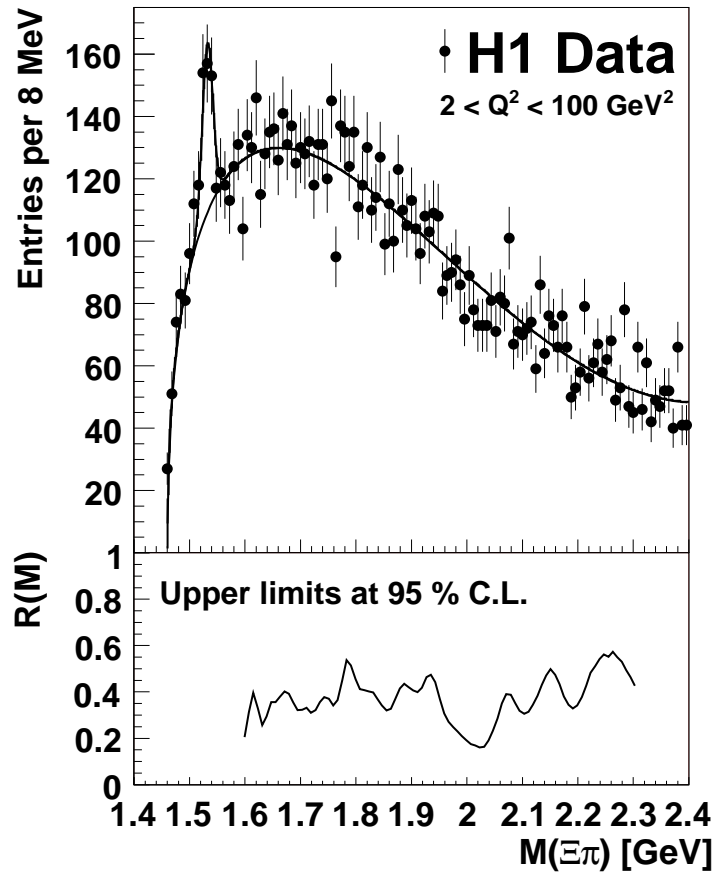
Figure 9.21: The upper part shows the mass spectrum of all possible charge combinations $(\Xi^-\pi^-,\ \Xi^-\pi^+,\ \overline{\Xi}^+\pi^+,\ \overline{\Xi}^+\pi^-)$. Overlaid on this spectrum is the result of a fit using a Gaussian for the $\Xi(1530)^0$ signal and the background function defined by equation 8.6. In the lower part the upper limit on R at 95 % C.L. is displayed.
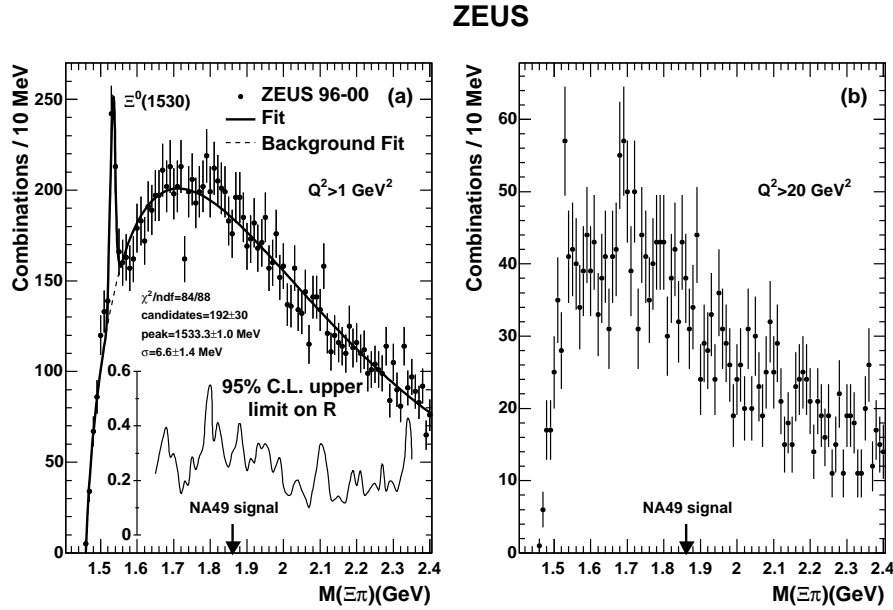
Figure 9.22: The mass spectrum of all possible charge combinations ($\Xi^- \pi^-$, $\Xi^- \pi^+$, $\overline{\Xi}^+ \pi^+$, $\overline{\Xi}^+ \pi^-$) as observed by the ZEUS Collaboration (a). The inlet displays the 95 % CL upper limit on the ratio R. The same mass spectrum for $Q^2 > 20\,\mathrm{GeV}$ is shown in the right figure (b).

9.8 Comparison with the ZEUS Measurement

The ZEUS Collaboration has also performed a search for resonant $\Xi \pi$ decays [116]. As already mentioned the ZEUS Collaboration has not seen any indication of a new signal, and upper limits on the ratio R introduced in equation 9.1 have been derived. The main difference with respect to this work is a different Q^2 range, starting at $Q^2 = 1\,\mathrm{GeV}^2$. In the ZEUS publication [116] only the upper limit on the combination of all possible charge assignments is shown (corresponding to figure 9.21 in this work). The results of the ZEUS Collaboration are displayed in figure 9.22. Their upper limits vary between 0.1 and 0.55 and are therefore well compatible with those measured at H1.

The ZEUS collaboration reported a hint for a structure in events with $Q^2 > 20\,\mathrm{GeV}^2$ at a mass around $1690\,\mathrm{MeV}$ representing the $\Xi(1690)^0$ baryonic state (see figure 9.22 b). In this analysis no hint for such a structure is observed (see figure 8.17).

Chapter 10

Limits Derived from the HERA II Data

The H1 experiment has collected, after the upgrade in 2001, roughly tree times the luminosity than in the HERA I period. In this section the data recorded in the year 2006 are analysed (corresponding to an integrated luminosity of $132\,\mathrm{pb^{-1}}$) and upper limits are extracted from this data set. A full analysis of the HERA II data is beyond the scope of this work and the following studies should therefore only be regarded as a first look at the new data.

The main difference to the analysis presented in the previous sections is the higher Q^2 selection. Due to the new geometry of the beam pipe, Q^2 is restricted to $5 < Q^2 < 100\,\mathrm{GeV^2}$ for the HERA II data set, which is the only change with respect to the HERA I data analysis.

10.1 The Ξ^- Mass Spectrum

The Ξ^- mass spectrum shown in figure 10.1 is obtained by an analogue procedure as described in section 8.2. A fit to this mass spectrum with a superposition of a Gaussian for the Ξ^- signal and a background function parameterized accordingly to equation 8.6 (with m_Ξ exchanged by m_Λ) yields a total number of 2528 ± 74 [1] reconstructed Ξ^- baryons at a mass of $(1322.2 \pm 0.1)\,\mathrm{MeV}$ and with a width of $(4.1 \pm 0.1)\,\mathrm{MeV}$. The width is within errors the same as obtained for the HERA I data set. The reconstructed mass of the Ξ^- baryon is slightly shifted (by $0.6\,\mathrm{MeV}$) to higher values. In the same figure the mass spectra of the Ξ^- and $\overline{\Xi}^+$ (charge conjugation excluded) are shown. The ratio of the Ξ^- baryons to the $\overline{\Xi}^+$ anti-baryons is within two sigma consistent with being one ($\frac{1331\pm52}{1200\pm51} = 1.11 \pm 0.06$).

10.2 The $\Xi^- \pi^\pm$ Combinations

The combination of the Ξ^- candidates with an additional track is done in the same way as described in section 8.3. In figure 10.2 the mass spectra of the $\Xi^- \pi^-$ and $\Xi^- \pi^+$ combinations are shown. Overlaid on these mass spectra is the result of a simultaneous fit using the function defined by equation 9.2. The fit yields a total of 296 ± 40 reconstructed $\Xi(1530)^0$ baryons at

---

[1]Due to the unknown efficiency (first of all that one of the trigger) and the different Q^2 range the number of reconstructed Ξ^- cannot be directly compared to the number extracted from the HERA I data set.
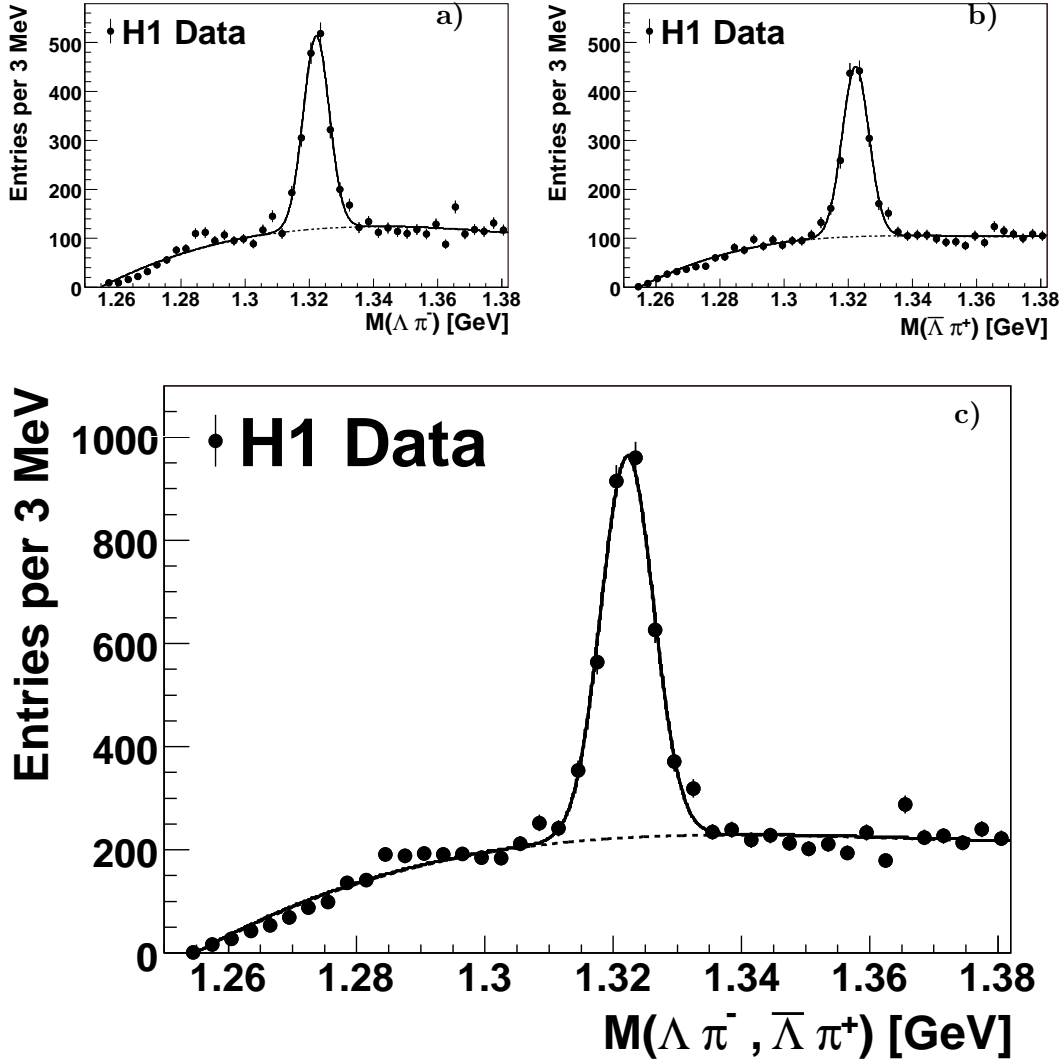
Figure 10.1: Reconstructed Ξ mass spectra for the HERA II data set with cuts mentioned section 8.2. a) only $\Lambda\,\pi^-$ combinations b) only $\bar{\Lambda}\,\pi^+$ combinations c) $\Lambda\,\pi^-$ and $\bar{\Lambda}\,\pi^+$ combinations. The solid lines show the result of a fit using a superposition of a Gaussian and the background function defined by equation 8.6.

a mass of $(1532.5 \pm 1.9)\,\mathrm{MeV}$ and with a width of $(14.1 \pm 2.4)\,\mathrm{MeV}$. The reconstructed mass is in agreement with the value obtained for the HERA I data set and is PDG compliant. The width is observed to be larger with respect to the HERA I data, which is most likely due to some deficits in the track reconstruction. Reprocessed data with an improved tracking are supposed to be available soon. A preliminary conclusion is that the reconstruction of the decay chain shown in figure 7.1 including tertiary vertices works appropriately also for the HERA II data and that the growth of the number of reconstructed $\Xi(1530)^0$ baryons is (at first order) as expected.
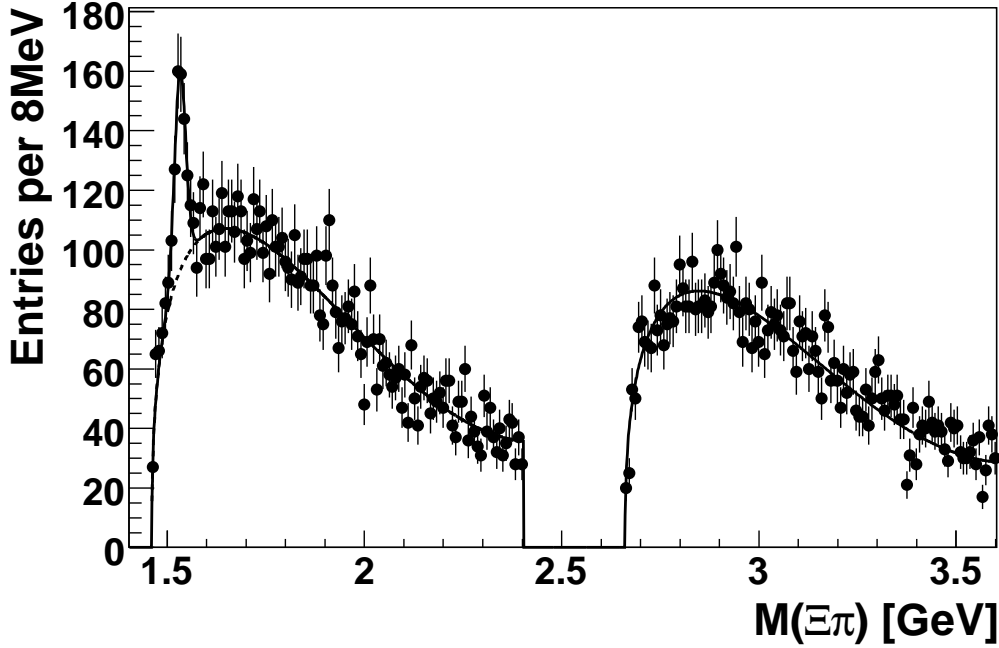
Figure 10.2: The reconstructed $\Xi^-\pi^+$ and the $\Xi^-\pi^-$ mass spectra for the HERA II data set. Overlaid on the spectrum is the result of a simultaneous fit to both mass spectra, as described in equation 9.2. The doubly charged mass spectra is artificially shifted by 1.2 GeV.

10.3   Extraction of the Upper Limit

No hint for any new baryonic state in the HERA II data is observed and therefore upper limits are derived in the same way as introduced in section 9. No new Monte Carlo sets are simulated. The limits are derived under the assumption that the resolution of a hypothetical new baryonic state is the same as in the HERA I case. Furthermore it is assumed that the efficiency correction factor in equation 9.1 is unchanged. Only the systematic uncertainties are changed for the extraction of the limit from the HERA II data (see section 9). The uncertainty on the number of reconstructed $\Xi(1530)^0$ baryons could be reduced to 13 %. On the other hand the uncertainty on the width of the possible new state is increased to 10 % due to the increase in the width of the $\Xi(1530)^0$ baryon. New MC sets are needed in order to have a better estimation of this number. The mass spectra and upper limits derived under these assumptions are shown in figure 10.3 and 10.4. Due to the higher statistics the upper limits could be improved with respect to that ones derived from the HERA I data set. They vary between 0.08 and 0.3 for both, the doubly charged and neutral combinations. The improvement is compatible with $\sqrt{\frac{N(\Xi(1530)^0)_{HERA\,I}}{N(\Xi(1530)^0)_{HERA\,II}}}$ which is naively expected.
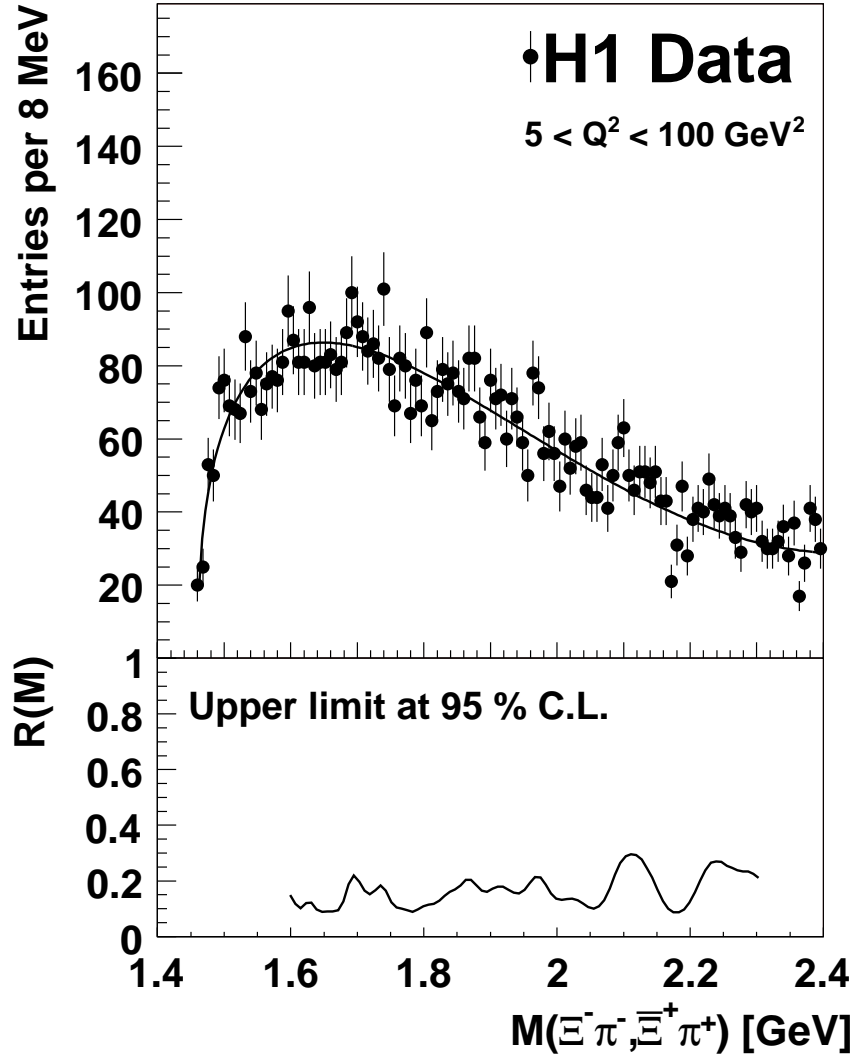
Figure 10.3: The $\Xi^- \pi^-$ mass spectrum together with the fitted background function (upper part) and the upper limit $R_{u.l.}(M)$ on the ratio R at 95 % C.L. for the charged combinations (lower part).
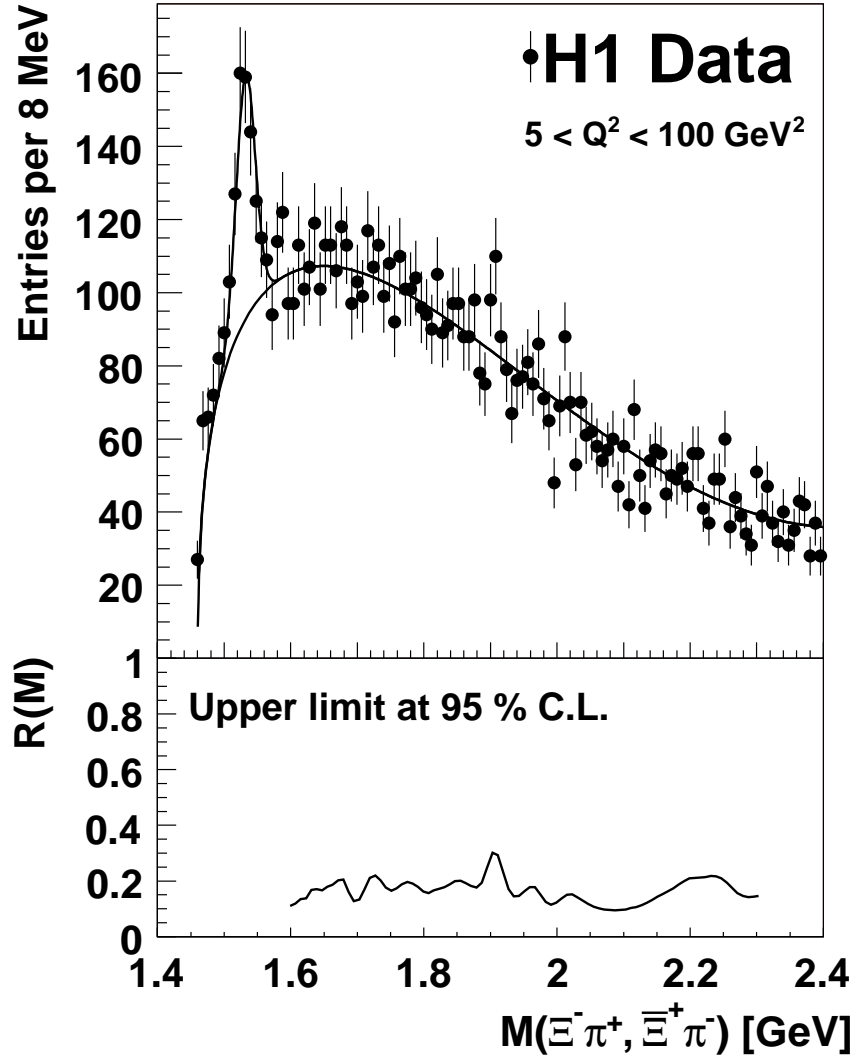
Figure 10.4: The $\Xi^-\pi^+$ mass spectrum together with the fitted background function (upper part) and the upper limit $R_{u.l.}(M)$ on the ratio R at 95 % C.L. for the neutral combinations.

Part III

Search for New Particles Decaying into ΛK_s^0

Chapter 11

Introduction

A search for narrow resonances decaying at the interaction point into the strange hadrons K_s^0 and Λ is performed. The decay channel under investigation is:

$$X \to K_s^0 \, \Lambda \to (\pi^+ \, \pi^-) \, (p \, \pi^-), \tag{11.1}$$

as illustrated in figure 11.1. This decay channel is particularly interesting with regard to
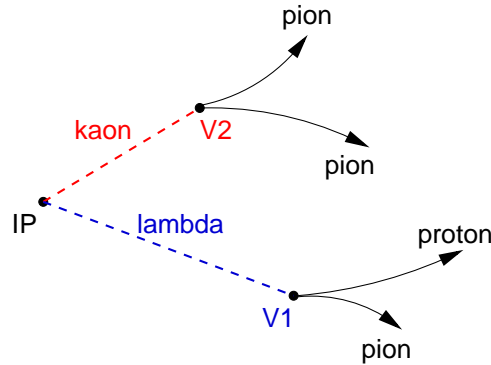
Figure 11.1: The decay of the state X (see equation 11.1). Here, "IP" denotes the interaction point.

pentaquark searches: Various theories predict a state named N_s^0 (see figure 2.16) that decays according to equation 11.1. The STAR Collaboration at RHIC [21] has observed a narrow peak in Au-Au collisions at $(1734 \pm 5) \, \text{MeV}$ in the invariant mass spectrum $M(K_s^0, \Lambda)$ with a width consistent with their experimental resolution of about $6 \, \text{MeV}$. The question arises whether this resonance is also observed in ep collisions at HERA.

The analysis is performed using 78 pb^{-1} of ep scattering data taken in the years 1999 and 2000 (HERA I). For this search the whole data sample is used (i.e. no DIS selection) in order to maximize the statistics. Furthermore, no specific subtrigger is required.

Chapter 12

Analysis of the Decay $X \to \Lambda\, K_s^0$

In a first part K_s^0 and Λ candidates are reconstructed and their combination is outlined. In the second part an interpretation of the results is provided.

12.1 Reconstruction of the Strange Hadrons K_s^0 and Λ

For the reconstruction of the strange hadrons only well measured, non-vertex fitted tracks are used, fulfilling the selection criteria introduced in section 4.2.1.1. Only events containing at least four selected tracks, two of each charge, are considered in the following. The K_s^0 and the Λ particles are identified by fitting two oppositely charged tracks to a common vertex using the 3DU routine (see section 4.2.2). The K_s^0 and Λ candidates fulfilling the following selection criteria are considered for the further analysis (see also section 5.1.1):

Fit probability: $P(\chi^2, n) > 1\,\%$,

Transverse momentum: $p_T(K_s^0) > 200\,\mathrm{MeV}$, $p_T(\Lambda) > 800\,\mathrm{MeV}$,

Two-dimensional decay length: $L(K_s^0) > 0.4\,\mathrm{cm}$, $L(\Lambda) > 0.75\,\mathrm{cm}$,

Uncertainty of L: $\delta L(K_s^0, \Lambda) < 0.5\,\mathrm{cm}$,

Significance of L: $S_L(K_s^0, \Lambda) > 4$,

Pseudorapidity: $|\eta(K_s^0, \Lambda)| < 1.75$,

Sign of d$'_{\mathbf{ca}}$: $d'_{ca}(track1) \cdot d'_{ca}(track2) < 0$,

Pointing angle : $|sin(\alpha)| < 0.2$ [1].

Furthermore, the tracks used for the K_s^0 reconstruction are explicitly excluded for the Λ identification. The contamination of Λ (K_s^0) decays in the K_s^0 (Λ) sample is discarded by a selection criterion on the corresponding mass as discussed in section 5.1.2. The mass spectra of all selected K_s^0 and Λ candidates are shown in figure 12.1. The reconstructed mass of both signals, extracted by a fit to these spectra using the function F defined by equation 5.11,

---

[1]The pointing angle is defined as the angle between the line connecting the interaction point with the decay vertex and the flight direction of the K_s^0 (Λ) candidate.

is compatible with the world average. The mean width of the two Gaussian functions (see equation 5.12) are measured to $\overline{\sigma}(K_s^0) = (10.6 \pm 0.2)\,\text{MeV}$ and $\overline{\sigma}(\Lambda) = (3.8 \pm 0.1)\,\text{MeV}$. As discussed in section 4.2.2, the resolution of the strange hadrons reconstructed with the 3DU routine improves with respect to those reconstruction with the 2DC one (see table 5.1) by approximately 20 %.
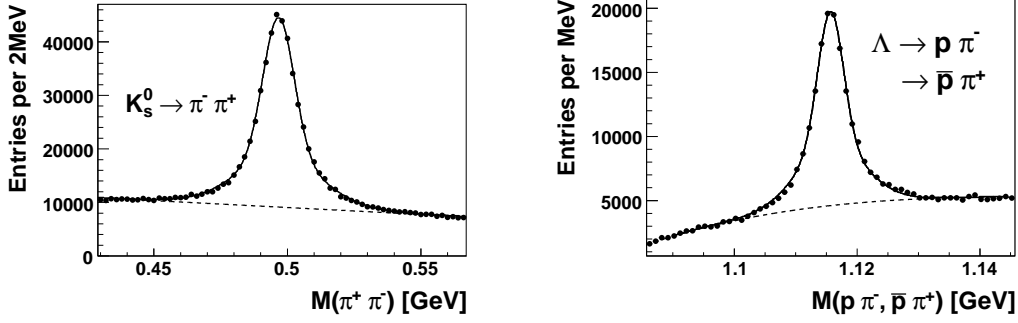
Figure 12.1: The mass spectra of the reconstructed K_s^0 (left) and Λ (right) candidates fulfilling the selection criteria. Overlaid on the data points is the result of a fit using the function F defined by equation 5.11.

12.2 Combination of the Reconstructed Λ and K_s^0 Candidates

For the reconstruction of the decay $X \to K_s^0 \Lambda$, the K_s^0 and Λ candidates are fitted to a common vertex by means of the VVF routine (see section 4.2.2). Thereby the reconstructed vertex is constraint to the *ep* interaction point of the event (see figure 11.1). The mass spectra of all selected K_s^0 and Λ candidates which are accepted by this fit is displayed in figure 12.2. The part of the mass spectra that is rejected by the fit is also shown in this figure. The constraint that the reconstructed K_s^0 and Λ candidates are compatible with being produced at the interaction point reduces the combinatorial background significantly since most of these events do not satisfy this requirement.

In the following only K_s^0 (Λ) candidates are considered with an invariant $\pi\pi$ ($p\,\pi$) mass within $\pm 20\,\text{MeV}$ ($\pm 9\,\text{MeV}$) of the nominal K_s^0 (Λ) mass, which is subsequently assigned to the selected K_s^0 (Λ) candidates. The mass boundaries are indicated in figure 12.2 by the dotted lines. All combinations fulfilling the following requirements are retained for the further analysis:

Fit probability: $P(\chi^2, n) > 1\,\%$ (see equation 4.22 for the definition of P)

Transverse momenutm: $p_T(X) > 1\,\text{GeV}$.

The invariant mass spectrum $M(K_s^0, \Lambda)$ of all selected combinations is shown in figure 12.3. For these combinations, the K_s^0 and Λ momenta obtained by the fit are used and the nominal masses are assigned to the candidates. An enhancement around a mass of $1.7\,\text{GeV}$ is observed. The same mass spectrum is enlarged for $M(K_s^0, \Lambda) < 1.85\,\text{GeV}$ in figure 12.4. Overlaid on the data points is the result of a fit with a superposition of a Gaussian accounting for a possible signal and a background term given by:

$$BG = P_0 \cdot (M - M_{K_s^0} - M_\Lambda)^{P_1}, \tag{12.1}$$
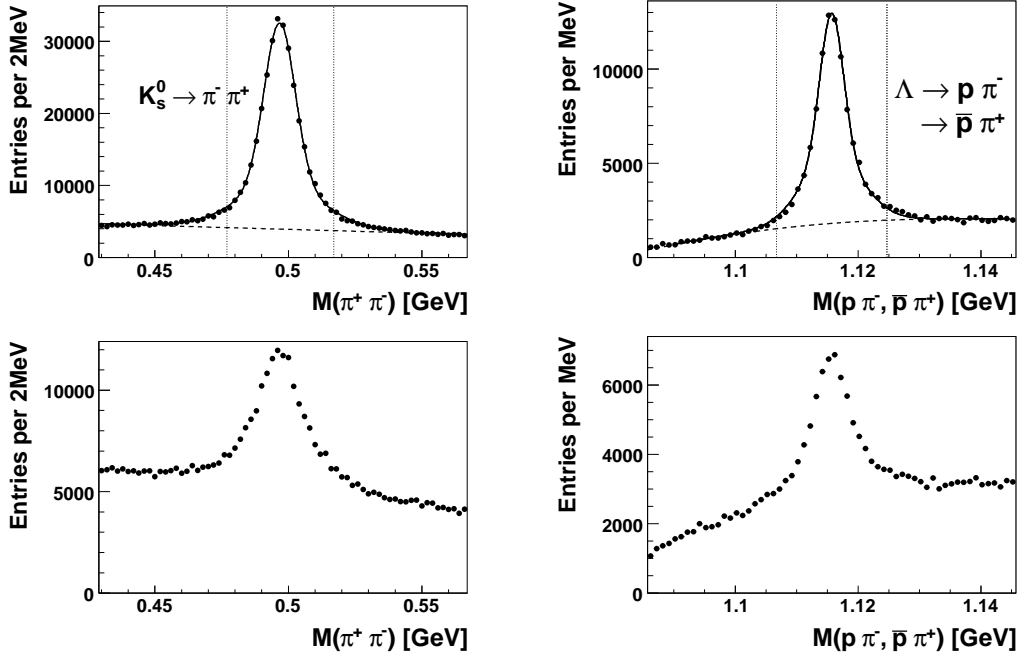
Figure 12.2: The reconstructed mass spectra of the K_s^0 (left) and Λ (right) candidates accepted by the vertex fit (top) and of those rejected by this fit (bottom). Overlaid on the data points is the result of a fit using the function F defined by equations 5.11. The dotted lines indicate the mass range used for the further analysis.
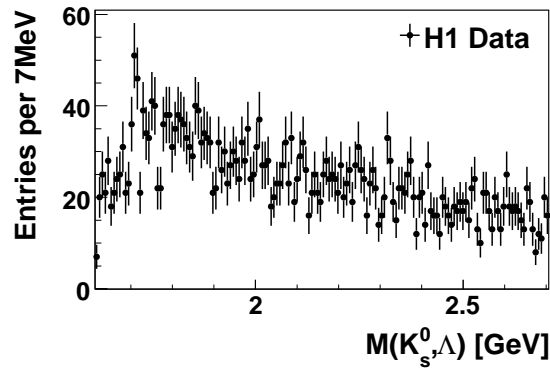
Figure 12.3: The mass spectrum $M(K_s^0,\Lambda)$ extracted from the HERA I data of all selected combinations.

where P_0 and P_1 are free parameters and $M_{K_s^0}$ and M_Λ the nominal K_s^0 and Λ masses, respectively. This fit ($\chi^2/n = 37.7/29$ [2]) yields a signal of 48 $\pm$ 12 events at a mass of (1'710 $\pm$ 2) MeV. The width of the signal is found to be (4.8 $\pm$ 1.2) MeV, consistent with the detector resolution obtained from a Monte Carlo simulation [3]. Therefore, the observed

---

[2] A fit with the same background function but without the Gaussian function has $\chi^2/n = 55.5/29$

[3] For the simulation of the state X the Δ^0 baryon is used. Its mass is set to 1.7 GeV and its intrinsic width to zero, allowing to study the detector resolution for such a hypothetical state.
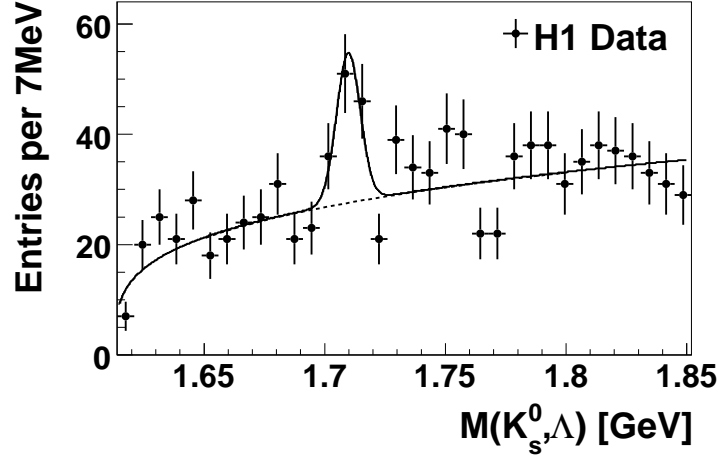
Figure 12.4: The mass spectrum $M(K_s^0, \Lambda)$ of all selected combinations for a reduced mass range. The solid line shows the result of a fit using the superposition of a Gaussian and the background function defined by equation 12.1 while the dashed line indicates the background only.

bump is consistent with the observation of the STAR collaboration. The signal to noise ratio calculated within $\pm 2\,\sigma$ of the reconstructed mass is found to be 0.6.

12.3   Examination of the Signal Candidate

In the following the observed signal candidate is investigated further in order to establish its authenticity.

12.3.1   Stability of the Signal Candidate

The following consistency checks are performed:

1. All properties of the signal (mass, width and entries) remain stable within the statistical accuracy with respect to shifts in the binning and also for changes of the bin size (from 5 MeV to 10 MeV). In figure 12.5 the invariant mass spectrum is displayed for a binning shifted by 3 MeV and for a reduced bin size of 5 MeV.

2. In order to test the charge conjugate state production of the signal candidate, the mass spectrum is shown for $K_s^0\,\Lambda$ and $K_s^0\,\overline{\Lambda}$ combinations separately in figure 12.6. The signal is found to be, within the statistical accuracy, equally distributed between these two cases (30 ± 9 for the $K_s^0\,\Lambda$ and 25 ± 9 for the $\overline{\Lambda}$ combinations). The reconstructed mass and width of the two signals are compatible with each other and also with the values obtained from the fit to the sum of the two spectra.

3. The combination of K_s^0 and Λ candidates built by the same tracks could produce a fake signal in the invariant mass spectrum. For the signal observed in figure 12.4 this effect is not seen from the Armenteros-Thompson figure (see section 4.2.4) of the K_s^0 and Λ
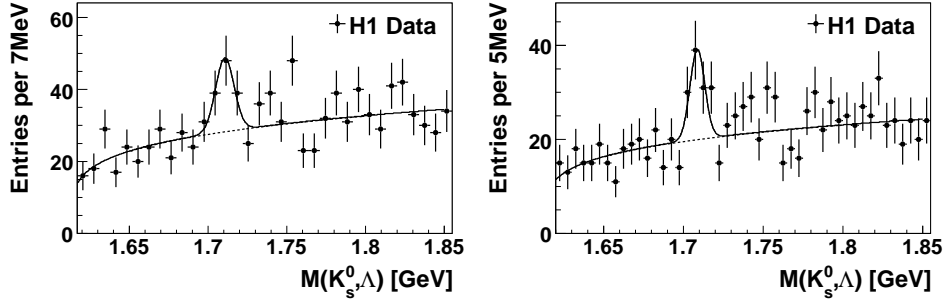
Figure 12.5: The mass spectrum $M(K_s^0, \Lambda)$ for a binning shifted by $3\,\text{MeV}$ (left) and for a reduced bin size of $5\,\text{MeV}$ (right). The solid lines show the result of a fit using the superposition of a Gaussian and the background function defined by equation 12.1 while the dashed line indicates the background only.
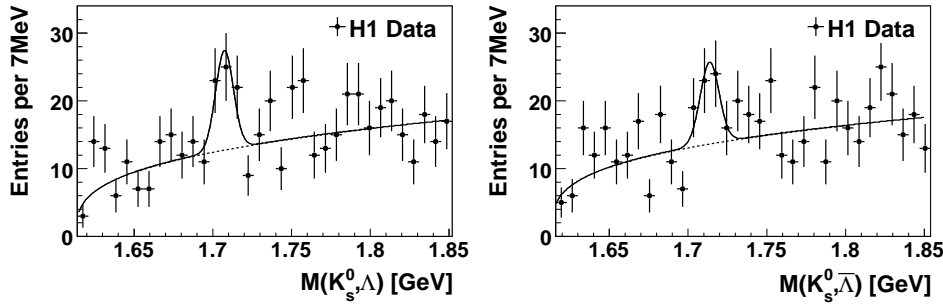
Figure 12.6: The invariant mass spectrum $M(K_s^0, \Lambda)$ (charge conjugation excluded, left) and $M(K_s^0, \overline{\Lambda})$ (right). The solid lines show the result of a fit using the superposition of a Gaussian and the background function defined by equation 12.1 while the dashed line indicates the background only.

candidates contributing to the signal region ($1.7 < M(K_s^0, \Lambda) < 1.72\,\text{GeV}$), as shown in figure 12.7. The structures representing the K_s^0 and Λ decays are well separated.

4. The application of the same track for the reconstruction of the strange hadrons can be excluded by examining the difference in p_T of the two positive (negative) charged tracks (one used for the K_s^0 reconstruction and one for the Λ reconstruction) and the difference in ϕ of the two tracks: $\Delta p_T^{+(-)} := p_T(\text{trk}^{+(-)}(K_s^0)) - p_T(\text{trk}^{+(-)}(\Lambda))$, $\Delta \phi^{+(-)} := \phi(\text{trk}^{+(-)}(K_s^0)) - \phi(\text{trk}^{+(-)}(\Lambda))$. These quantities are displayed for those combinations contributing to the signal region in figure 12.8. No clustering is observed, implying that the same track is not used twice. Nevertheless combinations with $\Delta p_T^{+(-)} < 0.05\,\text{GeV}$ or $\Delta \phi^{+(-)} < 0.1\,\text{rad}$ are excluded as a cross check. The resulting mass spectrum of the $K_s^0 \Lambda$ combinations is displayed in figure 12.9. As expected, only a few signal candidates are lost.

5. The invariant mass spectrum reconstructed from the K_s^0 and Λ candidates in the side band region ($|M(\pi, \pi)| - M_{K_s^0}| > 20\,\text{MeV}$, $|M(p, \pi)| - M_\Lambda| > 9\,\text{MeV}$) does not show any significant structure, see figure 12.10.
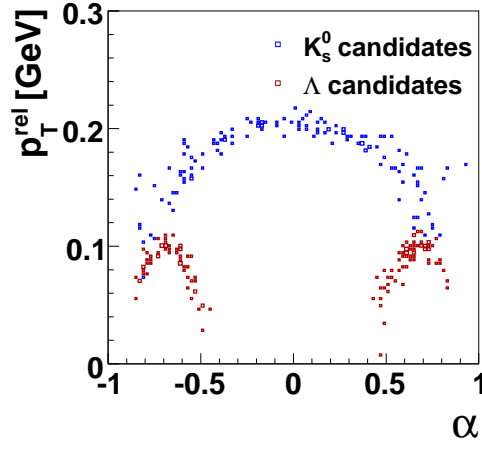
Figure 12.7: The Armenteros-Thompson figure for the K_s^0 (blue squares) and Λ (red squares) candidates contribution to the signal region.
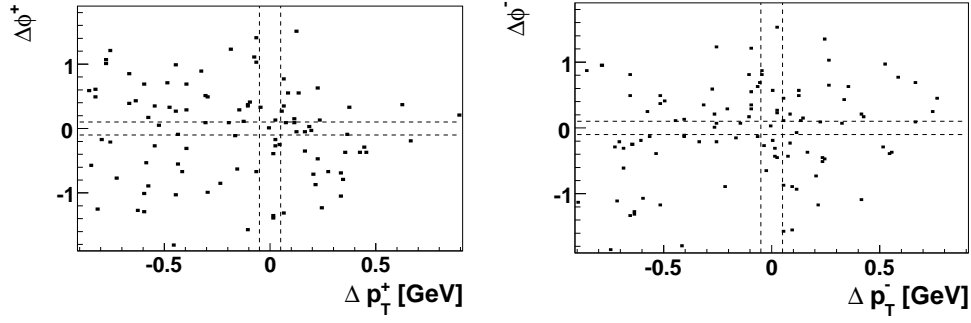
Figure 12.8: The distribution of $\Delta p_T^{+(-)}$ versus $\Delta\phi^{+(-)}$ for candidates contributing to the signal region. All combinations within the dashed lines are excluded for cross checks of the signal.
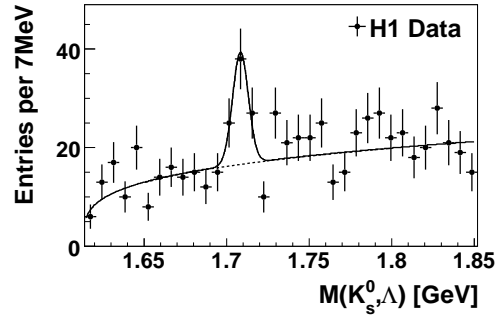
Figure 12.9: The mass spectrum $M(K_s^0, \Lambda)$ with the additional requirement on $\Delta p_T^{+(-)}$ and $\Delta\phi^{+(-)}$ (see also figure 12.8).
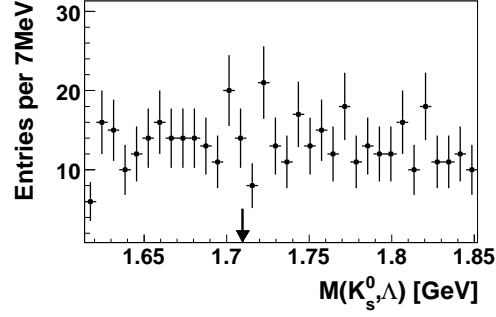
Figure 12.10: The mass spectrum $M(K_s^0, \Lambda)$ reconstructed from the side bands of the K_s^0 and Λ signals.

6. The signal remains stable within the statistical accuracy for a tighter K_s^0 and Λ selection ($|M(\pi, \pi)| - M_{K_s^0}| < 15\,\text{MeV}$, $|M(p, \pi)| - M_\Lambda| < 6\,\text{MeV}$). For this selection the signal comprises 38 ± 12 entries, compatible with the expected loss of roughly $10\,\%$ when selecting the K_s^0 and Λ candidates within $1.5\,\sigma$ of the nominal masses instead of $2\,\sigma$.

7. The extracted signal is stable under variation of the background function. The following variations are studied:

   • Adding a Polynomial of degree one to the background function given by equation 12.1

   • Exchanging the background function by a Polynomial of degree one.

The mass spectra together with the results of a fit with these functions are shown in figure 12.11.
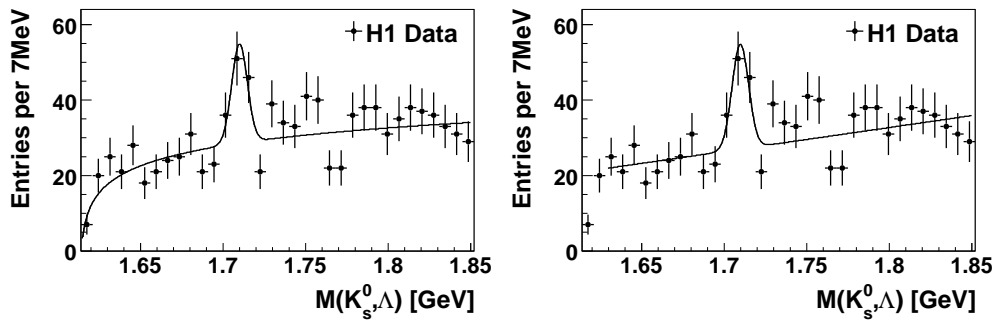
Figure 12.11: The signal extraction with different parameterisations of the background function. Left: Superposition of the background function defined by equation 12.1 and a Polynomial of degree one. Right: A Polynomial of degree one.

8. The signal remains stable with respect to variation of the selection criteria on $p_T(X)$ (from 0.5 to 1.5 GeV) and $P(\chi^2, n)$ (from 0 to 5 %).

12.3.2   Kinematic Properties of the Signal Candidate

The distribution of the kinematic variables $p_T(X)$, $\eta(X)$ and $\phi(X)$ is shown in figure 12.12 for events in the signal region ($1.697 < M(K_s^0, \Lambda) < 1.72\,\text{GeV}$) and for events in the background region ($M(K_s^0, \Lambda) < 1.68\,\text{GeV}$ or $M(K_s^0, \Lambda) > 1.74\,\text{GeV}$). All kinematic quantities are distributed similarly for the two regions, implying that the signal is not enhanced in a certain region of the phase space.
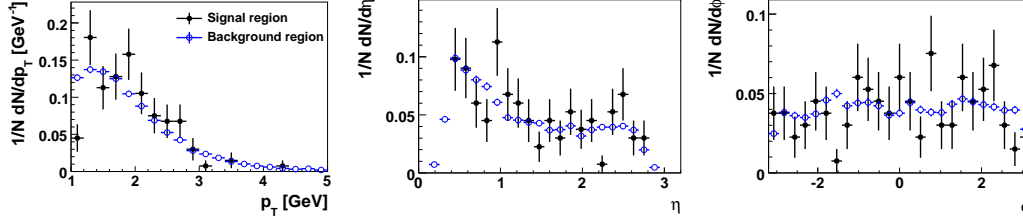
Figure 12.12: The $p_T(X)$ (left), $\eta(X)$ (middle) and $\phi(X)$ (right) distribution of the events in the signal region (black solid points) and in the background region (blue open points).

All these cross checks indicate that the observation lies within the data itself and is not artificially produced by the analysis treatment.

12.4   Interpretation of the Results

Assuming that the observed signal is a real resonance, a possible interpretation is the pentaquark state N_s^0 which should predominantly decay into $K_s^0 \Lambda$. The mass of this state is expected to be around $1.7\,\text{GeV}$ and its width is predicted to be small (see section 2.4). Another promising candidate for the interpretation of the signal is the excited baryon state $\Xi^0(1690)$. The mass of this state is $(1690 \pm 10)\,\text{MeV}$ and the width is less than $30\,\text{MeV}$ [26]. Other known states that can decay into $K_s^0 \Lambda$ are the $\Xi^0(1820)$ or the excited nucleon states $N(1650, 1675, 1700, 1710, 1720)$. They are disfavoured because of their mass or their large width ($\mathcal{O}(100\,\text{MeV})$). Therefore the most promising interpretation is that of the excited baryon $\Xi^0(1690)$ or the pentaquark state N_s^0. In the following attempts are made to distinguish between these two possible interpretations. A third possibility is that the signal candidate is caused by a statistical fluctuation.

The N_s^0 interpretation: The charged partner of this pentaquark state, the N_s^+ (see figure 2.16), should also be visible with the same amount of statistics. This state is expected to decay predominantly according to:

$$N_s^+ \quad \to \quad K^+ \Lambda, \tag{12.2}$$

$$\overline{N_s^-} \quad \to \quad K^- \overline{\Lambda} \tag{12.3}$$

    and should produce a signal in the $K^+ \Lambda$ and $K^- \overline{\Lambda}$ combinations at a mass of $1.7\,\text{GeV}$.

The $\Xi^0(1690)$ interpretation: The charged version of the excited baryon, the $\Xi^-(1690)$, should also be observable in this data set. This state decays according to [26]:

$$\Xi^-(1690) \quad \to \quad K^- \Lambda, \tag{12.4}$$

$$\overline{\Xi}^+(1690) \quad \to \quad K^+ \overline{\Lambda} \tag{12.5}$$

and is therefore expected to produce a signal in the $K^- \Lambda$ and $K^+ \overline{\Lambda}$ combinations at a mass of $1.7 \,\mathrm{GeV}$.

Statistical fluctuation: As the statistics of the signal candidate is small, it could also be a fluctuation. The probability that a background of $N_b = 82$ events, calculated within $\pm 2\,\sigma$ of the reconstructed mass, fluctuates to produce at least the number of events in the signal ($N_s = 48$) is $6 \cdot 10^{-7}$, assuming Poisson statistics. This probability corresponds to $5.0\,\sigma$ when expressed as an equivalent number of Gaussian standard deviations. A more reliable approach is provided by subtracting the uncertainty in the number of signal entries from N_s and adding it to N_b. The probability that a background of $N_b = 82{+}12$ events fluctuates to produce at least $N_s = 48{-}12$ signal entries, expressed as Gaussian standard deviations, is $3.7\,\sigma$. This interpretation is investigated further by analysing the HERA II data, see section 12.5.

The two most promising interpretations should therefore be distinguishable by examining the combination $K^\pm \Lambda$. However, at least two problems arise by this comparison: Firstly, the properties of the pentaquark states, if they exist, are not known and therefore predictions of decay modes are to be taken with care. Furthermore the N_s^+ state has never been observed up to the present date. Secondly, the combination of charged kaons with lambdas is different to the combination of neutral kaons with lambdas. The charged kaons are not reconstructed as resonances but only as single tracks which leads to a much larger background in these mass spectra.

12.4.1 $\Lambda\,K^\pm$ Combinations

Regardless of the possible problems mentioned above, the combination of charged kaons with lambdas is investigated. The Λ candidates are selected as described above (12.1). For the $K^\pm$ candidates, vertex-fitted tracks fulfilling the selection criteria introduced in section 4.2.1.1 are taken. As most of the selected particle tracks are $\pi^\pm$ mesons, further selection requirements on these tracks are applied. The fraction of $K^\pm$ mesons is enriched by using the information of the specific energy loss of the particles in the tracking chambers. The energy loss per flight length of the particles, dE/dx, is described by the Bethe-Bloch equation [26]. For the description of the energy loss in the H1 tracking chambers a semi-empirical approximation of the Bethe-Bloch parameterisation is used, see [163]. In figure 12.13 the specific energy loss of all selected vertex-fitted tracks is displayed as a function of their momentum p. Overlayed are the parameterisations for pions, kaons, protons and deuterons. Clearly visible are the three bands representing the pions, kaons and protons. For $p > 0.7\,\mathrm{GeV}$ the pion and kaon bands overlap and thus making a separation impossible. The parameterisation of the bands is used to calculate the likelihood probability that a given track is a pion, a kaon or a proton, see for example [76]. For this analysis only $K^\pm$ candidates are considered which have a probability, $LH(K^\pm)$, to be compatible with the corresponding parameterisation of larger than $8\,\%$. The energy loss of the tracks fulfilling this requirement is also shown in figure 12.13. Only the band compatible with the parameterisation of the kaon case remains. Furthermore, only $K^\pm \Lambda$ combinations with a transverse momentum larger than $1\,\mathrm{GeV}$ are considered. The resulting mass spectra of the different charge combinations $K^+ \Lambda$, $K^- \Lambda$, $K^+ \overline{\Lambda}$ and $K^- \overline{\Lambda}$ are shown in figure 12.14. Overlayed is the result of a fit to these spectra using the parameterisation
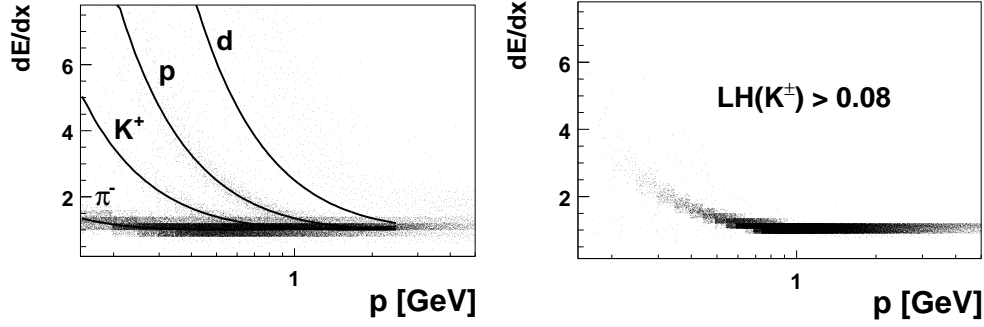
Figure 12.13: The specific energy loss dE/dx. Left: for all selected, vertex-fitted tracks. Overlayed is the parameterisation for $\pi^\pm$, $K^\pm$, protons (p) and deuterons (d). Right: for those used as $K^\pm$ candidates ($LH(K^\pm) > 8\%$).

given by:
$$B(M) = P_0 \cdot (M - M_{K^\pm} - M_\Lambda)^{P_1} \cdot (1 + P_2 \cdot M + P_3 \cdot M^2), \tag{12.6}$$

where $M_{K^\pm}$ and M_Λ denotes the nominal masses of the $K^\pm$ mesons and Λ baryons, respectively. In the lower part of the figure 12.14 the deviation of the data points from the fitted function are shown. No significant structure is observed in any of the four mass spectra. Therefore, no hint for the $\Xi^-(1690)$ state nor for the N_s^+ state is seen in the data.

For a further suppression of the background induced by the $\pi^\pm$ mesons, the total momentum of the $K^\pm$ candidates is restricted to $p < 0.7\,\text{GeV}$. The corresponding mass spectra are displayed in figure 12.15. The mass spectrum of the $K^+ \Lambda$ combinations shows two possible enhancements at masses around $1.66\,\text{GeV}$ and $1.73\,\text{GeV}$. These structures are not seen in any of the other charged combinations, strongly disfavouring an interpretation as real resonances. Furthermore, these structures are not stable under variation of the selection criteria and the binning.

The investigation of the $K^\pm \Lambda$ mass spectra did not lead to a clarification of the nature of the signal observed in figure 12.4.
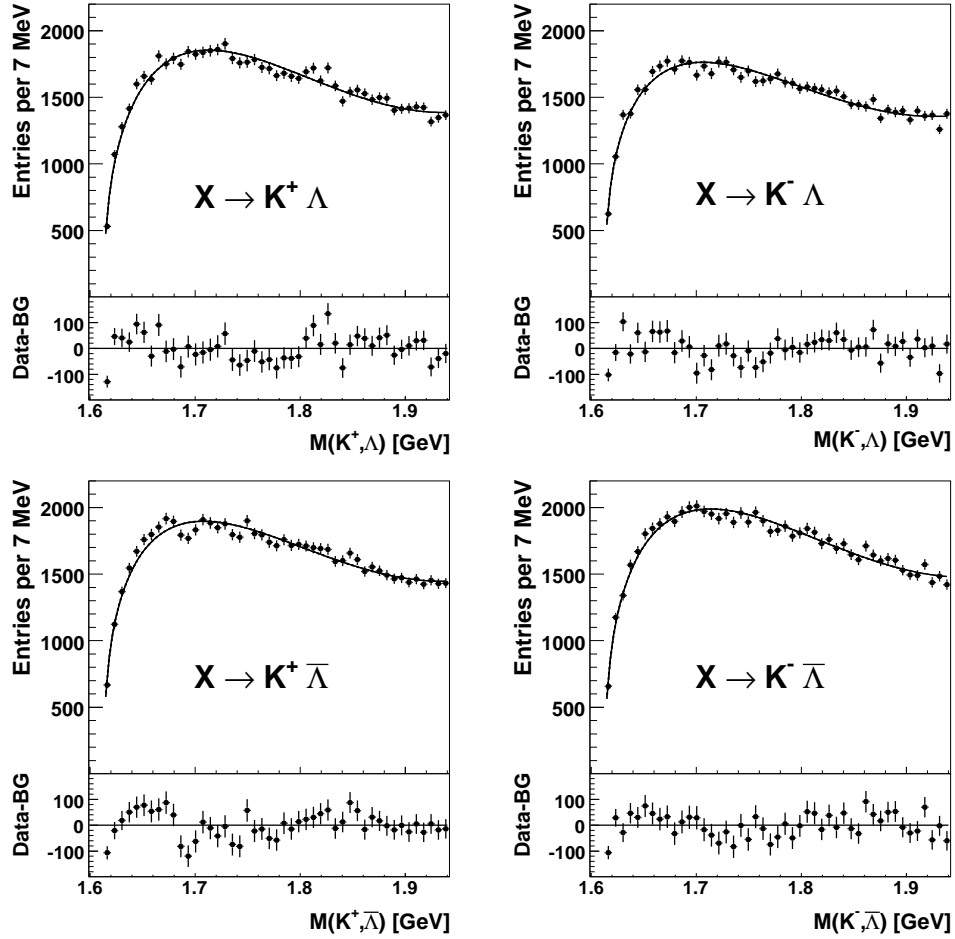
Figure 12.14: The reconstructed mass spectra for $K^+\Lambda$ (top left), $K^-\Lambda$ (top right), $K^+\overline{\Lambda}$ (bottom left) and $K^-\overline{\Lambda}$ (bottom right) combinations (charge conjugation excluded). Overlayed on the data points is the result of a fit using the function defined by equation 12.6. The difference of the invariant mass and the fit function is appended on the bottom of each figure.
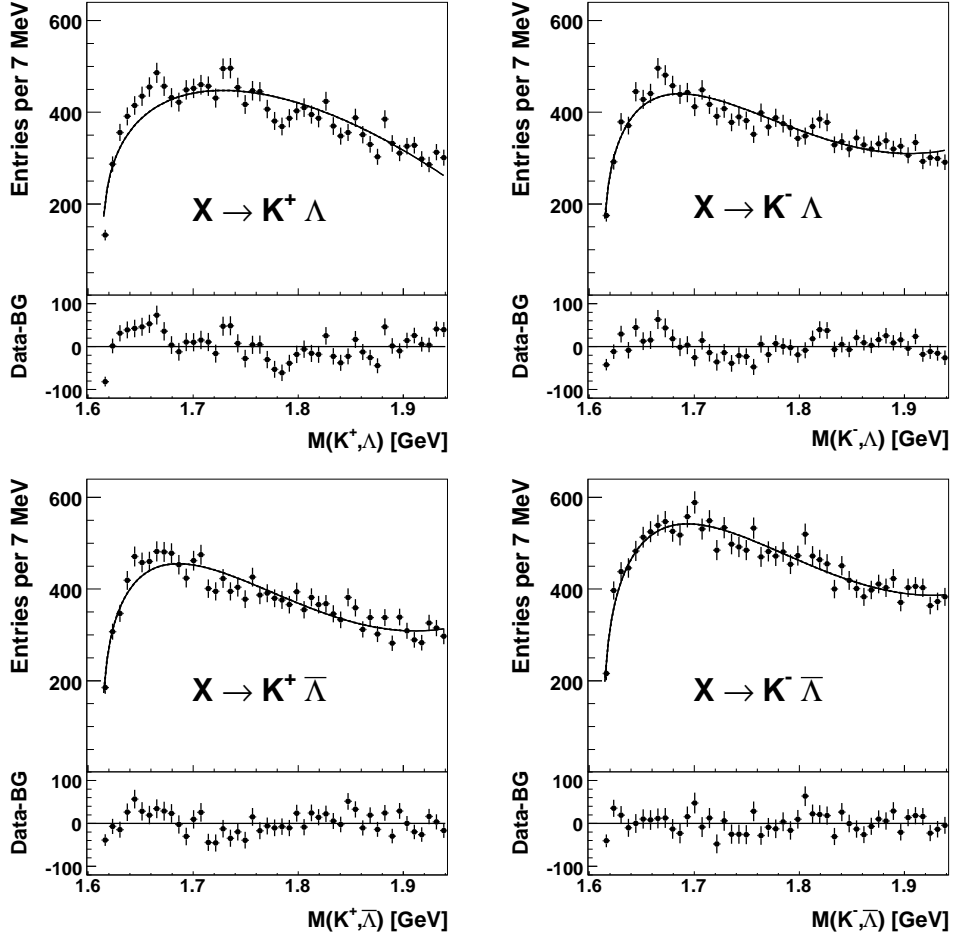
Figure 12.15: The reconstructed mass spectra for $p(K^{\pm}) < 0.7\,\mathrm{GeV}$ for $K^+\,\Lambda$ (top left), $K^-\,\Lambda$ (top right), $K^+\,\overline{\Lambda}$ (bottom left) and $K^-\,\overline{\Lambda}$ (bottom right) combinations (charge conjugation excluded). Overlayed on the data points is the result of a fit using the function defined by equation 12.6. The difference of the invariant mass and the fit function is appended on the bottom of each figure.

12.5 $K_s^0 \Lambda$ Combinations in the HERA II Data

In order to investigate whether the signal candidate observed in the HERA I data is a statistical fluctuation, the HERA II data recorded in the year 2005 and 2006 are analysed. This data set corresponds to an integrated luminosity of $257\,\mathrm{pb}^{-1}$, providing roughly three times the statistics analysed in the previous section. A full analysis of the HERA II data is beyond the scope of this work and the following studies should therefore only be regarded as a first look at the new data [4].

The reconstructed $K_s^0 \Lambda$ mass spectrum is obtained by exactly the same analysis procedure as in the HERA I case (see section 12.1 and 12.2) and is displayed in figure 12.16. The event
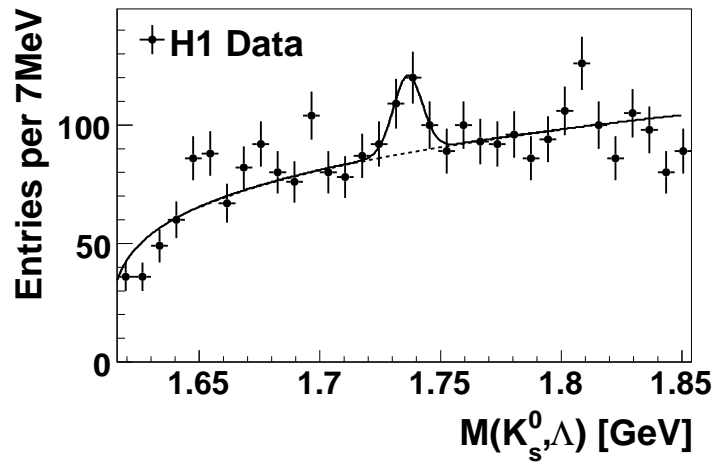
Figure 12.16: The mass spectrum $M(K_s^0, \Lambda)$ extracted from the HERA II data. All selection criteria introduced in sections 12.1 and 12.2 are applied. The solid line shows the result of a fit using a superposition of a Gaussian and the background function defined by equation 12.1 while the dashed line indicates the background only.

yield is compatible with the increase of the statistics. A small enhancement is observed at a mass of roughly $1730\,\mathrm{MeV}$. A fit to this mass spectra with a superposition of a Gaussian function and the background parameterisation defined by equation 12.1 is performed. This fit ($\chi^2/n = 47/29$) yields a total of 69 ± 24 signal entries at a mass of $(1736 \pm 2)\,\mathrm{MeV}$. The reconstructed width is $(6.0 \pm 2.2)\,\mathrm{MeV}$. Two problems arise when comparing the properties of the potential signal extracted from HERA I and II data: Firstly, the reconstructed mass is shifted by more than $20\,\mathrm{MeV}$. This is significantly larger than the statistical uncertainty of the measurements. However, systematic effects in the reconstruction of the particle tracks, which has changed between HERA I and II, could in principle lead to a shift in this order of magnitude, although this scenario is rather unlikely since the reconstructed mass of the K_s^0 mesons and Λ baryons is, within $1\,\mathrm{MeV}$, consistent with the world average. An analysis of the data with the final calibration and alignment of the detectors is needed for clarification of this point. Secondly, only 69 events are observed while the expected number of events for the HERA II period is about 140. This difference is not covered by the statistical accuracy of the measurement.

---

[4]At the time of this study, the final alignment and calibration constants were not yet available.

The results reported here are obtained from uncorrected data. The compatibility of the two signal candidates can only be tested by a rigorous analysis of the HERA II data. Furthermore, the determination of the production cross-section for the signal candidates observed in the HERA I and II data sets is needed to draw precise conclusions.

Chapter 13

Conclusion and Outlook

Spectroscopy of strange hadrons in ep collisions is studied in great detail. The measurement of the production cross-section of K_s^0 and Λ particles is complemented by a search for new resonances decaying into the strange particles $\Xi\,\pi$ or $K_s^0\,\Lambda$.

The cross-sections and ratios of the production of K_s^0 and Λ hadrons are measured differentially in deep-inelastic ep scattering events as a function of the event variables and the final state particle variables in the visible kinematic region defined by $2 < Q^2 < 100\,\mathrm{GeV}^2$ and $0.1 < y < 0.6$, $0.5 < p_T(K_s^0,\Lambda) < 3.5\,\mathrm{GeV}$ and $|\eta(K_s^0,\Lambda)| < 1.3$.

In general, the overall features of the ep data are found to be reproduced by the simulation when using the ALEPH-tuned JETSET parameters for the hadronisation process as extracted from e^+e^- collisions. Therefore this tuning should also be applicable for the description of pp collisions at the LHC. A more detailed study shows that the colour dipole model (CDM) implementation favours a strangeness suppression factor, λ_s, around 0.3 while within the matrix element and parton shower (MEPS) model a lower value around 0.2 is preferred. The results are also found to be compatible with the ZEUS measurements. Furthermore, the latest PDF set of CTEQ6L provides the most accurate description of the data.

However, the predictions fail to describe the details of the distributions in various regions of the phase space, in particular in the low p_T, low x and large positive η regions. A single λ_s value is clearly insufficient to describe the details of the production in the different kinematical quantities and regions. In the current region of the Breit frame the MEPS and CDM models give very similar predictions, both describing the K_s^0 and Λ cross-sections satisfactorily.

The measurement of the asymmetry in the production of Λ with respect to $\overline{\Lambda}$ is found to be consistent with zero within errors. Thus, no evidence of baryon number transport is visible in the measured data.

The Λ to K_s^0 cross-section ratio is better described by the CDM implementation than by the MEPS one. Therefore, the mechanism implemented in the colour dipole radiation model seems to better describe the baryon to meson ratio than those implemented in the parton shower. A tuning of the strangeness suppression factor λ_s and the diquark suppression factor λ_{qq} to the measured data is performed for the CDM implementation. Under the conservative assumption of a strange diquark suppression, λ_{sq}, between zero and one, the following ranges

are extracted:

$$\begin{aligned}
\lambda_s &\in [0.266, 0.298], \\
\lambda_{qq} &\in [0.101, 0.146].
\end{aligned}$$

The range quoted for λ_s is only valid for the PDF set CTEQ6L.

A search for new narrow baryonic resonances decaying into $\Xi^-\pi^-$ and $\Xi^-\pi^+$ and their charge conjugate states is performed with the H1 detector using a DIS data sample in the kinematic region $2 < Q^2 < 100\,\mathrm{GeV}^2$ and $0.05 < y < 0.7$, corresponding to a total integrated luminosity of $101\,\mathrm{pb}^{-1}$. The established $\Xi(1530)^0$ baryon state is observed by identifying its full decay chain. This includes the reconstruction of tertiary vertices which is successfully used in the H1 framework for the first time. The reconstruction procedure is cross checked by the measurement of the lifetime of the Ξ^- baryons which is found to be $c\,\tau(\Xi^-) = (5.16 \pm 0.35)\,\mathrm{cm}$ and therefore in good agreement with the world average value. In total, 163 ± 24 $\Xi(1530)^0$ baryons are reconstructed.

No signal of a new baryonic state is found in the mass range $1.6 - 2.3\,\mathrm{GeV}$, for either the combined or the four separate charge combinations ($\Xi^-\pi^-$, $\Xi^-\pi^+$, $\overline{\Xi}^+\pi^-$, $\overline{\Xi}^+\pi^+$). Therefore, mass dependent upper limits at 95% C.L. are set on the production ratio of hypothetical states, such as the pentaquark states Ξ^{--}_{5q} and Ξ^0_{5q}, to the total number of observed $\Xi(1530)^0$ baryons. For the neutral combinations these limits vary from 0.1 to 0.5 and for the charged combinations from 0.12 to 0.45. The results reported here are found to be similar to the limits published by the ZEUS Collaboration. With the HERA II data set these upper limits could be improved by approximately 30 %.

The overall H1 data statistics in the Ξ^- sample is comparable with the NA49 collaboration's data and therefore the limits derived within this work do not confirm the NA49 observation of potential pentaquark states.

The $K^0_s\Lambda$ combinations are investigated using $78\,\mathrm{pb}^{-1}$ of ep scattering data from the HERA I period. A resonant structure is observed at a mass of $(1710 \pm 2)\,\mathrm{MeV}$ and with a width of $(4.8 \pm 1.2)\,\mathrm{MeV}$, consistent with the detector resolution. This structure contains 48 ± 12 events and might be interpreted as the pentaquark state N^0_s or the excited baryon state $\Xi^0(1690)$. A study of the $K^\pm\Lambda$ combinations does not lead to a clarification of these two interpretations. A structure is also observed in the HERA II data. However, only half of the expected number of events are observed in the mass peak and its mean value is shifted by $26\,\mathrm{MeV}$ with respect to the observation in the HERA I data. A rigorous investigation of the HERA II data using the latest calibration and alignment constants is needed for clarification and a determination of the production cross-section for these signals is desirable. Nevertheless, it is shown that the combination of K^0_s and Λ particles bears interesting features and is worth being studied further.

Appendix A

Cross-Section Tables

The values of the cross-sections and their statistical and systematic uncertainties are listed in tables A.1 to A.3 for the K_s^0 production, in tables A.4 to A.6 for the Λ production and in tables A.7 to A.9 for the ratio $R(\Lambda/K_s^0)$ for all variables investigated within this work.

Table A.1: The differential K_s^0 cross-section values as a function of Q^2, x, y and W in the visible region defined by $2 < Q^2 < 100\,\mathrm{GeV}^2$, $0.1 < y < 0.6$, $0.5 < p_T < 3.5\,\mathrm{GeV}$ and $-1.3 < \eta < 1.3$. The bin ranges, the bin averaged cross section values, the statistical and the positive and negative systematic uncertainties are listed.

$\mathbf{ep \rightarrow e\,K_s^0\,X}$			
Q^2	$\mathrm{d}\sigma/\mathrm{d}Q^2$	stat.	syst. (+)	syst. (−)
$[\mathrm{GeV}^2]$	$[\mathrm{nb/GeV}^2]$			
2 − 2.5	5.73	0.10	0.58	0.71
2.5 − 3	4.05	0.08	0.29	0.29
3 − 4	3.08	0.05	0.21	0.21
4 − 5	2.00	0.03	0.12	0.13
5 − 7	1.332	0.018	0.082	0.082
7 − 10	0.764	0.011	0.045	0.047
10 − 15	0.417	0.006	0.023	0.024
15 − 25	0.197	0.003	0.012	0.012
25 − 100	0.0340	0.0004	0.0020	0.0021
x	$\mathrm{d}\sigma/\mathrm{d}x$	stat.	syst. (+)	syst. (−)
	$[\mathrm{pb}]$			
0.00004 − 0.0001	69.4	1.0	4.4	4.4
0.0001 − 0.0002	51.7	0.6	3.2	3.3
0.0002 − 0.0004	24.0	0.3	1.4	1.5
0.0004 − 0.001	7.07	0.07	0.43	0.43
0.001 − 0.01	0.315	0.004	0.019	0.019
y	$\mathrm{d}\sigma/\mathrm{d}y$	stat.	syst. (+)	syst. (−)
	$[\mathrm{nb}]$			
0.1 − 0.15	86.5	1.0	5.0	5.4
0.15 − 0.22	65.0	0.7	3.9	4.1
0.22 − 0.3	48.2	0.5	2.9	3.0
0.3 − 0.4	35.8	0.4	2.1	2.1
0.4 − 0.5	25.7	0.4	1.3	1.4
0.5 − 0.6	22.5	0.4	1.1	1.2
W	$\mathrm{d}\sigma/\mathrm{d}W$	stat.	syst. (+)	syst. (−)
$[\mathrm{GeV}]$	$[\mathrm{nb/GeV}]$			
100 − 115	0.1837	0.0025	0.0107	0.0114
115 − 135	0.1853	0.0022	0.0109	0.0116
135 − 155	0.1694	0.0021	0.0105	0.0107
155 − 175	0.1524	0.0019	0.0088	0.0090
175 − 195	0.1365	0.0018	0.0079	0.0077
195 − 220	0.1099	0.0015	0.0057	0.0060
220 − 250	0.0986	0.0014	0.0052	0.0053

Table A.2: The differential K_s^0 cross-section values as a function of p_T and η. More details are given in caption of table A.1.

$\mathbf{ep \rightarrow e\,K_s^0\,X}$				
p_T [GeV]	$\mathrm{d}\sigma/\mathrm{d}p_T$	stat.	syst. (+) [nb/GeV]	syst. (−)
0.5 − 0.6	34.6	0.5	2.0	2.1
0.6 − 0.7	29.6	0.4	1.7	1.7
0.7 − 0.8	25.5	0.4	1.4	1.5
0.8 − 0.9	20.4	0.3	1.1	1.2
0.9 − 1.1	15.2	0.2	0.9	0.9
1.1 − 1.3	10.46	0.14	0.61	0.63
1.3 − 1.6	6.91	0.10	0.46	0.46
1.6 − 2.2	3.13	0.04	0.20	0.20
2.2 − 3.5	0.83	0.02	0.06	0.06
η	$\mathrm{d}\sigma/\mathrm{d}\eta$	stat.	syst. (+) [nb]	syst. (−)
-1.3 − -1	8.08	0.12	0.41	0.42
-1 − -0.75	8.69	0.13	0.51	0.52
-0.75 − -0.5	8.64	0.12	0.44	0.46
-0.5 − -0.25	8.56	0.13	0.47	0.50
-0.25 − 0	8.79	0.16	0.56	0.59
0 − 0.25	8.65	0.14	0.58	0.60
0.25 − 0.5	7.58	0.13	0.52	0.52
0.5 − 0.75	7.99	0.13	0.55	0.56
0.75 − 1	7.98	0.15	0.54	0.54
1 − 1.3	8.06	0.13	0.54	0.54

Table A.3: The differential K_s^0 cross-section values as a function of p_T^{Breit} and x_p^{Breit} in target and current hemispheres of the Breit frame. More details are given in caption of table A.1.

$\mathbf{ep \rightarrow e\,K_s^0\,X}$				
p_T^{Breit} target	$\mathrm{d}\sigma/\mathrm{d}p_T^{Breit}$	stat.	syst. $(+)$	syst. $(-)$
[GeV]	[nb/GeV]			
0.5 – 1	21.20	0.19	1.20	1.23
1 – 1.25	10.05	0.16	0.57	0.57
1.25 – 1.5	6.12	0.13	0.35	0.37
1.5 – 2.5	2.04	0.04	0.12	0.12
2.5 – 4	0.230	0.008	0.011	0.011
p_T^{Breit} current	$\mathrm{d}\sigma/\mathrm{d}p_T^{Breit}$	stat.	syst. $(+)$	syst. $(-)$
[GeV]	[nb/GeV]			
0 – 0.6	2.00	0.05	0.14	0.16
0.6 – 3	0.277	0.009	0.031	0.036
x_p^{Breit} target	$\mathrm{d}\sigma/\mathrm{d}x_p^{Breit}$	stat.	syst. $(+)$	syst. $(-)$
	[nb]			
0 – 0.45	4.01	0.08	0.22	0.23
0.45 – 1	5.43	0.09	0.39	0.42
1 – 2	3.66	0.05	0.25	0.25
2 – 4	2.03	0.03	0.11	0.11
4 – 7	0.984	0.016	0.05	0.05
7 – 11	0.478	0.011	0.026	0.028
11 – 20	0.167	0.005	0.011	0.013
x_p^{Breit} current	$\mathrm{d}\sigma/\mathrm{d}x_p^{Breit}$	stat.	syst. $(+)$	syst. $(-)$
	[nb]			
0 – 0.3	3.27	0.08	0.18	0.20
0.3 – 1	1.20	0.04	0.14	0.17

Table A.4: The differential $\Lambda(\bar{\Lambda})$ cross-section values as a function of Q^2, x, y and W. More details are given in caption of table A.1.

$\mathbf{ep \rightarrow e\,\Lambda\,X}$				
Q^2 [GeV^2]	dσ/dQ^2	stat. [nb/GeV^2]	syst. (+)	syst. (−)
2 − 2.5	2.33	0.14	0.25	0.30
2.5 − 3	1.58	0.09	0.12	0.13
3 − 4	1.13	0.05	0.08	0.08
4 − 5	0.73	0.04	0.05	0.05
5 − 7	0.462	0.018	0.028	0.030
7 − 10	0.282	0.012	0.019	0.020
10 − 15	0.153	0.006	0.009	0.009
15 − 25	0.071	0.003	0.004	0.004
25 − 100	0.0120	0.0004	0.0006	0.0006
x	dσ/dx	stat. [pb]	syst. (+)	syst. (−)
0.00004 − 0.0001	28.1	1.1	2.0	2.0
0.0001 − 0.0002	20.1	0.7	1.4	1.4
0.0002 − 0.0004	8.5	0.3	0.5	0.5
0.0004 − 0.001	2.57	0.08	0.15	0.15
0.001 − 0.01	0.104	0.003	0.006	0.006
y	dσ/dy	stat. [nb]	syst. (+)	syst. (−)
0.1 − 0.15	27.9	1.1	1.6	1.8
0.15 − 0.22	24.7	0.8	1.6	1.6
0.22 − 0.3	17.4	0.6	1.3	1.3
0.3 − 0.4	14.2	0.5	0.9	1.0
0.4 − 0.5	10.9	0.5	0.7	0.7
0.5 − 0.6	9.1	0.4	0.5	0.5
W [GeV]	dσ/dW	stat. [nb/GeV]	syst. (+)	syst. (−)
100 − 115	0.055	0.003	0.006	0.007
115 − 135	0.063	0.002	0.004	0.004
135 − 155	0.070	0.003	0.004	0.004
155 − 175	0.055	0.002	0.004	0.004
175 − 195	0.052	0.002	0.004	0.004
195 − 220	0.047	0.002	0.003	0.003
220 − 250	0.041	0.002	0.002	0.002

Table A.5: The differential $\Lambda(\bar{\Lambda})$ cross-section values as a function of p_T and η. More details are given in caption of table A.1.

ep $\rightarrow$ e Λ X				
p_T [GeV]	$\mathrm{d}\sigma/\mathrm{d}p_T$	stat.	syst. (+) [nb/GeV]	syst. ($-$)
0.5 $-$ 0.6	8.4	0.8	0.8	0.8
0.6 $-$ 0.7	8.0	0.5	0.4	0.5
0.7 $-$ 0.8	7.9	0.5	0.5	0.5
0.8 $-$ 0.9	6.8	0.3	0.5	0.5
0.9 $-$ 1.1	6.1	0.2	0.4	0.4
1.1 $-$ 1.3	4.70	0.18	0.29	0.30
1.3 $-$ 1.6	3.05	0.10	0.20	0.20
1.6 $-$ 2.2	1.52	0.05	0.09	0.09
2.2 $-$ 3.5	0.42	0.02	0.02	0.02
η	$\mathrm{d}\sigma/\mathrm{d}\eta$	stat.	syst. (+) [nb]	syst. ($-$)
-1.3 $-$ -1	2.67	0.14	0.15	0.15
-1 $-$ -0.75	2.87	0.14	0.16	0.17
-0.75 $-$ -0.5	3.03	0.15	0.17	0.17
-0.5 $-$ -0.25	2.76	0.13	0.18	0.18
-0.25 $-$ 0	2.74	0.15	0.19	0.20
0 $-$ 0.25	2.92	0.15	0.21	0.22
0.25 $-$ 0.5	2.95	0.14	0.21	0.22
0.5 $-$ 0.75	3.36	0.17	0.23	0.23
0.75 $-$ 1	3.43	0.15	0.25	0.25
1 $-$ 1.3	3.88	0.16	0.28	0.31

Table A.6: The differential $\Lambda(\bar{\Lambda})$ cross-section values as a function of p_T^{Breit} and x_p^{Breit} in target and current hemispheres of the Breit frame. More details are given in caption of table A.1.

$ep \rightarrow e\,\Lambda\,X$				
p_T^{Breit} target [GeV]	$d\sigma/dp_T^{Breit}$	stat.	syst. $(+)$ [nb/GeV]	syst. $(-)$
$0.5 \; - \; 1$	6.97	0.19	0.38	0.40
$1 \; - \; 1.25$	4.52	0.17	0.28	0.28
$1.25 \; - \; 1.5$	2.71	0.13	0.17	0.17
$1.5 \; - \; 2.5$	1.01	0.04	0.06	0.06
$2.5 \; - \; 4$	0.114	0.009	0.007	0.008
p_T^{Breit} current [GeV]	$d\sigma/dp_T^{Breit}$	stat.	syst. $(+)$ [nb/GeV]	syst. $(-)$
$0 \; - \; 0.6$	0.307	0.028	0.017	0.018
$0.6 \; - \; 3$	0.051	0.004	0.004	0.004
x_p^{Breit} target	$d\sigma/dx_p^{Breit}$	stat.	syst. $(+)$ [nb]	syst. $(-)$
$0 \; - \; 0.45$	0.94	0.05	0.05	0.06
$0.45 \; - \; 1$	1.51	0.07	0.11	0.12
$1 \; - \; 2$	1.09	0.05	0.08	0.09
$2 \; - \; 4$	0.75	0.03	0.05	0.05
$4 \; - \; 7$	0.45	0.02	0.03	0.03
$7 \; - \; 11$	0.220	0.011	0.015	0.016
$11 \; - \; 20$	0.102	0.006	0.008	0.008
x_p^{Breit} current	$d\sigma/dx_p^{Breit}$	stat.	syst. $(+)$ [nb]	syst. $(-)$
$0 \; - \; 0.3$	0.55	0.05	0.04	0.04
$0.3 \; - \; 1$	0.21	0.02	0.03	0.03

Table A.7: The values of the ratio $R(\Lambda/K_s^0)$ of the differential cross-sections for $\Lambda(\bar{\Lambda})$ baryons to K_s^0 mesons as a function of Q^2, x, y and W. More details are given in caption of table A.1.

R(Λ/K_s^0)				
Q^2 [GeV^2]	R(Λ/K_s^0)	stat.	syst. (+)	syst. (−)
2 − 2.5	0.406	0.025	0.018	0.019
2.5 − 3	0.390	0.020	0.030	0.030
3 − 4	0.368	0.019	0.020	0.020
4 − 5	0.366	0.020	0.018	0.019
5 − 7	0.347	0.014	0.014	0.014
7 − 10	0.369	0.016	0.018	0.019
10 − 15	0.367	0.015	0.013	0.014
15 − 25	0.360	0.016	0.017	0.017
25 − 100	0.353	0.012	0.017	0.018
x	R(Λ/K_s^0)	stat.	syst. (+)	syst. (−)
0.00004 − 0.0001	0.405	0.017	0.024	0.025
0.0001 − 0.0002	0.390	0.014	0.019	0.020
0.0002 − 0.0004	0.355	0.011	0.012	0.013
0.0004 − 0.001	0.364	0.012	0.013	0.014
0.001 − 0.01	0.329	0.011	0.016	0.017
y	R(Λ/K_s^0)	stat.	syst. (+)	syst. (−)
0.1 − 0.15	0.323	0.013	0.013	0.013
0.15 − 0.22	0.380	0.014	0.013	0.014
0.22 − 0.3	0.361	0.013	0.020	0.021
0.3 − 0.4	0.397	0.014	0.019	0.020
0.4 − 0.5	0.426	0.020	0.018	0.019
0.5 − 0.6	0.407	0.020	0.015	0.016
W [GeV]	R(Λ/K_s^0)	stat.	syst. (+)	syst. (−)
100 − 115	0.301	0.015	0.013	0.013
115 − 135	0.339	0.014	0.014	0.015
135 − 155	0.409	0.017	0.012	0.014
155 − 175	0.359	0.015	0.014	0.015
175 − 195	0.378	0.016	0.021	0.021
195 − 220	0.424	0.018	0.023	0.024
220 − 250	0.411	0.019	0.013	0.014

Table A.8: The values of the ratio R(Λ/K_s^0) of the differential cross-sections for $\Lambda(\bar{\Lambda})$ baryons to K_s^0 mesons as a function of p_T and η. More details are given in caption of table A.1.

R(Λ/K_s^0)				
p_T [GeV]	R(Λ/K_s^0)	stat.	syst. (+)	syst. (−)
0.5 − 0.6	0.24	0.02	0.02	0.02
0.6 − 0.7	0.268	0.017	0.009	0.010
0.7 − 0.8	0.309	0.020	0.015	0.016
0.8 − 0.9	0.334	0.014	0.016	0.017
0.9 − 1.1	0.402	0.017	0.015	0.016
1.1 − 1.3	0.450	0.018	0.015	0.016
1.3 − 1.6	0.442	0.016	0.021	0.022
1.6 − 2.2	0.485	0.016	0.019	0.020
2.2 − 3.5	0.505	0.027	0.031	0.032
η	R(Λ/K_s^0)	stat.	syst. (+)	syst. (−)
-1.3 − -1	0.331	0.018	0.015	0.015
-1 − -0.75	0.330	0.017	0.018	0.018
-0.75 − -0.5	0.350	0.018	0.013	0.014
-0.5 − -0.25	0.323	0.016	0.015	0.016
-0.25 − 0	0.311	0.018	0.017	0.017
0 − 0.25	0.337	0.018	0.018	0.018
0.25 − 0.5	0.389	0.019	0.017	0.018
0.5 − 0.75	0.420	0.023	0.014	0.015
0.75 − 1	0.430	0.020	0.017	0.018
1 − 1.3	0.48	0.02	0.02	0.02

Table A.9: The values of the ratio R(Λ/K_s^0) of the differential cross-sections for $\Lambda(\bar{\Lambda})$ baryons to K_s^0 mesons as a function of p_T^{Breit} and x_p^{Breit} in the target and current hemispheres of the Breit frame. More detailes are given in caption of table A.1.

R(Λ/K_s^0)				
p_T^{Breit} target [GeV]	R(Λ/K_s^0)	stat.	syst. (+)	syst. (−)
0.5 − 1	0.329	0.009	0.008	0.009
1 − 1.25	0.449	0.019	0.015	0.016
1.25 − 1.5	0.443	0.023	0.017	0.018
1.5 − 2.5	0.493	0.019	0.020	0.021
2.5 − 4	0.495	0.043	0.026	0.027
p_T^{Breit} current [GeV]	R(Λ/K_s^0)	stat.	syst. (+)	syst. (−)
0 − 0.6	0.153	0.015	0.005	0.005
0.6 − 3	0.185	0.017	0.008	0.008
x_p^{Breit} target	R(Λ/K_s^0)	stat.	syst. (+)	syst. (−)
0 − 0.45	0.235	0.014	0.008	0.008
0.45 − 1	0.277	0.013	0.010	0.011
1 − 2	0.297	0.014	0.013	0.013
2 − 4	0.370	0.016	0.014	0.015
4 − 7	0.460	0.022	0.017	0.018
7 − 11	0.46	0.03	0.02	0.03
11 − 20	0.61	0.04	0.03	0.04
x_p^{Breit} current	R(Λ/K_s^0)	stat.	syst. (+)	syst. (−)
0 − 0.3	0.169	0.015	0.009	0.009
0.3 − 1	0.174	0.017	0.012	0.012

Appendix B

Mass Assignment to the Daughter Particles of the Λ

In the decay $\Lambda \to p\,\pi^-$ the proton has always a higher momentum than the pion if the momentum of the Λ is larger than approximately $300\,\mathrm{MeV}$. In the following this threshold is calculated.

The calculation starts with consideration in the rest-frame of the Λ. In this frame the pion and the proton decay back-to-back and their momentum is balanced due to momentum conservation: $\vec{p}_{rest}(p) = \vec{p}_{rest}(\pi) =: \vec{p}_{rest}$. If the z-axis is chosen to coincidence with the pion flight direction, four-vector conservation yields:

$$
\mathcal{P'}^{\mu}_{p} + \mathcal{P'}^{\mu}_{\pi} = \begin{pmatrix} \sqrt{m_p^2 + p_{rest}^2} \\ 0 \\ 0 \\ -p_{rest} \end{pmatrix} + \begin{pmatrix} \sqrt{m_\pi^2 + p_{rest}^2} \\ 0 \\ 0 \\ p_{rest} \end{pmatrix} = \begin{pmatrix} m_\Lambda \\ 0 \\ 0 \\ 0 \end{pmatrix} = \mathcal{P'}^{\mu}_{\Lambda}. \tag{B.1}
$$

This equation determines the momentum p of the proton (pion) in the Λ rest-frame:

$$
p_{rest} = \sqrt{\frac{(m_\Lambda^2 - m_p^2 - m_\pi^2)^2 - 4 \cdot m_p^2 \cdot m_\pi^2}{4 \cdot m_\Lambda^2}} = 100.58\,\mathrm{MeV} \tag{B.2}
$$

The maximal momentum of the pion is achieved if it is parallel to the flight direction of the Λ. Therefore, the boost that gives the maximal pion momentum in the laboratory frame is:

$$
\Lambda_{\mu\nu} = \begin{pmatrix} \gamma & 0 & 0 & \gamma\beta \\ 0 & 1 & 0 & 0 \\ 0 & 0 & 1 & 0 \\ \gamma\beta & 0 & 0 & \gamma \end{pmatrix} \tag{B.3}
$$

The four-momentum of the proton and the pion in that laboratory frame that lead to the

threshold condition are:

$$\mathcal{P}_{\nu,p} = \Lambda_{\mu\nu}\mathcal{P'}^{\mu}_{p} = \begin{pmatrix} \gamma\sqrt{m_p^2 + p_{rest}^2} - \gamma\beta p_{rest} \\ 0 \\ 0 \\ \gamma\beta\sqrt{m_p^2 + p_{rest}^2} - \gamma p_{rest} \end{pmatrix} \tag{B.4}$$

$$\mathcal{P}_{\nu,\pi} = \Lambda_{\mu\nu}\mathcal{P'}^{\mu}_{\pi} = \begin{pmatrix} \gamma\sqrt{m_\pi^2 + p_{rest}^2} + \gamma\beta p_{rest} \\ 0 \\ 0 \\ \gamma\beta\sqrt{m_\pi^2 + p_{rest}^2} + \gamma p_{rest} \end{pmatrix} \tag{B.5}$$

From these equations the condition that the proton must have a larger momentum than the pion translates to:

$$\gamma\beta\sqrt{m_p^2 + p_{rest}^2} - \gamma p_{rest} > \gamma\beta\sqrt{m_\pi^2 + p_{rest}^2} + \gamma p_{rest} \tag{B.6}$$

This leads directly to a condition on the velocity of the Λ in the laboratory frame:

$$\beta > \frac{2 \cdot p_{rest}}{E_p^{rest} - E_\pi^{rest}}, \tag{B.7}$$

where E_p^{rest} and E_π^{rest} are the energies of the proton and the pion in the Λ rest-frame, respectively. Together with equation B.2 and $\beta = \frac{p}{E}$ this finally implies:

$$p(\Lambda) \gtrsim 300\,\text{MeV}. \tag{B.8}$$

This value is an absolute upper limit because the decay where the pion has the same flight direction as the Λ is highly suppressed.

Appendix C

Systematic Uncertainties

In the following figures the effect of the different systematic sources on the cross-section measurements is shown for all investigated variables. For explanation see section 6.5.
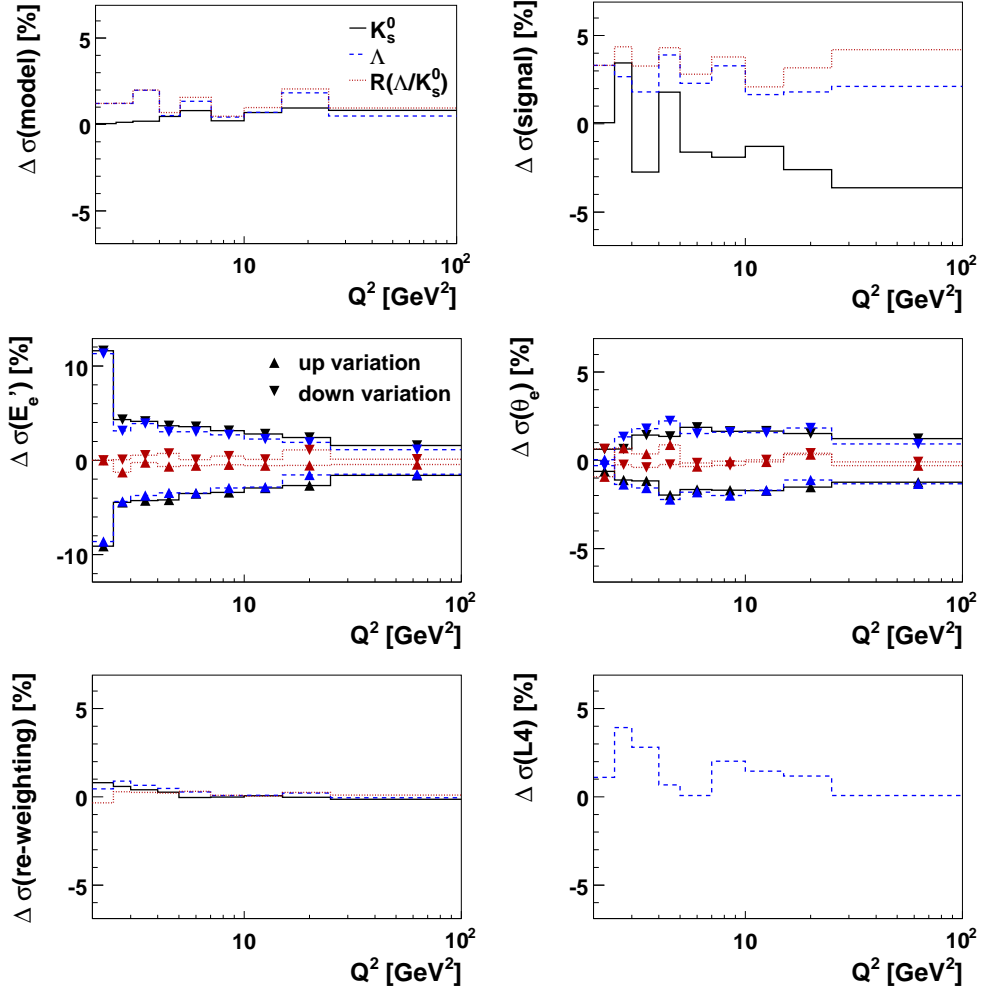
Figure C.1: The effect of the systematic sources on the differential cross-sections in Q^2 for the K_s^0 mesons (solid, black lines) for the Λ baryons (blue, dashed lines) and for the ratio $R(\Lambda/K_s^0)$ (red, dotted lines).
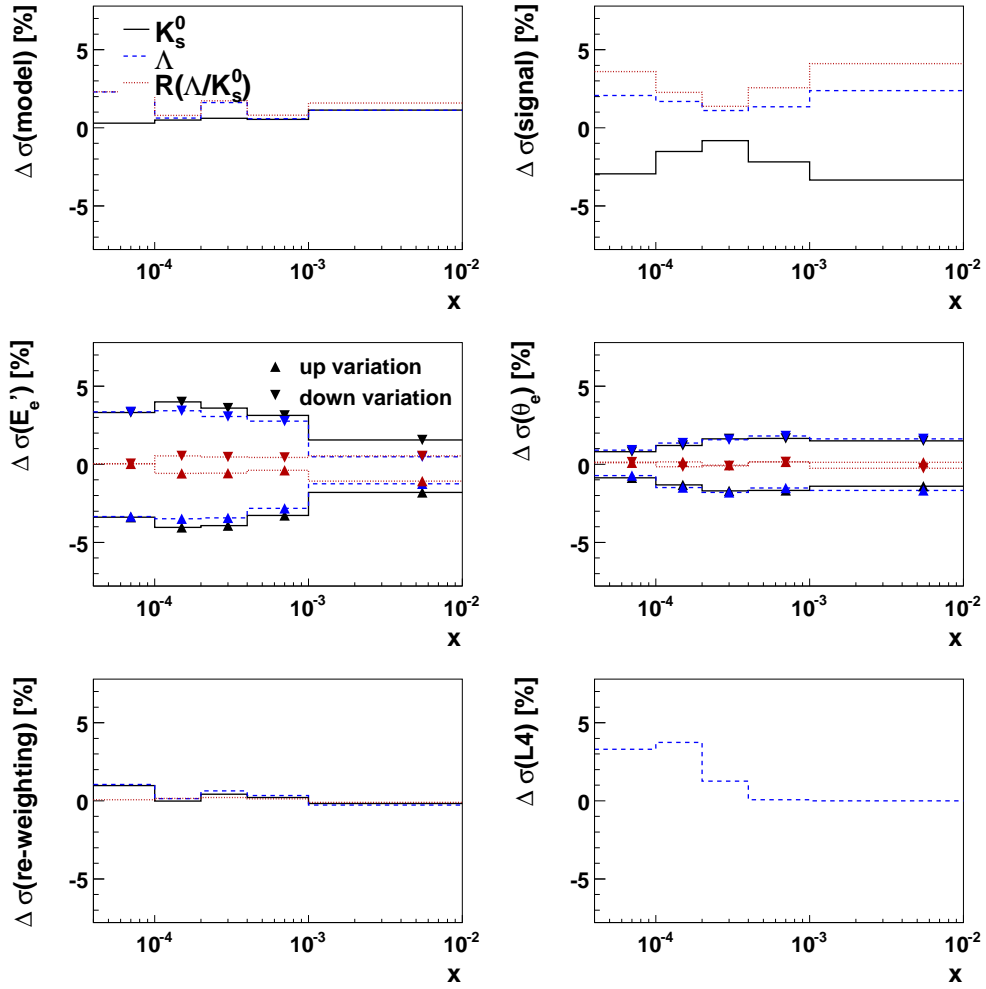
Figure C.2: The effect of the systematic sources on the differential cross-sections in x for the K_s^0 mesons (solid, black lines) for the Λ baryons (blue, dashed lines) and for the ratio $R(\Lambda/K_s^0)$ (red, dotted lines).
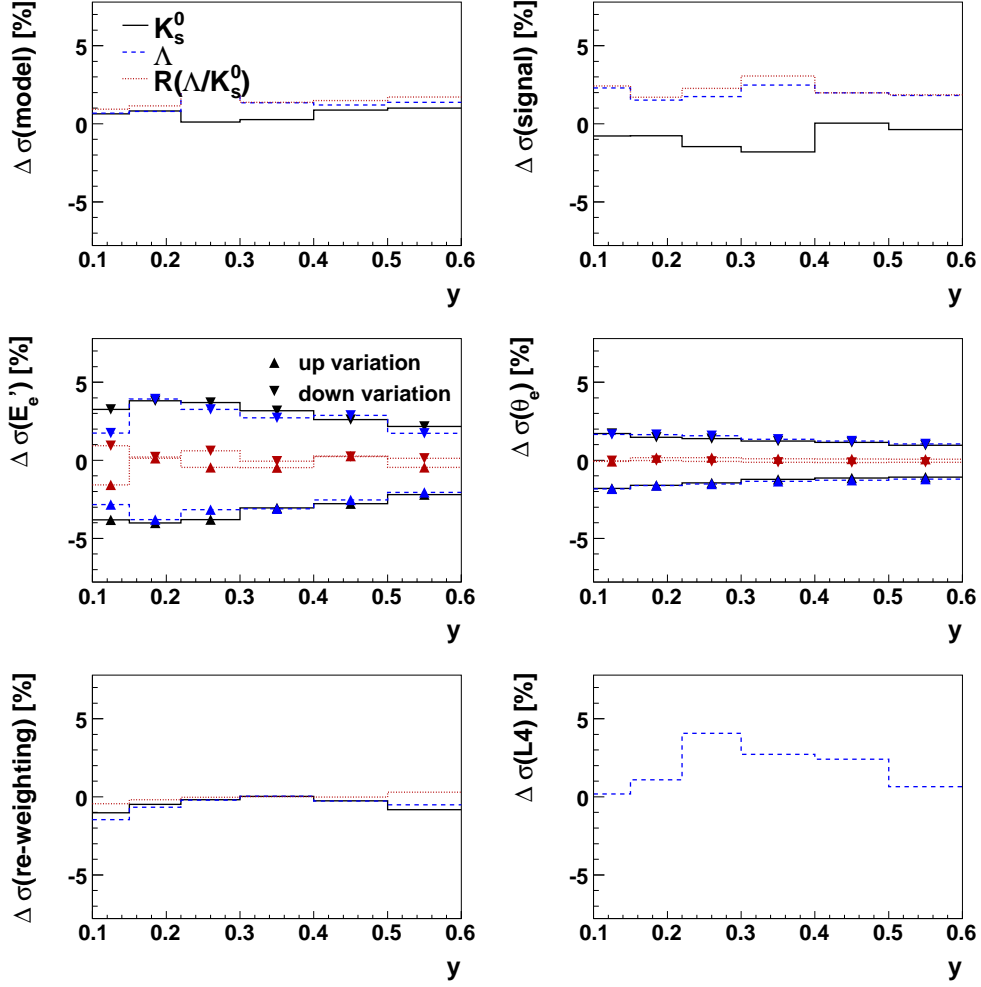
Figure C.3: The effect of the systematic sources on the differential cross-sections in y for the K_s^0 mesons (solid, black lines) for the Λ baryons (blue, dashed lines) and for the ratio $R(\Lambda/K_s^0)$ (red, dotted lines).
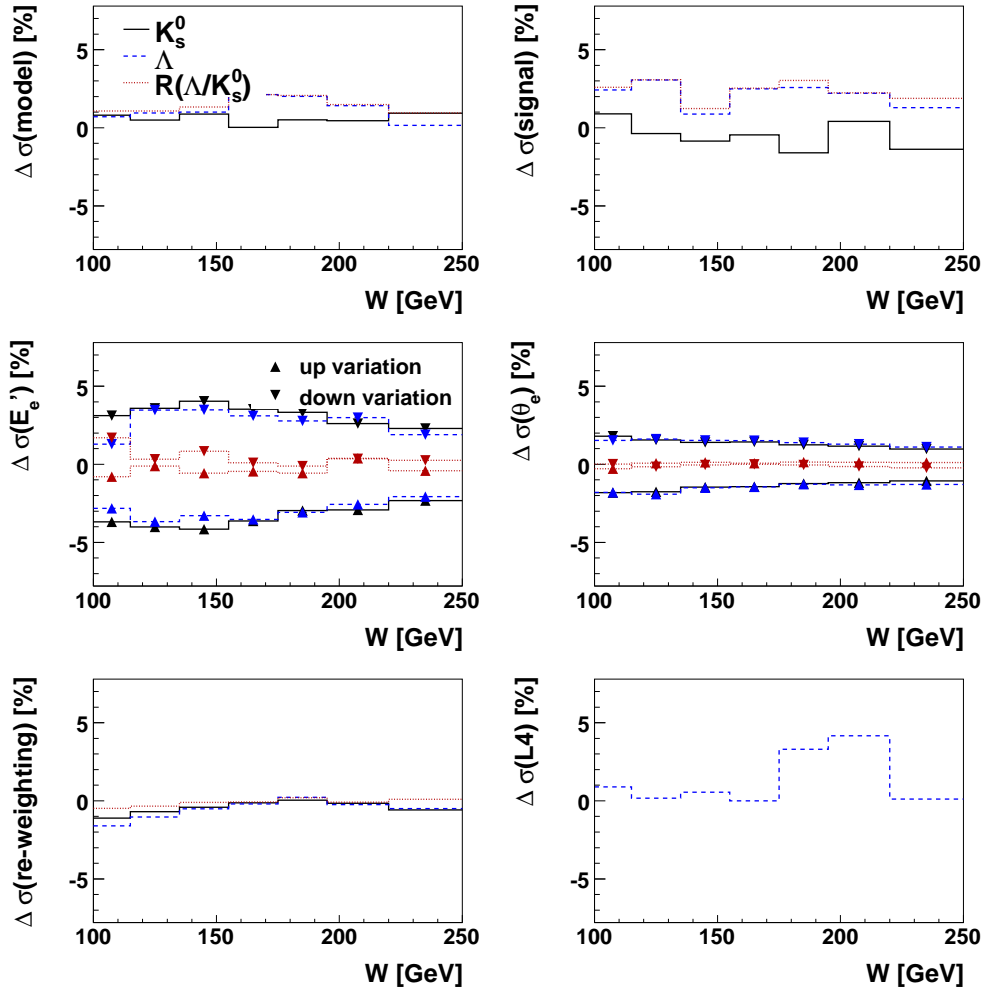
Figure C.4: The effect of the systematic sources on the differential cross-sections in W for the K_s^0 mesons (solid, black lines) for the Λ baryons (blue, dashed lines) and for the ratio $R(\Lambda/K_s^0)$ (red, dotted lines).
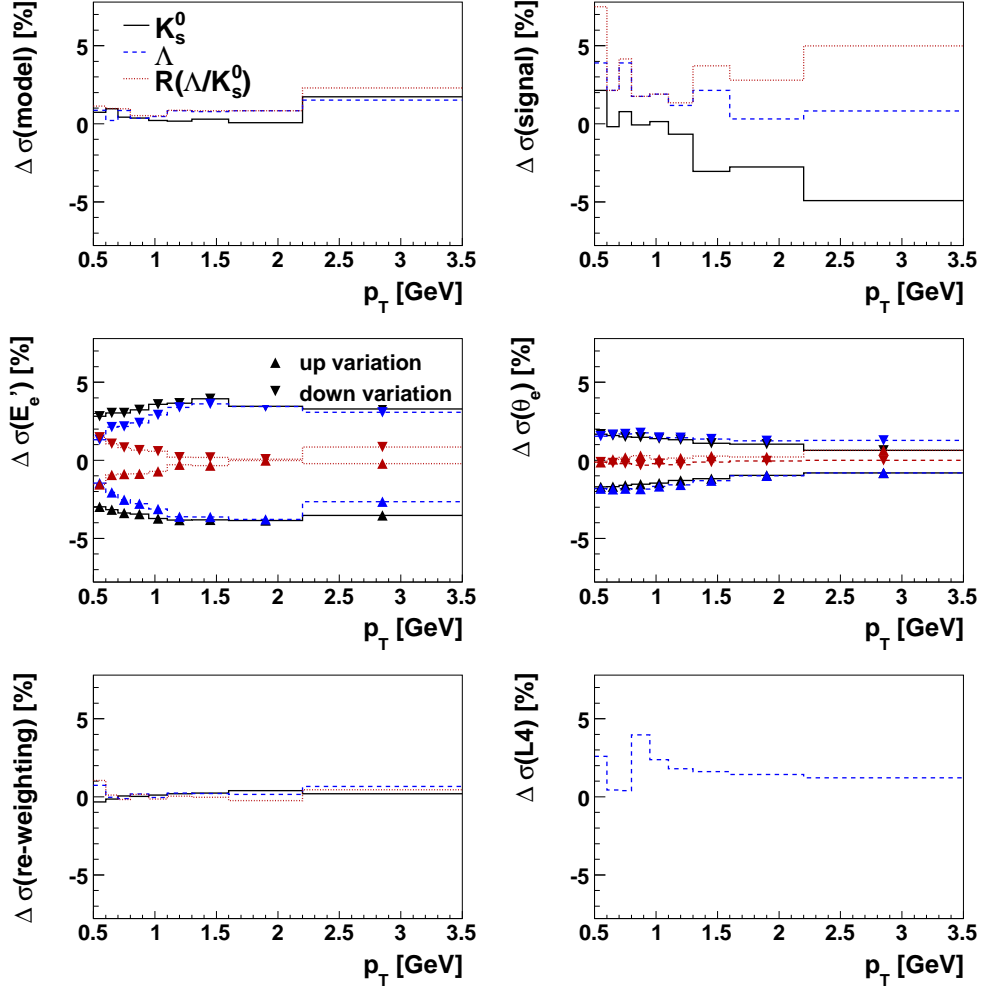
Figure C.5: The effect of the systematic sources on the differential cross-sections in p_T for the K_s^0 mesons (solid, black lines) for the Λ baryons (blue, dashed lines) and for the ratio $R(\Lambda/K_s^0)$ (red, dotted lines).
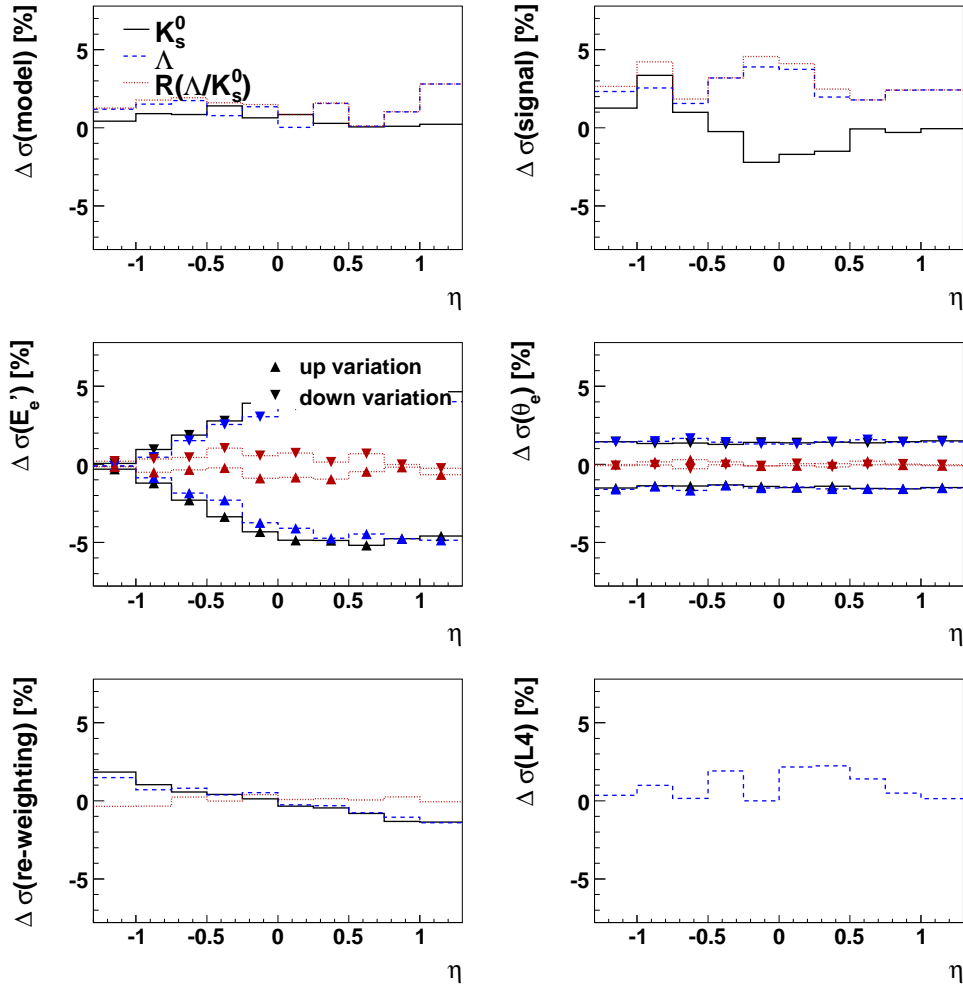
Figure C.6: The effect of the systematic sources on the differential cross-sections in η for the K_s^0 mesons (solid, black lines) for the Λ baryons (blue, dashed lines) and for the ratio $R(\Lambda/K_s^0)$ (red, dotted lines).
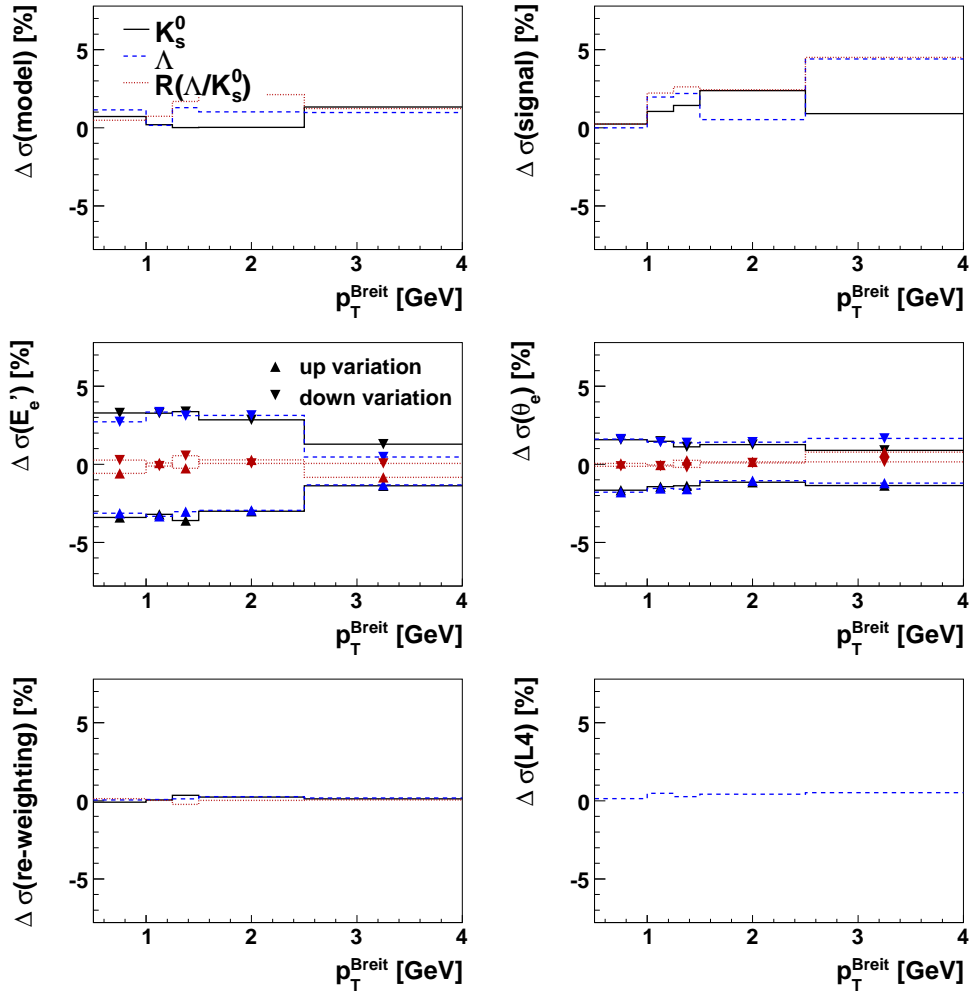
Figure C.7: The effect of the systematic sources on the differential cross-sections in p_T^{Breit} in the target hemisphere for the K_s^0 mesons (solid, black lines) for the Λ baryons (blue, dashed lines) and for the ratio $R(\Lambda/K_s^0)$ (red, dotted lines).
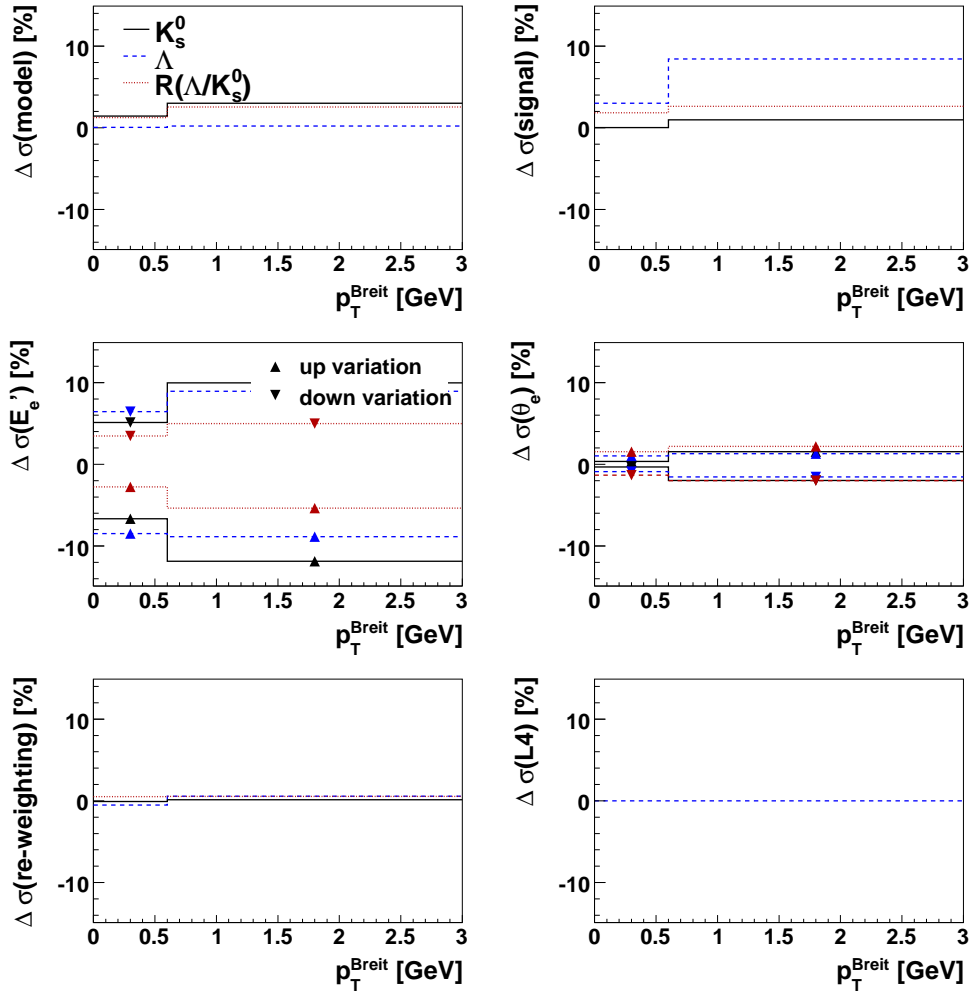
Figure C.8: The effect of the systematic sources on the differential cross-sections in p_T^{Breit} in the current hemisphere for the K_s^0 mesons (solid, black lines) for the Λ baryons (blue, dashed lines) and for the ratio $R(\Lambda/K_s^0)$ (red, dotted lines).
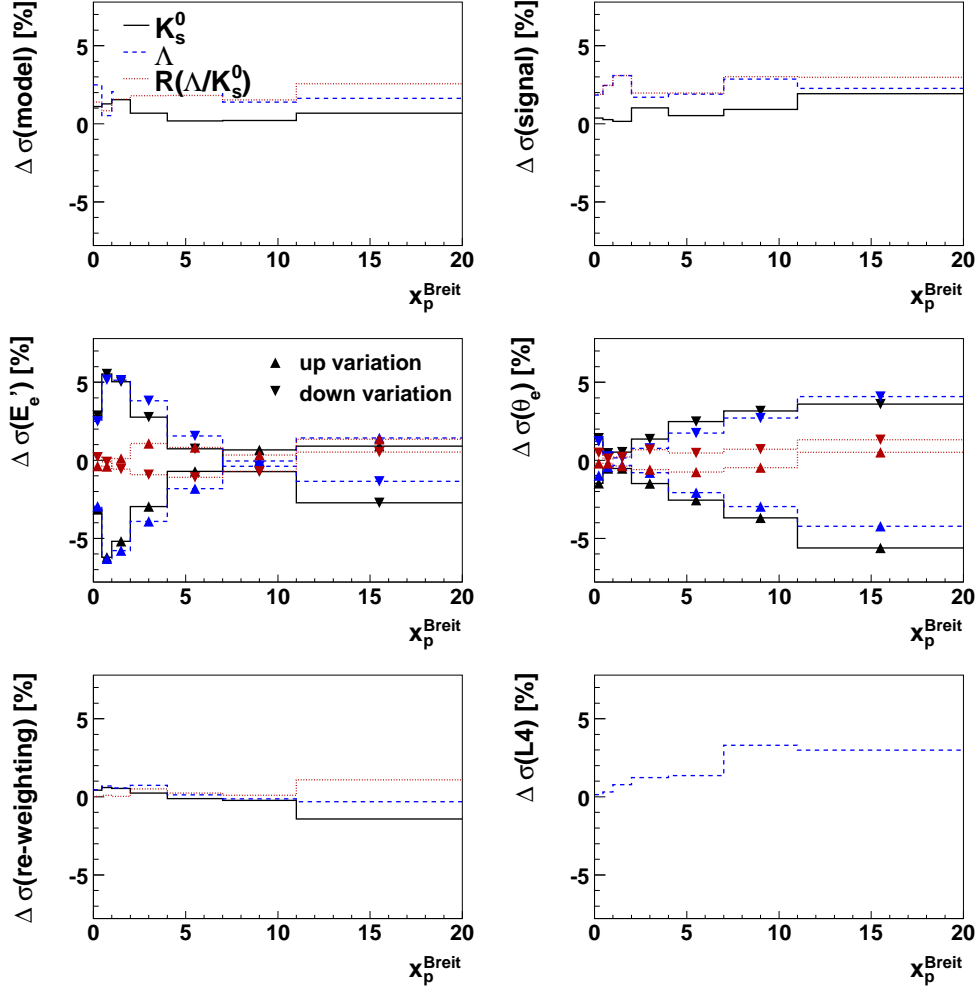
Figure C.9: The effect of the systematic sources on the differential cross-sections in x_p^{Breit} in the target hemisphere for the K_s^0 mesons (solid, black lines) for the Λ baryons (blue, dashed lines) and for the ratio $R(\Lambda/K_s^0)$ (red, dotted lines).
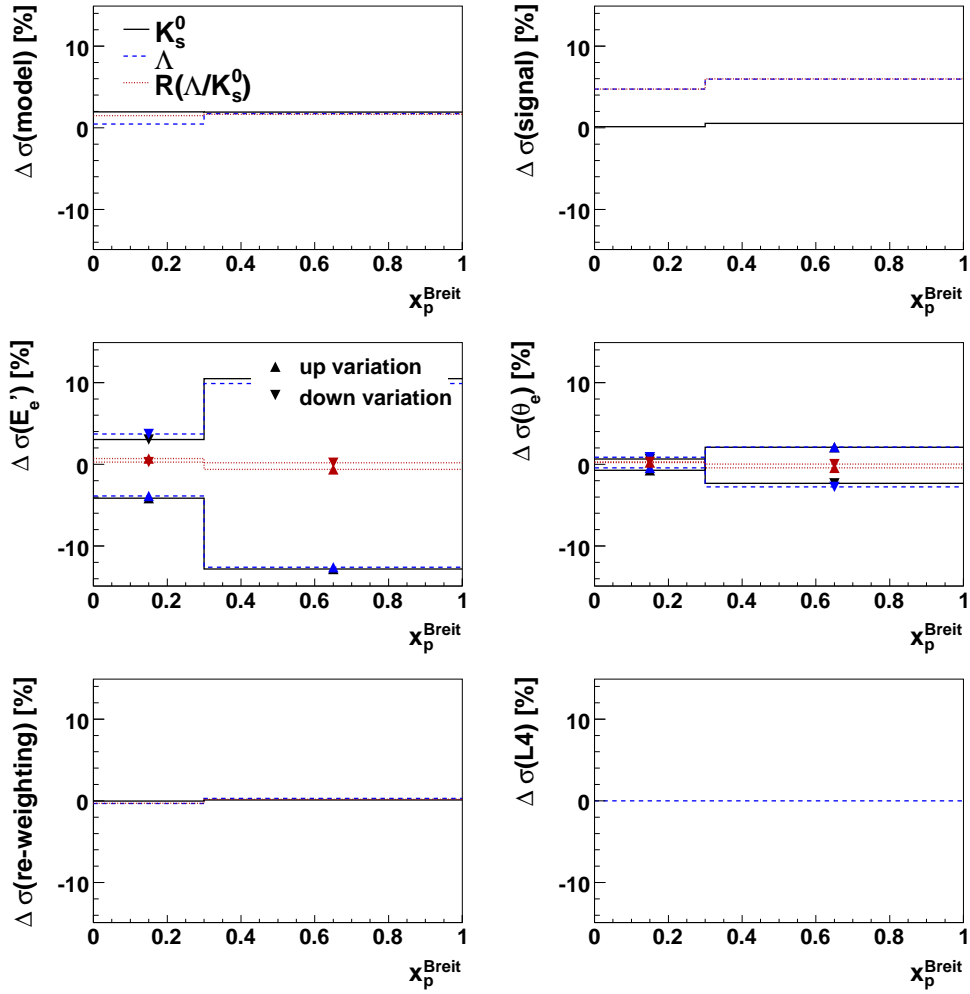
Figure C.10: The effect of the systematic sources on the differential cross-sections in x_p^{Breit} in the current hemisphere for the K_s^0 mesons (solid, black lines) for the Λ baryons (blue, dashed lines) and for the ratio $R(\Lambda/K_s^0)$ (red, dotted lines).

List of Figures

List of Tables

Bibliography

[1] J. J. Thomson, "Cathode rays," Phil. Mag. **44** (1897) 293.

[2] E. Rutherford, "The scattering of α and β particles by matter and the structure of the atom," Phil. Mag. **21** (1911) 669.

[3] J. Chadwick, "POSSIBLE EXISTENCE OF A NEUTRON," Nature **129** (1932) 312.

[4] C. D. Anderson, "THE POSITIVE ELECTRON," Phys. Rev. **43** (1933) 491.

[5] J. C. Street and E. C. Stevenson, "NEW EVIDENCE FOR THE EXISTENCE OF A PARTICLE OF MASS INTERMEDIATE BETWEEN THE PROTON AND ELECTRON," Phys. Rev. **52** (1937) 1003.

[6] H. Yukawa, "On the interaction of elementary particles," Proc. Phys. Math. Soc. Jap. **17** (1935) 48.

[7] C. M. G. Lattes, H. Muirhead, G. P. S. Occhialini and C. F. Powell, "PROCESSES INVOLVING CHARGED MESONS," Nature **159** (1947) 694.

[8] C. M. G. Lattes, G. P. S. Occhialini and C. F. Powell, "OBSERVATIONS ON THE TRACKS OF SLOW MESONS IN PHOTOGRAPHIC EMULSIONS. 1," Nature **160** (1947) 453.

[9] C. M. G. Lattes, G. P. S. Occhialini and C. F. Powell, "OBSERVATIONS ON THE TRACKS OF SLOW MESONS IN PHOTOGRAPHIC EMULSIONS. 2," Nature **160** (1947) 486.

[10] G. D. Rochester and C. C. Butler, "EVIDENCE FOR THE EXISTENCE OF NEW UNSTABLE ELEMENTARY PARTICLES," Nature **160** (1947) 855.

[11] M. Gell-Mann and A. Pais, "Behavior of neutral particles under charge conjugation," Phys. Rev. **97** (1955) 1387.

[12] M. Gell-Mann, "A Schematic Model Of Baryons And Mesons," Phys. Lett. **8** (1964) 214.

[13] G. Zweig, "An SU(3) Model For Strong Interaction Symmetry And Its Breaking," CERN-TH-401.

[14] R. Hofstadter, "Electron scattering and nuclear structure," Rev. Mod. Phys. **28** (1956) 214.

[15] D. H. Coward *et al.*, "Electron - Proton Elastic Scattering At High Momentum Transfers," Phys. Rev. Lett. **20** (1968) 292.

[16] R. L. Jaffe, "Perhaps A Stable Dihyperon," Phys. Rev. Lett. **38** (1977) 195 [Erratum-ibid. **38** (1977) 617].

[17] T. Nakano *et al.* [LEPS Collaboration], "Observation of S = +1 baryon resonance in photo-production from neutron," Phys. Rev. Lett. **91** (2003) 012002 [arXiv:hep-ex/0301020].

[18] D. Diakonov, V. Petrov and M. V. Polyakov, "Exotic anti-decuplet of baryons: Prediction from chiral solitons," Z. Phys. A **359** (1997) 305 [arXiv:hep-ph/9703373].

[19] A. Aktas *et al.* [H1 Collaboration], "Strangeness Production at Low Q2 in Deep Inelastic ep Scattering at HERA," DESY 08-095, submitted to Eur. Phys. J.

[20] A. Aktas *et al.* [H1 Collaboration], "Search for baryonic resonances decaying to Xi pi in deep-inelastic scattering at HERA," Eur. Phys. J. C **52** (2007) 507 [arXiv:0704.3594 [hep-ex]].

[21] S. Kabana [STAR Collaboration], "Exotic particle searches with STAR at RHIC," Acta Phys. Hung. A **24** (2005) 321 [arXiv:hep-ex/0406032].

[22] M. Del Degan, "A Search for Pentaquarks in ep Scattering at HERA," diploma thesis, Eidgenössische Technische Hochschule, Zürich, 2004.

[23] H. Abramowicz and A. Caldwell, "HERA collider physics," Rev. Mod. Phys. **71** (1999) 1275 [arXiv:hep-ex/9903037].

[24] R. Devenish and A.Cooper-Sarkar, "Deep Inelatic Scattering," Oxford University Press, 2004.

[25] F. Halzen and A. D. Martin, "Quarks & Leptons: An Introductory Course in Modern Particle Physics," John Wiley & Sons, 1984.

[26] W. M. Yao *et al.* [Particle Data Group], "Review of particle physics," J. Phys. G **33**, 1 (2006).

[27] J. D. Bjorken, "Asymptotic Sum Rules At Infinite Momentum," Phys. Rev. **179** (1969) 1547.

[28] C. G. . Callan and D. J. Gross, "High-energy electroproduction and the constitution of the electric current," Phys. Rev. Lett. **22** (1969) 156.

[29] E. D. Bloom *et al.*, "High-Energy Inelastic E P Scattering At 6-Degrees And 10-Degrees," Phys. Rev. Lett. **23** (1969) 930.

[30] M. Breidenbach *et al.*, "Observed Behavior Of Highly Inelastic Electron-Proton Scattering," Phys. Rev. Lett. **23** (1969) 935.

[31] L. W. Mo, "High-Energy Muon Scatterings At Fermilab/Serpukhov," Published in Lepton-Photon Symp.1975:651.

[32] R. E. Taylor, "Deep Inelastic Electron And Muon Scattering," Published in Palermo Conf.1975:0377.

[33] S. Aid *et al.* [H1 Collaboration], "A Measurement and QCD Analysis of the Proton Structure Function $F_2(x, Q\, 2)$ at HERA," Nucl. Phys. B **470** (1996) 3 [arXiv:hep-ex/9603004].

[34] J. J. Aubert *et al.* [European Muon Collaboration], "Measurement of the nucleon structure function F_2 in muon - iron interactions at 120-GeV, 250-GeV and 280-GeV," Phys. Lett. B **105** (1981) 322.

[35] D. J. Gross and F. Wilczek, "Asymptotically Free Gauge Theories. 1," Phys. Rev. D **8** (1973) 3633.

[36] H. Georgi and H. D. Politzer, "Electroproduction scaling in an asymptotically free theory of strong interactions," Phys. Rev. D **9** (1974) 416.

[37] C. Adloff *et al.* [H1 Collaboration], "Measurement and QCD analysis of neutral and charged current cross sections at HERA," Eur. Phys. J. C **30** (2003) 1 [arXiv:hep-ex/0304003].

[38] J. C. Collins and D. E. Soper, "The Theorems of Perturbative QCD," Ann. Rev. Nucl. Part. Sci. **37** (1987) 383.

[39] V. N. Gribov and L. N. Lipatov, "Deep Inelastic E P Scattering In Perturbation Theory," Sov. J. Nucl. Phys. **15** (1972) 438 [Yad. Fiz. **15** (1972) 781].

[40] L. N. Lipatov, "The parton model and perturbation theory," Sov. J. Nucl. Phys. **20** (1975) 94 [Yad. Fiz. **20** (1974) 181].

[41] G. Altarelli and G. Parisi, "Asymptotic Freedom In Parton Language," Nucl. Phys. B **126** (1977) 298.

[42] Y. L. Dokshitzer, "Calculation Of The Structure Functions For Deep Inelastic Scattering And E+ E- Annihilation By Perturbation Theory In Quantum Chromodynamics. (In Russian)," Sov. Phys. JETP **46** (1977) 641 [Zh. Eksp. Teor. Fiz. **73** (1977) 1216].

[43] E. A. Kuraev, L. N. Lipatov and V. S. Fadin, "Multi - Reggeon Processes In The Yang-Mills Theory," Sov. Phys. JETP **44** (1976) 443 [Zh. Eksp. Teor. Fiz. **71** (1976) 840].

[44] E. A. Kuraev, L. N. Lipatov and V. S. Fadin, "The Pomeranchuk Singularity In Non-abelian Gauge Theories," Sov. Phys. JETP **45** (1977) 199 [Zh. Eksp. Teor. Fiz. **72** (1977) 377].

[45] I. I. Balitsky and L. N. Lipatov, "The Pomeranchuk Singularity In Quantum Chromodynamics," Sov. J. Nucl. Phys. **28** (1978) 822 [Yad. Fiz. **28** (1978) 1597].

[46] M. Ciafaloni, "Coherence Effects in Initial Jets at Small q**2 / s," Nucl. Phys. B **296** (1988) 49.

[47] S. Catani, F. Fiorani and G. Marchesini, "QCD Coherence In Initial State Radiation," Phys. Lett. B **234** (1990) 339.

[48] S. Catani, F. Fiorani and G. Marchesini, "Small X Behavior Of Initial State Radiation In Perturbative QCD," Nucl. Phys. B **336** (1990) 18.

[49] G. Marchesini, "QCD coherence in the structure function and associated distributions at small x," Nucl. Phys. B **445** (1995) 49 [arXiv:hep-ph/9412327].

[50] X. Artru and G. Mennessier, "String model and multiproduction," Nucl. Phys. B **70** (1974) 93.

[51] B. Andersson, G. Gustafson, G. Ingelman and T. Sjostrand, "Parton Fragmentation And String Dynamics," Phys. Rept. **97** (1983) 31.

[52] B. Andersson, G. Gustafson and B. Soderberg, "A Probability Measure On Parton And String States," Nucl. Phys. B **264** (1986) 29.

[53] T. Sjostrand and M. Bengtsson, "The Lund Monte Carlo For Jet Fragmentation And E+ E- Physics. Jetset Version 6.3: An Update," Comput. Phys. Commun. **43** (1987) 367.

[54] T. Sjostrand, "High-energy physics event generation with PYTHIA 5.7 and JETSET 7.4," Comput. Phys. Commun. **82** (1994) 74.

[55] C. Michael and M. Teper, "The Glueball Spectrum in SU(3)," Nucl. Phys. B **314** (1989) 347.

[56] T. Zimmermann, "Measurement of Resonance Decays $X \rightarrow K_s^0 K_s^0$ at HERA," diploma thesis, Eidgenössische Technische Hochschule, Zürich, 2004.

[57] D. Diakonov, "Instantons at work," Prog. Part. Nucl. Phys. **51** (2003) 173 [arXiv:hep-ph/0212026].

[58] C. S. Wu, E. Ambler, R. W. Hayward, D. D. Hoppes and R. P. Hudson, "EXPERIMENTAL TEST OF PARITY CONSERVATION IN BETA DECAY," Phys. Rev. **105** (1957) 1413.

[59] J. H. Christenson, J. W. Cronin, V. L. Fitch and R. Turlay, "Evidence For The 2 Pi Decay Of The K(2)0 Meson," Phys. Rev. Lett. **13** (1964) 138.

[60] L. K. Gibbons *et al.* [E731 Collaboration], "CP and CPT symmetry tests from the two-pion decays of the neutral kaon with the Fermilab-E731 detector. (Revised version)," Phys. Rev. D **55** (1997) 6625.

[61] W. Hofmann, "PRODUCTION OF STRANGE PARTICLES IN HADRONIZATION PROCESSES," Nucl. Phys. A **479**, 337 (1988).

[62] A.K. Wroblewski, "Soft Hadron Physics," Plenary talk given at 25 ICHEP, Singapore 1990, published in H.E.Phys. 1990: 125 (QCD161:H51:1990).

[63] W. Bartel *et al.* [JADE Collaboration], "Charged Particle And Neutral Kaon Production In E+ E- Annihilation At Petra," Z. Phys. C **20** (1983) 187.

[64] M. Althoff *et al.* [TASSO Collaboration], "A Detailed Study Of Strange Particle Production In E+ E- Annihilation At High-Energy," Z. Phys. C **27** (1985) 27.

[65] M. Derrick *et al.*, "Hadron Production In E+ E- Annihilation At S**(1/2) = 29-Gev," Phys. Rev. D **35** (1987) 2639.

[66] P. D. Acton *et al.* [OPAL Collaboration], "A Measurement of strange baryon production in hadronic Z0 decays," Phys. Lett. B **291** (1992) 503.

[67] G. Alexander *et al.* [OPAL Collaboration], "Strange baryon production in hadronic Z0 decays," Z. Phys. C **73** (1997) 569.

[68] G. Alexander *et al.* [OPAL Collaboration], "Sigma+, Sigma0 and Sigma- hyperon production in hadronic Z0 decays," Z. Phys. C **73** (1997) 587.

[69] P. Abreu *et al.* [DELPHI Collaboration], "Production of strange particles in the hadronic decays of the Z0," Phys. Lett. B **275** (1992) 231.

[70] P. Abreu *et al.* [DELPHI Collaboration], "Strange baryon production in Z hadronic decays," Z. Phys. C **67** (1995) 543.

[71] P. Abreu *et al.* [DELPHI Collaboration], "pi+-, K+-, p and anti-p production in Z0 → q anti-q, Z0 → b anti-b, Z0 → u anti-u, d anti-d, s anti-s," Eur. Phys. J. C **5** (1998) 585.

[72] R. Barate *et al.* [ALEPH Collaboration], "Studies of quantum chromodynamics with the ALEPH detector," Phys. Rept. **294** (1998) 1.

[73] G. Abbiendi *et al.* [OPAL Collaboration], "Leading particle production in light flavour jets," Eur. Phys. J. C **16** (2000) 407 [arXiv:hep-ex/0001054].

[74] S. Aid *et al.* [H1 Collaboration], "Strangeness production in deep-inelastic positron proton scattering at HERA," Nucl. Phys. B **480** (1996) 3 [arXiv:hep-ex/9607010].

[75] C. Adloff *et al.* [H1 Collaboration], "Photoproduction of K0 and Lambda at HERA and a comparison with deep inelastic scattering," Z. Phys. C **76** (1997) 213 [arXiv:hep-ex/9705018].

[76] C. Risler, "Produktion seltsamer neutraler Teilchen in tiefinelastischer Streuung bei HERA," Ph.D. thesis, 2004, Universität Hamburg (in German), available from http://www-h1.desy.de/publications/theses_list.html.

[77] M. Derrick *et al.* [ZEUS Collaboration], "Neutral strange particle production in deep inelastic scattering at HERA," Z. Phys. C **68** (1995) 29 [arXiv:hep-ex/9505011].

[78] S. Chekanov *et al.* [ZEUS Collaboration], "Measurement of K0(S), Lambda, anti-Lambda production at HERA," Eur. Phys. J. C **51** (2007) 1 [arXiv:hep-ex/0612023].

[79] R. J. Fries, B. Muller, C. Nonaka and S. A. Bass, "Hadronization in heavy ion collisions: Recombination and fragmentation of partons," Phys. Rev. Lett. **90** (2003) 202303 [arXiv:nucl-th/0301087].

[80] S. A. Bass, B. Muller and D. K. Srivastava, "Net baryon density in Au + Au collisions at the Relativistic Heavy Ion Collider," Phys. Rev. Lett. **91**, 052302 (2003) [arXiv:nucl-th/0212103].

[81] M. Arneodo *et al.* [European Muon Collaboration], "Strangeness production in deep inelastic muon nucleon scattering at 280-GeV," Z. Phys. C **34** (1987) 283.

[82] D. Strottman, "Multi - Quark Baryons And The Mit Bag Model," Phys. Rev. D **20** (1979) 748.

[83] M. Praszalowicz, "SU(3) SKYRMION," Published in Cracow Workshop 1987:112.

[84] H. Weigel, "Radial excitations of low-lying baryons and the Z+ penta-quark," Eur. Phys. J. A **2** (1998) 391 [arXiv:hep-ph/9804260].

[85] R. L. Jaffe and F. Wilczek, "Diquarks and exotic spectroscopy," Phys. Rev. Lett. **91**, 232003 (2003) [arXiv:hep-ph/0307341].

[86] M. Karliner and H. J. Lipkin, "The constituent quark model revisited: Quark masses, new predictions for hadron masses and K N pentaquark," arXiv:hep-ph/0307243.

[87] A. De Rujula, H. Georgi and S. L. Glashow, "Hadron Masses In A Gauge Theory," Phys. Rev. D **12**, 147 (1975).

[88] C. Alt *et al.* [NA49 Collaboration], "Observation of an exotic S = -2, Q = -2 baryon resonance in proton proton collisions at the CERN SPS," Phys. Rev. Lett. **92** (2004) 042003 [hep-ex/0310014].

[89] H. Y. Cheng, C. K. Chua and C. W. Hwang, "Light-front approach for heavy pentaquark transitions," Phys. Rev. D **70** (2004) 034007 [arXiv:hep-ph/0403232].

[90] "Pentaquark Theta+, constituent quark structures, and prediction of charmed Theta/c0 and bottomed Theta/b+," Phys. Rev. D **69** (2004) 094029 [arXiv:hep-ph/0308176].

[91] P. Z. Huang, Y. R. Liu, W. Z. Deng, X. L. Chen and S. L. Zhu, "Heavy pentaquarks," Phys. Rev. D **70** (2004) 034003 [arXiv:hep-ph/0401191].

[92] I. W. Stewart, M. E. Wessling and M. B. Wise, "Stable heavy pentaquark states," Phys. Lett. B **590** (2004) 185 [arXiv:hep-ph/0402076].

[93] B. Wu and B. Q. Ma, "Exotic baryons with charm number +-1 from Skyrme model," Phys. Rev. D **70** (2004) 034025 [arXiv:hep-ph/0402244].

[94] A. Aktas *et al.* [H1 Collaboration], "Evidence for a narrow anti-charmed baryon state," Phys. Lett. B **588** (2004) 17 [arXiv:hep-ex/0403017].

[95] M. A. Nowak, M. Praszalowicz, M. Sadzikowski and J. Wasiluk, "Chiral doublers of heavy-light baryons," Phys. Rev. D **70** (2004) 031503 [arXiv:hep-ph/0403184].

[96] S. Nussinov, "Remarks on the Theta (1540) pentaquark," Phys. Rev. D **69** (2004) 116001 [arXiv:hep-ph/0403028].

[97] M. Karliner and H. J. Lipkin, "The anticharmed exotic baryon Theta/c and its relatives," arXiv:hep-ph/0307343.

[98] R. L. Jaffe, "Perhaps A Stable Dihyperon," Phys. Rev. Lett. **38** (1977) 195 [Erratum-ibid. **38** (1977) 617].

[99] B. Aubert *et al.* [BABAR Collaboration], "Observation of a narrow meson decaying to $D_s^+ \pi^0$ at a mass of 2.32-GeV/c^2," Phys. Rev. Lett. **90** (2003) 242001 [arXiv:hep-ex/0304021].

[100] V. D. Burkert, "Have pentaquark states been seen?," Int. J. Mod. Phys. A **21** (2006) 1764 [arXiv:hep-ph/0510309].

[101] K. H. Hicks, "Experimental search for pentaquarks," Prog. Part. Nucl. Phys. **55** (2005) 647 [arXiv:hep-ex/0504027].

[102] M. Danilov and R. Mizuk, "Experimental review on pentaquarks," arXiv:0704.3531 [hep-ex].

[103] J. M. Link *et al.* [FOCUS Collaboration], "Search for a strongly decaying neutral charmed pentaquark," Phys. Lett. B **622** (2005) 229 [arXiv:hep-ex/0506013].

[104] S. Chekanov *et al.* [ZEUS Collaboration], "Search for a narrow charmed baryonic state decaying to D*+- p-+ in e p collisions at HERA," Eur. Phys. J. C **38** (2004) 29 [arXiv:hep-ex/0409033].

[105] K. Krüger for the H1 Collaboration, "Investigation of the $D^* p$ Resonance in the $3\,\mathrm{GeV}$ Region with HERAII Data," presented at the XVI International Workshop on Deep-Inelastic Scattering, April 7-11, 2008, London.

[106] V. Kubarovsky *et al.* [CLAS Collaboration], "Observation of an exotic baryon with S = +1 in photoproduction from the proton," Phys. Rev. Lett. **92** (2004) 032001 [Erratum-ibid. **92** (2004) 049902] [arXiv:hep-ex/0311046].

[107] V. Kubarovsky and S. Stepanyan [CLAS Collaboration], "Evidence for an exotic baryon state, Theta(1540)+, in photoproduction reactions from protons and deuterons with CLAS," AIP Conf. Proc. **698** (2004) 543 [arXiv:hep-ex/0307088].

[108] M. Battaglieri *et al.* [CLAS Collaboration], "Search for Theta(1540)+ pentaquark in high statistics measurement of gamma p → anti-K0 K+ n at CLAS," Phys. Rev. Lett. **96** (2006) 042001 [arXiv:hep-ex/0510061].

[109] B. McKinnon *et al.* [CLAS Collaboration], "Search for the Theta+ pentaquark in the reaction gamma d → p K- K+ n," Phys. Rev. Lett. **96** (2006) 212001 [arXiv:hep-ex/0603028].

[110] D. G. Ireland *et al.* [CLAS Collaboration], "A Bayesian analysis of pentaquark signals from CLAS data," Phys. Rev. Lett. **100** (2008) 052001 [arXiv:0709.3154 [hep-ph]].

[111] M. I. Adamovich *et al.* [WA89 Collaboration], "Search for the exotic Xgr –(1860) resonance in 340 GeV c Sigma –nucleus interactions," Phys. Rev. C **70** (2004) 022201 [hep-ex/0405042].

[112] S. Schael *et al.* [ALEPH Collaboration], "Search for pentaquark states in Z decays," Phys. Lett. B **599** (2004) 1.

[113] J. Z. Bai *et al.* [BES Collaboration], "Search for the pentaquark state in psi(2S) and J/psi decays to K0(S) p K- anti-n and K0(S) anti-p K+ n," Phys. Rev. D **70** (2004) 012004 [hep-ex/0402012].

[114] I. Abt *et al.* [HERA-B Collaboration], "Limits for the central production of Theta+ and Xi– pentaquarks in 920-GeV p A collisions," Phys. Rev. Lett. **93** (2004) 212003 [hep-ex/0408048].

[115] A. Airapetian *et al.* [HERMES Collaboration], "Search for an exotic S = -2, Q = -2 baryon resonance at a mass near 1862-MeV in quasi-real photoproduction," Phys. Rev. D **71** (2005) 032004 [hep-ex/0412027].

[116] S. Chekanov *et al.* [ZEUS Collaboration], "Search for pentaquarks decaying to Xi pi in deep inelastic scattering at HERA," Phys. Lett. B **610** (2005) 212 [hep-ex/0501069].

[117] E. S. Ageev *et al.* [COMPASS Collaboration], "Search for the Phi(1860) pentaquark at COMPASS," Eur. Phys. J. C **41** (2005) 469 [hep-ex/0503033].

[118] J. M. Link *et al.* [FOCUS Collaboration], "Search for a strongly decaying neutral charmed pentaquark," Phys. Lett. B **622** (2005) 229 [arXiv:hep-ex/0506013].

[119] V. V. Barmin *et al.* [DIANA Collaboration], "Further evidence for formation of a narrow baryon resonance with positive strangeness in K+ collisions with Xe nuclei," Phys. Atom. Nucl. **70** (2007) 35 [arXiv:hep-ex/0603017].

[120] W. Buchmüller and G. Ingelman (editors), "Physics at HERA, Volume 3", proceedings of the workshop, Hamburg, October 29-30, 1991.

[121] R. Brun *et al.*, GEANT3, Technical Report CERN-DD/EE/84-1, CERN, 1987.

[122] G. A. Schuler and H. Spiesberger, in *Proc. of the Workshop on HERA Physics*, edited by W. Buchmuller and G. Ingelman (DESY, Hamburg,1992),vol.3,p. 1419.

[123] J. Pumplin, D. R. Stump, J. Huston, H. L. Lai, P. Nadolsky and W. K. Tung, "New generation of parton distributions with uncertainties from global QCD analysis," JHEP **0207**, 012 (2002) [arXiv:hep-ph/0201195].

[124] M. Gluck, E. Reya and A. Vogt, "Dynamical Parton Distributions Of The Proton And Small X Physics," Z. Phys. C **67** (1995) 433.

[125] G. Ingelman, A. Edin and J. Rathsman, "LEPTO 6.5 - A Monte Carlo Generator for Deep Inelastic Lepton-Nucleon Scattering," Comput. Phys. Commun. **101**, 108 (1997) [arXiv:hep-ph/9605286].

[126] B. Andersson, G. Gustafson, L. Lonnblad and U. Pettersson, "Coherence Effects in Deep Inelastic Scattering," Z. Phys. C **43**, 625 (1989).

[127] L. Lönnblad, "Rapidity gaps and other final state properties in the colour dipole model for deep inelastic scattering," Z. Phys. C **65**, 285 (1995).

[128] L. Lönnblad, "Ariadne Version 4: A Program For Simulation Of QCD Cascades Implementing The Colour Dipole Model," Comput. Phys. Commun. **71**, 15 (1992).

[129] A. Kwiatkowski, H. Spiesberger and H. J. Mohring, "HERACLES: AN EVENT GENERATOR FOR e p INTERACTIONS AT HERA ENERGIES INCLUDING RADIATIVE PROCESSES: VERSION 1.0," Comput. Phys. Commun. **69**, 155 (1992).

[130] T. Sjostrand, S. Mrenna and P. Skands, "PYTHIA 6.4 physics and manual," JHEP **0605** (2006) 026 [arXiv:hep-ph/0603175].

[131] G. A. Voss and B. H. Wiik, "The Electron proton collider HERA," Ann. Rev. Nucl. Part. Sci. **44** (1994) 413.

[132] I. Abt *et al.* [H1 Collaboration], "The H1 detector at HERA," Nucl. Instrum. Meth. A **386** (1997) 310.

[133] I. Abt *et al.* [H1 Collaboration], "The Tracking, calorimeter and muon detectors of the H1 experiment at HERA," Nucl. Instrum. Meth. A **386** (1997) 348.

[134] C. Kleinwort, "H1 Alignement Experience" in *Proc. of the First LHC Detector Alignment Workshop*, edited by S. Blusk et al. CERN-2007-004, p.41.

[135] S. Burke *et al.*, "Track Finding and Fitting in the H1 Forward Track Detector," DESY Report, **95-132**.

[136] J. Burger *et al.*, "The Central jet chamber of the H1 experiment," Nucl. Instrum. Meth. A **279** (1989) 217.

[137] S. Egli, C. A. Meyer, P. Robmann, U. Straumann, P. Truoel, R. Eichler and R. Holzreuter, "THE CENTRAL INNER Z DRIFT CHAMBER OF THE H1 EXPERIMENT," Nucl. Instrum. Meth. A **283** (1989) 487.

[138] K. Muller *et al.*, "Construction and performance of a thin cylindrical multiwire proportional chamber with cathode pad readout for the H1 experiment," Nucl. Instrum. Meth. A **312** (1992) 457.

[139] D. Pitzl *et al.*, "The H1 silicon vertex detector," Nucl. Instrum. Meth. A **454** (2000) 334 [arXiv:hep-ex/0002044].

[140] B. Andrieu *et al.* [H1 Calorimeter Group], "The H1 liquid argon calorimeter system," Nucl. Instrum. Meth. A **336** (1993) 460.

[141] R. D. Appuhn *et al.* [H1 SPACAL Group], "The H1 lead/scintillating-fibre calorimeter," Nucl. Instrum. Meth. A **386** (1997) 397.

[142] W. Hildesheim *et al.*, "The Plug Calorimeter Users Guide," H1 Internal Note, **372** (08/1994).

[143] J. Ebert, "The H1-Tail Catcher Hardware and Software Performance," H1 Internal Note, **448** (08/1995).

[144] T. Nicholls *et al.* [H1 SPACAL Group], "Performance of an electromagnetic lead / scintillating fiber calorimeter for the H1 detector," Nucl. Instrum. Meth. A **374** (1996) 149.

[145] I. Abt *et al.* [H1 Collaboration], "Technical Proposal for the Upgrade of the Backward Region of the H1 Detector," DESY Internal Report, **PRC-93-02**.

[146] H. Bethe and W. Heitler, "On the Stopping of fast particles and on the creation of positive electrons," Proc. Roy. Soc. Lond. A **146** (1934) 83.

[147] H1 Collaboration, "Luminosity Measurement in the H1 Experiment at HERA," Proceedings of the International Conference on High Energy Physics, DESY, 1996.

[148] K. Hoeger, "Measurement of x, y and Q^2 in neutral current events," Band I of the proceedings of the workshop *Physics at HERA*, Hamburg (1991) 43.

[149] U. Bassler and G. Bernardi, "On the kinematic reconstruction of deep inelastic scattering at HERA: The Sigma method," Nucl. Instrum. Meth. A **361** (1995) 197 [arXiv:hep-ex/9412004].

[150] S. Glazov, privat communications.

[151] J. Gassner, "A Measurement of D-Meson Production at HERA by Decay Vertex Identification," Ph.D. thesis, Eidgenössische Technische Hochschule, Zürich, 2002.

[152] W. Erdmann, "SV - a package for secondary vertex fitting," http://www-h1.desy.de/iwork/ibtag/workpages/werdmann/sv/sv.html.

[153] R. Luchsinger and C. Grab, "Vertex reconstruction by means of the method of Kalman filter," Comput. Phys. Commun. **76** (1993) 263.

[154] R. P. Feynman, "Photon-Hadron Interactions", Benjamin, N.Y. (1972).

[155] S. Chekanov, "Issues in leading particle and charm production in DIS at HERA," Proceedings of the workshop *Monte Carlo Generators for HERA Physics*, Hamburg (1999) 309.

[156] J. Breitweg *et al.* [ZEUS Collaboration], "Angular and current-target correlations in deep inelastic scattering at HERA," Eur. Phys. J. C **12** (2000) 53 [arXiv:hep-ex/9905050].

[157] R. W. Thompson, A. V. Buskirk, L. R. Etter, C. J. Karzmark and R. H. Rediker, "AN UNUSUAL EXAMPLE OF V0 DECAY," Phys. Rev. **90** (1953) 1122.

[158] J. Podolanski and R. Armenteros, "Analysis of V-Events," Phil. Mag. **45** (1954) 13.

[159] B. Z. Kopeliovich and B. G. Zakharov, "Novel Mechanisms Of Baryon Number Flow Over Large Rapidity Gap," Z. Phys. C **43** (1989) 241.

[160] B. Kopeliovich and B. Povh, "Baryon asymmetry of the proton sea at low x," Z. Phys. C **75**, 693 (1997) [arXiv:hep-ph/9607486].

[161] T. Junk, "Confidence level computation for combining searches with small statistics," Nucl. Instrum. Meth. A **434** (1999) 435 [hep-ex/9902006].

[162] R. D. Cousins and V. L. Highland, "Incorporating systematic uncertainties into an upper limit," Nucl. Instrum. Meth. A **320** (1992) 331.

[163] J. Steinhart, "Die Messung des totalen $c\bar{c}$-Photoproduktions-Wirkungsquerschnittes durch die Rekonstruktion von Λ_c-Baryonen unter Verwendung der verbesserten dE/dx-Teilchenidentifikations am H1 Experimant bei HERA," Dissertation, University of Hamburg, 1999.

Acknowledgments

Working in a large international collaboration like H1 was a very pleasant and challenging activity. This work would not have been possible without the assistance of many people. I am indebted to everybody contributing to the success of the H1 experiment. However, there are some people whom I owe special thanks:

Firstly, i would like to thank my supervisor, Ralph Eichler, not only for giving me the opportunity to work on this interesting topic but also for his competent advice during my investigations. I'd also like to thank Urs Langenegger for acting as co-examiner and for his valuable comments on this thesis.

This work would not have been possible without the outstanding support of my advisor Christoph Grab. With his expert knowledge he was always a great help when the analysis got stuck. Furthermore, I am especially grateful to him for carefully proof-reading the thesis.

Special thanks go to the present and former members of the ETH group, Guillaume Leibenguth, Michel Sauter, Tobias Zimmermann, Nik Berger, Ron Weber, Simon Baumgartner, David Meer and Salvatore Mangano not only for their friendly assistance, but also for their moral support. I am grateful to Guillaume Leibenguth for proof-reading this thesis. On a more private side I would like to thank these people for showing me the hip locations in Hamburg and spending some long nights there.

Many other people helped me with the physical details of the analysis. I would like to especially mention the present and former conveners of the HaQ-working group: Christiane Risler, Dan Traynor and Günter Grindhammer for their pieces of advice. Great help not only on tracking issues but also on other technical and physical problems was provided by Daniel Pitzl. Benno List introduced me to the beauty of well-written C++ code.

I thank Anna Falkiewicz for spending some long nights working on the last polishing of the cross-section analysis for the publication.

On a more personal note I thank Petra Häfliger and Markus Bischofberger for spending relaxing coffee breaks and fine dinners in Zürich's downtown.

Finally, I want to thank my wife Nadine for her patience and love. Being married with a particle physicist doing such obscure things is for sure not always easy. I want to especially thank my children Jana Alina and Dario Leandro, the sunshine in my life, to whom this thesis is dedicated. In return they will be forced to read this work until they understand it; fair is fair. Last but not least I want to thank my parents for their support during my whole education.

Curriculum Vitae

MARC ANGELO DEL DEGAN

Born April 14 1978
in Zürich, Switzerland

Citizen of Buja, Italy

EDUCATION

2005 – 2008	Doctoral studies at ETH Zürich, research at the H1 experiment at DESY, Hamburg
2004	Diploma in Physics at ETH Zürich, awarded with the *Willi-Studer prize*, diploma thesis *"A Search for Pentaquarks in ep Scattering at HERA"* in the group of Prof. Ralph Eichler
1998 – 2004	Studies of physics at ETH Zürich
1998	Eidgenössische Matura Typus C
1992 - 1998	Gymnasium in Pfäffikon SZ